TESIS DOCTORAL

A multiwavelength and multiscale study of Luminous and Ultraluminous Infrared Galaxies in the local Universe

Rubén Herrero Illana

Memoria presentada para optar al grado de
Doctor en Física y Matemáticas

Directores:
Dr. Miguel Ángel Pérez Torres
Dr. Antonio Alberdi Odriozola

Universidad de Granada
Programa de Doctorado en Física y Matemáticas

Editor: Editorial de la Universidad de Granada
Autor: Rubén Herrero Illana
D.L.: GR 265-2015
ISBN: 978-84-9083-280-6

A mis padres.

A Zaira.

Agradecimientos

Detrás de una tesis doctoral hay siempre mucho trabajo y sacrificio. Pero aun con todo mi esfuerzo, me confieso incapaz de haber completado este proyecto sin la ayuda de mucha gente que, de una u otra manera, ha contribuido para que esto saliera adelante. Cada uno ha ayudado a su manera: de algunos he aprendido sobre Ciencia, otros me han ayudado a olvidarme de ella por un momento, y otros *simplemente* han estado ahí apoyándome a lo largo del camino. Tanto es así, que esta tesis va a comenzar con una injusticia, pues para ser honesto esta sección debería ser más larga que cualquiera de los capítulos del libro que tienes en tus manos. Y es que una tesis es algo más que el trabajo científico de cuatro años: es una etapa, parte de un proyecto vital, y como tal son muchas las personas que de una u otra manera han estado involucradas y merecen mi agradecimiento.

La primera posición en esta lista no admite discusión: gracias papá y mamá, por apoyarme como sólo unos padres saben hacer, por haberme enseñado con vuestro ejemplo el valor del esfuerzo y la fuerza de la ilusión, y sobre todo por haber querido dármelo todo y haber tenido la sensatez de no siempre hacerlo. Gracias por haber intentado educarme en el difícil equilibrio entre mantener los pies en la tierra y a la vez dejar que mi cabeza se fuera a las estrellas. Quiero agradecerle también su apoyo al resto de mi familia: a mi hermano David, a mis tíos, a mis primos (¡nunca perdáis la curiosidad por las cosas, Sara y Álvaro!) y a mis abuelos, los que estáis y los que no, por haberme apoyado siempre desde que me marché de Burgos para estudiar *esas cosas del cielo*.

Una tesis no es tal sin un mentor que te guíe, te enseñe y corrija tus errores. En mi caso he tenido la enorme suerte de no tener un mentor, sino dos. Gracias Miguel y Antxon por todo lo que me habéis enseñado, por

ser el perfecto ejemplo de sinergia, por haber estado siempre disponibles para escucharme y por haber sabido elegir los momentos exactos en los que ser directores, consejeros, maestros y amigos. Sin duda, esta tesis es tan vuestra como mía. Gracias también al resto del grupo de trabajo: Mónica, Francesco, Joel y Naím, así como Cristina y Gabriela durante mi primer año, por vuestro apoyo durante todo este tiempo.

La componente social a lo largo de un doctorado es fundamental para no perder la cordura. Tuve la suerte de llegar a Granada y encontrarme de frente con Rubén, Fran y Haritz, que de cordura andaban escasos. Uno de los mejores recuerdos que guardaré de este periodo son todas esas fiestas locas y viajes de carretera con vosotros tres. Eso sí, alguien os lo tenía que decir: sois muy feos. Hay otra lista interminable de gente en Granada a quien me siento en la obligación de agradecerle su amistad: Silvia, Sol, Caro, Gabi, Andre, Fede, Antía, Ari, Lorena... estos cuatro años nunca habrían sido lo mismo sin vosotros.

El ambiente en el trabajo también es importante en el día a día y para sobrellevar los momentos más grises en los que ese programa se niega a compilar o esos datos no te dicen lo que quieres oír. Gracias a mis compañeros del Instituto de Astrofísica de Andalucía, por crear una atmósfera agradable en la que trabajar. Mención especial a Paco y a Ana, el mejor conserje y la mejor guarda que el IAA puede desear.

I want to thank Rob Beswick and Tom Muxlow for their help during my stay in Manchester in 2011 and Aaron Evans, George Privon and Sabrina Stierwalt for their support in Charlottesville during the summer of 2013. Still in the international section, a special thank you to Jack and Colette for their friendship, hospitality and support: most probably, this thesis wouldn't be written in English if it wasn't for everything I learned with you. Go raibh maith agat!

Gracias al hospital Saint-André de Burdeos y a Rocío, por ser mi intérprete y enfermera improvisada durante la operación de apendicitis más oportuna que ha existido nunca, y gracias al ministerio de economía y competitividad

por hacerme sentir como un espía capturado en acto de servicio cuando su gobierno reniega de él.

Gracias a los pucelanos: Marcos, Lente, Irene, Amaia y Marta, por haber seguido ahí desde hace ya once años, por vuestra amistad y por haber sido los mejores testigos de mi evolución. Aunque no hablo con vosotros todo lo que me gustaría, os tengo siempre presentes.

Y gracias a los canarios. Fue en Tenerife donde empecé a descubrir la Astronomía junto a mucha otra gente, algunos de los cuales se convirtieron en buenos amigos de esos que confías en conservar a pesar del tiempo y la distancia. Eskerrik asko Eneko por contagiarme tu optimismo y tus ansias de libertad. Gracias Parda por tus empeños por intentar mantener a la gente unida. Gracias Lore por transmitirme tu tranquilidad, entonces y ahora. Gracias Alba, Jorge, Agus, Alberto, Bea, Carol, Pablo, Itziar, por todos los buenos momentos.

Recuerdo con especial cariño mi primer contacto real con la investigación en un caluroso verano, allá por 2009, en el LAEFF. Mi agradecimiento para toda la gente que trabajaba allí por haberme hecho sentir como en casa durante aquellos tres meses. Sobre todo, gracias Fran por confiar en mí, por ser un jefe excepcional y por engancharme a este mundillo. Y gracias Amelia: ahora valoro aún más todo el tiempo que perdiste explicándole trivialidades a un yogurín mientras terminabas de escribir tu tesis.

Y por último, las líneas más difíciles, esas que te dejan un sabor agridulce porque, ya antes de empezar a escribirlas sabes que nunca podrán reflejar todo lo que realmente quieres expresar. Gracias Zaira por ser como eres, por compartir tu día a día conmigo y hacerme verlo todo de otro color. Gracias por esforzarte en conocerme como nadie, por tu risa contagiosa y por dejarte querer. Eres lo mejor que me llevo de todo este tiempo y cada día que pasa me alegro más de tenerte a mi lado. Gracias por compartir mis cargas, que contigo pierden su peso. ¡Ahora te toca a ti!

Rubén Herrero Illana

Granada, 19 de septiembre de 2014

Declaración

El doctorando, Rubén Herrero Illana, y los directores de la tesis, Miguel Ángel Pérez Torres y Antonio Alberdi Odriozola, garantizamos, al firmar esta tesis doctoral, que el trabajo ha sido realizado por el doctorando bajo la dirección de los directores de la tesis y hasta donde nuestro conocimiento alcanza, en la realización del trabajo, se han respetado los derechos de otros autores a ser citados, cuando se han utilizado sus resultados o publicaciones.

Granada, a 19 de septiembre de 2014

Miguel Ángel Pérez Torres

Antonio Alberdi Odriozola

Rubén Herrero Illana

Resumen en castellano

Esta tesis comprende un estudio multifrecuencia de las galaxias luminosas y ultraluminosas en el infrarrojo (LIRGs y ULIRGs, respectivamente) en el Universo local, estudiadas a diferentes escalas espaciales. El trabajo se ha centrado en las propiedades de los brotes de formación estelar masiva, en la contribución de los núcleos activos de galaxias (AGN) y en la interrelación entre ambos fenómenos. El estudio de las (U)LIRGs locales es el mejor escenario para comprender las propiedades de estos objetos a distancias cosmológicas, donde su contribución domina el fondo cósmico infrarrojo.

La primera aproximación al estudio de las (U)LIRGs ha consistido en un estudio de línea espectral en el rango milimétrico con datos obtenidos en el radiotelescopio IRAM 30 m de Pico Veleta, en Granada, de 56 (U)LIRGs de la muestra del proyecto GOALS. Hemos observado y analizado espectros de varias líneas moleculares, centrándonos en el estudio del monóxido de carbono (CO), conocido trazador del gas molecular. Hemos explorado la relación entre ambos, así como las propiedades del gas molecular que se derivan de su estudio. Además de caracterizar nuestra muestra, este estudio nos ha permitido confirmar la hipótesis de que el cociente isotópico entre ^{12}CO y ^{13}CO es proporcional a la temperatura del polvo presente en las (U)LIRGs, lo que se explicaría con una disminución de la profundidad óptica de ^{12}CO con la temperatura. Asimismo hemos estudiado la cinemática y la distribución del gas a partir de los perfiles espectrales de varias líneas moleculares.

En una segunda parte, hemos analizado la región del kiloparsec central de una muestra de 12 LIRGs, hemos hecho hincapié en la importancia del estudio multifrecuencia con el objetivo de derivar las propiedades de la formación estelar en estas galaxias, así como en el estudio de la contribución de

los posibles núcleos activos de galaxias a la luminosidad bolométrica de las (U)LIRGs. En una de las galaxias, la LIRG NGC1614, hemos realizado un profundo estudio multifrecuencia, incluyendo datos radio, infrarrojo, óptico y rayos X. Estos datos nos han permitido establecer, entre otras cosas, que la emisión infrarroja de la región circunnuclear está dominada completamente por un potente brote de formación estelar y, en caso de que exista un AGN, éste es completamente irrelevante. Hemos realizado también un estudio exploratorio donde hemos utilizado un mapa de Paschenα para desarrollar un método para aislar las dos componentes predominantes en la emisión radio a 8.4 GHz: la emisión térmica y la emisión sincrotrón. Esta descomposición nos ha permitido utilizar los diferentes porcentajes de cada emisión en diferentes regiones para obtener las edades aproximadas de las mismas, permitiéndonos comprender mejor el fenómeno de los brotes de formación estelar masiva (starbursts).

Asimismo, hemos estudiado la formación estelar masiva en la LIRG cercana más luminosa, Arp 299, a través de las supernovas que explotan tanto en el núcleo de su región más brillante (Arp 299-A), como en sus alrededores. Gracias a imágenes radio del interferómetro e-MERLIN obtenidas a partir del proyecto de legado LIRGI (IPs: J. Conway & M.Á. Pérez-Torres) descubrimos la contrapartida en radio de la supernova SN2010P. Utilizando varias épocas de observación, modelamos su curva de luz a lo largo del tiempo, siendo capaces de establecer su naturaleza como supernova de tipo IIb. Otra supernova en el sistema (SN2010O), cuya explosión ocurrió apenas unos días antes que la de la SN2010P, no mostró sin embargo emisión radio, a pesar de nuestros esfuerzos por detectarla en diferentes épocas. Este radiosilencio en épocas tardías se debe probablemente a su rápida evolución, compatible con una supernova de tipo Ib. En cuanto a nuestro estudio de las supernovas en la región central de Arp 299-A, utilizamos técnicas de radiointerferometría de muy larga base (VLBI). Analizando observaciones de varias épocas a lo largo de 2.5 años utilizando el European VLBI Network (EVN) pudimos confirmar 25 fuentes compactas, la mayor parte de las cuales son supernovas o remanentes de supernovas, que nos permitieron derivar una tasa de explosión de supernovas de $\sim$0.8 SN por año, compatible

con estudios anteriores. Encontramos además que la mayor parte de la formación estelar en Arp 299-A tiene lugar en los 150 parsec centrales.

La última aproximación al estudio de las (U)LIRGs realizado en esta tesis doctoral ha consistido en el uso de técnicas de radiointerferometría de muy larga base (VLBI) con el fin de resolver las regiones más nucleares de estas galaxias. Dado que las observaciones radio no están afectadas por la extinción debida al polvo y gracias a la alta resolución angular que proporcionan las observaciones VLBI, esta técnica es la única con la que se puede realizar un estudio de este tipo a escalas nucleares. Es en estas regiones donde se producen los brotes de formación estelar más violentos y donde la interacción entre éstos y la presencia de los núcleos activos que existen en algunas (U)LIRGs se hace más evidente. Hemos estudiado las supernovas detectadas mediante VLBI en los núcleos de tres galaxias con brotes de formación estelar, Arp 299-A, Arp 220 y M82, para determinar cómo se distribuyen espacialmente. Esta distribución radial, que parece responder a un perfil exponencial, ha sido extensamente estudiada con anterioridad en regiones circungalácticas, pero las zonas nucleares han sido sistemáticamente excluidas de estos estudios por la falta de observaciones con la resolución necesaria. Estas observaciones presentan una gran dificultad debido tanto a la alta resolución necesaria como a la extinción por el polvo que existe en las zonas nucleares de las galaxias con una elevada tasa de formación estelar. Ambos problemas pueden ser resueltos utilizando técnicas de radio-VLBI. En este trabajo descubrimos que la distribución radial de las supernovas cambia radicalmente en las zonas más internas de estas galaxias, proporcionando evidencias de la existencia de discos circunnucleares, discos que fueron propuestos por modelos teóricos y cuyos tamaños característicos son compatibles con los obtenidos aquí.

Este trabajo pone de manifiesto la importancia del estudio multifrecuencia para derivar los mecanismos que juegan un papel importante en los procesos de formación estelar en (U)LIRGs.

Abstract

This dissertation deals with the multiwavelength study of luminous and ultraluminous infrared galaxies (LIRGs and ULIRGs, respectively) in the local Universe under different spatial scales. The work is focused on the properties of massive starbursts, the contribution of active galactic nuclei (AGN) and the interplay between both phenomena. The study of local (U)LIRGs is the best scenario where to understand the properties of these objects at cosmological distances, where their luminosity contribution dominates the cosmic infrared background.

Our first approach to the study of (U)LIRGs consisted of a spectral line study in the millimeter range, obtained with the IRAM 30 m radio-telescope in Pico Veleta, Granada of a subsample of 56 (U)LIRGs from the GOALS project sample. We observed and analyzed spectra of several molecular features, focusing in the study of carbon monoxide (CO), a well-known tracer of cold molecular gas. We explored the relation between them as well as the properties of molecular gas. Besides of the sample characterization, we confirmed the increase of the isotopic ratio $^{12}CO/^{13}CO$ with the dust temperature, explained by the ^{12}CO optical depth decreasing with temperature. We have also studied the kinematics and gas distribution using the spectral profiles of several molecular transitions.

In a second part of this thesis, we analyzed the central kiloparsec region of a sample of 12 LIRGs, stressing the importance of the multiwavelength approach, aimed at deriving the star formation processes of these galaxies, as well as to study the contribution of the putative AGN to the bolometric luminosity in our sample. For one of these LIRGs, NGC 1614, we performed a deep multiwavelength study, including data from radio, infrared, optical and X-rays. These data allowed us to establish that the the IR emission

in the circumnuclear region is completely dominated by a powerful starburst and, in case it hosts an AGN, its contribution is irrelevant. We also performed an exploratory study where, using the Paschenα emission, we developed a method to isolate the two main component of the radio emission at 8.4 GHz: thermal and non-thermal (synchrotron). This decomposition allowed us to differentiate the ages at different regions, yielding to a better understanding of starburst processes.

We also studied the massive star formation in the most luminous nearby LIRG, Arp 299, through the study of supernovae (SNe), both in its most luminous nucleus (Arp 299-A) and in its surroundings. We used radio data from the e-MERLIN interferometer, obtained for the LIRGI project (PIs: J. Conway & M.Á. Pérez-Torres), to discover the radio counterpart of supernova SN2010P. We used additional radio data at four frequencies, for a total of 13 epochs, and modeled the light curve of SN2010P, which allowed us to type it as a IIb, i.e., a stripped-envelope core-collapse supernova. Another supernova (SN2010O) exploded in the system a few days earlier, but did not show any radio emission despite our several attempts to detect it at different epochs. This radio-silence in late time observations is probably due to its rapid evolution, compatible with a Type Ib supernova. Regarding the study of SNe in the nuclear region of Arp 299-A, we used very long baseline interferometry (VLBI) radio techniques. We analyzed several epochs spanning 2.5 years using the European VLBI Network (EVN), which permitted us to confirm 25 compact sources, most of them SNe or SN remnants, and allowed us to derive a core-collapse SN rate of $\sim$0.8 SN yr^{-1}, compatible with previous studies. We also found that most of the star formation in Arp 299-A is taking place in the inner 150 parsecs.

Our final approach to the study of (U)LIRGs consists of the use of radio-VLBI techniques aimed at resolving the innermost regions of these galaxies, where massive and violent starbursts are taking place, and where their interaction with AGN is more evident. Since radio is not affected by dust extinction and given the very high angular resolution achieved with VLBI observations, this is the only technique with which we can perform such a

deep study. We used SNe previously detected in the nuclei of three starburst galaxies, Arp 299-A, Arp 220, and M82, to determine (for the first time) their spatial distribution. Their radial distribution, which follows and exponential profile, has been thoroughly studied by other authors in galactic scales, but the nuclear regions have been systematically excluded from those studies due to the high angular resolution needed as well as the extreme dust extinction of these objects. Both issues can be overcome using radio-VLBI techniques. We found that the radial distribution of supernovae changes drastically in the innermost regions of these galaxies, yielding evidence for the existence of circumnuclear disks, proposed by theoretical models and whose sizes are compatible with those obtained by us.

This work emphasizes the importance of a multiwavelength approach to study the mechanisms that play an important role in the star formation processes in (U)LIRGs.

Contents

List of Figures

LIST OF FIGURES

List of Tables

Glossary

$\odot$ solar symbol; widely used to refer to solar mass ($M_\odot$) or solar luminosity ($L_\odot$).

AGN Active Galactic Nucleus; name for the central region of a galaxy when it has an abnormally high luminosity.

ALMA Atacama Large Millimeter / submillimeter Array; an interferometer of 66 antennas in Atacama desert in Chile.

AO Adaptive Optics; telescope technology used to correct the deformations of the wavefront due to atmospheric distortions.

CASA *Common Astronomy Software Applications*; New generation radio data reduction package developed by NRAO.

CCSN Core-Collapse Supernova; a violent explosion caused by the gravitational collapse of a massive star.

CSM circumstellar medium; space around stars.

e-MERLIN electronic Multi Element Remotely Linked Interferometer Network; a seven antenna interferometer across England.

EVN European VLBI Network; set of radio antennas working as an interferometer spread across Europe, Asia, South Africa and Puerto Rico.

EW Equivalent Width; measure of the area of a spectral line.

HST *Hubble Space Telescope*; an international 2.4 m mirror space telescope.

IMF Initial Mass Function; a function that describes the initial histogram of mass distribution of a population of stars.

IR infrared; range of the electromagnetic spectrum with wavelengths spanning from 740 nm to $\sim 300\,\mu$m.

IRAS *Infrared Astronomical Satellite*; a space infrared telescope with a mirror of 0.6 m launched in 1983.

LINER Low-Ionization Nuclear Emission-line Region; a type of AGN defined by its spectral line emission.

LIRG Luminous Infrared Galaxy; a galaxy with an infrared luminosity between $10^{11} L_\odot$ and $10^{12} L_\odot$.

LIRGI Luminous Infrared Galaxy Inventory; e-MERLIN legacy project aimed at studying a sample of LIRGs in radio.

mas milli-arcsecond; 10^{-3} arcseconds.

NRAO National Radio Astronomy Observatory; USA center for research and development of radio astronomy.

PA Position Angle; major position angle of the elliptic disk of a galaxy.

pc parsec; distance corresponding to a parallax of one second (~ 3.26 light-years, $\sim 3.09 \times 10^{13}$ km).

QSO Quasi Stellar Object; a type of AGN characterized by its extreme luminosity.

quasar quasi stellar radio source; see QSO.

SB starburst; short episode of intense star formation.

SED Spectral Energy Distribution; brightness versus frequency profile of a source.

SFR Star Formation Rate; rate at which new stars form, measured usually in $M_\odot$/yr.

SKA Square Kilometer Array; a future interferometer with a square kilometer collecting area to be built in South Africa, Australia and New Zealand.

SMA sub-millimeter array; Interferometer of eight antennas located in Mauna Kea, Hawaii.

SMBH Super Massive Black Hole; a black hole with a mass $\gtrsim 10^6 M_\odot$.

SN Supernova; a violent stellar explosion.

SNR Supernova remnant; the remaining structure consequence of a supernova explosion.

ULIRG Ultra Luminous Infrared Galaxy; a galaxy with an infrared luminosity higher than $10^{12} L_\odot$.

VLA Very Large Array; a 27 identical 25 m antennas interferometer in USA. Its complete designation is Karl G. Jansky VLA.

VLBA Very Long Baseline Array; an interferometer in the USA consisting of ten identical antennae from Hawaii to the Virgin Islands.

VLBI Very Long Baseline Interferometry; interferometry technique where antennas are separated by large distances.

VLT Very Large Telescope; set of four 8.2 m telescopes in Paranal, Chile, operated by ESO.

It must be borne in mind that the tragedy of life doesn't lie in not reaching your goal. The tragedy lies in having no goal to reach. It isn't a calamity to die with dreams unfulfilled, but it is a calamity not to dream. It is not a disaster to be unable to capture your ideal, but it is a disaster to have no ideal to capture. It is not a disgrace not to reach the stars, but it is a disgrace to have no stars to reach for.

Benjamin E. Mayes

1 Introduction

THINK of a galaxy. The first picture that usually comes to our minds is that of a vast and peaceful collection of stars, sometimes forming majestic spiral arms, sometimes in an elliptical swarm, calmly waiting for the end of their lives. It is a reassuring image. But galaxies can get furious, too. Encounters and collisions of galaxies can trigger extreme bursts of star formation, powerful nuclear activity, tidal tails, and disruptions that reshape them in new intricate and time-evolving forms. This thesis deals with the study of luminous and ultraluminous infrared galaxies, many of which belong to the fascinating group of interacting galaxies. Through this chapter, I introduce this type of objects, together with the related basic aspects about star formation and active galactic nuclei. In the last part, I describe the most common radio emission processes and give an overview on the radio astronomy tools used in this thesis, together with a brief description of the facilities used in this thesis to obtain our data.

1.1 Luminous and Ultraluminous Infrared Galaxies

The first infrared (IR) observations of extragalatic sources were published by Johnson (1966), with observations up to a wavelength of 3.4 μm. Soon after that, a few sources were discovered to have an abnormally large infrared luminosity (e.g., NGC 1068 in Low & Aumann, 1970) compared to the general behavior of all other galaxies. During the 70s and early 80s the search for infrared emission in galaxies continued with new observational results. However, it wasn't until 1983, with the launch of the *Infrared Astronomical Satellite (IRAS)*, when these sources with IR excess were found to be extremely common. Taxonomically, those with an IR luminosity, $L_{\rm IR}$[1], between 10^{11} and $10^{12} L_{\odot}$ were named Luminous Infrared Galaxies (LIRGs) and even brighter sources ($L_{\rm IR} \geq 10^{12} L_{\odot}$) were called Ultra Luminous Infrared Galaxies (ULIRGs). For LIRGs and ULIRGs, the IR emission is larger than the emission at all the other wavelengths combined (Sanders & Mirabel, 1996) and, although it seems clear that their large infrared luminosities arise from dust reprocessing, the nature of the nuclear engine responsible for the dust heating remains an open question, with two main candidates: a nuclear starburst (e.g., Farrah *et al.*, 2003), AGN activity, or, most likely, a combination of both phenomena (e.g., Veilleux *et al.*, 1995; Yuan *et al.*, 2010; Alonso-Herrero *et al.*, 2012). Some examples of local (U)LIRGs are shown in Figure 1.1, three of which (Arp 220, Arp 299, and NGC 1614) are widely discussed in this thesis.

At low redshift, (U)LIRGs do not dominate the energy production: the total IR luminosity from these type of galaxies in the *IRAS* Bright Galaxy Sample (Soifer *et al.*, 1989) represents only a 6% of the IR emission in the local Universe (Soifer & Neugebauer, 1991). At higher redshift, however, LIRGs and ULIRGs are the largest contributors to the Cosmic Infrared Background (CIB; see review by Lagache *et al.*, 2005). Furthermore, (U)LIRGs dominate the Star Formation Rate (SFR) at high redshift (see Figure 1.2), thus making them important to understand how galaxies form and evolve. In particular, ULIRGs are very numerous at $z \geq 1$, but rare in the local Universe, being the closest one Arp 220 (studied in Chapter 6), which is 77 Mpc away. However, since (U)LIRGs dominate the SF at high redshift, the detailed study of local samples is very important, since they constitute the basis for the study at higher z.

[1]Throughout this thesis, $L_{\rm IR}$ will refer to the infrared luminosity between 8 and 1000 μm.

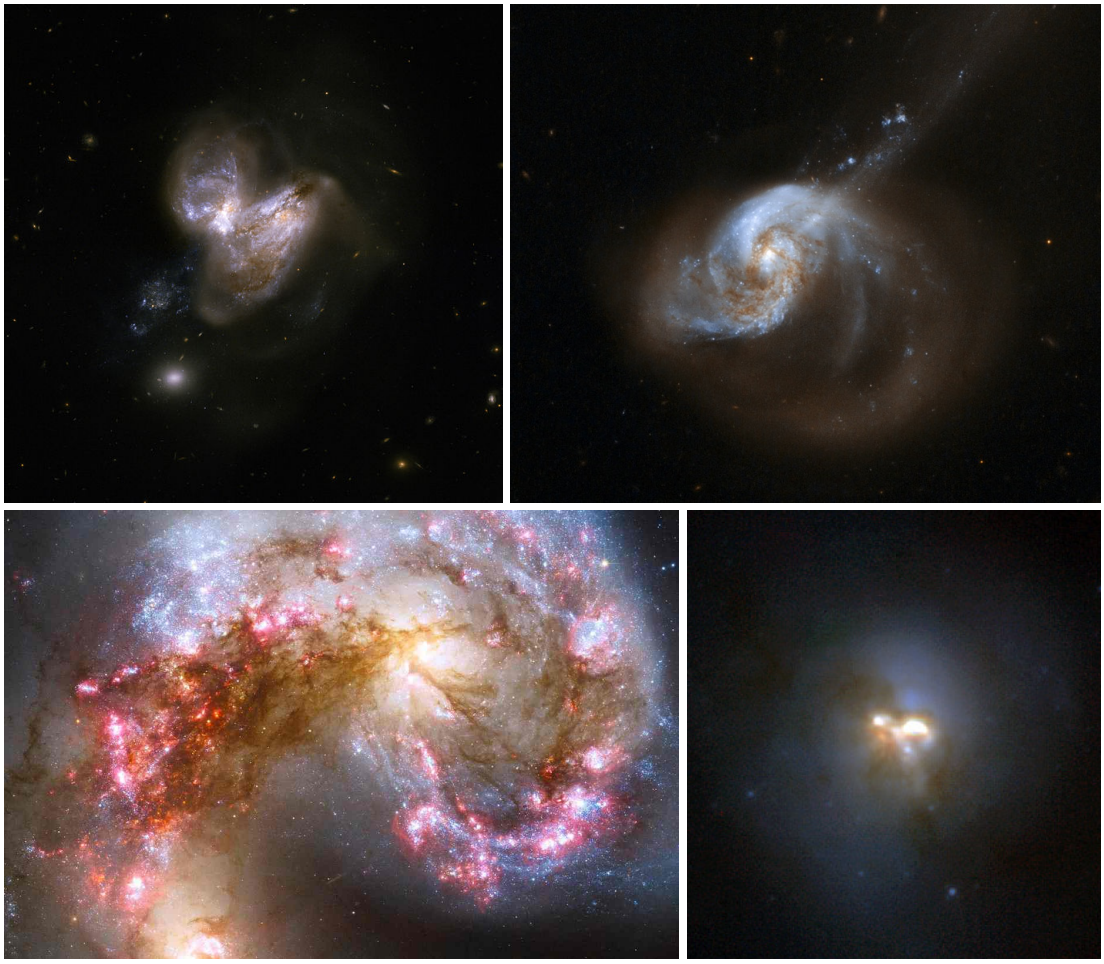

Figure 1.1: Some examples of (U)LIRGs - Top left: HST color composition of Arp 299 (LIRG), merger system in an early stage and known for being a distinguished supernova factory. Top right: HST ACS composition of NGC 1614, showing conspicuous tidal tails. It is a LIRG in a late stage of interaction. Bottom left: *The Antennae galaxy* (Arp 244) HST optical composition. It is formed by galaxies NGC 4038 and NGC 4039 in an advanced stage of merging. Bottom right: HST NICMOS near-infrared composition of Arp 220, the closest ULIRG and actually the brightest object in the local Universe. Credits in the same order: NASA, ESA, the Hubble Heritage (STScI/AURA)-ESA/Hubble Collaboration, and A. Evans (University of Virginia, Charlottesville/NRAO/Stony Brook University); NASA, ESA, the Hubble Heritage (STScI/AURA)-ESA/Hubble Collaboration, and A. Evans (University of Virginia, Charlottesville/NRAO/Stony Brook University); NASA, ESA, and the Hubble Heritage Team (STScI/AURA)-ESA/Hubble Collaboration; R. Thompson (U. Arizona) et al., NICMOS, HST and NASA.

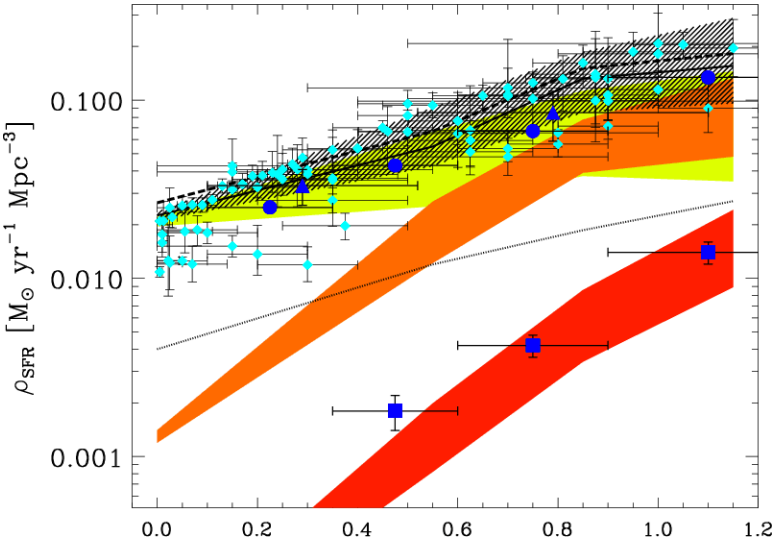

Figure 1.2: Star Formation Rate density versus redshift - Evolution of the total SFR density (striped area) compared with SFR density of normal galaxies (yellow area), LIRGs (orange area) and ULIRGs (red area). From Magnelli *et al.* (2009).

1.2 Star formation and supernovae

Although the involved mechanisms are not yet well understood, it has been known for long that interactions among galaxies can trigger star formation (e.g., Bushouse, 1986; Kennicutt *et al.*, 1987). Weedman *et al.* (1981) used for the first time the word *starburst* to describe the intense periods of star formation activity in the nucleus of NGC 7714. Ever since, this term has been used to describe short episodes of intense star formation, up to $\sim 500\,M_\odot\,\mathrm{yr}^{-1}$ with lifetimes of $\sim 10^7\,\mathrm{yr}$ for the most extreme star-forming galaxies (Kennicutt, 1998), in contrast with the sustained lower SFR of normal spiral galaxies, such as the Milky Way, with a rate of $\sim 1\,M_\odot\,\mathrm{yr}^{-1}$ (e.g., Robitaille & Whitney, 2010).

Different approaches have been used to model starbursts given an assumed initial mass function (IMF; $\Phi(m) \propto \mathrm{d}N/\mathrm{d}m$): an instantaneous event (e.g., Leitherer & Heckman, 1995; Leitherer *et al.*, 1999), a continuous star formation (e.g., Leitherer *et al.*, 1999; Kewley *et al.*, 2001), a Gaussian combination of bursts (e.g., Alonso-Herrero *et al.*, 2001), or an exponentially decaying starburst (e.g., Efstathiou *et al.*, 2000).

Estimating the star formation rate in galaxies is possible through different tracers (see Cram *et al.*, 1998; Kennicutt, 1998), such as the number of O stars as probed by

the ultraviolet (UV) flux, the radio continuum at 18 cm, or several recombination lines.

A good tracer of massive SFR is the supernova (SN) rate present in (U)LIRGs: once massive stars ($M \gtrsim 8M_{\odot}$) consume their hydrogen and helium, the temperature in their cores can reach the fusion threshold of heavier elements, leading to the production of iron, the heaviest energetically profitable element in the fusion process. Iron starts then to accumulate in a compact core in the nucleus of the star while the nuclear reactions keep going, maintaining the Fe production. When this core reaches $1.4M_{\odot}$ (Chandrasekhar, 1931) it can no longer compensate its own gravitational attraction. Not being able to hold this mass, the core collapses over itself. In a matter of seconds, the core explodes as a *Core-Collapse Supernova* (CCSN), whose final product is, depending on the initial mass, either a neutron star or a black hole.

Although the SN rate ($\nu_{\rm SN}$) of normal galaxies, including ours, is about one in fifty years (Diehl *et al.*, 2006), the high SFR of starburst galaxies imply supernova rates up to one per year (e.g., Arp 299-A; see Neff *et al.*, 2004; Pérez-Torres *et al.*, 2009b).

Overcoming the problem of dust obscuration with near-IR or radio observations, the direct detection of CCSNe can be used to trace massive star formation. With information on the initial mass function, star formation rates can be estimated at any mass range. Alternatively, if the SFR is known for low-mass stars, the IMF can be constrained.

There is a known correlation between $\nu_{\rm SN}$ and the infrared luminosity (e.g., Condon, 1992; Mattila & Meikle, 2001), which is also another star formation tracer. Indeed, there is a tight linear correlation in star-forming galaxies between the far-infrared luminosity and the radio emission at 18 cm (van der Kruit, 1973; de Jong *et al.*, 1985; Helou *et al.*, 1985; Condon, 1992). Helou *et al.* (1985) defined a parameter to measure this correlation: the *q-factor*, defined as:

$$q = \log\left(\frac{\mathrm{FIR}/3.75\times10^{12}\,\mathrm{Hz}}{S_{1.49\,\mathrm{GHz}}}\right), \tag{1.1}$$

where $S_{1.49\,\mathrm{GHz}}$ is the flux density at 1.49 GHz in units of $\mathrm{W\,m^{-2}\,Hz^{-1}}$, and FIR an approximation to the flux between 40 and 120 μm, measured in $\mathrm{W\,m^{-2}}$ and defined as:

$$\mathrm{FIR} = 1.26\times10^{-14}\,(2.58\,S_{60\,\mu\mathrm{m}} + S_{100\,\mu\mathrm{m}}), \tag{1.2}$$

with $S_{60\,\mu\mathrm{m}}$ and $S_{100\,\mu\mathrm{m}}$ being the *IRAS* fluxes in Jy at 60 and 100 μm, respectively. The mean value of the *q-factor* in the *IRAS* Bright Galaxy Sample starbursts is $\langle q \rangle = 2.34$ (Condon & Broderick, 1991; Yun *et al.*, 2001).

The origin for the FIR-radio correlation is usually associated with a star formation origin: dust reprocesses massive-star UV radiation into far infrared photons, while the explosions of those same stars as supernovae accelerate the cosmic ray electrons, responsible for the radio non-thermal synchrotron radiation (e.g., Voelk, 1989; Lisenfeld *et al.*, 1996; Lacki *et al.*, 2010; Lacki & Thompson, 2010). Thermal bremsstrahlung (free-free emission) is also linked to this correlation (e.g., Murphy *et al.*, 2011), arising from H II regions. The FIR-radio correlation not only holds through ~ 6 orders of magnitude, but the usually called FIR-radio *conspiracy* continues at cosmological distances, as shown by Garrett (2002) for a sample of *Hubble* Deep Field North (HDF-N) galaxies.

A known exception for this correlation occurs in AGN dominated galaxies, that diverge from the trend (Condon & Broderick, 1988), typically with $q < 2.0$, but sometimes with values above the average.

1.3 Active Galactic Nuclei

We now know that —the one time exotic and conjectural— black holes populate the vastness of the Universe. Those with a mass $\gtrsim 10^6\,M_\odot$, are called supermassive black holes (SMBHs) and are located in the center of many galaxies. Active galactic nuclei (AGN) are believed to be the manifestation of SMBH accretion. Their emission spans through the whole electromagnetic spectrum, covering up to 20 orders of magnitude in frequency, from γ-ray to radio (Padovani, 1999), with bolometric luminosities between $\sim 10^{40}$ and $\sim 10^{48}\,\mathrm{erg\,s^{-1}}$ (e.g., Fabian, 1999; Woo & Urry, 2002). To maintain these high luminosities, there must be a continuous supply of matter into their accretion disks.

Although $\sim 18\%$ of LIRGs contain AGN, only in $\sim 10\%$ of the LIRGs with an AGN, the AGN emission is the dominant mechanism, i.e., contribute with more than a 50% to the total infrared luminosity (Petric *et al.*, 2011). This means that most of the AGN are actually hidden in their hosts as low-luminosity AGN (LLAGN).

There is one possible exception to the accretion origin for the luminosity of AGN: the Low-Ionization Nuclear Emission-line Regions (LINERs), traditionally classified as AGN, are sources whose emission is sometimes associated with stellar processes (e.g., Shields, 1992).

Despite nine orders of magnitude difference in their size scales, SMBHs and host galaxy properties are correlated (e.g., Marconi & Hunt, 2003), suggesting a co-evolution between bulges and SMBHs. Furthermore, a correlation between the star formation rate and the black hole accretion rate exists at both circumnuclear ($\sim 1\,$kpc) scales (Diamond-Stanic & Rieke, 2012, , see Fig. 1.3) and nuclear ($\sim 100\,$pc) scales (Esquej *et al.*, 2014). This apparent co-evolution has been named the *starburst-AGN connection*.

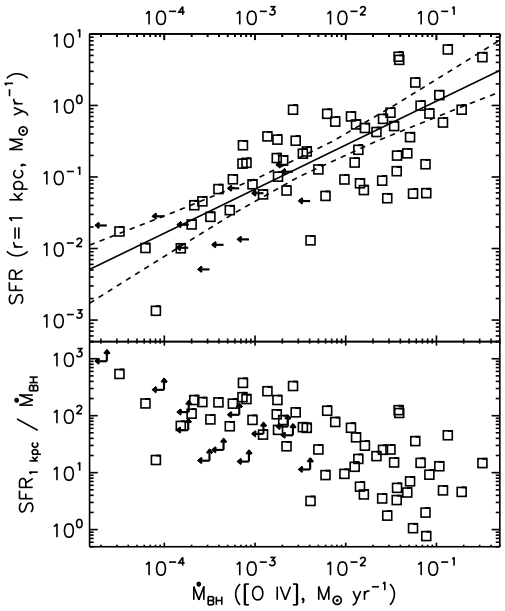

Figure 1.3: Star formation rate vs black hole accretion rate - Relation measured at 1-kpc scales for a sample of Seyfert galaxies. From Diamond-Stanic & Rieke (2012).

1.4 The starburst-AGN connection: (U)LIRGs evolution

Most LIRGs are starburst-dominated (e.g., Petric *et al.*, 2011; Stierwalt *et al.*, 2013), but many also contain AGN. Both phenomena seem to be responsible for the large $L_{\rm IR}$

shown by (U)LIRGs. These two mechanisms are in fact linked to each other (see, e.g., Shao *et al.*, 2010) with feedback mechanisms.

While almost every low-redshift (U)LIRG with $\log(L_{\rm IR}/L_{\odot}) > 11.5$ is an interacting system, the lower end luminosity population of LIRGs has a significant fraction ($\sim 40\%$) of isolated spiral galaxies (Sanders & Ishida, 2004), and among the non-isolated, only a small fraction are major mergers (Alonso-Herrero *et al.*, 2006). ULIRGs, on the other hand, tend to be late-stage major mergers (Sanders & Mirabel, 1996). This merger-stage scheme suggests an evolutionary pathway, first postulated by Sanders *et al.* (1988), where the gravitational interaction triggers the star formation, which is the dominant mechanism in the initial stages and later evolves to a quasi-stellar object (QSO).

Figure 1.4 shows a schematic outline by Hopkins *et al.* (2008) showing the evolutionary phases of a major merger: the first stage is an initial quiescent isolated phase driven by secular processes, followed by early interaction tidal torques than can cause relatively weak star formation and black hole accretion. It is in a more advanced stage of the merging process when massive inflows of gas trigger intense starbursts and feed the SMBH, which remains heavily obscured by dust and gas. Once the nuclear reservoir of gas has been depleted by starbursts and AGN (through supernovae feedback), and dust is removed by radiation pressure and/or SN winds, the SMBH becomes observable as an optical quasar. With no more gas available, both star formation and accretion extinguish, leading to a quiescent elliptical galaxy. This scenario is supported by a number of numerical simulations (e.g., Toomre & Toomre, 1972; Barnes & Hibbard, 2009; Hopkins *et al.*, 2008; Privon *et al.*, 2013), as well as by the common dynamical properties of ULIRGs and QSO host galaxies (Rothberg *et al.*, 2013).

Although there is a wide agreement in the general picture, several aspects of (U)LIRGs evolution are still open. Indeed, there is a significant fraction of (1) AGN-dominated systems prior to coalescence and (2) already merged SB-dominated systems (Veilleux *et al.*, 2009) that do not fit in the above scheme. Some examples include an alternative scenario where SMBH growth would be slowly produced by inward gas transport in bulgeless galaxies (Kormendy *et al.*, 2011), or a putative evolutionary sub-phase followed by some ULIRGs that would not pass through a QSO phase (Farrah *et al.*, 2009). Additionally, recent evidences suggest that the evolutionary pathway for local LIRGs is somewhat different, with a delay between the peak of star formation activity and the

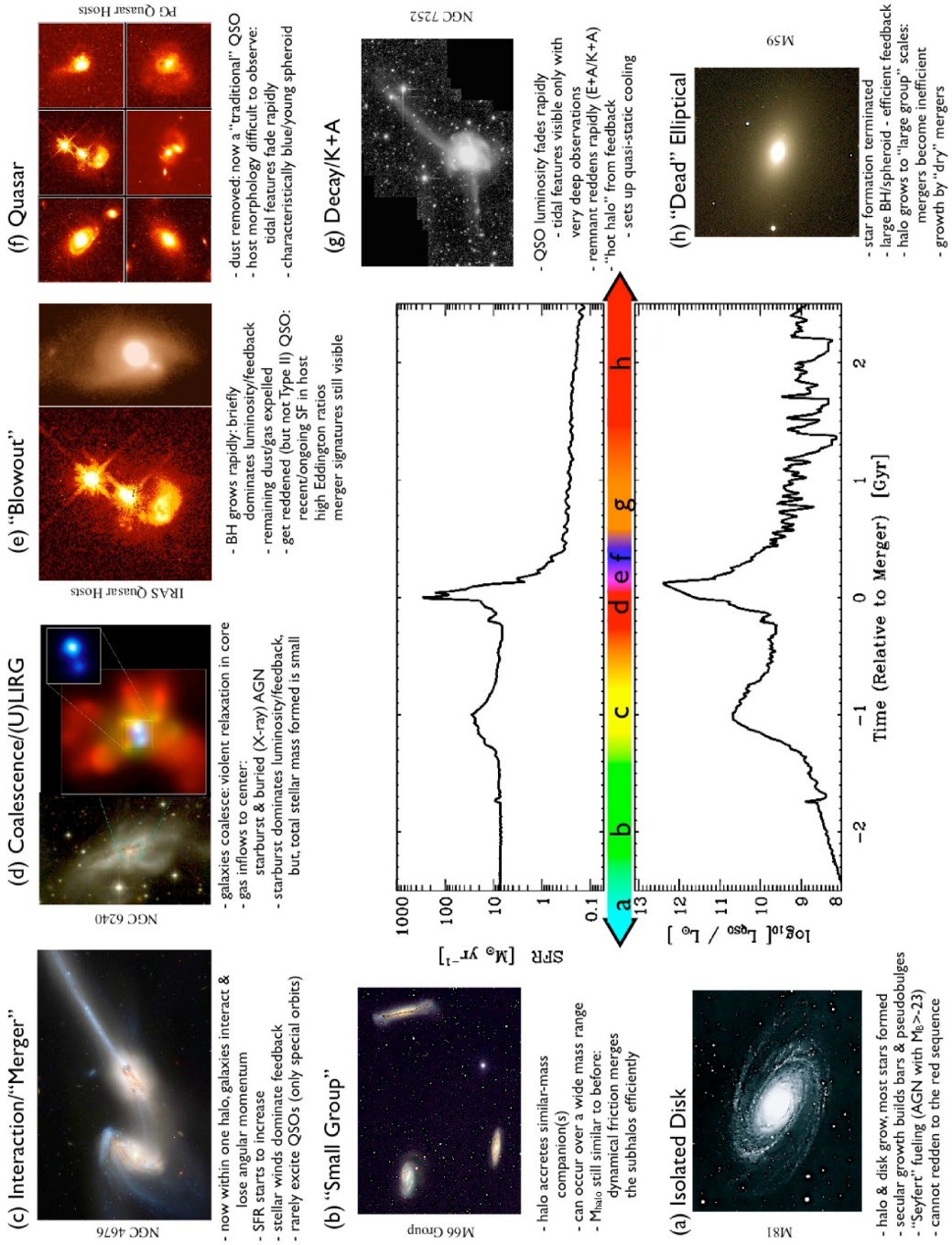

Figure 1.4: Schematic diagram of the evolutionary pathway of a merger - From Hopkins *et al.* (2008).

AGN phase (Alonso-Herrero *et al.*, 2013a), as predicted from numerical simulations (Hopkins, 2012).

1.5 The radio spectral behavior of (U)LIRGs

An important part of the work of this thesis is based on radio and millimeter observations. Due to their particularities, I give here a brief introduction to their basis and techniques. Observations at mm wavelengths are often split from radio astronomy and simply named *mm-astronomy*. However, from a technical point of view, both are analogous, and here I refer to both of them simply as radio.

Since the serendipitous discovery of the first extraterrestrial radio signal by Karl Jansky (Jansky, 1933), radio astronomy development has been exponential. Major milestones of this science include the detection of the cosmic microwave background (Penzias & Wilson, 1965; Dicke *et al.*, 1965) –namely the echoes of the Big Bang–, the discovery of pulsars by Jocelyn Bell and her PhD advisor (Hewish *et al.*, 1968), the verification of Einstein's predictions of gravitational radiation through the discovery of a binary pulsar (Hulse & Taylor, 1974) and, in a more technical context, the development of *aperture synthesis* (Ryle, 1952), linking radio astronomy to interferometry, which will be introduced here as well. The four findings above were all awarded[1] with the Nobel Prize in recognition to their outstanding contribution to astronomy.

Along the years, sources of very different nature were discovered to show radio emission. Several physical processes can produce this emission in different forms and with different physical origins. Continuum emission processes relevant in the study of (U)LIRGs include (1) thermal emission, due to the thermal motion of charged particles; (2) thermal bremsstrahlung, also called free-free emission, due to the deceleration of free electrons when deflected by an ionized atomic nucleus; and (3) synchrotron radiation, a non-thermal process due to the presence of strong magnetic fields, where charged particles are accelerated in circular or spiral trajectories to relativistic speeds, radiating large amounts of energy.

For the case of starbursts galaxies, including starburst-dominated (U)LIRGs, each of the above mechanisms dominates in different parts of the spectrum and present different spectral behaviors. Figure 1.5 shows the radio SED of the prototype starburst

[1]The discovery of pulsars and the development of aperture synthesis shared the prize in 1974.

galaxy M82, where the quoted three continuum emission processes dominate at different wavelength windows: a non-thermal synchrotron-dominated frequency range from ~ 1 to 30 GHz, characterized by a steep spectral index; a thermal free-free dominated range from ~ 30 to 100 GHz, with a flat spectrum; and finally, a third region dominated by thermal dust emission, whose outcome increases importantly with frequency.

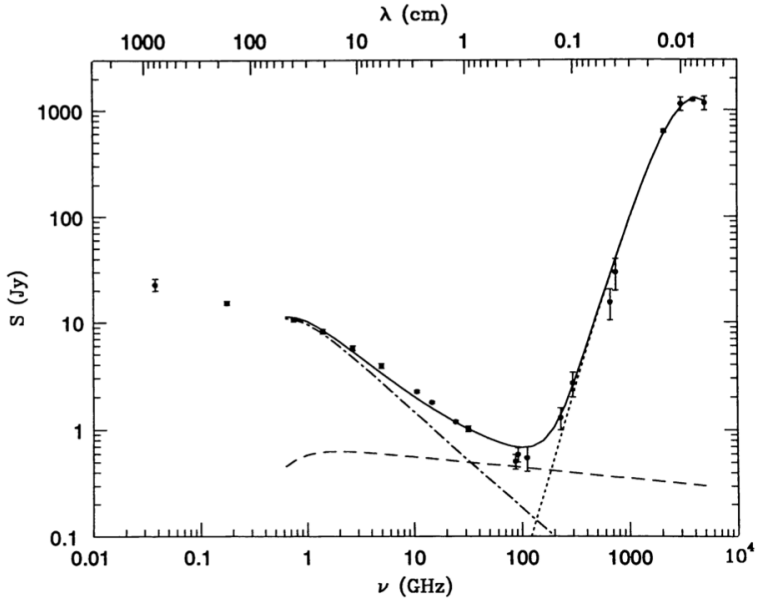

Figure 1.5: Radio/FIR Spectral Energy Distribution of M82 - The radio continuum of this starburst galaxy is the sum of three components: *the steep*, from ~ 1 to 30 GHz and dominated by synchrotron radiation (dot-dash line), *the flat*, between 30 and 100 GHz, due to thermal free-free emission (dashed line) and *the inverted*, dominated by thermal dust re-emission (dotted line). M82 is analyzed analyzed in Chapter 6. Extracted from Condon (1992).

Synchrotron and thermal free-free emission can be used as clocks to trace starburst in (U)LIRGs. Indeed, synchrotron radiation is mostly due to electrons accelerated in supernova remnants, thus tracing star formation from one to ten million years ago. On the other hand, thermal free-free emission mostly comes from H II regions, tracing present star formation.

The other group of relevant radiation processes in radio (and mm-)astronomy have a non-continuous nature. These are produced by neutral (H I) and recombination hydrogen spectral lines, molecular rotational and vibrational lines and maser emission. All these features are relevant in the study of (U)LIRGs, since they can be used to

characterize them. In particular spectral lines and ratios among them can be used to study the kinematics of these sources (very relevant in mergers), to trace star formation and study the AGN contribution, and to constrain density and temperature. As an example, Figure 1.6 shows a part of the mm-spectrum of M82 around 3 mm, which includes several of the species commonly used in molecular studies. Chapter 2 focuses in the study of molecular gas in (U)LIRGs through CO observations.

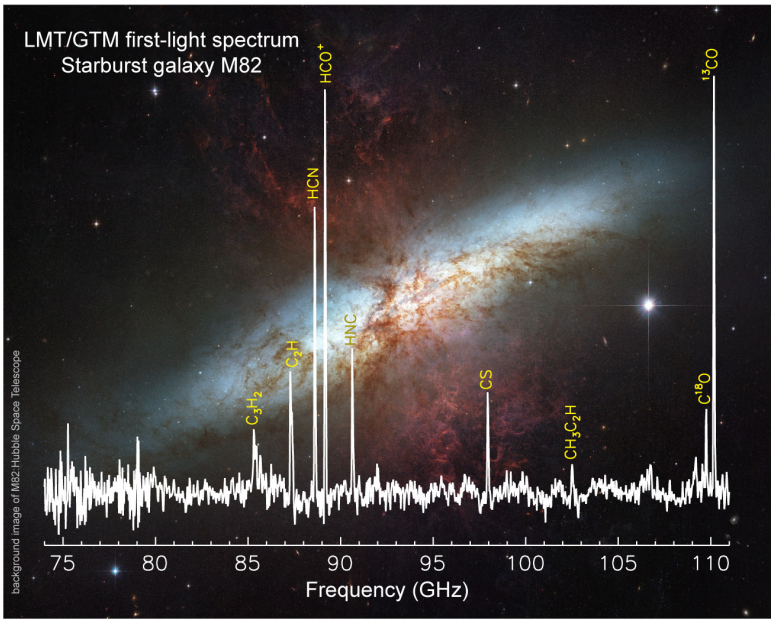

Figure 1.6: Molecular lines in M82 - The spectrum shows several molecular features in the 3 mm window between 74 to 111 GHz, observed during the first-light observations of the Large Millimeter Telescope (LMT). Credit: Large Millimeter Telescope.

Radio astronomy has another important advantage. The main problem of optical and, to some extend, near-infrared observations in dust-enshrouded environments is the extinction of the light that causes an obscuration of observed sources. The visual extinction towards some extreme ULIRG examples can be larger than 45 mag (Genzel *et al.*, 1998). The issue of obscuration is illustrated in Figure 1.7 with the case of Barnard 68, a nearby molecular cloud ($\sim$ 150 pc away), and has no effect in radio domains.

It is so close to us that there are no stars in the line of sight between it and us. What we see in short wavelengths, or to be more precise, what we do not see at all, are the background stars behind the cloud. We can notice how, as we observe at longer

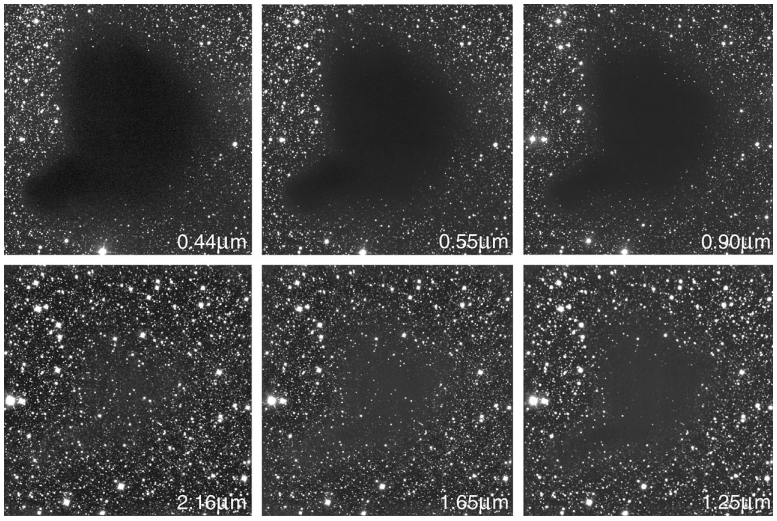

Figure 1.7: Molecular Cloud Barnard 68 - Imaged in six different wavebands, clockwise from the blue to the near-infrared. Obscuration caused by the cloud diminishes with increasing wavelength. Credit: ESO.

wavelengths, the cloud becomes progressively transparent and background stars begin to be seen. Radio observations are a very powerful tool to face dust-enshrouded regions.

Nonetheless, there is an important drawback in single-dish radio observations. The angular resolution, θ, that can be achieved with a telescope in the case of being limited by diffraction is a function of both the wavelength of observation, λ, and the diameter of the aperture, D, and is given by

$$\theta \propto \frac{\lambda}{D}. \tag{1.3}$$

The bigger the aperture is, the finer the resolution it achieves. Indeed, in order to achieve Hubble Space Telescope (HST) resolution ($\sim 0.05''$, with a mirror of 2.4 m) in a radio observation at a wavelength of 1 cm, we would need a mirror –actually an antenna dish– of 50 km of diameter. It is at this point where interferometry plays a crucial role.

While radio/mm single dish antennas are conceptually analogous to traditional reflector telescopes, interferometry emerges from a different principle. Several antennas can observe simultaneously a target in the sky and make interfere the signal of each pair of antennas in a correlator. The so called *visibility function*, which measures how the resulting interferences are, is the Fourier transform of the brightness distribution of the observed region in the sky. Measuring the visibility function for each possible separation

of a pair of antennas as seen from the source in the sky (baseline) and performing an inverse Fourier transform, it is possible thus to obtain a map of the target, with the same angular resolution (synthesized beam) as a single telescope with a diameter equivalent to the distance of the two most distant antennas in the array. The sampling of the visibility functions (the uv-plane) can be improved for a given baseline thanks to the Earth-rotation. A comprehensive description of the whole radio-interferometric process can be found in Taylor *et al.* (1999).

1.6 Facilities used in this research

This thesis makes use of both spectral and imaging techniques in a large range of the electromagnetic spectrum, from X-ray to radio cm-wavelengths. The fundamental observations, however, are based on four spectral windows.

1.6.1 Near-IR

Our near-IR K-band imaging data, originally aimed at detecting new CCSNe and used for a multiwavelength study of a sample of LIRGs (Chapter 4), were obtained from two instruments from two 8 m class telescopes: (1) NIRI in the Gemini-North telescope using the ALTAIR adaptive optics (AO) facility and with plate scales of 22 or 54 mas/pixel (depending of the camera), and NACO in the Very Large Telescope (VLT) UT4, with a plate scale of 27 mas/pixel, and also assisted by an AO system.

1.6.2 Mid-IR

Our mid-IR 8.7 μm imaging data, used for a comparative study of the LIRG NGC 1614 (Chapter 3), comes from T-ReCS (Thermal-Region Camera Spectrograph), installed in the 8.1 m Gemini-South telescope, have a plate scale of 89 mas/pixel.

1.6.3 Millimeter range

We have made use the IRAM 30 m telescope on Pico Veleta, Spain, which is a single dish parabolic antenna with observing capabilities at 0.8, 1, 2, and 3 mm. In particular we used the EMIR multi-band receiver to obtain spectra at 3 mm of several molecular species aimed at studying the molecular gas in (U)LIRGs (Chapter 2). The FWHM of

the main beam in our observed range is $\sim 22''$, comprising most of the emission of our studied sample.

1.6.4 Radio

Our radio observations were taken with four different facilities:

- **VLA** - The Karl G. Jansky Very Large Array (VLA) is a radio interferometer formed by 27 identical antennas, each with a diameter of 25 m, located in New Mexico, USA. Currently, the VLA can observe at ten different bands, spanning from 58 MHz ($\sim$ 5 m) to 50 GHz ($\sim$ 0.6 cm). The antennas are distributed in a Y-shape array and can be moved through a system of rails and placed in different pods, varying their baselines and hence, the angular resolution. There are four different VLA configurations, from the very extended A-configuration (baselines from 0.68 to 36 km), to the compact D-configuration (baselines from 35 m to 1 km). Most of the data used in this thesis comes from observations at A-configuration, which yields a resolution of $\sim 0.20''$ for X-band (3.6 cm).

- **e-MERLIN** - This radio-interferometer is formed by seven antennas located across England, with a maximum baseline of 217 km, thus being a Very Long Baseline Interferometry (VLBI) array. It has three receivers centered at 18, 5 and 1.3 cm, with angular resolutions from 12 to 150 mas. This array is further described in Chapter 5 in the frame of the legacy project LIRGI.

- **EVN** - The European VLBI Network (EVN) is a VLBI facility across Europe, Asia, South Africa and Puerto Rico, with a longest possible baseline of around 14 000 km. The EVN is not a dedicated array, i.e., each station is operated by different institutions and works independently. Only when an EVN session is organized, several times a year, all antennas work together as an array. The angular resolutions achieved are of the order of the milli-arcsecond. Figure 1.8 shows currently participating and associated EVN antennas all over the world.

- **VLBA** - This VLBI facility is formed by ten identical 25 m antennas spread across the USA, from Hawaii to the Virgin Islands. Unlike the EVN, the VLBA is a dedicated array. Several observations have been performed using both EVN and VLBA infrastructures, observations known as *global-VLBI*.

Figure 1.8: European VLBI Network stations - VLBI facility across Europe, Asia, South Africa and Puerto Rico. The image shows current EVN antennas (both participating and associated), plus the correlator at JIVE (the Netherlands). Credit: JIVE.

1.7 Thesis outline

This thesis aims at understanding the nature of (U)LIRGs from a multiwavelength point of view and considering these galaxies at different scale sizes. It is organized as follows: in Chapter 2 I present a study, at galactic scales, of the molecular gas of a sample of (U)LIRGs using millimeter observations from the IRAM 30m single dish telescope. Chapter 3 is an exploratory multiwavelength study focused on the central kiloparsec region of the LIRG NGC 1614, used as a case study and extended, in Chapter 4, to a sample of eleven additional LIRGs. In Chapter 5, I present very high angular resolution radio images of the LIRG Arp 299 that led to the detection and classification of SN2010P, a new supernova close to one of the nuclei of Arp 299. Chapter 6 considers the innermost region of these sources ($\lesssim 100\,\mathrm{pc}$), where we took advantage of VLBI techniques to achieve the great angular resolution needed to study the nuclear star formation and the interplay between starburst and AGN. Finally, I draw the conclusions in Chapter 7 and state the future perspectives in Chapter 8.

If we knew what it was we were doing, it would not be called research.

Albert Einstein

2

Tracing molecular gas in (U)LIRGs

Based on the results from Herrero-Illana, Privon, et al. (2014, in prep.) and Privon, Herrero-Illana, et al. (2014, in prep.).

STARS are formed in molecular clouds. Hence, the study of molecular gas is key to understand star formation. Unfortunately, the most common molecule in the Universe, the molecular hydrogen, lacks dipolar moment and a has a low mass that requires very high temperatures to excite its rotational transitions, making H_2 mostly invisible to us (see Kennicutt & Evans, 2012, for a review). Indirect tracers are used instead. The most common of these tracers is carbon monoxide (CO), whose excitation is easier than other tracers. In this chapter, I present our work on a survey of (U)LIRGs with the single-dish IRAM 30 m telescope, where we observed four molecular transitions. We focused on the CO features to study the molecular gas properties of

the sample.

2.1 Introduction

Since the discovery of (U)LIRGs as a significant galaxy population by *IRAS* in the 1980s, both single-dish and interferometric surveys of CO have been carried out in these galaxies to characterize the molecular gas responsible for the ongoing star formation (e.g., Tinney *et al.*, 1990; Sanders *et al.*, 1991; Aalto *et al.*, 1995; Solomon *et al.*, 1997; Downes & Solomon, 1998; Bryant & Scoville, 1999; Yao *et al.*, 2003; Narayanan *et al.*, 2005; Papadopoulos *et al.*, 2012b).

CO has a low excitation energy and critical density that makes it easily excited in molecular clouds, and therefore is used as a good tracer for molecular gas in the interstellar medium (ISM), probing star formation. In particular the rotational transition ^{12}CO (1−0), at a rest frequency of $\sim 115.3\,\mathrm{GHz}$ ($\sim 2.6\,\mathrm{mm}$) is the most studied feature. However, ^{12}CO $(1-0)$ traces relatively low density and low temperature gas, and the study of higher transitions or other molecules is needed to to study other phases of the molecular gas.

Most studies use a constant factor to derive the H_2 mass from the CO luminosity (i.e., $\alpha = M(\mathrm{H_2})/L'_{\mathrm{CO}}$). This direct conversion relies on several assumptions, the most important ones being the optical thickness of the line, virialized molecular clouds which are not overlapped in the line of sight, a size-line width power law relation (Larson, 1981), and a relatively similar constant cloud temperature. Furthermore, the conversion factor depends on metallicity (Israel, 2000). The wide use of the relation contrasts with its fragility, but it is still the most reliable tool available to us. A complete review on the CO-to-H_2 conversion factor can be found in Bolatto *et al.* (2013).

CO observations are useful not only to derive the molecular gas mass (and distribution in the case of interferometric studies), but also to study the kinematics of molecular clouds.

In this study we present an extensive survey of CO observations on a sample of 56 nearby, bright (U)LIRGs selected from the Great Observatories All-Sky LIRG Survey (GOALS, Armus *et al.*, 2009). We aim at characterizing the molecular gas as traced by CO, while the study of HCN and HCO^+ will be presented in a future study (Privon, Herrero-Illana, et al., *in prep.*). We focused this study on the gas-to-dust properties of

the sample, the star formation efficiency, the ratio between ^{12}CO and its isotopologue ^{13}CO (between 30 and 70 times less abundant; Langer & Penzias, 1990) and the CO spectral line profiles. This is the most complete uniformly observed sample of (U)LIRGs so far.

2.2 Sample selection

Our sources are selected from the GOALS sample, which consists of 180 luminous and 22 ultraluminous nearby IR galaxies selected from the IRAS Revised Bright Galaxy Sample (Sanders *et al.*, 2003), with $f_{60\,\mu\mathrm{m}} > 5.24\,\mathrm{Jy}$. GOALS comprises observations with the *Hubble Space Telescope (HST)*, the *Spitzer Space Telescope* (both imaging and spectroscopy), *GALEX* and *Chandra X-ray Observatory*, being the most complete multiwavelength sample of nearby, bright (U)LIRGs. These observations are completed with ground-based H I and near-IR spectroscopic data. GOALS contains a sufficient number of LIRGs to sample the complete range of galaxy-galaxy interactions and mergers. Our sample of 56 (U)LIRGs is formed by those sources accessible from Pico Veleta which had not been previously observed by the IRAM 30 m telescope. Our sample luminosity ranges between $1.0 \times 10^{11} L_{\odot}$ and $2.1 \times 10^{12} L_{\odot}$, 52 being LIRGs, and four ULIRGs.

2.3 Observations and data reduction

The observations were carried out with the EMIR multi-band receiver at the IRAM 30 m telescope (see Fig. 2.1) on Pico Veleta, Spain, in five observing periods: June 2010, September 2011, December 2011, October 2012, and March 2014 (PI: K. Iwasawa), with a total of 56 observed sources. We tuned the receiver in two frequency windows: one around HCN and HCO$^+$ (full results will be shown in Privon et al., *in prep.*), and the other one around $^{12}\mathrm{CO}(1-0)$ and $^{13}\mathrm{CO}(1-0)$. All the observations were performed in wobbler switching mode. The complete list of sources is shown in Table 2.1. The pointing coordinates for the sources were taken from the position of the peaks of Spitzer IRAC channel 4 images.

Figure 2.1: IRAM 30 m telescope - Located in Pico Veleta, Granada (Spain), it is a 30 m single dish parabolic antenna observing at 0.8, 1, 2, and 3 mm. Credit: IRAM.

We performed the data reduction using the CLASS[1] software package, which consisted of gain elevation calibration, platforming correction (when the FTS backend was used), order 1 baseline subtraction, averaging of spectra and smoothing to $\sim 25\,\mathrm{km\,s^{-1}}$. We obtained line fluxes by integrating all channels within the line profile. Observations are summarized in Table 2.2 and spectra are shown in Figure 2.2. Together with the ^{12}CO and ^{13}CO observations, we used the HCN and HCO^+ data to compare the line profiles of all transitions (see section 2.5.5).

Three of the sources (IRAS F05189-2524, IRAS 22491-1808 and IRAS 07251-0248) were re-observed under director's discretionary time in March 2014 (program D01-13; PI: R. Herrero-Illana), since we found hints of an unexpected behavior in their ^{13}CO line intensities (see section 2.5.3).

We increased our observed sample with other GOALS sources, observed as well with the IRAM 30 m telescope. They belong to previous published studies with CO measurements, yielding a total of 76 sources: 56 from our observations, 13 from Graciá-Carpio *et al.* (2006), and seven from Costagliola *et al.* (2011).

[1] `http://iram.fr/IRAMFR/GILDAS/`

Table 2.1: Source list

Source name	R.A. (J2000)	Dec. (J2000)	D_L (Mpc)	$f_{12\mu m}$ (Jy)	$f_{25\mu m}$ (Jy)	$f_{60\mu m}$ (Jy)	$f_{100\mu m}$ (Jy)	$\log(L_{\rm FIR})$ ($\log(L_\odot)$)	$\log(L_{\rm IR})$ ($\log(L_\odot)$)
NGC0034	00 11 06.55	-12 06 27.90	84.1	0.35	2.39	17.05	16.86	11.34	11.44
MCG-02-01-051A	00 18 50.17	-10 21 44.78	109.0	...	...	...	...	...	...
MCG-02-01-051B	00 18 50.90	-10 22 36.19	109.0	...	...	...	...	...	...
IC1623	01 07 47.53	-17 30 25.88	79.6	1.03	3.65	22.93	31.55	11.5	11.65
MCG-03-04-014	01 10 08.96	-16 51 09.79	144.0	0.34	0.9	7.25	10.33	11.49	11.63
IRAS F01364-1042	01 38 52.92	-10 27 11.41	210.0	0.16	0.44	6.62	6.88	11.73	11.76
IC214	02 14 05.47	05 10 25.21	129.0	0.26	0.62	5.28	8.57	11.25	11.37
UGC01845	02 24 07.99	47 58 10.81	67.0	0.35	1.07	10.31	15.51	10.95	11.07
NGC0958	02 30 42.85	-02 56 20.51	80.6	0.62	0.94	5.85	15.08	11.04	11.17
ESO550-IG025	04 21 20.00	-18 48 39.38	135.0	0.22	0.51	5.69	9.47	11.35	11.45
UGC03094	04 35 33.83	19 10 18.19	106.0	0.53	0.84	6.35	12.85	11.21	11.35
NGC1797	05 07 44.85	-08 01 08.69	63.4	0.33	1.35	9.56	12.76	10.86	11.0
IRAS 05170+0535	05 19 40.41	05 38 42.79	...	0.58	4.5	14.45	9.5	11.7	11.81
IRAS F05189-2524	05 21 01.47	-25 21 45.40	187.0	0.74	3.47	13.25	11.84	11.93	12.11
IRAS 05187-1017	05 21 06.54	-10 14 46.79	122.0	0.08	0.19	5.39	8.04	11.19	11.23
IRAS F06076-2139	06 09 45.81	-21 40 23.70	165.0	0.06	0.63	6.43	8.47	11.51	11.59
NGC2341	07 09 12.00	20 36 10.01	73.8	...	...	...	...	...	...
NGC2342	07 09 18.06	20 38 10.39	75.4	0.46	1.64	7.73	24.1	11.18	11.25
IRAS 07251-0248	07 27 37.55	-02 54 54.11	400.0	0.07	0.66	6.49	6.35	12.27	12.32
IRAS F09111-1007b	09 13 36.40	-10 19 30.00	237.0	...	...	...	...	...	...
IRAS F09111-1007a	09 13 38.80	-10 19 20.32	237.0	...	...	...	...	...	...
UGC05101	09 35 51.60	61 21 11.81	177.0	0.25	1.02	11.68	19.91	11.87	11.95
CGCG011-076	11 21 08.28	-02 59 39.01	117.0	0.48	0.76	5.85	9.18	11.2	11.37
CGCG011-076	11 21 12.22	-02 59 02.18	117.0	0.48	0.76	5.85	9.18	11.2	11.37
IRAS F12224-0624	12 25 03.89	-06 40 51.71	125.0	0.11	0.2	5.99	8.13	11.23	11.27
CGCG043-099	13 01 50.80	04 19 59.99	175.0	0.3	0.47	5.25	8.06	11.49	11.62
ESO507-G070	13 02 52.35	-23 55 17.69	106.0	0.25	0.8	13.04	15.71	11.42	11.49
NGC5104	13 21 23.10	00 20 32.89	90.8	0.39	0.74	6.78	13.37	11.09	11.2
IC4280	13 32 53.30	-24 12 25.88	82.4	0.38	0.68	6.1	12.36	10.96	11.08
NGC5258	13 39 57.25	00 49 47.60	98.4	0.57	1.34	10.73	19.97	11.43	11.55

Continued on Next Page...

Table 2.1 – *Continued*

Source name	R.A. (J2000)	Dec. (J2000)	D_L (Mpc)	$f_{12\mu m}$ (Jy)	$f_{25\mu m}$ (Jy)	$f_{60\mu m}$ (Jy)	$f_{100\mu m}$ (Jy)	$\log(L_{\rm FIR})$ ($\log(L_\odot)$)	$\log(L_{\rm IR})$ ($\log(L_\odot)$)
UGC08739	13 49 13.91	35 15 26.21	81.4	0.35	0.42	5.79	15.89	11.03	11.08
NGC5331A	13 52 16.20	02 06 05.62	143.0	...	...	...	...	...	...
CGCG247-020	14 19 43.21	49 14 11.90	120.0	0.15	0.84	6.01	8.47	11.2	11.32
IRAS F14348-1447	14 37 38.34	-15 00 22.79	387.0	0.1	0.55	6.82	7.31	12.26	12.3
CGCG049-057	15 13 13.09	07 13 32.02	65.4	0.05	0.95	21.89	31.53	11.23	11.27
NGC5936	15 30 00.86	12 59 22.20	67.1	0.48	1.47	8.73	17.66	10.93	11.07
IRAS F16164-0746	16 19 11.79	-07 54 02.81	128.0	0.17	0.59	10.29	13.22	11.48	11.55
CGCG052-037	16 30 56.50	04 04 58.51	116.0	0.25	0.81	7.0	11.23	11.26	11.38
IRAS F16399-0937	16 42 40.21	-09 43 14.41	128.0	0.27	1.13	8.42	14.72	11.44	11.56
NGC6285	16 58 23.99	58 57 21.31	78.7	0.47	0.62	9.24	23.11	11.26	11.32
NGC6286	16 58 31.55	58 56 12.19	76.1	0.47	0.62	9.24	23.11	11.26	11.32
IRAS F17138-1017	17 16 35.76	-10 20 39.80	84.0	0.63	2.12	15.18	19.02	11.27	11.42
UGC11041	17 54 51.83	34 46 34.50	77.5	0.51	0.69	5.84	12.78	10.91	11.04
CGCG141-034	17 56 56.63	24 01 01.31	93.4	0.18	0.56	6.24	10.55	11.04	11.13
IRAS 18090+0130	18 11 38.41	01 31 40.12	121.0	0.3	0.81	7.73	15.64	11.49	11.58
NGC6701	18 43 12.50	60 39 11.20	62.4	0.55	1.32	10.05	20.05	10.93	11.05
NGC6786	19 10 54.00	73 24 35.71	103.0	0.43	1.42	7.58	10.77	11.26	11.43
UGC11415	19 11 04.40	73 25 32.02	104.0	0.43	1.42	7.58	10.77	11.26	11.43
ESO593-IG008	19 14 31.15	-21 19 06.31	222.0	0.18	0.51	6.38	9.37	11.77	11.87
NGC6907	20 25 06.60	-24 48 32.11	50.1	1.19	1.94	14.14	29.59	10.89	11.03
IRAS 21101+5810	21 11 30.40	58 23 03.19	174.0	0.15	0.82	7.94	11.08	11.65	11.75
ESO602-G025	22 31 25.49	-19 02 04.31	110.0	0.27	0.91	5.42	9.64	11.13	11.27
UGC12150	22 41 12.18	34 14 57.01	93.5	0.37	0.82	8.0	15.58	11.18	11.29
IRAS F22491-1808	22 51 49.36	-17 52 24.82	351.0	0.09	0.54	5.54	4.64	12.09	12.11
CGCG453-062	23 04 56.55	19 33 07.09	109.0	0.19	0.54	7.19	11.73	11.23	11.31
NGC7591	23 18 13.52	06 33 26.50	71.4	0.28	1.27	7.87	14.87	10.94	11.05

Note. — IRAS flux densities and infrared luminosities are obtained from Sanders *et al.* (2003).
$L_{\rm FIR} = L(40 - 400\,\mu{\rm m})$; $L_{\rm IR} = L(8 - 1000\,\mu{\rm m})$

Table 2.2: Spectral data

Source name	Transition	Date	Time (min)	T_{sys} (K)
NGC0034	^{12}CO, ^{13}CO	2011-09	10.5	278, 182
MCG-02-01-051A	^{12}CO, ^{13}CO	2011-12	21.0	188, 138
MCG-02-01-051B	^{12}CO, ^{13}CO	2011-12	16.0	197, 142
IC1623	^{12}CO, ^{13}CO	2011-12	21.5	200, 143
MCG-03-04-014	^{12}CO, ^{13}CO	2011-12	16.0	175, 133
IRAS F01364-1042	^{12}CO, ^{13}CO	2011-09	21.0	171, 135
IC214	^{12}CO, ^{13}CO	2011-12	16.0	183, 177
UGC01845	^{12}CO, ^{13}CO	2012-10	10.0	204, 140
NGC0958	^{12}CO, ^{13}CO	2012-10	15.5	285, ···
ESO550-IG025	^{12}CO, ^{13}CO	2011-09	16.0	222, 157
UGC03094	^{12}CO, ^{13}CO	2012-10	10.0	197, 136
NGC1797	^{12}CO, ^{13}CO	2012-10	15.5	219, 148
IRAS 05170+0535	^{12}CO, ^{13}CO	2011-09	10.5	170, 122
IRAS F05189-2524	^{12}CO, ^{13}CO	2014-03	128.0	236, 173
IRAS 05187-1017	^{12}CO, ^{13}CO	2014-03	51.0	166, 117
IRAS F06076-2139	^{12}CO, ^{13}CO	2011-09	16.0	200, 145
NGC2341	^{12}CO, ^{13}CO	2014-03	25.5	235, 150
NGC2342	^{12}CO, ^{13}CO	2012-10	15.5	169, 117
IRAS 07251-0248	^{12}CO, ^{13}CO	2014-03	21.5	136, 106
IRAS F09111-1007b	^{12}CO, ^{13}CO	2011-09	21.5	184, ···
IRAS F09111-1007a	^{12}CO, ^{13}CO	2011-09	21.5	189, ···
UGC05101	^{12}CO, ^{13}CO	2010-06	53.0	159, 122
CGCG011-076	^{12}CO, ^{13}CO	2014-03	30.5	203, 134
CGCG011-076	^{12}CO, ^{13}CO	2012-10	10.0	201, 179
IRAS F12224-0624	^{12}CO, ^{13}CO	2014-03	20.5	190, 126
CGCG043-099	^{12}CO, ^{13}CO	2011-09	26.5	194, 141
ESO507-G070	^{12}CO, ^{13}CO	2011-12	10.5	227, 135
NGC5104	^{12}CO, ^{13}CO	2012-10	10.0	186, 151
IC4280	^{12}CO, ^{13}CO	2012-10	10.0	252, 178
NGC5258	^{12}CO, ^{13}CO	2011-12	10.5	243, 145
UGC08739	^{12}CO, ^{13}CO	2012-10	15.5	232, 166
NGC5331A	^{12}CO, ^{13}CO	2011-09	16.0	176, 134
CGCG247-020	^{12}CO, ^{13}CO	2012-10	20.5	309, 231
IRAS F14348-1447	^{12}CO, ^{13}CO	2011-09	10.5	173, 147
CGCG049-057	^{12}CO, ^{13}CO	2012-10	61.5	253, 179
NGC5936	^{12}CO, ^{13}CO	2012-10	10.0	176, 122
IRAS F16164-0746	^{12}CO, ^{13}CO	2011-12	10.5	240, 152
CGCG052-037	^{12}CO, ^{13}CO	2012-10	20.0	182, 125
IRAS F16399-0937	^{12}CO, ^{13}CO	2011-12	16.0	243, 154
NGC6285	^{12}CO, ^{13}CO	2011-12	10.5	170, 109
NGC6286	^{12}CO, ^{13}CO	2011-12	10.5	216, 116
IRAS F17138-1017	^{12}CO, ^{13}CO	2011-12	10.5	245, 141
UGC11041	^{12}CO, ^{13}CO	2012-10	10.0	196, 148
CGCG141-034	^{12}CO, ^{13}CO	2012-10	10.0	171, 118
IRAS 18090+0130	^{12}CO, ^{13}CO	2011-09	16.0	186, 137
NGC6701	^{12}CO, ^{13}CO	2012-10	10.5	211, 155

Continued on Next Page...

Table 2.2 – *Continued*

Source name	Transition	Date	Time (min)	$T_{\rm sys}$ (K)
NGC6786	^{12}CO, ^{13}CO	2011-09	10.5	193, 134
UGC11415	^{12}CO, ^{13}CO	2011-09	10.5	192, 134
ESO593-IG008	^{12}CO, ^{13}CO	2014-03	20.5	190, 147
NGC6907	^{12}CO, ^{13}CO	2012-10	15.5	367, 245
IRAS 21101+5810	^{12}CO, ^{13}CO	2011-09	10.5	165, 127
ESO602-G025	^{12}CO, ^{13}CO	2014-03	25.5	251, 162
UGC12150	^{12}CO, ^{13}CO	2012-10	15.5	247, 156
IRAS F22491-1808	^{12}CO, ^{13}CO	2014-03	133.0	142, 117
CGCG453-062	^{12}CO, ^{13}CO	2012-10	15.5	293, 177
NGC7591	^{12}CO, ^{13}CO	2014-03	13.0	219, 147

Note. — System temperatures are given for ^{12}CO and ^{13}CO, respectively. Although both transitions were observed simultaneously, they were located in different sub-bands, and hence the different $T_{\rm sys}$.

2.4 Results

In Table 2.3 we show the derived properties from the observations. Figure 2.2 shows the CO spectra (both ^{12}CO and ^{13}CO) as well as the corresponding HCN and HCO$^+$ spectra. IRAC images at 8.0 μm are showed, with the beam corresponding to CO lines (inner circle) and HCN and HCO$^+$ lines (outer circle).

From the 56 observed sources, we detected ^{12}CO in 53 ($\sim$ 95%), and ^{13}CO in 31 ($\sim$ 55%). Line intensities and luminosities for ^{12}CO and ^{13}CO were obtained integrating over the same velocity range, corresponding to the CO profile edges, with a median velocity width of 661 km s^{-1}, with $\sim$ 54% of the sources showing a multiple peak profile (see Fig. 2.2. The CO luminosities, measured in K km s^{-1} pc^2, were obtained as follows (Solomon *et al.*, 1992):

$$L'_{\rm n CO} = 3.25 \times 10^7 (S_{\rm CO}\Delta v)\nu_{\rm obs}^{-2} D_L^2 (1+z)^{-3}, \tag{2.1}$$

where $S_{\rm CO}\Delta v$ is the velocity integrated flux (Jy km s^{-1}), $\nu_{\rm obs}$ is the observed frequency (GHz), D_L is the luminosity distance (Mpc) and z is the redshift. Considering that $\nu_{\rm rest} = \nu_{\rm obs}(1+z)$, we can rewrite eq. (2.1) as:

$$L'_{\rm n CO} = A_{n\rm CO} \times 10^3 \left(\frac{S_{\rm CO}\Delta v}{\rm Jy\,km\,s^{-1}}\right)\left(\frac{D_L}{\rm Mpc}\right)^2 (1+z)^{-1}, \tag{2.2}$$

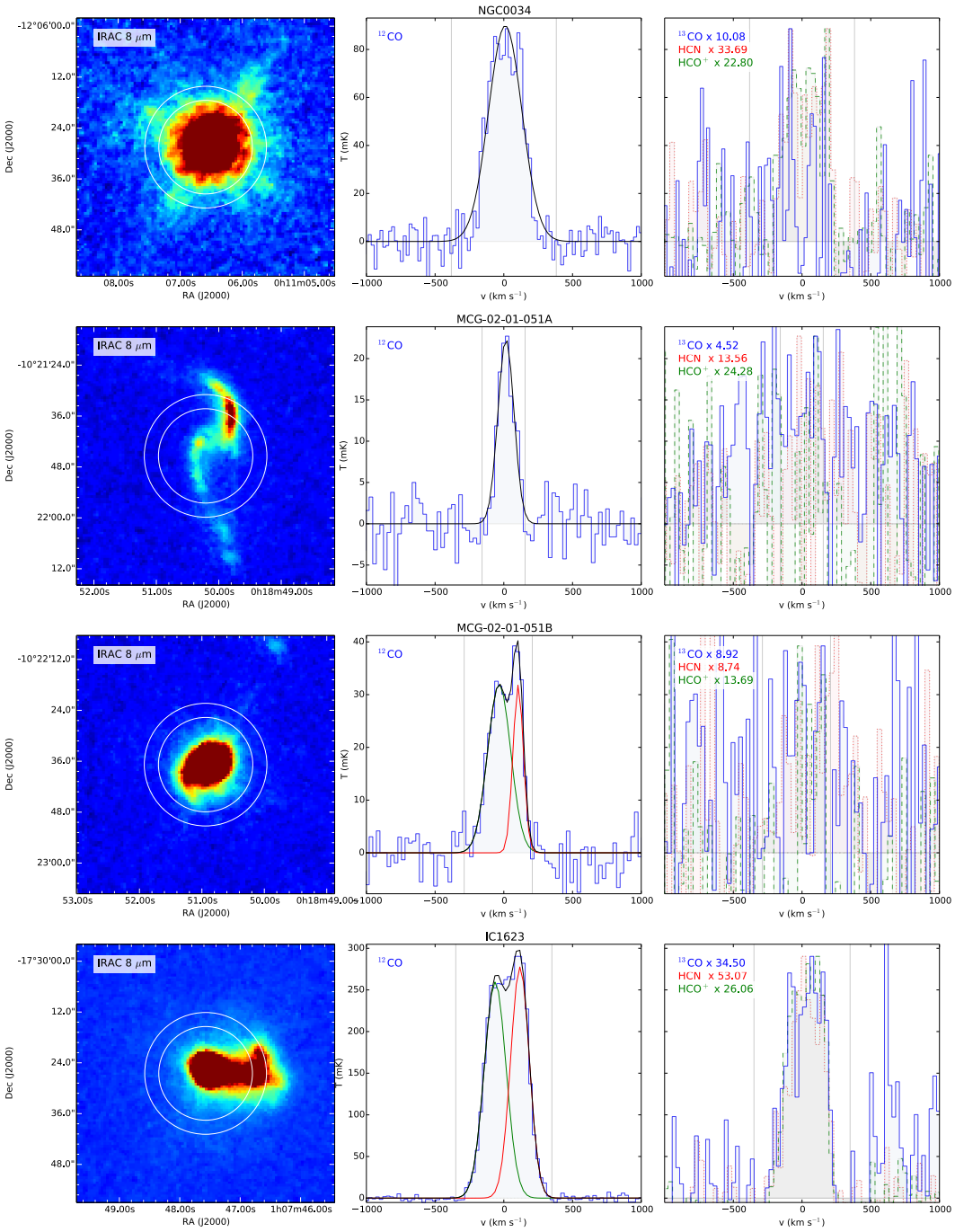

Figure 2.2: Spectral line profiles comparison - Left: *Spitzer* IRAC 8 μm image for each source. Overlapped circumferences represent the pointing position and beam sizes corresponding to CO and ^{13}CO (inner), and HCN and HCO$^+$ (outer). Middle: CO spectra, fitted with one to three Gaussian components. Gray vertical lines correspond to the velocity integration limits. Right: overlapped profiles of ^{13}CO (blue, solid line), HCN (red, dotted line), and HCO$^+$ (green, dashed line) in the same velocity range as the CO spectrum. The spectra have been normalized to the peak of the CO line, and the normalization factor is shown for each line.

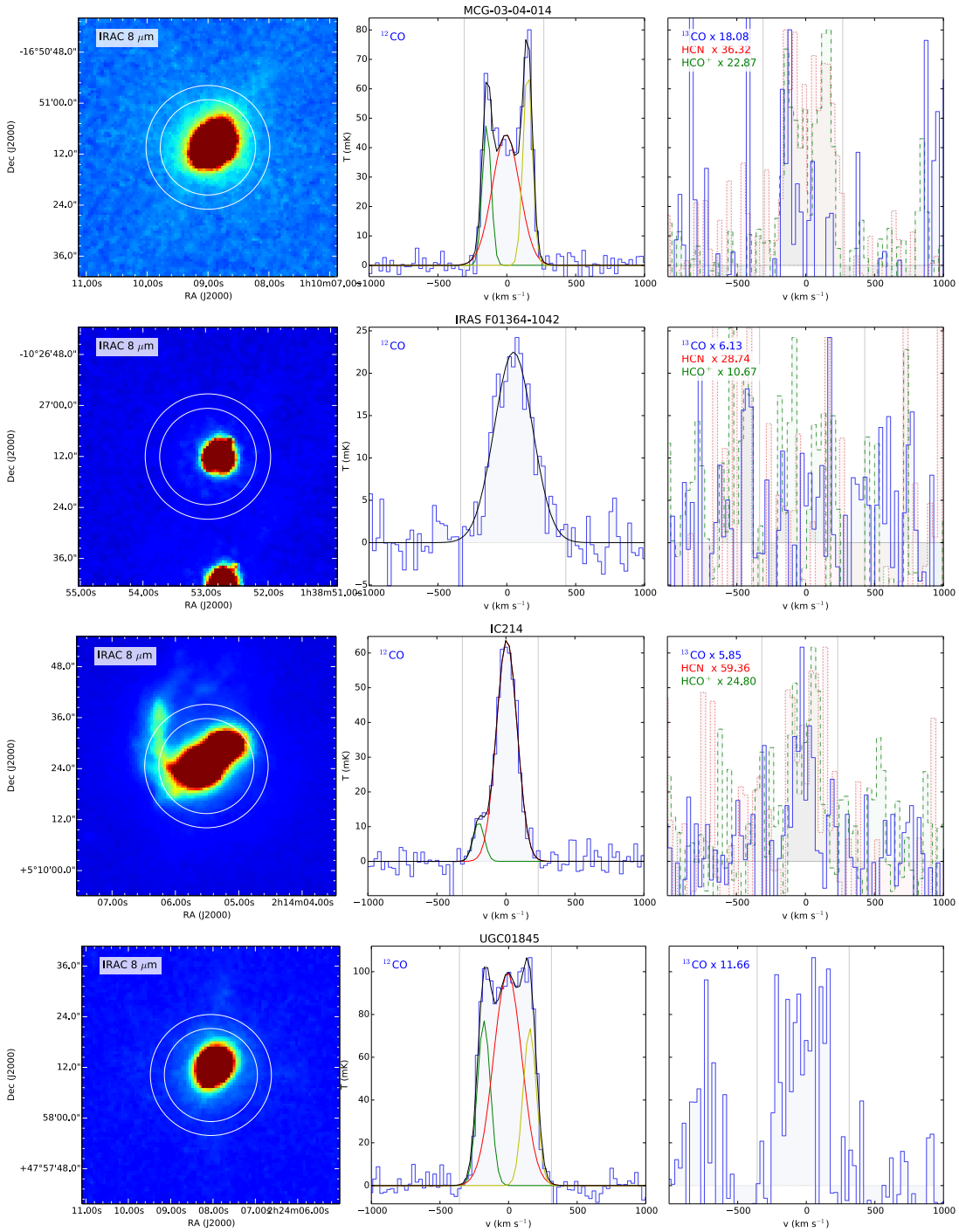

Figure 2.2: Spectral line profiles comparison - *Continued.*

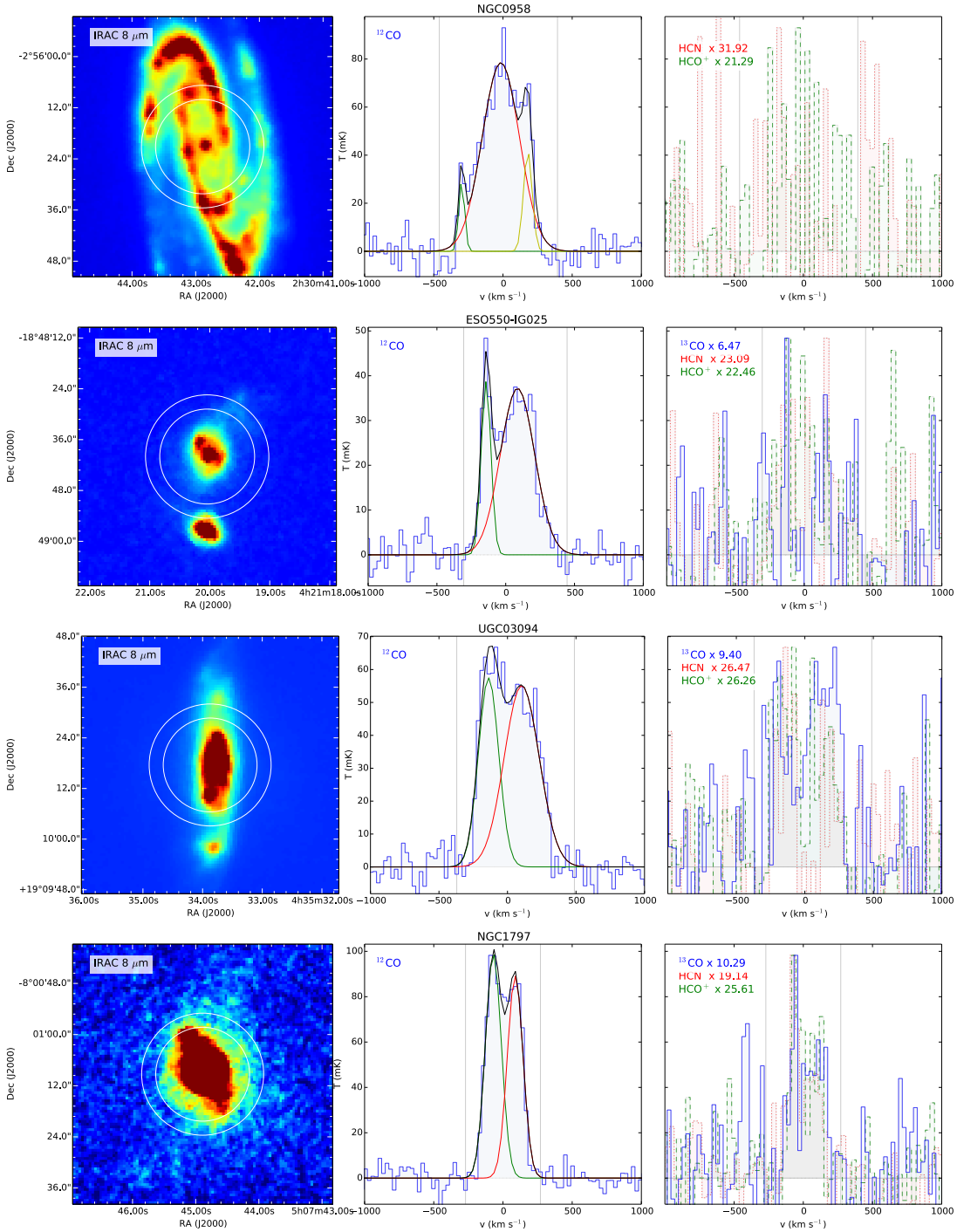

Figure 2.2: Spectral line profiles comparison - *Continued.*

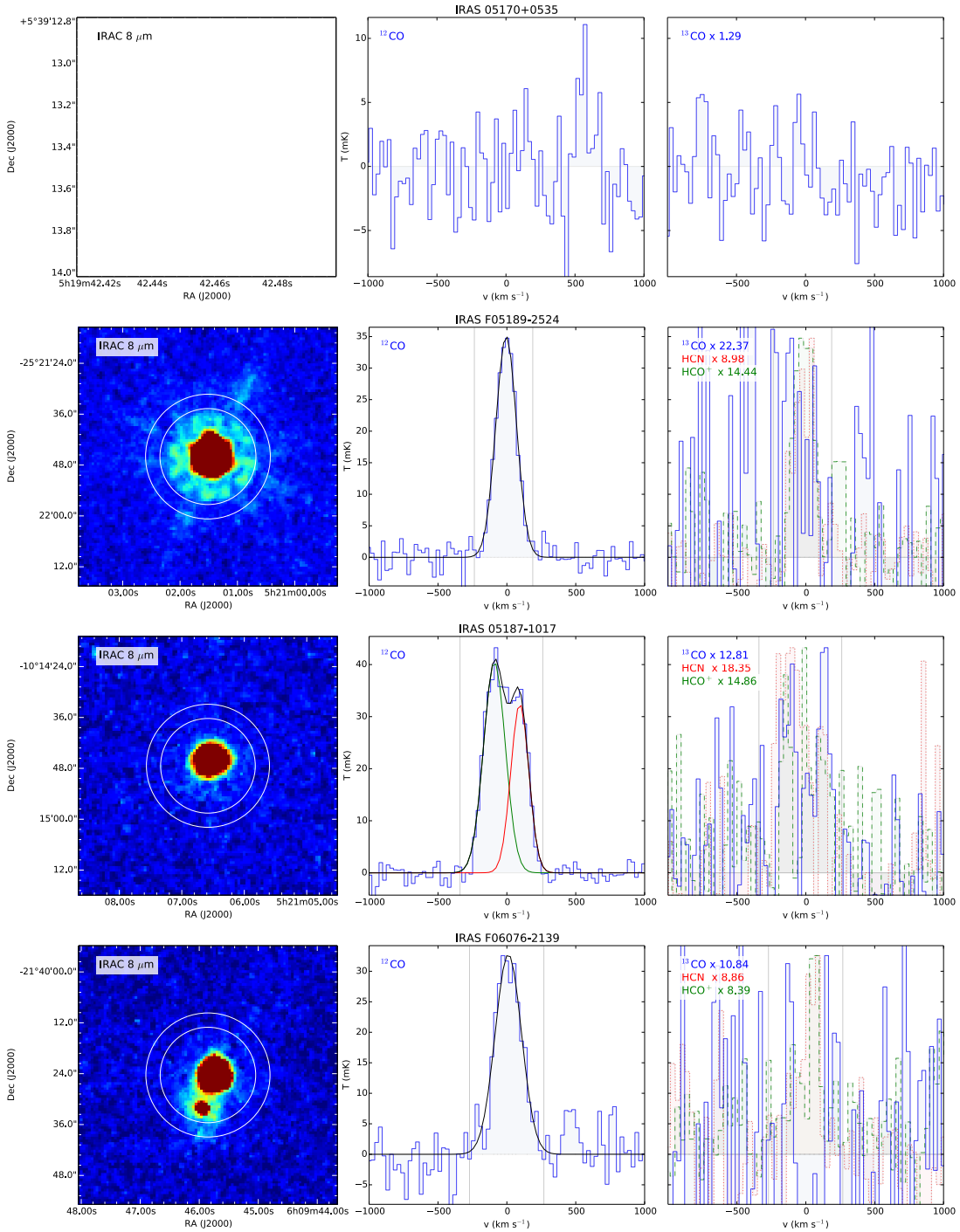

Figure 2.2: Spectral line profiles comparison - *Continued.*

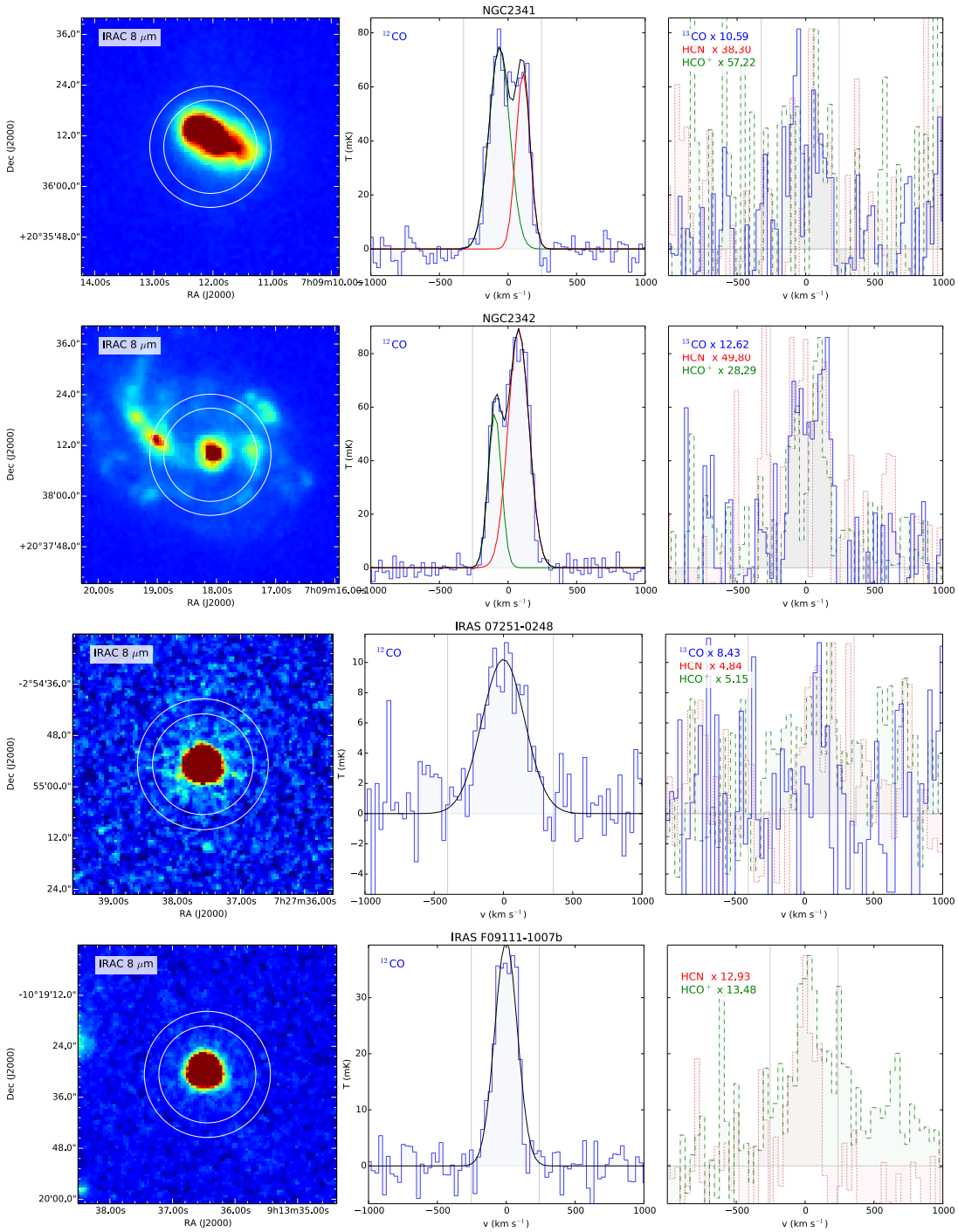

Figure 2.2: Spectral line profiles comparison - *Continued.*

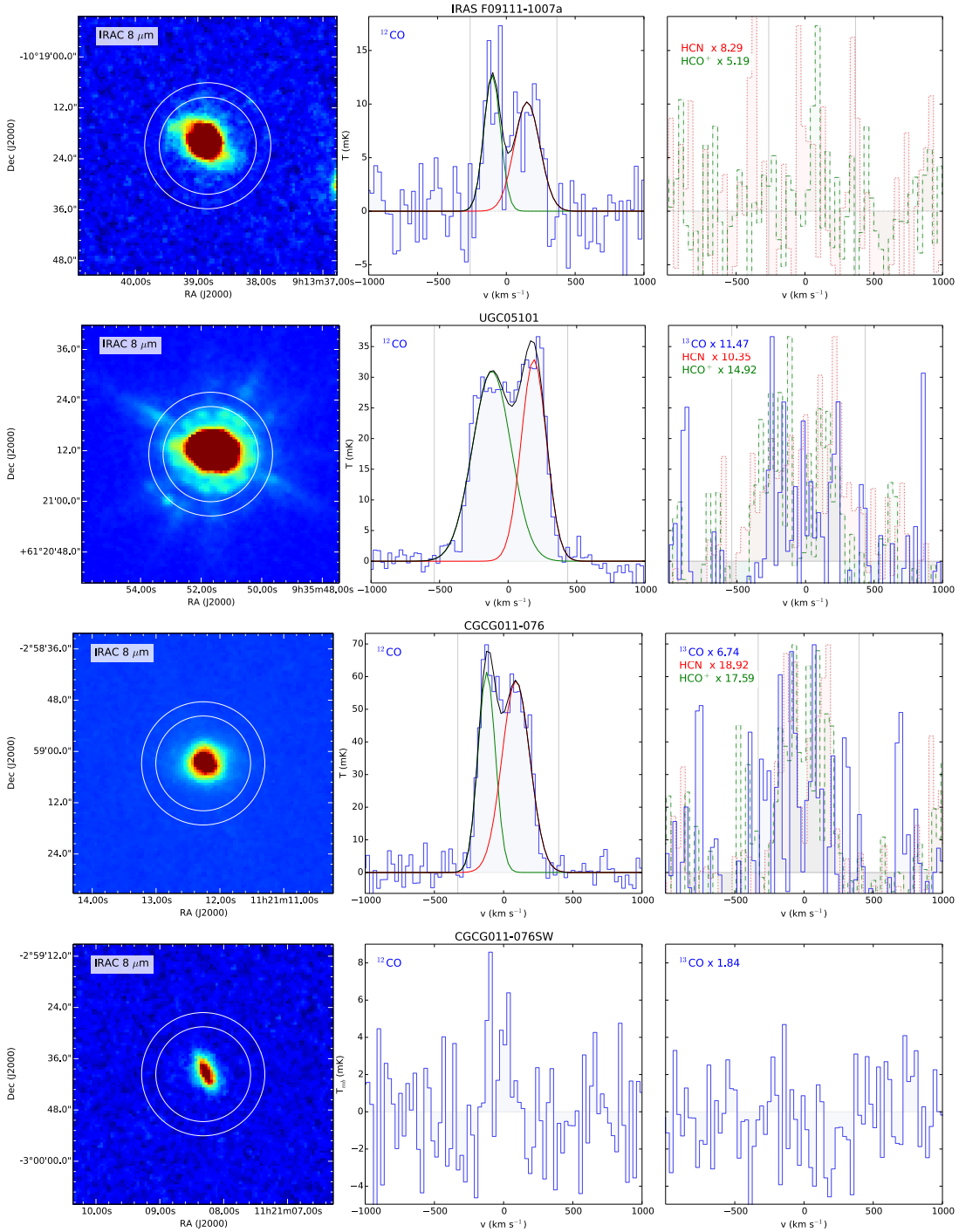

Figure 2.2: Spectral line profiles comparison - *Continued.*

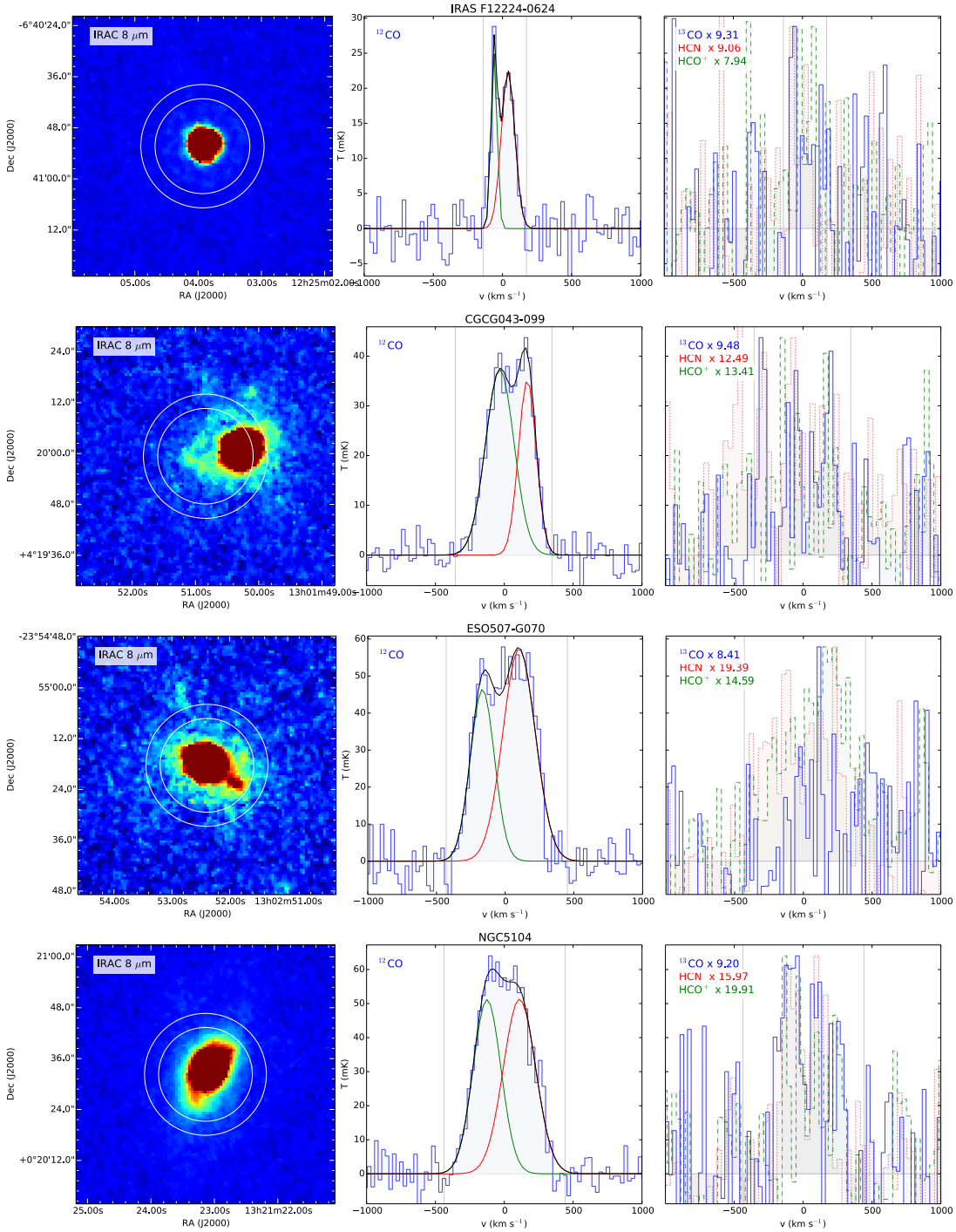

Figure 2.2: Spectral line profiles comparison - *Continued.*

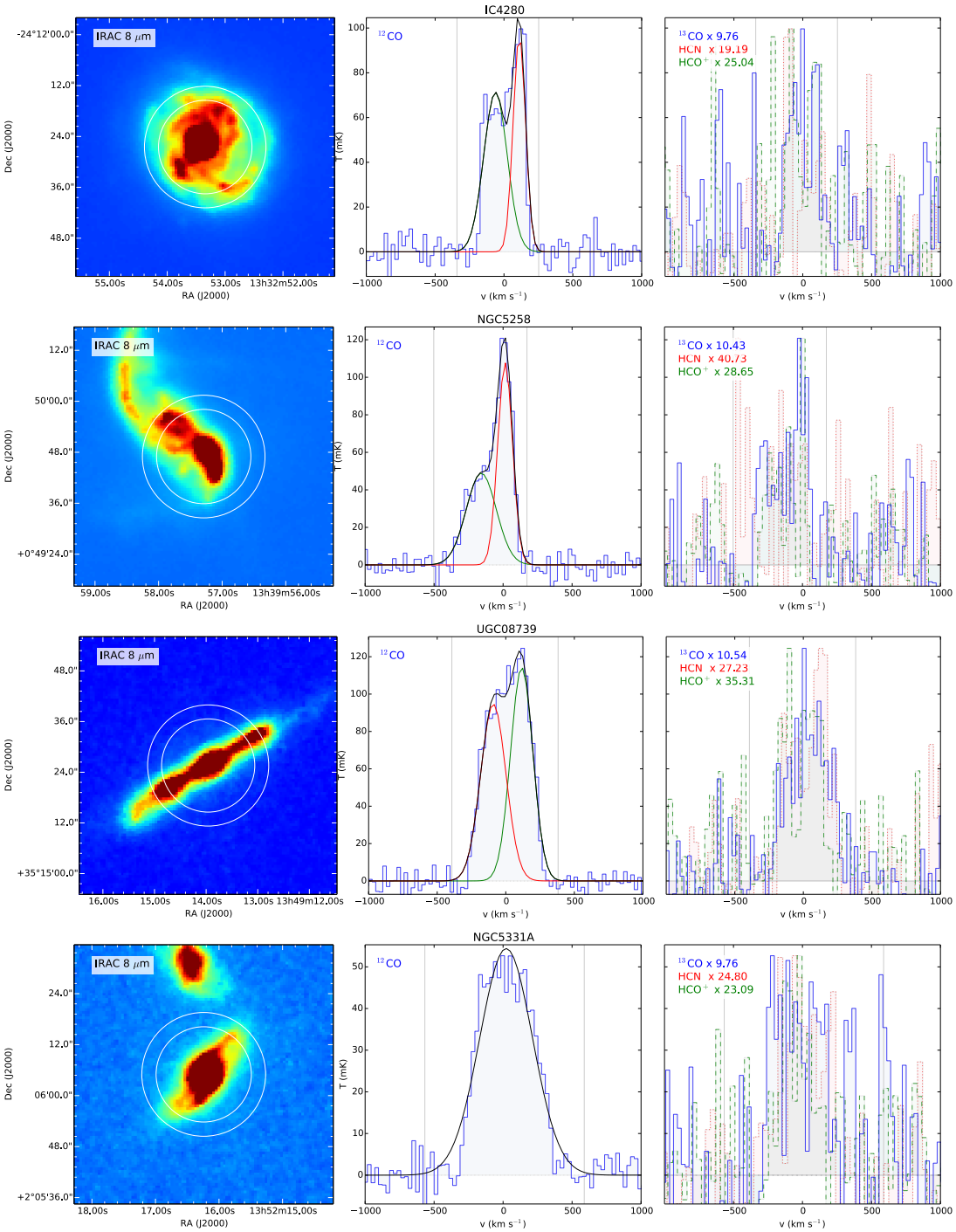

Figure 2.2: Spectral line profiles comparison - *Continued.*

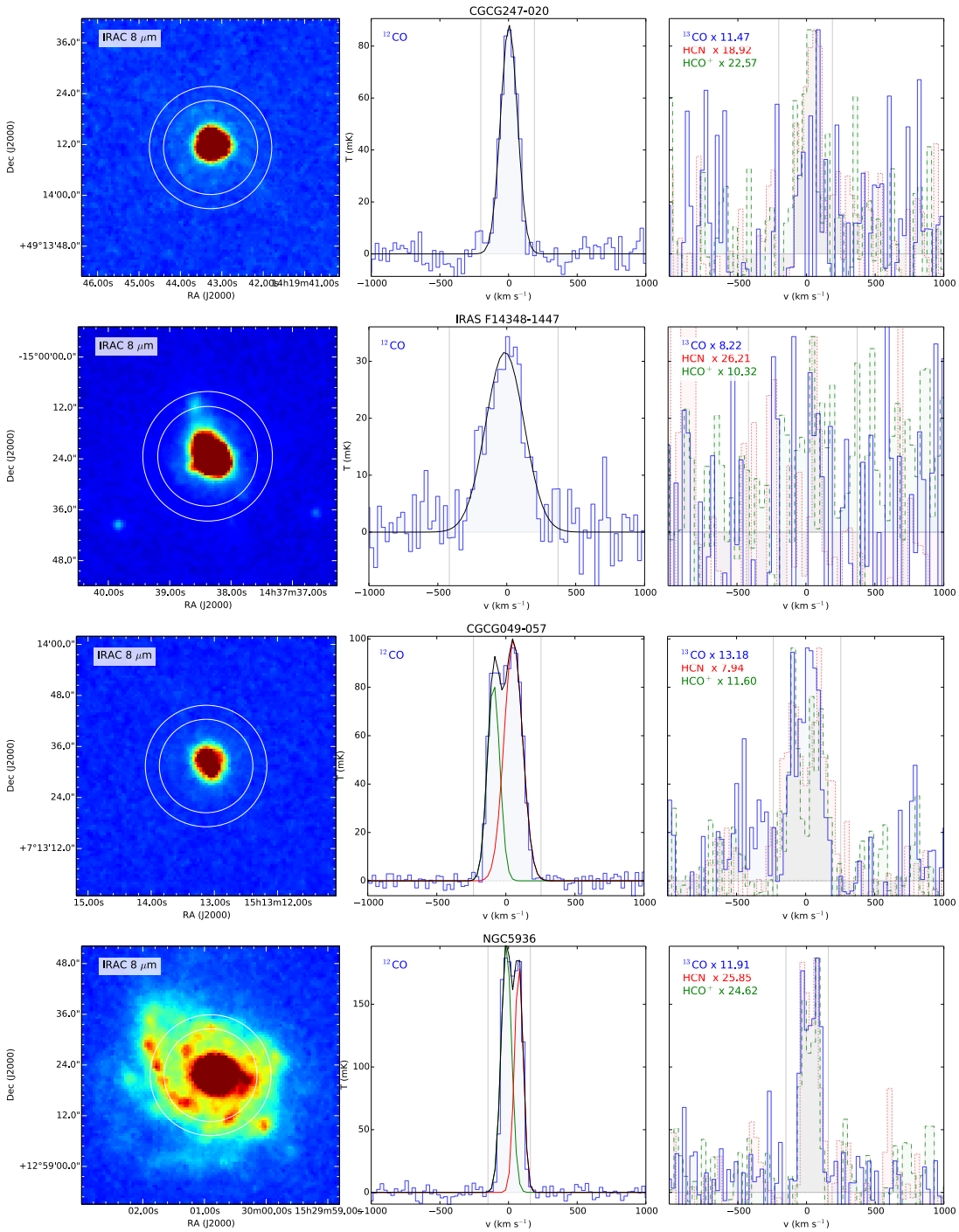

Figure 2.2: Spectral line profiles comparison - *Continued.*

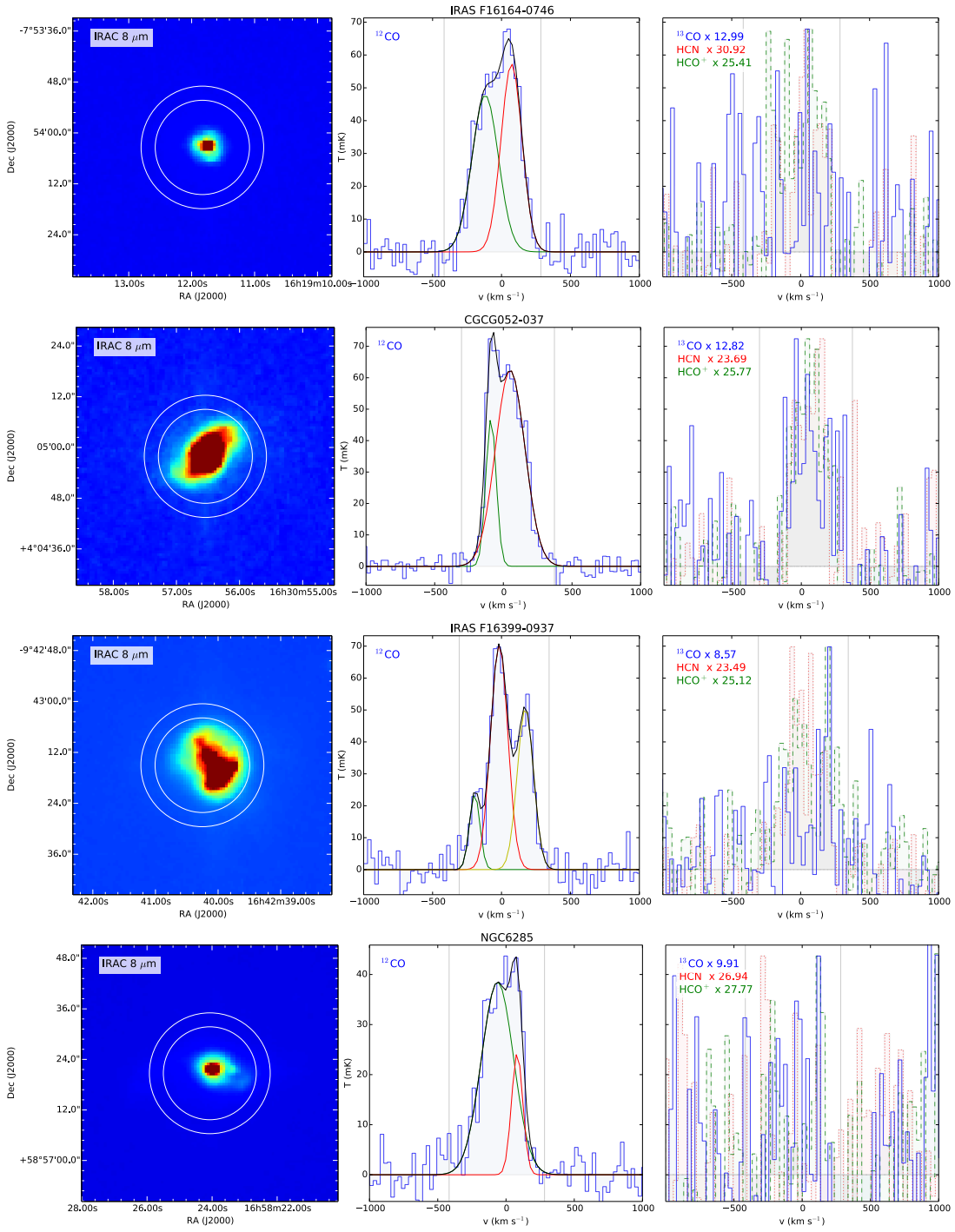

Figure 2.2: Spectral line profiles comparison - *Continued.*

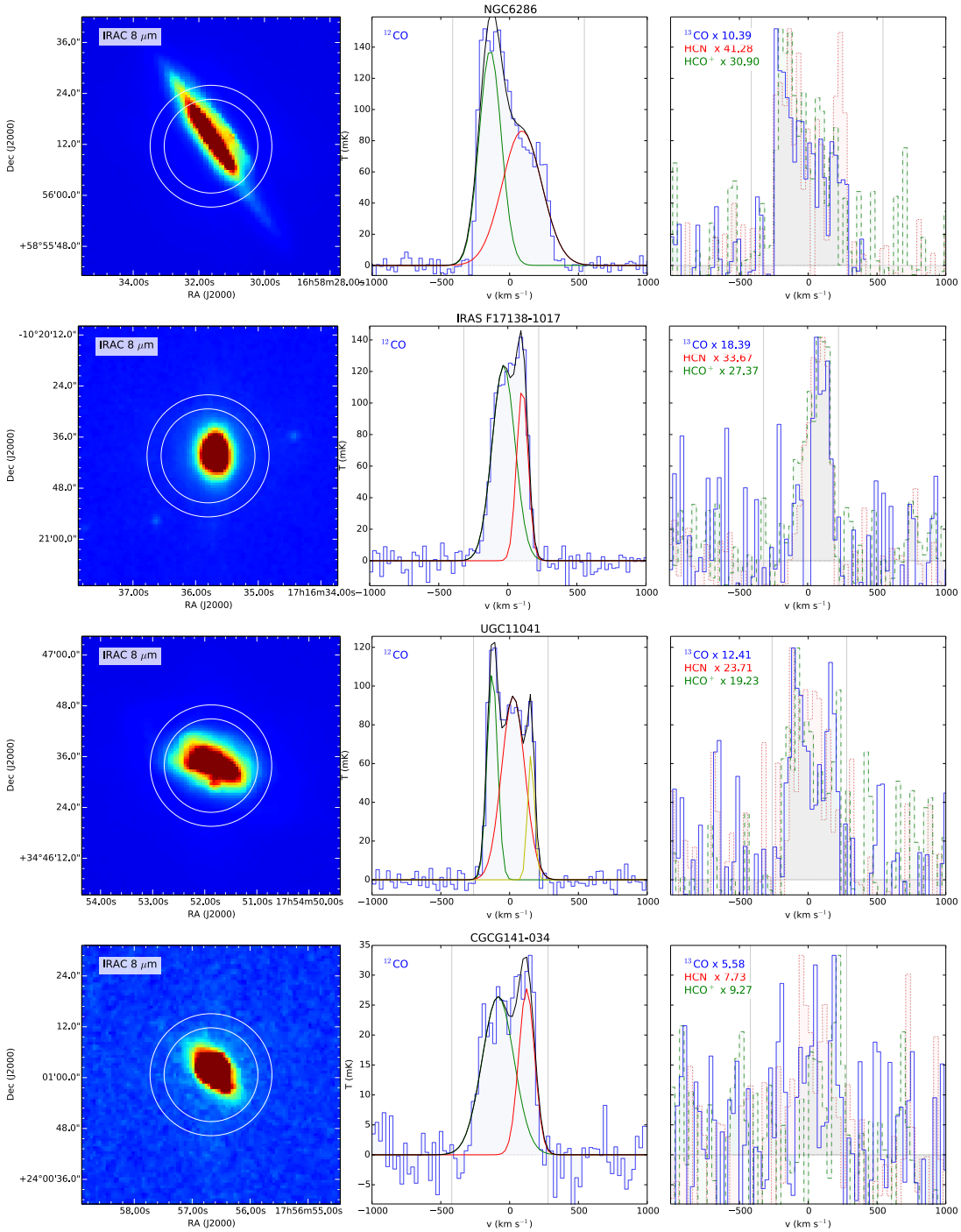

Figure 2.2: Spectral line profiles comparison - *Continued.*

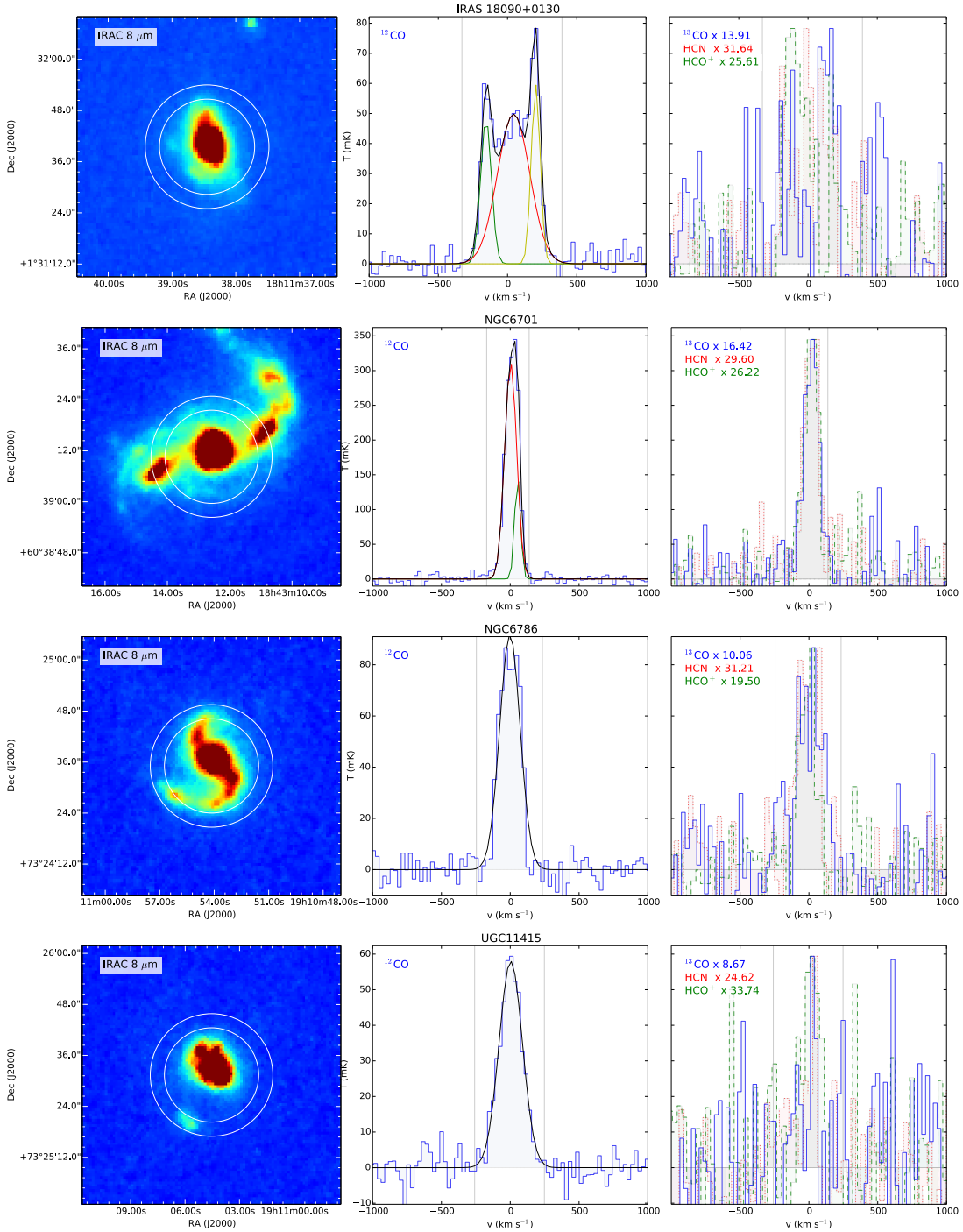

Figure 2.2: Spectral line profiles comparison - *Continued.*

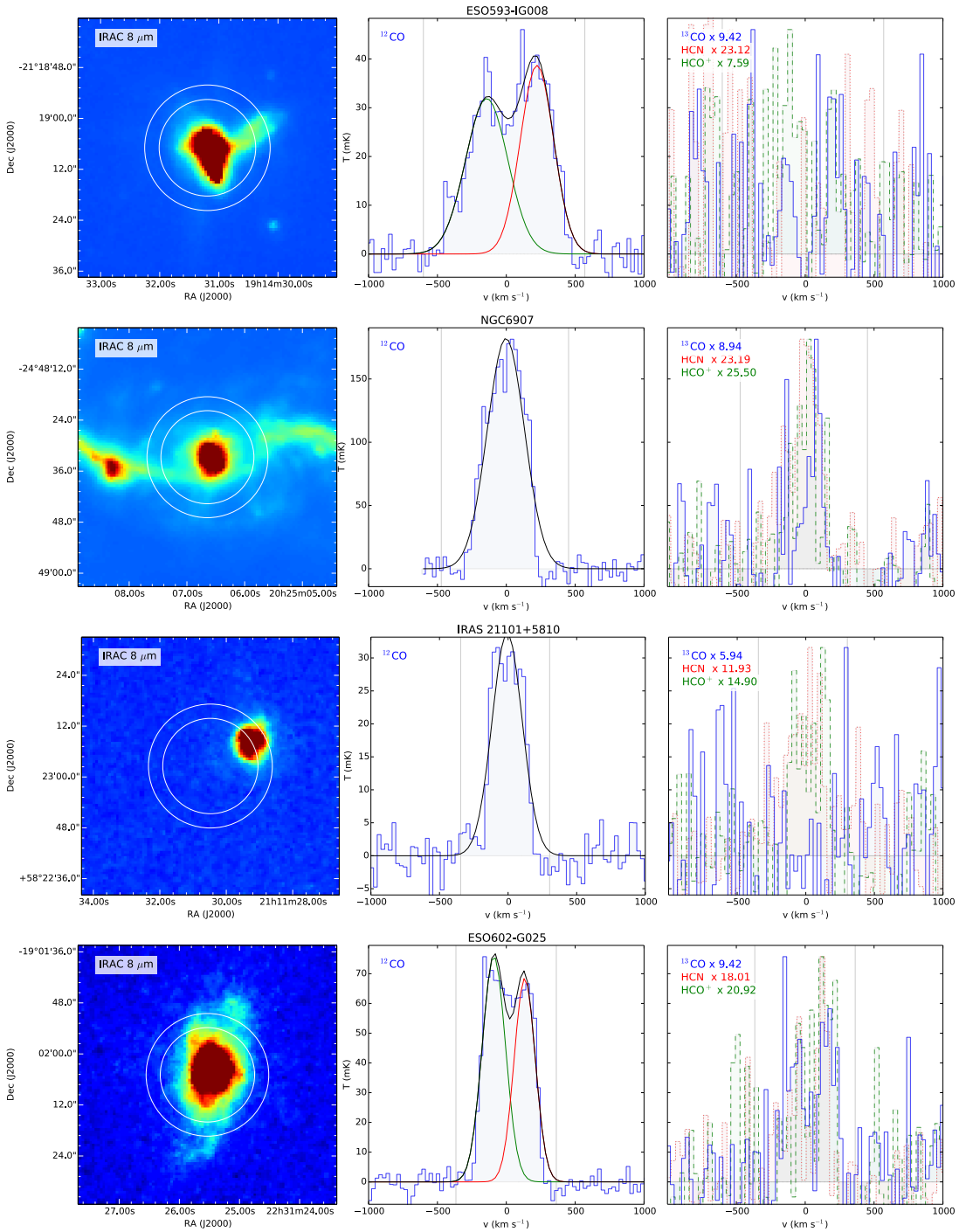

Figure 2.2: Spectral line profiles comparison - *Continued.*

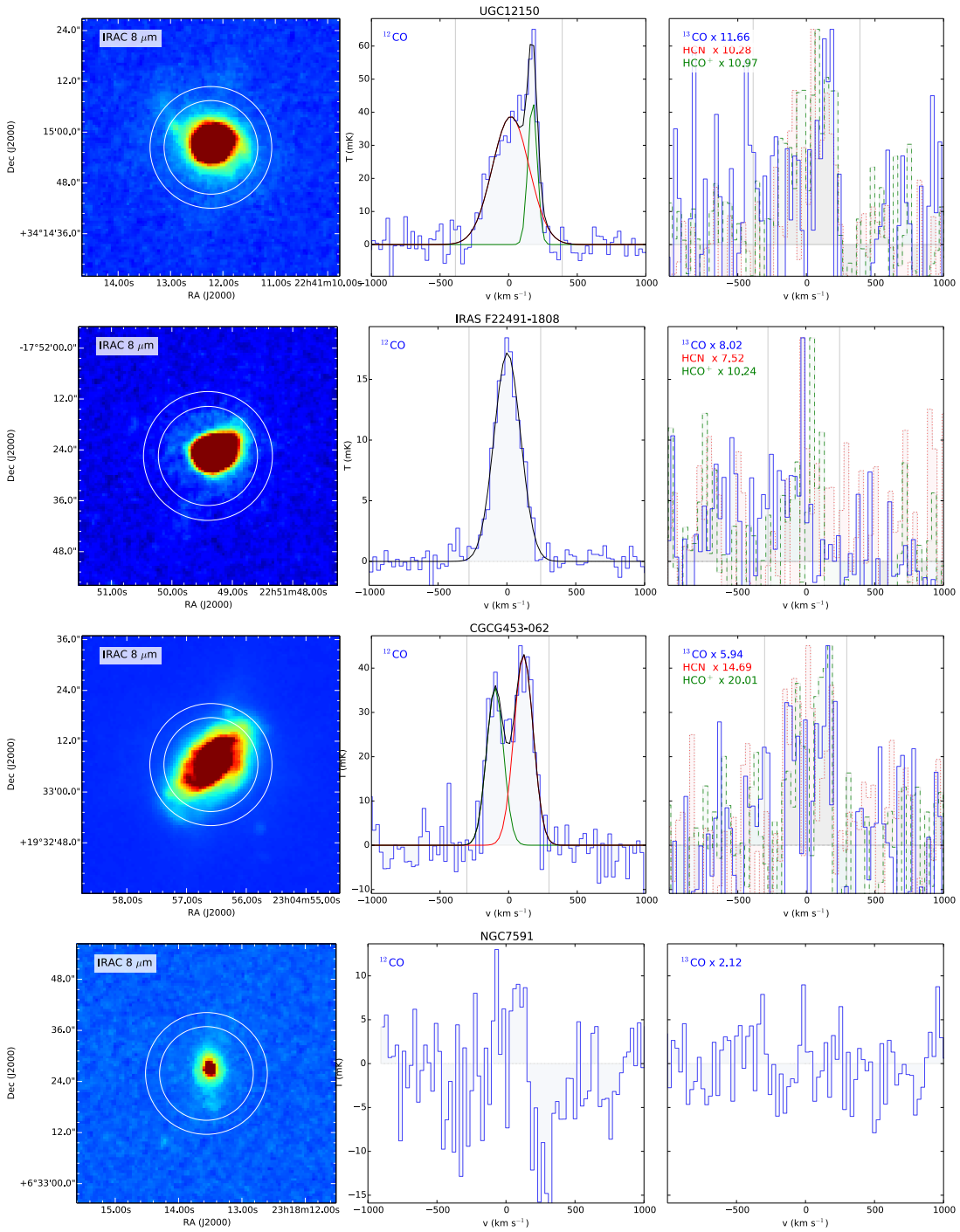

Figure 2.2: Spectral line profiles comparison - *Continued.*

Table 2.3: Observation results

Source name	$S_{\rm CO}\Delta v$	$S_{^{13}\rm CO}\Delta v$	$L'_{\rm CO}/10^8$	$L'_{^{13}\rm CO}/10^8$	$z_{\rm CO}$	$M_{\rm H_2}/10^9$	$M_{\rm dust}/10^7$
	(Jy km s^{-1})	(Jy km s^{-1})	(K km s^{-1} pc^2)	(K km s^{-1} pc^2)		($M_\odot$)	($M_\odot$)
(1)	(2)	(3)	(4)	(5)	(6)	(7)	(8)
NGC0034	126.0 ± 3.6	1.8 ± 1.8	20.97 ± 0.60	0.34 ± 0.31	0.01939	8.39 ± 0.24	0.38
MCG-02-01-051A	15.1 ± 1.3	4.6 ± 1.3	4.20 ± 0.36	1.44 ± 0.36	0.02711	1.68 ± 0.14	···
MCG-02-01-051B	45.8 ± 1.6	4.0 ± 1.6	12.71 ± 0.45	1.26 ± 0.45	0.02711	5.08 ± 0.18	···
IC1623	469.2 ± 1.9	10.9 ± 1.3	69.94 ± 0.29	1.83 ± 0.19	0.01996	27.98 ± 0.11	1.19
MCG-03-04-014	96.0 ± 1.2	0.5 ± 1.8	46.22 ± 0.57	0.27 ± 0.85	0.03506	18.49 ± 0.23	1.30
IRAS F01364-1042	37.4 ± 1.4	0.7 ± 1.4	37.75 ± 1.39	0.79 ± 1.37	0.04822	15.10 ± 0.55	0.99
IC214	62.8 ± 1.7	5.9 ± 1.1	24.35 ± 0.66	2.59 ± 0.44	0.03016	9.74 ± 0.27	1.10
UGC01845	208.0 ± 2.5	11.3 ± 1.9	22.06 ± 0.27	1.35 ± 0.20	0.01570	8.82 ± 0.11	0.49
NGC0958	144.1 ± 4.2	···	22.04 ± 0.65	···	0.01929	8.82 ± 0.26	1.76
ESO550-IG025	70.3 ± 2.7	2.9 ± 1.4	29.80 ± 1.15	1.37 ± 0.58	0.03209	11.92 ± 0.46	1.39
UGC03094	130.9 ± 2.8	12.7 ± 1.4	34.44 ± 0.75	3.75 ± 0.37	0.02446	13.78 ± 0.30	1.68
NGC1797	126.4 ± 2.2	7.3 ± 1.1	12.01 ± 0.21	0.78 ± 0.11	0.01497	4.80 ± 0.09	0.29
IRAS 05170+0535	···	···	···	···	0.03008	···	···
IRAS F05189-2524	31.0 ± 0.5	0.8 ± 0.5	24.93 ± 0.41	0.74 ± 0.40	0.04278	9.97 ± 0.16	1.03
IRAS 05187-1017	62.0 ± 0.6	3.2 ± 0.6	21.54 ± 0.21	1.25 ± 0.21	0.02865	8.61 ± 0.08	0.80
IRAS F06076-2139	37.6 ± 1.7	-1.3 ± 1.1	23.64 ± 1.08	-0.94 ± 0.72	0.03754	9.45 ± 0.43	1.20
NGC2341	105.0 ± 2.3	6.8 ± 1.2	13.50 ± 0.30	0.98 ± 0.15	0.01708	5.40 ± 0.12	···
NGC2342	111.5 ± 1.7	7.2 ± 1.2	14.96 ± 0.23	1.09 ± 0.15	0.01755	5.98 ± 0.09	3.44
IRAS 07251-0248	18.0 ± 1.4	0.5 ± 0.7	63.13 ± 4.93	1.88 ± 2.48	0.08769	25.25 ± 1.97	2.72
IRAS F09111-1007b	38.5 ± 1.1	···	49.26 ± 1.42	···	0.05426	19.70 ± 0.57	···
IRAS F09111-1007a	19.2 ± 1.9	···	24.53 ± 2.40	···	0.05468	9.81 ± 0.96	···
UGC05101	86.6 ± 1.5	1.5 ± 0.8	62.59 ± 1.12	1.21 ± 0.56	0.03930	25.04 ± 0.45	5.12
CGCG011-076SW	···	···	···	···	0.02469	···	0.93
CGCG011-076	114.3 ± 2.6	8.3 ± 2.6	36.64 ± 0.84	3.00 ± 0.83	0.02477	14.66 ± 0.34	0.93
IRAS F12224-0624	19.9 ± 0.9	1.0 ± 0.9	7.25 ± 0.31	0.41 ± 0.31	0.02644	2.90 ± 0.13	0.72
CGCG043-099	72.8 ± 1.3	4.9 ± 1.3	51.56 ± 0.93	3.89 ± 0.93	0.03737	20.62 ± 0.37	1.69
ESO507-G070	126.2 ± 3.6	3.2 ± 1.5	33.30 ± 0.95	0.96 ± 0.39	0.02138	13.32 ± 0.38	0.82
NGC5104	131.6 ± 2.9	9.1 ± 2.2	25.56 ± 0.56	1.98 ± 0.42	0.01859	10.22 ± 0.22	1.25
IC4280	119.7 ± 3.5	8.4 ± 1.8	19.19 ± 0.57	1.51 ± 0.28	0.01626	7.68 ± 0.23	1.00

Continued on Next Page...

Table 2.3 – *Continued*

Source name	$S_{CO}\Delta v$ (Jy km s^{-1})	$S_{^{13}CO}\Delta v$ (Jy km s^{-1})	$L'_{CO}/10^8$ (K km s^{-1} pc^2)	$L'_{^{13}CO}/10^8$ (K km s^{-1} pc^2)	z_{CO}	$M_{H_2}/10^9$ ($M_\odot$)	$M_{dust}/10^7$ ($M_\odot$)
(1)	(2)	(3)	(4)	(5)	(6)	(7)	(8)
NGC5258	128.6 ± 3.2	9.9 ± 1.9	29.21 ± 0.72	2.53 ± 0.43	0.02305	11.69 ± 0.29	1.95
UGC08739	208.4 ± 2.7	14.2 ± 1.3	32.59 ± 0.42	2.51 ± 0.21	0.01678	13.03 ± 0.17	2.13
NGC5331A	119.7 ± 2.5	8.6 ± 1.7	56.85 ± 1.20	4.60 ± 0.80	0.03308	22.74 ± 0.48	···
CGCG247-020	63.4 ± 1.9	2.4 ± 1.4	21.37 ± 0.65	0.90 ± 0.47	0.02584	8.55 ± 0.26	0.74
IRAS F14348-1447	53.0 ± 2.8	···	175.25 ± 9.39	···	0.08263	70.10 ± 3.76	3.50
CGCG049-057	120.1 ± 1.1	7.2 ± 1.1	12.17 ± 0.11	0.83 ± 0.11	0.01302	4.87 ± 0.04	0.89
NGC5936	155.8 ± 1.7	11.1 ± 1.2	16.61 ± 0.18	1.33 ± 0.13	0.01334	6.65 ± 0.07	0.96
IRAS F16164-0746	104.9 ± 3.2	2.2 ± 1.9	40.14 ± 1.23	0.97 ± 0.74	0.02366	16.06 ± 0.49	1.11
CGCG052-037	100.5 ± 1.3	5.2 ± 1.3	31.67 ± 0.40	1.85 ± 0.40	0.02449	12.67 ± 0.16	1.17
IRAS F16399-0937	99.0 ± 2.5	4.7 ± 1.2	37.91 ± 0.95	2.04 ± 0.47	0.02702	15.16 ± 0.38	2.15
NGC6285	65.7 ± 1.9	1.6 ± 1.3	9.58 ± 0.28	0.26 ± 0.18	0.01912	3.83 ± 0.11	2.45
NGC6286	270.4 ± 3.0	19.6 ± 1.4	36.90 ± 0.41	3.01 ± 0.19	0.01873	14.76 ± 0.16	2.29
IRAS F17138-1017	174.7 ± 2.8	5.3 ± 1.1	29.08 ± 0.47	1.00 ± 0.19	0.01730	11.63 ± 0.19	0.67
UGC11041	161.5 ± 2.3	11.3 ± 1.7	22.90 ± 0.32	1.80 ± 0.24	0.01625	9.16 ± 0.13	1.05
CGCG141-034	53.3 ± 2.6	5.4 ± 1.3	10.94 ± 0.53	1.25 ± 0.26	0.02012	4.37 ± 0.21	0.79
IRAS 18090+0130	113.1 ± 2.0	4.8 ± 1.3	38.61 ± 0.68	1.85 ± 0.46	0.02886	15.44 ± 0.27	2.62
NGC6701	202.3 ± 2.1	14.0 ± 1.3	18.66 ± 0.20	1.46 ± 0.12	0.01315	7.46 ± 0.08	0.92
NGC6786	77.2 ± 2.2	7.8 ± 1.1	19.18 ± 0.53	2.17 ± 0.27	0.02510	7.67 ± 0.21	0.71
UGC11415	58.8 ± 2.2	2.4 ± 1.1	14.88 ± 0.56	0.67 ± 0.28	0.02532	5.95 ± 0.22	0.72
ESO593-IG008	112.5 ± 2.5	3.9 ± 1.7	126.76 ± 2.84	4.89 ± 1.94	0.04881	50.70 ± 1.14	2.84
NGC6907	278.4 ± 4.4	5.3 ± 3.7	16.59 ± 0.26	0.35 ± 0.22	0.01061	6.64 ± 0.10	0.96
IRAS 21101+5810	42.8 ± 1.9	0.4 ± 1.3	29.91 ± 1.32	0.35 ± 0.88	0.03920	11.96 ± 0.53	1.93
ESO602-G025	134.4 ± 2.0	8.2 ± 1.3	38.05 ± 0.56	2.61 ± 0.37	0.02517	15.22 ± 0.22	1.08
UGC12150	77.3 ± 2.7	2.9 ± 1.4	15.89 ± 0.56	0.67 ± 0.28	0.02151	6.35 ± 0.22	1.49
IRAS F22491-1808	19.5 ± 0.6	1.1 ± 0.6	53.42 ± 1.55	3.52 ± 1.54	0.07769	21.37 ± 0.62	1.16
CGCG453-062	60.4 ± 3.0	2.6 ± 1.2	16.81 ± 0.83	0.82 ± 0.33	0.02486	6.72 ± 0.33	1.11
NGC7591	···	···	···	···	0.01604	···	0.80

Note. — (1) Source name; (2) Velocity integrated flux for ^{12}CO; (3) Idem for ^{13}CO; (4) ^{12}CO line luminosity; (5) ^{13}CO line luminosity; (6) Redshift obtained from the ^{12}CO feature; (7) Derived molecular hydrogen mass; (8) Derived molecular dust mass from IRAS flux densities.

where $A_{^{12}CO} = 2.4$ and $A_{^{13}CO} = 2.7$, considering $\nu_{\rm rest}(^{12}{\rm CO}) = 115.271\,{\rm GHz}$ and $\nu_{\rm rest}(^{13}{\rm CO}) = 110.201\,{\rm GHz}$.

We obtained the molecular gas mass ($M_{\rm H_2}$) from the integrated CO intensities assuming a constant CO-to-H_2 conversion factor, $\alpha_{\rm CO}$. This factor depends on the metallicity, gas density, temperature and dynamic state of the ISM (see, e.g., Solomon *et al.*, 1997; Downes & Solomon, 1998; Yao *et al.*, 2003; Papadopoulos *et al.*, 2012a). We used $\alpha_{\rm CO} = 4\,M_\odot\,({\rm K\,km\,s^{-1}\,pc^2})^{-1}$, as derived for molecular clouds in the Milky Way (Young & Scoville, 1991).

Dust is ubiquitous in (U)LIRGs and hence, the study of dust properties is essential to fully explore the ISM properties of (U)LIRGs. We obtained the dust masses and temperatures from the IRAS 60 μm and 100 μm flux densities as obtained by Young *et al.* (1986) and Young *et al.* (1989):

$$M_{\rm dust} = 4.78 \left(\frac{f_{100\,\mu m}}{\rm Jy}\right) \left(\frac{D_L}{\rm Mpc}\right)^2 \left(e^{143.88/T_{\rm dust}} - 1\right) M_\odot, \tag{2.3}$$

where the dust temperature, $T_{\rm dust}$ is:

$$T_{\rm dust} = -(1+z)\left(\frac{82}{\ln(0.3 f_{60\,\mu m}/f_{100\,\mu m})} - 0.5\right). \tag{2.4}$$

This is a simple way to estimate the dust parameters. However, IRAS flux densities are only sensitive to warm dust ($T \gtrsim 25$K). An alternative to this classic approach is to obtain dust masses and temperatures is through model fitting the far-IR Spectral Energy Distribution (SED). U *et al.* (2012) presented a full study of the SED of a sub-sample of (U)LIRGs from GOALS, where they fitted the mid-IR and sub-millimeter portion of the SED with different dust models to compute the dust masses and temperatures using the code developed by Casey (2012). A total of 23 sources from U *et al.* (2012) overlaps with our sample. In Section 2.5.2 we analyze the dust properties and compare both approaches.

2.5 Discussion

2.5.1 Molecular gas content

We show in Figure 2.3 the relation between $L'_{\rm CO}$ and both the total IR luminosity, $L_{\rm IR}(8-1000\,\mu{\rm m})$, and far-IR luminosity, $L_{\rm FIR}(40-400\,\mu{\rm m})$, obtained from Sanders

et al. (2003). We have plotted our sources as well as the GOALS sources observed by Graciá-Carpio *et al.* (2006) and Costagliola *et al.* (2011).

Since $L_{\rm IR}$ and $L_{\rm FIR}$ are used as tracers of star formation, and stars form from molecular gas, the correlation between these magnitudes is easy to explain. Figure 2.3 also shows fits to the data with the form:

$$\begin{aligned} \log(L'_{\rm CO}) &= (0.49 \pm 0.09)\log(L_{\rm IR}) + (3.86 \pm 1.02) \\ \log(L'_{\rm CO}) &= (0.48 \pm 0.09)\log(L_{\rm FIR}) + (4.02 \pm 0.99). \end{aligned} \tag{2.5}$$

The data is color-coded using the 6.2 μm PAH equivalent width (EW), obtained from Stierwalt *et al.* (2013), used as a diagnostic for AGN presence and contribution, where lower values of the PAH EW are a sign of AGN dominated sources, while higher values of the PAH EW are typical of starburst-dominated systems. Regarding the sources that lay close to the correlation, there is a weak trend in the data, with the sources with a higher $L'_{\rm CO}$ being more dominated by AGN, suggesting a link between AGN and the molecular gas content as traced by the CO luminosity, i.e., molecular gas is feeding the AGN. No significant differences are found between the use of $L_{\rm IR}$ or $L_{\rm FIR}$.

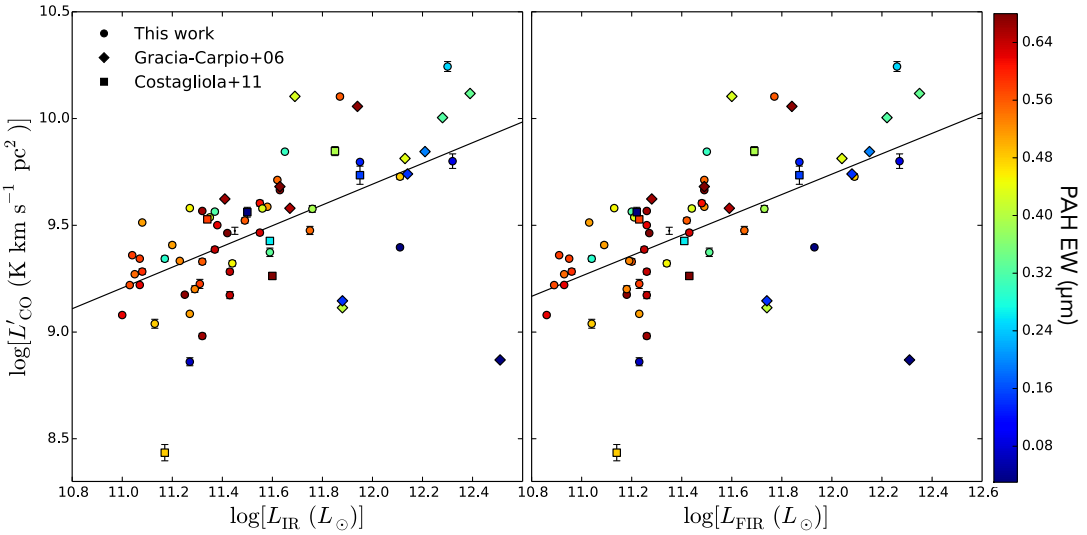

Figure 2.3: CO line luminosity compared with IR and FIR luminosities - Solid black lines show linear fits, yielding $\log(L'_{\rm CO}) = a\log(L_{\rm IR}) + b$ and $\log(L'_{\rm CO}) = a\log(L_{\rm FIR}) + b$. Data is color-coded using the 6.2 μm PAH EW, obtained from Stierwalt *et al.* (2013).

The ratio between $L_{\rm IR}$ and $M(\rm H_2)$ can be understood as the star formation efficiency

(SFE), measured in $L_{\odot}\,M_{\odot}^{-1}$. Since $M(\mathrm{H_2})$ and L'_{CO} are linked through a constant factor, we can equally use $L_{\mathrm{IR}}/L'_{\mathrm{CO}}$. SFE is known to correlate with the IR luminosity, with the most luminous (U)LIRGs showing larger SFE (e.g., Sanders *et al.*, 1991). We have plotted the SFE versus L_{IR} and L_{FIR} for our sample in Figure 2.4). We fitted the data, yielding:

$$\begin{aligned} \log\left(L_{\mathrm{IR}}/L'_{\mathrm{CO}}\right) &= (0.51 \pm 0.09)\log(L_{\mathrm{IR}}) - (3.86 \pm 1.02) \\ \log\left(L_{\mathrm{FIR}}/L'_{\mathrm{CO}}\right) &= (0.52 \pm 0.09)\log(L_{\mathrm{FIR}}) - (4.02 \pm 1.02), \end{aligned} \tag{2.6}$$

which can be directly obtained also from equations (2.5).

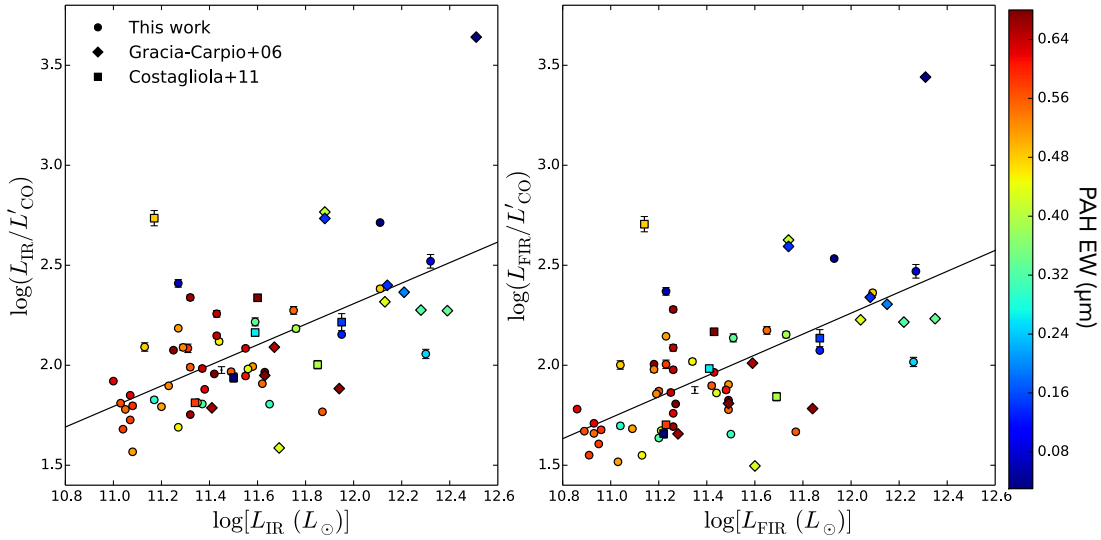

Figure 2.4: Star formation efficiency compared with IR and FIR luminosities - The black solid line is a power law fit to the data, with $\log\left(L_{\mathrm{IR}}/L'_{\mathrm{CO}}\right) = a\log(L_{\mathrm{IR}}) + b$ and $\log\left(L_{\mathrm{FIR}}/L'_{\mathrm{CO}}\right) = a\log(L_{\mathrm{FIR}}) + b$. L_{IR} and L_{FIR} are measured in solar luminosities ($L_{\odot}$), while L'_{CO} is measured in $\mathrm{K\,km\,s^{-1}\,pc^2}$. Data is color-coded using the 6.2 μm PAH EW, obtained from Stierwalt *et al.* (2013).

As shown in Fig. 2.4, (U)LIRGs with higher values of $L_{\mathrm{IR}}/L'_{\mathrm{CO}}$, tend to be AGN dominated. This scheme suggests that the AGN may be contributing significantly to the heating of dust.

2.5.2 Dust-to-gas ratios

Dust mass has been widely used to estimate the molecular gas present in high redshift galaxies relaying in a constant gas-to-dust mass ratio (see Scoville *et al.*, 2014, and

references therein). Figure 2.5 shows the variation of the star formation efficiency (as measured by $L_{\rm IR}/L'_{\rm CO}$) with dust temperature. The figure illustrates the differences between obtaining the $T_{\rm dust}$ from the IRAS flux densities (black symbols, only sensitive to warm dust) and obtaining it through a model fit to the far-IR SED (red symbols), as done by U *et al.* (2012), being more sensitive to cooler dust. The different slopes observed in Fig. 2.5 arises from this difference: as the dust temperature obtained from the far-IR SED fitting includes cool dust, it is including the contribution from cooler stars, thus yielding a higher star formation efficiency.

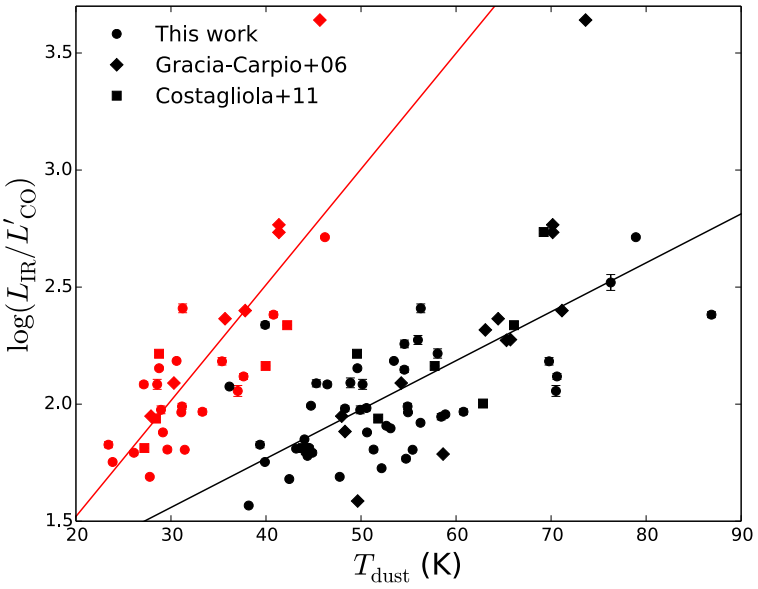

Figure 2.5: Star formation efficiency versus dust temperature - We have obtained dust temperatures ($T_{\rm dust}$) using both the classic approach (black) and from the far-IR model fit (red). Solid lines show a fit to each of the data sets. See main text for details.

We show in Figure 2.6 the molecular gas-to-dust mass ratio compared with the infrared luminosity, as found by Sanders *et al.* (1991), showing that the CO-to-H_2 conversion factor does not depend on luminosity. Our sample has a median value of $M(H_2)/M_{\rm dust} = 956$ when using the IRAS flux densities (i.e., warm dust), and $M(H_2)/M_{\rm dust} = 621$ when fitting the far-IR SED, a factor ~ 1.5 smaller. Still, these values are significantly larger than the median value of 387 obtained by Sanders *et al.* (1991) for a sample of (U)LIRGs. However, the differences between our dust-go-gas ratio (obtained from the IRAS flux densities) and that of Sanders *et al.* (1991) are due

entirely to the difference in the CO-to-H_2 conversion factor used, and the manner in which Sanders *et al.* (1991) calculated the dust mass.

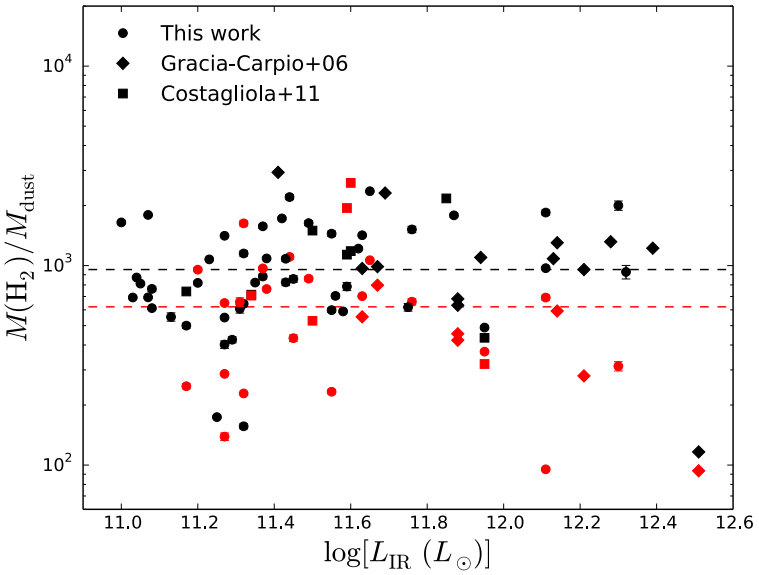

Figure 2.6: Molecular gas-to-dust mass ratio versus IR luminosity - Data are plotted with dust parameters obtained from IRAS flux densities (black) and through far-IR SED fitting (red). The dashed lines show the $M(H_2)/M_{\mathrm{dust}}$ median value for each data set.

2.5.3 ^{12}CO / ^{13}CO isotopic ratio

There is a well known correlation between the ^{12}CO /^{13}CO ratio and the dust temperature (e.g., Young & Sanders, 1986; Aalto *et al.*, 1995). This is usually explained by the optical depth of the ^{12}CO line decreasing with increasing temperature (assuming a correlation between dust and gas temperature), although indirect effects also apply: the presence of diffuse molecular gas or the effects of photodissociation further suppressing ^{13}CO, for example.

There are a sufficient number of ^{13}CO detections in our observations to re-examine the ^{12}CO /^{13}CO ratio. In Figure 2.7 we show the relation for the sources in our sample between ^{12}CO /^{13}CO and the ratio between the 60 μm and 100 μm IRAS flux density ratio (f_{60}/f_{100}), used as a proxy for the dust temperature, and compare it with the results from previous studies. We obtained the intensity line ratios by directly

integrating channels in the same velocity range for both lines. We derived the error of this ratio using a Monte Carlo simulation using 10 000 samples and following a similar prescription as Crocker *et al.* (2012). The correlation confirms the general trend in which dust temperature increases with the ^{12}CO/^{13}CO ratio.

In our original observations, three sources in our sample (IRAS F05189-2524, IRAS 22491-1808 and IRAS 07251-0248) showed isotopic ratios lower than 10, with $f_{60}/f_{100} > 0.9$, which is at odds with the correlation. Although their ^{13}CO detection threshold was above 3σ, we requested director's discretionary time (program D01-13; PI: R. Herrero-Illana) to reobserve those three sources and confirm that result. After further integration, the tentantive ^{13}CO lines were shown to be spurious and no outliers were confirmed.

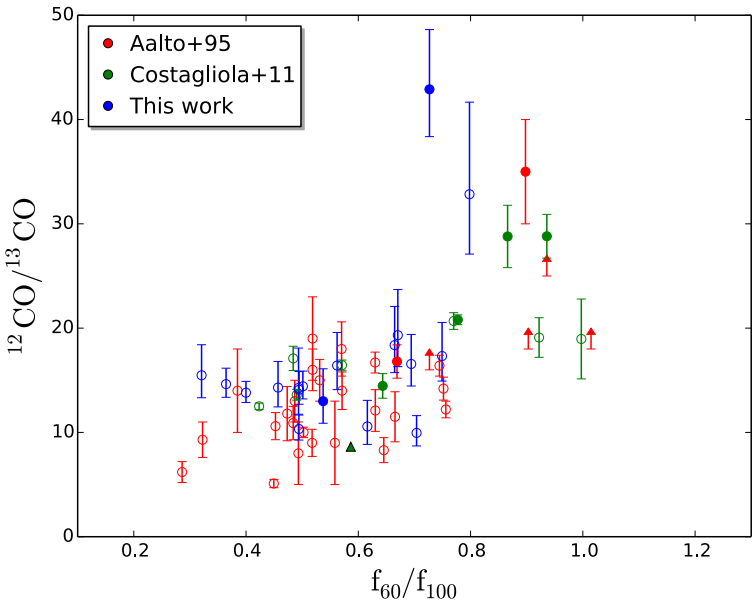

Figure 2.7: CO over ^{13}CO intensity ratio plotted versus IRAS fluxes ratio f_{60}/f_{100}, used as a proxy for the dust temperature - The sources are from different samples: this work (blue), Aalto *et al.* (1995, red), and Costagliola *et al.* (2011, green). Filled circles indicate those galaxies with $L_{\rm FIR} \gtrsim 3 \times 10^{11}$.

2.5.4 HCN and HCO$^+$ transitions

Although we have focused or work on the CO features, our observations also comprise data on two more transitions: HCN $(1-0)$ at 88.63 GHz, and HCO$^+$ $(1-0)$ at

89.19 GHz. I list here the main preliminary results derived from the study of these lines that will be published by Privon *et al.* (2014, *in prep.*).

HCN $(1-0)$ and HCO^+ $(1-0)$ have higher critical densities than CO ($n_c \sim 3\times10^6\,cm^{-3}$ and $\sim 2\times10^5\,cm^{-3}$, respectively, at 30 K), and thus trace denser molecular hydrogen. Furthermore, several authors have proposed that the presence of AGN enhance the HCN emission relative to the HCO^+ emission (e.g., Kohno *et al.*, 2003; Imanishi & Nakanishi, 2006; Davies *et al.*, 2012), suggesting that the ratio HCN / HCO^+ is a good AGN indicator. In our study, we have compared this ratio with several mid-IR AGN indicators, concluding that, while the AGN can enhance the HCN emission relative to HCO^+, a similar level of enhancement is also present for many star forming dominated systems. This hampers a simple interpretation of this line ratio. It is important to proceed with caution when using HCN and HCO^+ emission as tracers of activity in (U)LIRGs.

2.5.5 Line profiles

Figure 2.2 shows the spectra obtained from our IRAM 30 m observations. From the 56 sources in our sample, we clearly detected ^{12}CO in 53 of them. From those, 13 have a single Gaussian profile (24.5%), 20 have an extended square profile (37.7%), and 30 show a double horn profile: seven with a symmetric profile (13.2%), and 23 presenting asymmetry (43.4%), i.e., one peak significantly brighter than the other.

The different observed CO profiles have been explained as rotating disks of gas at different inclinations with respect to the line of sight (Kruegel *et al.*, 1990; Downes & Solomon, 1998; Narayanan *et al.*, 2005; Bertram *et al.*, 2007). Namely, a single Gaussian component is indicative of a face-on disk, where the velocity distribution in the line of sight is dominated by turbulence, while a double horn profile arises when the galactic disk (or ring) presents a certain inclination with respect to the line of sight.

Kruegel *et al.* (1990) used simple models of inclined disks with an inner rigid solid rotation curve and an outer flat rotation curve. If the beam is too small to resolve the rigid solid rotation part, then a single Gaussian profile is still observed, with the line width increasing with inclination. However, from Figure 2.2 it seems clear that the IRAM 30 m beam for our ^{12}CO observations (outer circumference in left panels) covers most of the emission of most of our sources, assuming that the IRAC 8 μm emission region is coincident with the CO emission region.

If inclination was the only factor that determines the spectral shape, we would expect to find a Gaussian profile only in completely face-on galaxies. However, we find that almost one fourth of our sample show a single Gaussian peak, which is not statistically consistent with a random orientation of the galaxies, moreover when some of the galactic disks have been disrupted by merging processes. Furthermore, there should be a clear differentiation when comparing single and double peak profiles with the inclination of each corresponding galaxy. We have obtained the inclinations between the line of sight and the polar axis from the Hyperleda database (i.e, 0° for face-on galaxies and 90° for edge-on galaxies). Figure 2.8 compares the distribution with galaxy inclination of those spectra visually classified as single-peaked and those classified as double-peaked. For comparison, and since the inclination probability distribution of a disk is non-trivial, we also show the inclination histogram corresponding to 2.2 million galaxies from the Hyperleda database. The expected distribution for a sample with random orientations (top panel) is resembled in our sample (bottom pannel, red dotted line), but there is no evidence that single peak spectra (plotted in blue in Fig. 2.8) correspond to smaller inclinations than double peak ones (dashed green). A possible explanation is due to the way the inclination is obtained, based on the apparent axis ratio and the morphological type, which may have not been well determined for disrupted interacting systems. However, our sample has a significant fraction of isolated LIRGs where inclination should be well determined.

An alternative explanation is that the line profiles may have an intrinsic nature, with Gaussian profiles being indicative of concentrated gas in the nuclear region and no significant amount of gas in the flat part of the rotation curve, while double horn profiles are suggestive of disks or rings of molecular gas. The high incidence of asymmetric profiles, suggestive of molecular gas irregularly distributed along the galaxy, can be explained by disturbances produced by ongoing galaxy interactions, characteristic of (U)LIRGs.

A complementary factor that can affect spectral profiles is optical depth: optically thick regions with a particular velocity would modify the spectral shape. We have compared the ^{12}CO line profiles with those of higher density star formation tracers such as ^{13}CO, HCN or HCO$^+$, which are much less abundant and thus less likely to be optically thick. For most of the sources where the higher density tracers have enough signal to noise to determine their profile, they are consistent with the ^{12}CO profiles

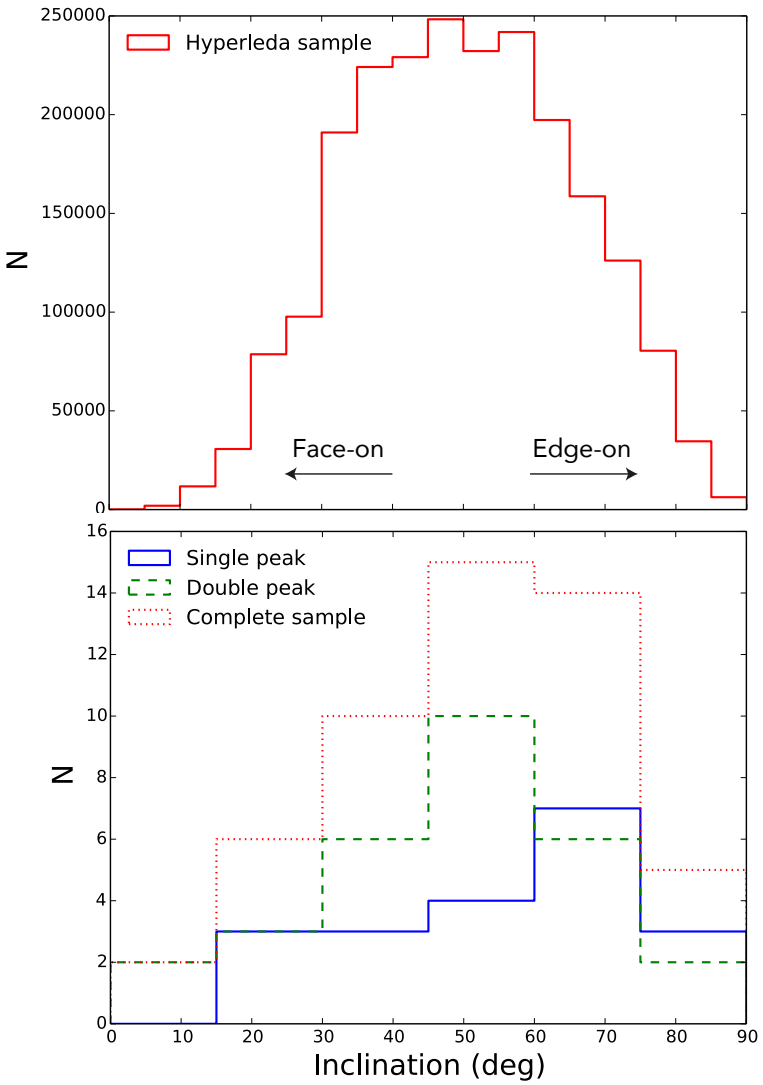

Figure 2.8: Spectral profiles compared with inclination of galactic disks - Top: Probability distribution of the inclination angle obtained from 2.2 million galaxies from the Hyperleda database. Bottom: The histogram compares the number of single (solid, blue line) and double peak (dashed, green line) profiles for different inclinations obtained from Hyperleda database and defined as the angle between the line of sight and the polar axis. The red dotted line corresponds to the distribution for the complete sample. Note that single peak profiles do not show any trend towards smaller inclinations as expected in the geometrical-only explanation of spectral profiles.

in most cases, with the exception of UGC 08739 and NGC 6286, which show different asymmetries for different molecules. An alternative explanation to optical depth effects is a different spatial distributions of molecules along the galactic disk.

2.6 Summary

We observed 56 (U)LIRGs with the IRAM 30 m telescope In this work, we have focused on the ^{12}CO $(1-0)$ transition as a tracer of molecular gas. This is the summary of our study:

1. ^{12}CO and ^{13}CO were observed simultaneously in the same band. Our ^{12}CO detection rate is 95%, while we detected ^{13}CO in a 55% of our sources, as expected from ^{13}CO being much less abundant than ^{12}CO .

2. We found a higher fraction of AGN dominated systems, as traced by the 6.2 μm PAH EW, in the high end of our luminosity range, which correlates with the CO luminosity. This supports the idea that the molecular gas is both forming stars and feeding the central SMBH.

3. We obtained the dust temperature of our sources using two approaches: the classical equation using only IRAS flux densities and a complete far-IR SED fitting. The first approach is sensitive only to warm dust ($T_{\rm dust} \gtrsim 25\,{\rm K}$), while the latter is also sensitive to cooler dust temperatures, yielding different slopes in the relation between $T_{\rm dust}$ and the star formation efficiency. We conclude that the gas-to-dust ratio is then being underestimated when the complete far-IR SED is not considered.

4. We revised the variation between the ratio of ^{12}CO and its isotopologue ^{13}CO with the dust temperature proxy f_{60}/f_{100}, finding that our sample follows the known relation.

5. The median velocity width of our ^{12}CO detections is 661 km s^{-1}. We found that 30 sources in our sample show a multiple peak profile, most of them with asymmetric profiles. We have analyzed the relation with the inclination of our galaxies and concluded that the observed profiles correspond not only to inclination, but also to different intrinsic gas distribution in the systems.

Somewhere, something incredible
is waiting to be known.

Carl Sagan

3

An exploratory multiwavelength study of the LIRG NGC 1614

Based on the results published in Herrero-Illana et al. *(2014).*

As I have shown in the previous chapter, single-dish observations offer a very useful and efficient way —in terms of observing time— to derive the molecular properties of the ISM in (U)LIRGs. However, the lack of spatial resolution is a caveat that imposes a limit to the comprehension of star formation in general, and of (U)LIRGs in particular. The spatial information accessible at different ranges of the electromagnetic spectrum can improve our understanding of this objects. Up to now, in this PhD thesis, I have only discussed the overall behavior of (U)LIRGs (IRAM 30-m beam covers most of the galactic structure in the studied sample).

However, we know that different properties of the galaxies show up at different scales. Through the next two chapters, I will focus on a multiwavelength comparison of

the central kiloparsec region of a sample of galaxies. In the present chapter, I present a complete multiwavelength study of the LIRG NGC 1614, and Chapter 4 extends this study to a sample of eleven more LIRGs.

3.1 NGC 1614: a case study

Luminous Infrared Galaxies are known to closely follow the far-infrared (FIR) to radio correlation, and hence must host either a burst of star formation, or an active galactic nucleus (AGN) at their center, or both. Disentangling whether an AGN, or a starburst is the dominant heating mechanism is essential to understand the role of the IR-phase in galaxy evolution (see, e.g. Alonso-Herrero *et al.*, 2012, 2013a). The central kpc regions of LIRGs are heavily dust enshrouded, which prevents their study at optical wavelengths. Fortunately, at infrared wavelengths the extinction is significantly lower than in the optical, and radio is essentially extinction-free, which permits the study of the innermost regions of LIRGs, if the required spatial resolution is available. Also, sub-arcsecond imaging with *Chandra* allows to image the inner central regions of LIRGs, thanks to the penetrating power of X-rays. Therefore, high-angular (sub-arcsecond) resolution observations of local ($D \lesssim 100$ Mpc) LIRGs at infrared, radio, and X-rays can be efficiently used to study their central regions, in general, as well as to disentangle a putative AGN from a starburst.

NGC 1614 (IRAS 04315-0840) is a galaxy merger in a late stage of interaction (see Figure 1.1 in Chapter 1), with strong tidal tails and only one obvious nucleus, though there is evidence for the remnant of a secondary one (Neff *et al.*, 1990; Väisänen *et al.*, 2012). At a distance of 64 Mpc (de Vaucouleurs *et al.* 1991; $1''$ corresponds to 310 pc), NGC 1614 has an infrared luminosity $L_{\rm IR} \simeq 4 \times 10^{11} L_{\odot}$ (Sanders *et al.*, 2003). Using the photometric information from the IRAS Bright Galaxy Sample (Sanders *et al.*, 2003) and from the NRAO VLA Sky Survey (Condon *et al.*, 1998), the derived q-factor (Helou *et al.*, 1985) is 2.46, well within the FIR-to-radio correlation.

The central kpc region of NGC 1614 hosts a prominent circumnuclear ring of star formation of ~ 600 pc diameter, revealed in Paα (Alonso-Herrero *et al.*, 2001). Recently, several authors have suggested that the ring is formed by an inner Lindblad resonance, where the gas is driven to it through dust lanes (Olsson *et al.*, 2010; König *et al.*, 2013). The existence of an AGN at the center of NGC 1614 is still a matter of debate: Risaliti

et al. (2000) classified the hard X-ray emitting source in the central region of the galaxy as an AGN. However, the low signal-to-noise detection of the power-law continuum makes its interpretation uncertain (Olsson *et al.*, 2010). Sub-millimeter array (SMA) observations of NGC 1614 seem to indicate a nuclear, non-thermal component, but which cannot be ascribed solely to an AGN, or to a starburst (Wilson *et al.*, 2008). Yuan *et al.* (2010) have classified NGC 1614 as a starburst-AGN composite (albeit with a significantly larger contribution from the starburst), using their new optical classification scheme. More recently, Väisänen *et al.* (2012) have used 3.3 μm spatially resolved polycyclic aromatic feature (PAH) imaging and continuum diagnostics to argue that an obscured AGN can be ruled out, concluding that NGC 1614 is a pure starburst.

In this chapter, I present sub-arcsecond angular resolution radio (3.6 and 6 cm), mid-IR (8.7μm), optical (0.4 and 0.8μm), and *Chandra* X-ray images of the central kpc region of NGC 1614 to study in detail the central kpc region of this LIRG. The main aim of this study is to shed light on the AGN/SB controversy existing in the literature, as well as to discuss the striking morphological similarities between the radio and mid-IR images, which suggest a common origin for both emission mechanisms.

3.2 Observations and data reduction

In this section, I describe our sub-arcsecond resolution radio (3.6 cm), mid-IR (8.7 μm), PAH (3.3 μm), Paα (1.9 μm) and optical (0.4 and 0.8 μm) observations of NGC 1614, which show striking morphological similarities (see Fig. 3.1), as well as *Chandra* X-ray data and multi-epoch, archival VLA data at 3.6 and 6 cm, aimed at characterizing the spectral index of the nucleus and the star-forming (SF) ring, as well as to study its variability (see Figs. 3.3 and 3.5). In Table 3.1, I show the log for the radio and infrared observations discussed in this study.

3.2.1 Radio

Our team observed NGC 1614 on November 2004 and May 2006 using the Karl G. Jansky Very Large Array (VLA) in A configuration at 3.6 cm (project code AC749), in full polarization mode. The total synthesized bandwidth was of 100 MHz. We used 3C 48 as the absolute flux density calibrator, and 0420-014 (R.A.(J2000.0)=$04^{\rm h}23^{\rm m}15^{\rm s}.801$; Dec.(J2000.0)=$-01°20'33.07''$), at an angular distance of 7.7° from NGC 1614, for

Table 3.1: Observations summary

Date	Instrument	Wavelength	FWHM (arcsec)	rms (μJy)	Peak (mJy)	Astrometric shift (arcsec)
May 1986	VLA	6.0 cm	0.71×0.43	65	4.91	0
Jul 1999	VLA	6.0 cm	0.60×0.42	30	4.46	0
Jul 1999	VLA	3.6 cm	0.50×0.36	35	2.65	0
Nov 2004	VLA	3.6 cm	0.42×0.25	16	1.63	0
May 2006	VLA	3.6 cm	0.41×0.24	19	1.51	0
Feb 1998	*HST*/NICMOS	1.9 μm	0.15	0.5	0.19	0.59
Aug 2006	*HST*/ACS	0.4 μm	0.10	1.0	0.02	1.24
Aug 2006	*HST*/ACS	0.8 μm	0.10	1.9	0.04	1.24
Sep 2006	Gemini/T-ReCS	8.7 μm	0.38	30	1.64	1.17
Jan 2009	UKIRT/UIST	3.3 μm	0.33	28	0.22	64.0

Note. — The quoted angular resolution corresponds to the diffraction-limited FWHM for the radio and optical images, and is seeing-limited for the IR ones. The rms and peak flux density are given in units of mJy/beam and mJy/pixel for the radio and optical/IR images, respectively.

phase-calibration purposes. We used the NRAO *AIPS* package for all data reduction steps, including amplitude and phase calibration, as well as imaging. We imaged the source using a pixel size of $0.05''$ and applied a natural weighting scheme, which resulted in a final synthesized beam of $0.42'' \times 0.25''$ at a position angle of -33.8° for the observations on 2004, and a very similar one for the 2006 observations ($0.41'' \times 0.24''$; -28.47°). We used our VLA image on 2004 as the reference one, to compare with the infrared images. For this, we increased the pixel size of our radio images up to $0.089''$.

To study the variability of the circumnuclear region in NGC 1614, we also used publicly available VLA continuum data of NGC 1614 in A-configuration obtained in May 1986 (project code AN37) at 6.0 cm, and in July 1999 (project code AL503) at 3.6 and 6.0 cm. We reduced these data in an analogous manner to that previously described for the 3.6 cm data. We also used the same absolute flux density and phase calibrators mentioned above, thus ensuring that the relative astrometry was close to the milliarcsecond level. We obtained our images in the same manner, using an automatic script to prevent any systematic errors. In all cases, we used a natural weighting scheme for the *u*-*v* data in the imaging process, using each time the same pixel size and convolving synthesized beam. The off-source r.m.s. noise attained in the final images was in good agreement with the expected theoretical thermal noise.

Table 3.2: Regions of enhanced radio and IR emission in NGC 1614 and their integrated fluxes

Region	Center (J2000)	Diameter (arcsec)	Diameter (pc)	Paα (mJy)	3.3 μm (mJy)	8.7 μm (mJy)	3.6 cm (mJy)
A	00.010s, 44.55″	0.40	124	1.9 ± 0.2	1.5 ± 0.2	21 ± 2	1.41 ± 0.05
B	59.990s, 45.11″	0.86×0.41	266×127	3.9 ± 0.4	3.5 ± 0.4	44 ± 4	2.95 ± 0.12
C	00.030s, 45.70″	0.40	124	2.2 ± 0.2	1.5 ± 0.2	19 ± 2	0.96 ± 0.04
D	00.070s, 45.12″	0.40	124	2.5 ± 0.3	1.4 ± 0.2	22 ± 2	1.07 ± 0.04
N	00.027s, 45.12″	0.60	186	4.3 ± 0.4	3.6 ± 0.4	49 ± 5	1.70 ± 0.08
T	00.027s, 45.12″	2.50	773	47.1 ± 4.7	45.9 ± 4.6	799 ± 80	26.49 ± 2.20
R	00.027s, 45.12″	T−N	T−N	42.8 ± 4.3	42.3 ± 4.3	750 ± 75	24.78 ± 2.10

Note. — Coordinates are given with respect to 4h34m, −8°34'. Region B is an ellipse with a position angle of 0°, for which we give major and minor axes. Region R is the ring defined by subtracting region N from total region T. The Paα values are continuum-subtracted. The radio fluxes correspond to the image from November 2004, used as the reference radio image along the chapter.

3.2.2 Infrared

We made use of the Gemini/T-ReCS 8.7 μm imaging data presented by Díaz-Santos *et al.* (2008), observed on 16-30 September 2006, using the T-ReCS instrument on the Gemini South telescope with a plate scale of 0.089″ px^{-1}, with a total on-source integration time of 1680 s. A detailed description of the observations and data reduction can be found in Díaz-Santos *et al.* (2008).

We also used Paα observation obtained in February 1998 with the NICMOS camera on-board the *Hubble Space Telescope* (*HST*), using the filter F190N on NIC2, with a plate scale of 0.076″ px^{-1}, and centered at 1.89 μm, for a total on-target time of 640 s, presented in Alonso-Herrero *et al.* (2001). A nearby filter (F187N) was used to remove the stellar continuum. Details on the data reduction are presented in Alonso-Herrero *et al.* (2000, 2001).

Finally, we made use of UIST Integral Field Unit observations on UKIRT performed in 6 and 26 January 2009, at 3.3 μm with a total on-target exposure time of 4800 s. The plate scale of the raw data was 0.12″ px^{-1} by 0.24″ px^{-1}, yet the spatial resolution was similar to the IR data above. The observations covered the 2.9 to 3.6 μm range, and a continuum subtracted map of the 3.3 μm PAH feature was specifically used here. For further details see Väisänen *et al.* (2012).

3.2.3 Optical

We used publicly available optical images of NGC 1614 taken in 2006 with the ACS camera, on board the *HST*. In particular, we retrieved broad-band images with filters F435W (centered at 4328.2 Å $\sim 0.4\,\mu$m, $\sim$ B-band) and F814W (centered at 8057.0 Å $\sim 0.8\,\mu$m, $\sim$ I-band). The pixel size of these images corresponds to $0.049''$ px^{-1}.

We reduced the images using the on-the-fly *HST* pipeline, applying the highest quality reference files that were available at the time of retrieval. The calibrated F435W image had only few cosmic rays remaining. However, the F814W image was severely contaminated with cosmic rays, which were removed as explained in Miralles-Caballero *et al.* (2011).

3.2.4 X-Rays

We used publicly available archival data of NGC 1614 from ACIS-S, on board *Chandra*, taken on 21 November 2012. The pixel scale is $0.49''$ px^{-1}, and the spectral range covers from 0.2 to 10 keV. We used the CXC Chandra Interactive Analysis of Observations software package (CIAO[1]), version 4.3, for the data reduction, which was made in the same way as described in Hernández-García *et al.* (2013).

We extracted a nuclear spectrum of NGC 1614 from a $3''$ aperture circular region centered at RA=$4^{\rm h}34^{\rm m}0^{\rm s}.03$, DEC=$-8°34'45''$ (J2000.0). We extracted the background spectrum from a $5''$ aperture source-free circular region, in the same chip as the target, and close to the source, to minimize effects related to the spatial variations of the CCD response.

3.2.5 Image alignment and estimation of flux density uncertainties

We aligned the images by taking as reference position the flux density peak of the innermost region of our reference radio image (3.6 cm map from November 2004), and then shifted the peaks of our 8.7 μm and Paα images so as to make them coincide with the radio peak, with an estimated uncertainty of $0.04''$. The 3.3 μm PAH map was aligned by matching the corresponding strong 3–4 μm continuum nucleus to the nucleus seen in the 8.7 μm and Pa-alpha maps, with an estimated uncertainty of $0.05''$.

[1] http://cxc.harvard.edu/ciao4.3/

For the optical *HST* images, which did not show a clear morphological correlation with the radio, or the infrared images, we used reference images at the intermediate wavelengths of 1.1 μm and 1.6 μm. The resulting images are shown in Fig. 3.1. Table 3.1 shows the astrometric shift applied to the images with respect to the VLA astrometry.

To estimate the uncertainty in the (integrated) flux densities obtained for any given region, we used the following equation, which takes into account both thermal noise and systematic uncertainties,

$$\sigma \simeq \sqrt{N_b \times \mathrm{rms}^2 + (\eta \times S_{\mathrm{int}})^2}, \tag{3.1}$$

where rms is the off-source root mean square of the image; η is a factor that accounts for uncertainties in the calibration system (we used $\eta = 0.03$ for the VLA radio images and $\eta = 0.10$ for the optical and IR images, which are conservative values); S_{int} is the integrated flux of the region of interest; and N_b corresponds to the number of beams that fits into a given region (the number of pixels in that region), for the radio (optical/IR) images.

3.3 Results and Discussion

3.3.1 Radio and infrared images

In Figure 3.1, I show our 3.6 cm continuum VLA image of NGC 1614 from November 2004 and the 8.7 μm continuum T-ReCS image at similar angular resolution. I also show the *HST*/NICMOS continuum-subtracted Paα image for comparison. The outer circle in the images covers essentially all the emission at each wavelength, and has a radius of ~ 780 pc. We identified five regions within the circumnuclear ring: A, B, C, and D, which correspond to areas of strong emission, and an additional region, N, which roughly delimits the nuclear region ($r \lesssim 90$ pc). For convenience, Figure 3.1 shows two additional regions: R, which corresponds to the whole ring, and T, which encompasses the entire region (ring and nucleus, R+N). I show the locus and size for each of those regions, as well as their integrated 3.6 cm, 8.7 μm, 3.3 μm and Paα fluxes, in Table 3.2.

The most conspicuous feature is the prominent mid-IR emission of the nucleus, N, which contrasts with its rather faint emission at radio wavelengths (see Fig. 3.1 and Table 3.2). The regions to the northwest of the ring, A and B, show a mid-IR/radio

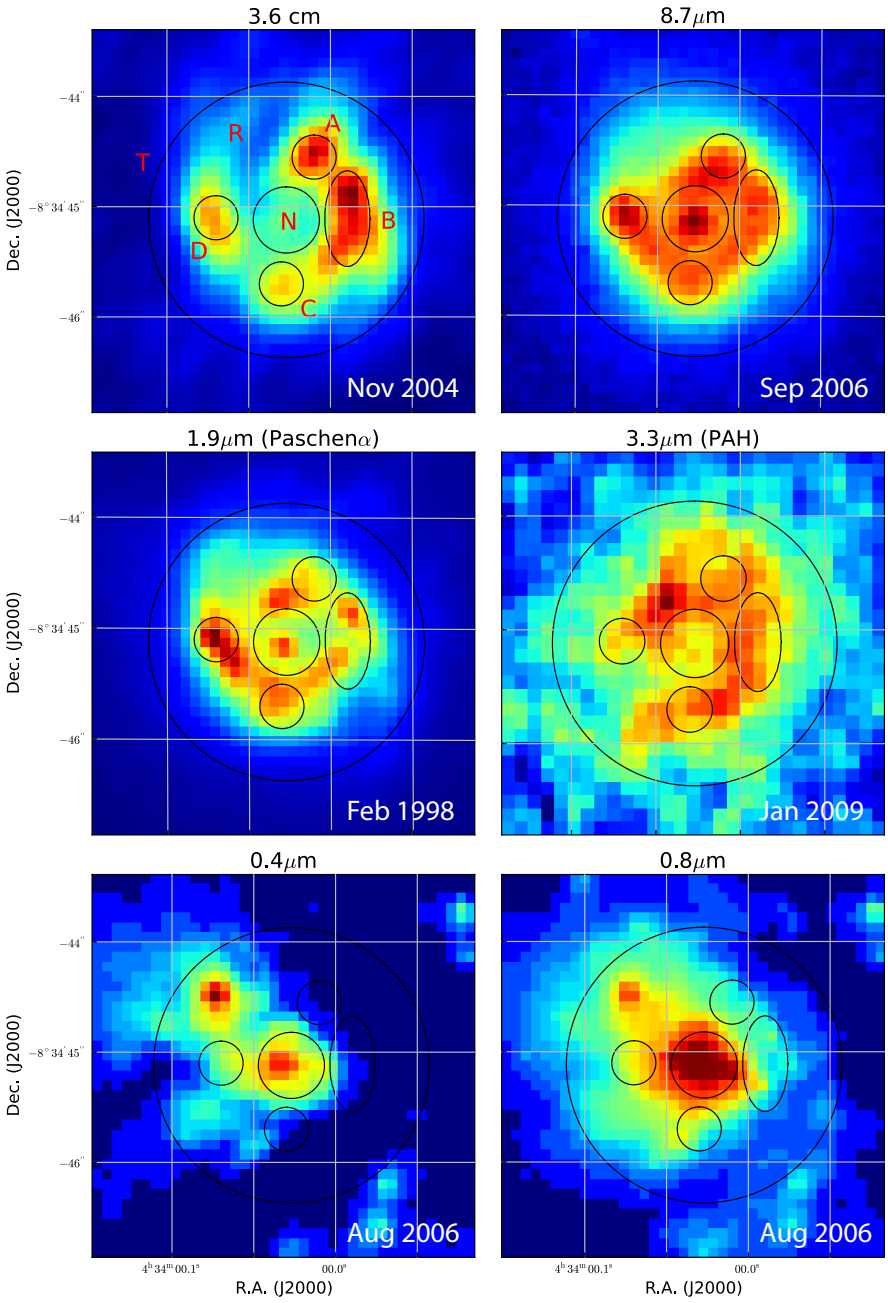

Figure 3.1: Multi-wavelength comparison of the nuclear region of NGC 1614 - The top panels show radio (left) and mid-IR (right). The central panels show continuum-subtracted Paschen α (left) and the 3.3 μm PAH feature (right). The bottom panels show *HST*/ACS images at 0.4 μm (left) and 0.8 μm (right), B (F435W) and I (F814W) filters, respectively. Based on the radio emission, we defined seven regions to compare the images, including the nuclear region (N), the whole ring (R) and the total area (T). Note the close similarity in the star formation ring and the contrast in the nuclear region between the radio and mid-IR wavelengths. Pixel sizes are the same for all images, except for the PAH feature map. Color scales are independent. See Fig. 2 in Díaz-Santos *et al.* (2008) for a mid-IR/Paα ratio image.

ratio below the average of the whole ring (R), while regions C and D show the opposite behavior.

Figure 3.2 shows the azimuthal profiles at all three wavelengths, starting from the central pixel (the brightest pixel in region N for the 3.6 cm and 8.4 μm images) and towards eight cardinal directions, separated by 45° from each other. To adequately compare the profiles, we normalized the radio continuum and Paα fluxes to the median of the ratios (8.7 μm/3.6 cm) of each region for the case of the mid-IR image, and to the median of the ratios (Paα/3.6 cm) for the Paα image. We therefore increased the values of the 3.6 cm and Paα values by factors of 19.3 and 10.8, respectively, which allows to see more clearly variations in the whole circumnuclear region.

Figure 3.2 also shows that both the continuum 8.7 μm and Paα emission follow almost exactly the same trend from the very center up to the outermost regions of the star-forming ring, as found by Díaz-Santos *et al.* (2008). Overall, the same trend is also seen when comparing the IR azimuthal profiles against those of the radio continuum. The remarkable morphological similarities seen at both radio and mid-infrared wavelengths in most regions of the circumnuclear ring strongly suggest that the mechanisms responsible for the emission must be related. König *et al.* (2013) show a similar plot (see their Fig. 6), with the azimuthal profile of the CO (2–1) and Paα emission displayed together with the radio emission at three different bands. The peaks of radio and mid-infrared emission in the ring would pinpoint then the regions where most of the starburst activity has taken place in the last 10-20 Myr. The 8.7 μm mid-IR flux includes both warm dust continuum and PAH emission. The PAH emission is known to vary quite significantly from one SF region to another, or one galaxy to another, depending on the exact physical conditions (see, e.g., Calzetti *et al.*, 2007; Díaz-Santos *et al.*, 2010).

There are morphological differences between the 3.3μm PAH feature map and the rest of the IR and radio images. Imanishi & Nakanishi (2013) have suggested that either an age differentiation, or different dust extinction between the regions may explain those differences.

Olsson *et al.* (2010) ascribed the radio emission at 3.6 and 6.0 cm from NGC 1614 mainly to free-free emission from H II regions (mainly due to massive stars). As we shall show in the following sections, the non-thermal contribution from core-collapse supernovae

(CCSNe) and supernova remnants (SNRs) is also significant within the circumnuclear ring, implying the existence of young starbursts in the ring of NGC 1614.

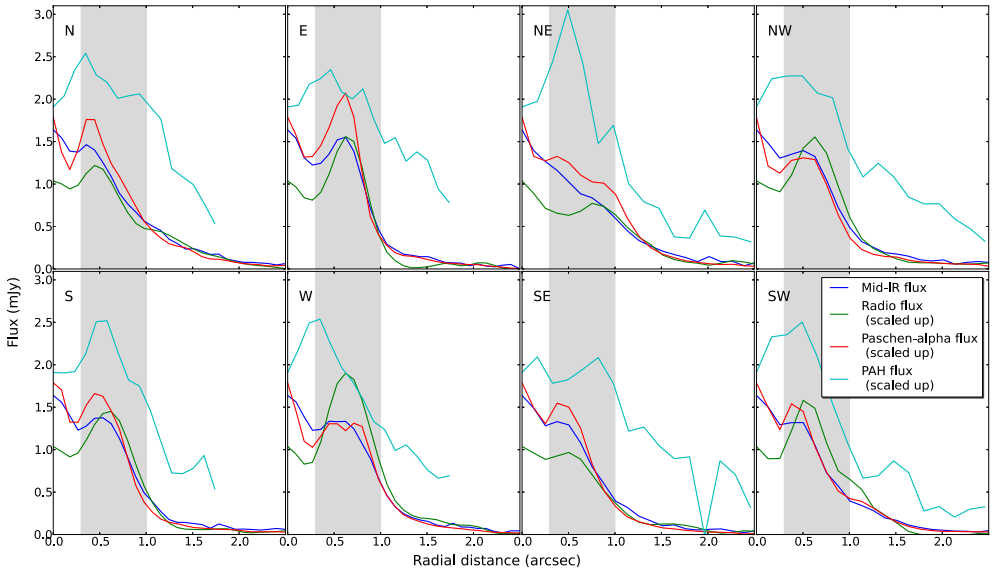

Figure 3.2: Azimuthal profile of the fluxes - Mid-IR (8.7 μm, in blue), radio (3.6 cm from Nov 2004, in green), Paα (1.9 μm, in red) and continuum-subtracted PAH feature (3.3 μm, in cyan) , starting from the center of the images. Radio, Paα and PAH fluxes are scaled up by the median of the 8.7 μm/3.6 cm, 8.7 μm/Paα and 8.7 μm/3.3 μm ratios, respectively (factors 19.2, 10.8 and 13.6). The profile is shown for eight cardinal directions, with an azimuthal binning of the size of a pixel (0.116″ for the 3.3 μm image and 0.089″ for the other cases). The shaded area, from 0.3 to 1.0 arcsec, corresponds to the approximate width of the star formation ring.

Table 3.3: Flux density and spectral index for NGC 1614 (circum)-nuclear region

	6.0 cm		3.6 cm			Spectral index	
Region	1986 (mJy)	1999 (mJy)	1999 (mJy)	2004 (mJy)	2006 (mJy)	Total average	Non-thermal average
A	1.40 ± 0.06	1.46 ± 0.05	1.29 ± 0.05	1.26 ± 0.04	1.23 ± 0.04	-0.48 ± 0.06	-0.56 ± 0.10
B	3.42 ± 0.12	3.71 ± 0.11	3.09 ± 0.10	3.01 ± 0.09	2.88 ± 0.09	-0.53 ± 0.17	-0.72 ± 0.16
C	1.15 ± 0.05	1.23 ± 0.04	0.91 ± 0.04	1.00 ± 0.03	0.97 ± 0.03	-0.74 ± 0.04	-1.44 ± 0.13
D	1.22 ± 0.06	1.13 ± 0.04	0.98 ± 0.04	1.08 ± 0.04	1.00 ± 0.04	-0.62 ± 0.03	-1.14 ± 0.22
N	2.57 ± 0.10	2.81 ± 0.09	1.85 ± 0.07	1.79 ± 0.06	1.79 ± 0.06	-0.68 ± 0.13	-1.30 ± 0.53
T	34.06 ± 1.06	35.70 ± 1.08	25.61 ± 0.79	26.39 ± 0.80	25.45 ± 0.77	-0.73 ± 0.25	-1.19 ± 0.63
R	31.48 ± 0.98	32.89 ± 0.99	23.77 ± 0.73	24.60 ± 0.74	23.66 ± 0.72	-0.73 ± 0.25	-1.18 ± 0.63

Note. — Both images at 6.0 cm were mapped with a beam of 0.71×0.43 arcsec and the three epochs at 3.6 cm with a beam of 0.50×0.36 arcsec. The (two-point) spectral index was obtained for the 6.0 and 3.6 cm simultaneous observations of NGC 1614 carried out in 1999. Col. 7 shows the average spectral indices obtained directly from the spectral index map, while col. 8 spectral indices are obtained from the isolated non-thermal emission (see main text for details).

3.3.2 Radio variability and spectral index of the circumnuclear ring in NGC 1614

In star forming regions, non-thermal radio emission and variability are usually good tracers of recently exploded supernovae. I show in Fig. 3.3 the radio interferometric images of NGC 1614 at 6.0 cm (epochs 1986 and 1999) and 3.6 cm (epochs 1999, 2004 and 2006), obtained with the VLA in A configuration, and imaged using the same restoring beam at all epochs, for consistency. In Table 3.3, I show the integrated flux for each defined region and for each epoch.

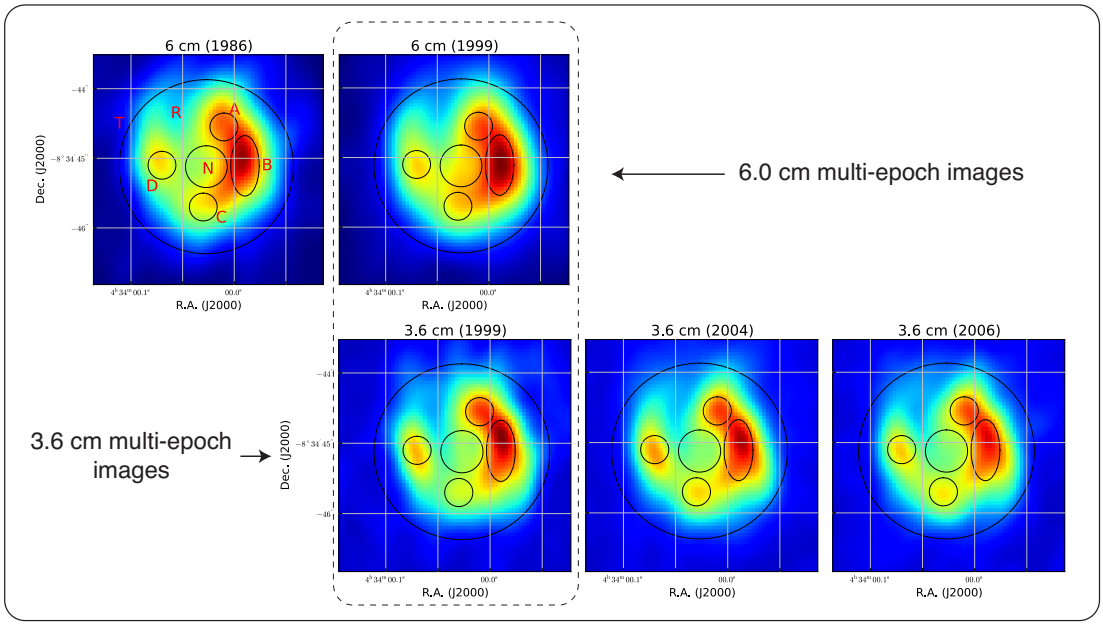

Figure 3.3: Sub-arcsecond resolution radio continuum images of NGC 1614 - Top panels show images at a wavelength of 6 cm from observations in 1986 (left) and 1999 (right). Bottom panels show 3.6 cm maps from observations in 1999 (left; quasi-simultaneously taken also at 6 cm), 2004 (center) and 2006 (right). Images of the same frequency were mapped with the same beam. In all cases, the bulk of the radio emission is within a circumnuclear star-forming ring of radius ~ 390 pc. Note that the peaks of the brightest regions at 3.6 cm have a maximum whose position coincides rather well with the peaks seen at 6 cm, but for region B, whose maxima clearly peak at different positions. The color scale is the same for each epoch but independent for each wavelength, corresponding to [0.1, 5.0] mJy/beam for the 6 cm band and [-0.17, 2.65] mJy/beam for 3.6 cm. See main text and Table 3.3 for details.

The images at each wavelength look overall similar, and the total radio emission

at 3.6 and 6.0 cm has not varied among the epochs, within the uncertainties. In fact, while there seems to be an apparent increase of the flux density between 1986 and 1999 at 6 cm (see Fig. 3.3, top panel) for several regions, including N and B (the brightest spot in the circumnuclear ring), this variability is not quantitatively significant ($\lesssim 1\sigma$, see Table 3.3) and hence we cannot claim they are real. Similarly, the images at 3.6 cm between 1996 and 2006 (Fig. 3.3, bottom panel) suggest that the flux density in region B has been steadily decreasing from 1996 till 2006, while region C would have experienced a rise and decrease of flux density during this period, possibly indicating supernova activity. Again, the variations are not significant, and unfortunately we lack further observations that could have allowed us to confirm, or rule out, those variations. However, the peaks of the regions sometimes show significant changes from epoch to epoch, suggesting that supernova events may be occurring. Still, it seems that no very radio bright, Type IIn supernova ($L_{\nu,\mathrm{peak}} \gtrsim 10^{28}$ erg s^{-1} Hz^{-1}) has exploded in NGC 1614 during the 1986-2006 period. Such bright supernovae are known to evolve slowly and stay bright for $\gtrsim 10$ yr, e.g. SN 1986J in NGC 891 (Pérez-Torres *et al.*, 2002), or some of the supernovae in the compact nuclear starbursts of Arp 299-A (Pérez-Torres *et al.*, 2009b; Bondi *et al.*, 2012) and Arp 220 (Parra *et al.*, 2007; Batejat *et al.*, 2011). Yet, we cannot exclude completely the possibility of a Type IIn SN having exploded and be missed by us, given the scarcity of the radio observations.

We used the quasi-simultaneous 3.6 and 6.0 cm observations in 1999 to derive the average spectral index α ($S_\nu \propto \nu^\alpha$) for each of the regions defined in Figs. 3.1 and 3.3. The values in col. 7 of Table 3.3 result from obtaining an average value of each region from the spectral index map created with the actual observations at 6.0 and 3.6 cm from 1999 (which are the combination of the thermal free-free and non-thermal synchrotron radio emission), while col. 8 shows the intrinsic synchrotron radio spectral index, once the thermal component is subtracted from the total radio emission (see section 3.3.4 for details). The overall non-thermal spectral index for both the ring and the total area is $\alpha \simeq -1.2$. Such steep spectral index suggests that most of the diffuse, extended synchrotron radio emission is due to supernovae and supernova remnants. Note, however, that the brightest regions in the ring have spectral indices significantly flatter than -1.2, which might suggest that the synchrotron radio emission is mostly powered by SN remnants, rather than by recently exploded SNe.

The [Fe II] emission line at 1.26 and 1.64 μm has also been proposed as a tracer of the supernova rate in nearby starburst galaxies (see, e.g., Moorwood & Oliva, 1988; Greenhouse *et al.*, 1991; Colina & Perez-Olea, 1992; Colina, 1993; Vanzi & Rieke, 1997; Alonso-Herrero *et al.*, 2003), both in a pixel-by-pixel basis, and as an integrated approach. The [Fe II] 1.26 μm emission in NGC 1614 shows a C-shape morphology in the circumnuclear star-forming ring (Rosenberg *et al.*, 2012), with the brightest emitting region matching approximately region D in our 3.6 and 6.0 cm images, i.e., an apparent anti-correlation between the maxima in the continuum VLA radio emission and the [Fe II] 1.26 μm. However, after correcting for extinction the [Fe II] image, this anti-correlation disappears (Rosenberg, private communication).

3.3.3 Spatially resolved X-ray emission

We fitted the *Chandra* spectrum using standard procedures within the X-ray software XSPEC[1] version 12.7.0. We fitted the data using four different models: (i) a pure thermal model (MEKAL), where the thermal emission is responsible for the bulk of the X-ray energy distribution; (ii) an absorbed power-law model (PL), which corresponds to a non-thermal source representing an AGN; (iii) a composite of a thermal plus an absorbed power-law model (MEPL); and (iv) a thermal model with tuned individual abundances (VMEKAL), which models the metal abundance pattern of type II SNe (see, e.g., Iwasawa *et al.*, 2011; Zaragoza-Cardiel *et al.*, 2013). In all models, we kept fixed the Galactic absorption to the predicted value using the NH tool within FTOOLS (Dickey & Lockman, 1990; Kalberla *et al.*, 2005).

Neither the MEKAL nor the PL models yielded satisfactory fits to the data. The MEPL model fitted the data well, but with a physically unrealistic power-law index of $\Gamma = 3.1$. Using a MEPL model to fit *XMM-Newton* data (with a circular aperture of $\sim 15''$), Pereira-Santaella *et al.* (2011) obtained a luminosity four times higher, with $\Gamma = 2$. Our best fit turned out to be the VMEKAL, which is shown in Fig. 3.4, together with the soft and hard X-ray maps. This model finds abundances for Mg XI (1.36 keV), Si XIII (1.85 keV) and S XV (2.4 keV). The corresponding luminosity in the soft band for this model is $\log L(0.5-2\mathrm{keV}) = 40.78^{+0.04}_{-0.05}$ erg/s, while there are not enough counts in the hard band to derive a realistic value for the luminosity. The fitted temperature is $kT = 1.7 \pm 0.7$ keV.

[1] http://heasarc.gsfc.nasa.gov/xanadu/xspec/

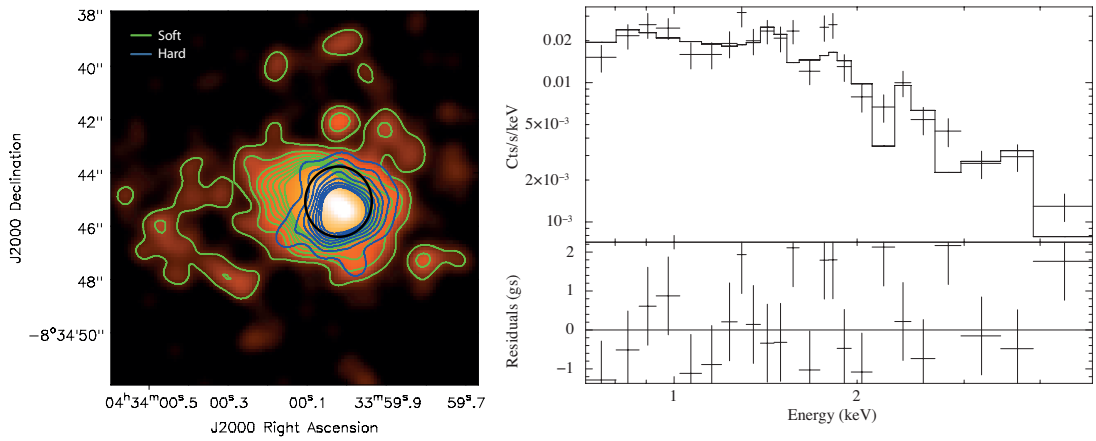

Figure 3.4: *Chandra* map (left) and spectrum fit (right) for NGC 1614 - The map shows the image of the total X-ray emission with the overlapped contours of the soft band (0.5–2.0 keV, in green) and the hard band (2.0–10.0 keV, in blue). The black circle corresponds to region T. Note that the emission is significantly more compact in the hard band than in the soft band.

3.3.4 Thermal free-free and non-thermal (synchrotron) radio emission

The bulk of the continuum radio emission observed in the central region of NGC 1614 comes from its circumnuclear ring (Fig. 3.1), where a strong burst of star-formation is ongoing (Alonso-Herrero *et al.*, 2001). Massive stars and their associated H II regions would be responsible for the thermal free-free radio emission, while supernovae and supernova remnants would account for the non-thermal synchrotron radio emission. Disentangling the contribution from each of those two components is non-trivial from radio measurements alone, since it would require observations at several frequencies in the range from ~ 20 cm down to $\lesssim 1$ cm, and ideally with the same angular resolution, which is not our case.

Here, we estimated the expected thermal free-free continuum radio emission from extinction corrected Paα measurements. Then, using our (extinction-free) continuum radio data at 3.6 cm from November 2004, we inferred the amount of radio emission that is of non-thermal, synchrotron origin. As a bonus, from the Paα measurements we obtained one of the most relevant physical parameters in the starburst in NGC 1614, namely its Lyman photon ionizing flux, $N_{\rm ion}$, which is used in Section 3.3.5 to compare

with the value derived from the SED fitting of the starburst in the circumnuclear region of NGC 1614. In fact, using standard relations (see Colina *et al.*, 1991) and the Paα to Hα recombination ratio and assuming no photon leakage, we can derive the ionizing photon flux, $N_{\rm ion}$, as:

$$N_{\rm ion} = 6.27 \times 10^{12} L_{\rm Pa\alpha}\ {\rm s}^{-1}, \tag{3.2}$$

where $N_{\rm ion}$ is measured in photons/s and $L_{\rm Pa\alpha}$ is the Paα extinction-corrected luminosity, in erg/s. From our continuum-subtracted Paα image, we obtain a flux density of ~ 47.1 mJy for the emission of the whole region, T, which corresponds to an absorbed $L_{\rm Pa\alpha} = 3.6 \times 10^{41}$ erg s^{-1}. This luminosity translates into an (absorbed) ionizing photon flux of $N_{\rm ion} \approx 2.27 \times 10^{54}$ s^{-1}. To obtain the relevant, unabsorbed ionizing photon flux, we corrected for the extinction, A_V. Fortunately, the extinction towards NGC 1614 is well studied, and is in the range $A_V = 3 - 5$ (see, e.g., Neff *et al.*, 1990; Puxley & Brand, 1994; Alonso-Herrero *et al.*, 2001; Kotilainen *et al.*, 2001; Rosenberg *et al.*, 2012). Assuming a value of $A_V = 4$, and using our observed Paα, we obtain the unabsorbed Paα flux by using standard H I recombination lines ratios, for Case B (Baker & Menzel, 1938), and using that

$$\frac{F(\lambda)}{I(\lambda)} = 10^{-C(H\beta)[f(\lambda)+1]}, \tag{3.3}$$

where $F(\lambda)$ and $I(\lambda)$ are the absorbed and unabsorbed fluxes, respectively, $C(H\beta)$ is the reddening coefficient, and $f(\lambda)$ is the reddening function (Cardelli *et al.*, 1989). The resulting unabsorbed Paα flux is $\simeq 80.2$ mJy, corresponding to an unabsorbed ionizing photon flux of $N_{\rm ion} \approx 3.87 \times 10^{54}$ s^{-1}.

Using standard relations between Paα and Hβ (e.g., Osterbrock, 1989) and Eq. 3 from Condon (1992), we can obtain the thermal continuum radio emission as:

$$S_{\rm thermal} = 1.076 \times 10^{13} \times F({\rm Pa}\alpha)\, \nu^{-0.1}, \tag{3.4}$$

with $S_{\rm thermal}$ in mJy, the unabsorbed Paα flux, F(Paα), in erg cm^{-2} s^{-1}, and ν in GHz, and where we have assumed for simplicity a temperature of 10 000 K and $N_{\rm e} = 10^4$ cm^{-3}, which are typical of compact (i.e., size $\lesssim 1$ pc) starburst regions. (The uncertainty in our estimates is dominated by the plasma electron temperature, since $S_{\rm th} \propto T_e^{0.52}$. A value of $T_e = 20000$ K would result in a thermal continuum radio flux $\sim 23\%$ higher.) In

this way, we isolated the thermal and non-thermal contributions to the radio emission, which are shown in Table 3.4 and in Fig. 3.5. The corresponding thermal free-free radio flux density is 11.03 mJy at 3.6 cm for the whole region, T, and is about 42% of the total 3.6 cm radio emission in the central regions of NGC 1614. Since our Paα measurements are much less affected by extinction than optical measurements, our decomposed values have a much weaker dependence on the actual value of the extinction. Indeed, allowing for an extinction A_V in the range $(3-5)$, results in thermal free-free radio flux densities in the range $(9.65 - 12.60)$ mJy.

In summary, we obtained the thermal radio emission from a scaled version of the Paα image, and the non-thermal radio emission as the result of the subtraction of the thermal emission from the total radio emission at 3.6 cm from November 2004. The ratio of thermal free-free to synchrotron radio emission can be used as an indicator of the starburst age of each region in the circumnuclear ring of NGC 1614. Regions where there is essentially no synchrotron radio emission imply that supernovae have not yet started to explode, indicating ages of at most ~ 4 Myr, while regions where the supernovae have already started to explode would be older. The models by Perez-Olea & Colina (1995) provide a quantitative estimate of the thermal free-free emission from massive stars, and non-thermal radio continuum emission from supernovae and supernova remnants. The ratios of thermal to non-thermal radio emission (see Table 3.4 and Fig. 3.5) for regions A and B are about $\sim$ 0.5, while those of regions C and D of 1.1 and 1.2, respectively. The ratios above (and the free-free thermal continuum luminosities) can be well explained if the emission in regions C and D come from instantaneous bursts with ages $\lesssim 5.5$ Myr, where supernovae have only recently started to explode. On the other hand, the emission from regions A and B would come from slightly older ($\sim$ 8 Myr) bursts, where essentially all exploding supernovae come from stars with masses in the 20-30 $M_\odot$ range.

We note that the above discussion is valid at 3.6 cm and is made under the assumption of a constant extinction of $A_V = 4$ and variations across the ring may affect the thermal to non-thermal ratios. In fact, there seems to exist a gradient of the extinction increasing towards the west, as shown in Fig. 1 of König *et al.* (2013). Considering an extinction of $A_V = 5$ for regions A and B, and $A_V = 3$ for regions C and D, we still obtain thermal to non-thermal radio emission ratios of ~ 0.6 for regions A and B, ~ 0.7 for region C, and ~ 0.8 for region D. A deeper discussion has been added in section 3.5.

The images of the decomposed radio emission help to understand the apparent paradox of the prominent mid-IR emission of the nucleus, N, which shows rather faint emission at radio wavelengths (see Fig. 3.1 and Table 3.2). Since the thermal free-free emission is directly proportional to the Paα flux, the decomposed images would indicate that the radio emission from the nuclear region is dominated by thermal free-free emission (for any A_V in the range $3-5$), which in turn suggests it is powered by a starburst, rather than an AGN, as we show in Section 3.4.

In the absence of low-frequency absorption, we would expect that the emission at lower frequencies (e.g., 21 cm) should be dominated by synchrotron emission, in contrast to the 3.6 and 6.0 cm images, where the contribution of the thermal emission is relevant. In fact, when we scale the non-thermal emission at 3.6 cm (Fig. 3.5) to 21 cm, using our derived non-thermal spectral indices (see Table 3.3), one would expect to recover the emission from the MERLIN image at 21 cm shown in Fig. 4 in Olsson *et al.* (2010). Although the extrapolated image correlates, in general terms, well with the Olsson et al. image, all regions of NGC 1614, except regions A and N, show at 21 cm a lower flux density than expected, with the radio emission from region D being especially suppressed. This should not come as a surprise, as those starburst regions have many massive stars that create big H II regions around them. Those H II regions are very efficient low-frequency absorbers, as demonstrated by, e.g., the large emission measure (EM) values in the vicinities of SN2000ft in the circumnuclear starburst of NGC 7469 (Alberdi *et al.*, 2006; Pérez-Torres *et al.*, 2009a), or around supernova A0 in Arp 299A (Pérez-Torres *et al.*, 2009b). Indeed, the low-frequency absorption implies that region D, the one showing the least flux density at 21 cm, has an EM $\approx 1.2 \times 10^7\,\mathrm{cm}^{-6}\,\mathrm{pc}$, a value very similar to that found for in the vicinities of supernovae SN 2000ft in NGC7469, or A0 in Arp 299-A. Regions B and C have moderate EM values ($\approx [3.3, 4.7] \times 10^6\,\mathrm{cm}^{-6}\,\mathrm{pc}$). Finally, regions A and N have negligible EM values and essentially their radio emission is not being efficiently suppressed at low frequencies. While a discussion of the specific reasons for the differences in the low-frequency absorption displayed by the circumnuclear regions of NGC 1614 is beyond the scope of this study, I just note here that our results are in agreement with all regions being synchrotron dominated at 21 cm, but whose emission is being significantly suppressed in some regions by low-frequency absorption that is most likely due to foreground absorbers, i.e., H II regions. The main exceptions are regions A and N, which seems to

suffer very little low-frequency absorption, possibly due to a smaller density in those region, as indicated by the low EM values.

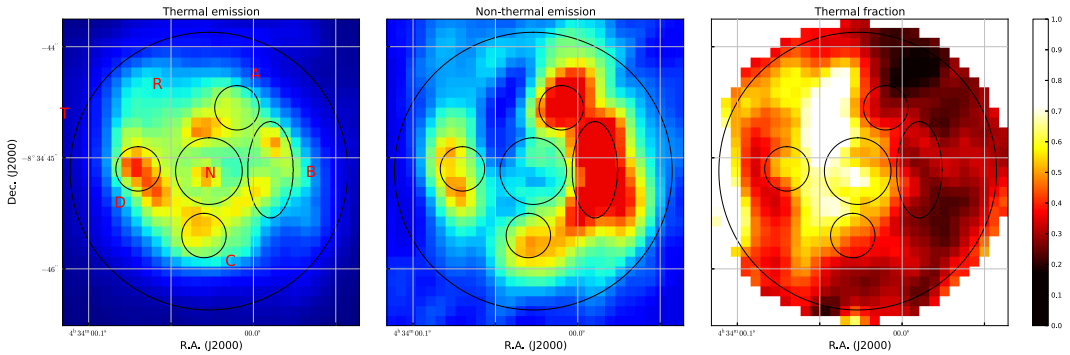

Figure 3.5: NGC 1614 thermal and non-thermal emission - Decomposition of the 3.6 cm flux from November 2004 of the central region of NGC 1614 into thermal (left panel, scaled version of the Paα applying an uniform extinction of $A_V = 4$) and non-thermal (middle panel, thermal radio emission subtracted from the total radio flux) components. The map shows the image of the total X-ray emission with the overlapped contours of the soft band (0.5–2.0 keV, in green) and the hard band (2.0–10.0 keV, in blue). The black circle corresponds to region T. Note that the emission is significantly more compact in the hard band than in the soft band.

3.3.5 The star-formation and core-collapse supernova rates in NGC 1614

The main goal of this section is to determine two of the most important parameters of any starburst, which are its star-formation rate (SFR) and its core-collapse supernova rate. The (constant) CCSN rate, $\nu_{\rm CCSN}$, can be related to the (constant) SFR as follows (Pérez-Torres *et al.*, 2009a):

$$\nu_{\rm CCSN} = {\rm SFR}\left(\frac{\alpha-2}{\alpha-1}\right)\left(\frac{m_{\rm SN}^{1-\alpha}-m_u^{1-\alpha}}{m_l^{2-\alpha}-m_u^{2-\alpha}}\right), \tag{3.5}$$

where SFR is the (constant) star formation rate in $\rm M_\odot\,yr^{-1}$, m_l and m_u are the lower and upper mass limits of the initial mass function (IMF, $\Phi \propto m^{-\alpha}$), and $m_{\rm SN}$ is the minimum mass of stars that yield supernovae, assumed to be 8 $\rm M_\odot$(e.g., Smartt, 2009). Mattila & Meikle (2001) found an empirical relationship between $L_{\rm IR}$ and $\nu_{\rm CCSN}$: $\nu_{\rm CCSN} \simeq 2.7\times10^{-12}\,(\rm L_{IR}/\,L_\odot)\,yr^{-1}$. This implies a CCSN rate for the circumnuclear starburst of NGC 1614 of $\simeq 1.08\,\rm SN\,yr^{-1}$, for $\rm L_{IR} \simeq 4.0\times10^{11} L_\odot$, which according to

Table 3.4: Thermal and non-thermal radio emission in NGC 1614

Region	$S_{\rm th}$ (mJy)	$S_{\rm syn}$ (mJy)	$L_{\rm th}$ (10^{27} erg s^{-1} Hz^{-1})	$L_{\rm syn}$ (10^{27} erg s^{-1} Hz^{-1})	Unabs. $L_{\rm Pa\alpha}$ (10^{40} erg s^{-1} Hz^{-1})	$N_{\rm ion}$ (10^{53} s^{-1})
(1)	(2)	(3)	(4)	(5)	(6)	(7)
A	0.45	0.96	2.22	4.69	2.55	1.60
B	0.92	2.03	4.49	9.97	5.15	3.23
C	0.51	0.46	2.49	2.24	2.86	1.79
D	0.58	0.48	2.86	2.37	3.29	2.06
N	1.01	0.69	4.97	3.38	5.70	3.58
T	11.03	15.47	54.03	75.79	62.07	38.92
R	10.01	14.77	49.07	72.41	56.37	35.34

Note. — Col. 1: Region name; Col. 2: Thermal fraction of the flux at 3.6 cm, obtained as a scaled version of the Paα image assuming a constant extinction of $A_V = 4$); Col. 3: Synchrotron fraction of the flux at 3.6 cm, (obtained as Col. 1 subtracted from the total radio emission); Col.4: Thermal radio luminosity at 3.6 cm; Col. 5: Synchrotron radio luminosity at 3.6 cm; Col. 6: Unabsorbed Paα luminosity; Col. 7: Number of ionizing photons.

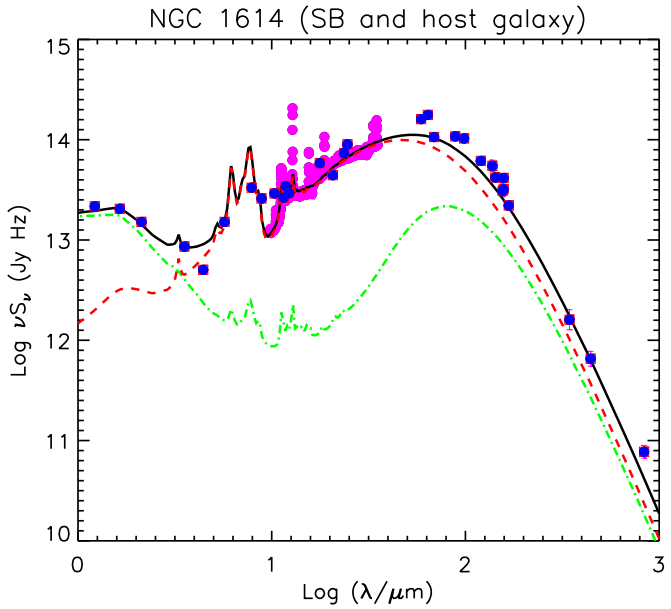

Figure 3.6: NGC 1614 SED fitting - Photometric data points are plotted in blue, while *Spitzer* IRS spectrum is shown in pink. Lines show the overall fit (solid black), the starburst contribution (dashed red) and the host galaxy contribution (dot-dashed green).

Table 3.5: SED model fitting

Parameter	Value
$L_{\rm SB}$	$10^{11.39} L_\odot$
e-folding time of SB	35.4 Myr
Age of SB	29.5 Myr
$\rm SFR_{max}$	$85.1 M_\odot\,\rm yr^{-1}$
$\rm SFR_{mean}$	$57.7 M_\odot\,\rm yr^{-1}$
	(averaged over 29.5 Myr)
$\nu_{\rm SN}$	$0.43\,\rm yr^{-1}$
$N_{\rm ion}$	$10^{54.54}\,\rm s^{-1}$

equation 3.5 corresponds to a (constant) SFR of $\approx 52.9\,\rm M_\odot\,yr^{-1}$. However, a constant star-formation process is likely to be, for LIRGs in general, and for NGC 1614 in particular, a poor approximation to the actual starburst scenario (Alonso-Herrero *et al.*, 2001).

The opposite case to a constant SFR is that of a single instantaneous starburst. For example, Rosenberg *et al.* (2012) used Starburst 99 (Leitherer *et al.*, 1999) to model the emission of NGC 1614 within an instantaneous starburst scenario, and obtained an average age for the starburst of 6.4 Myr and an integrated SN rate of $0.9\,\rm yr^{-1}$. U *et al.* (2012) found a star formation rate of $\rm SFR_{UV+IR} \simeq 51.3\,M_\odot\,yr^{-1}$. Alonso-Herrero *et al.* (2001) modeled the star formation of NGC 1614 using two Gaussian bursts, each of them with a FWHM of 5 Myr, separated by 5 Myr, obtaining an age of ~ 11 Myr after the peak of the first burst, i.e., a total age of ~ 16 Myr. From the extinction corrected [Fe II], they predicted a supernova rate of $0.3\,\rm SN\,yr^{-1}$.

An intermediate approach is that of an exponentially decaying starburst, which is the approach we have followed here. Namely, we modeled the near-IR to sub-millimeter spectral energy distribution (SED) of NGC 1614 by combining pure starburst models from Efstathiou *et al.* (2000), revised by Efstathiou & Siebenmorgen (2009), and models for the host galaxy. The latter models the emission from the stars using the models by Bruzual & Charlot (2003) and the emission from diffuse (cirrus) dust using the model of Efstathiou & Siebenmorgen (2009). The fit is shown in Fig. 3.6, where photometric data points were obtained from NED, Soifer *et al.* (2001), Skrutskie *et al.* (2006), and Ishihara *et al.* (2010).

The best fit starburst model yields a bolometric luminosity of $10^{11.39} L_{\odot}$, an initial star formation rate of 85.1 $M_{\odot}\,yr^{-1}$(57.7 $M_{\odot}\,yr^{-1}$ averaged over the duration of the starburst), a core-collapse supernova rate of $0.43\,SN\,yr^{-1}$, and an ionizing photon flux of $3.47 \times 10^{54}\,s^{-1}$.

3.4 Is there an AGN in the center of NGC 1614?

The nuclear region, N, shows a non-thermal spectral index of $\alpha \sim -1.30$. Such a steep spectral index seems to be at odds with an AGN origin for the radio emission of region N, but can be reconciled with the scenario of a compact starburst, powered by supernovae and supernova remnants. While such a high value of α is not rare or extreme for starbursts (see, e.g., NGC 253 in Heesen *et al.*, 2011), it implies heavy synchrotron losses and, given the large radiation field in the nuclear region (see the prominent 8.7 μm continuum and Paα line emission), also large inverse Compton losses. We note that the radio spectral index is the average value over region N, of ~ 90 pc in radius, so in principle we cannot rule out completely the existence of a hidden AGN inside that region, as found in other LIRGs, e.g., in Arp 299-A (Pérez-Torres *et al.*, 2010). However, even if there is an AGN, its radio luminosity would not contribute more than $\sim$ 6% and $\sim$ 7.6% at 3.6 and 6.0 cm, respectively (see Table 3.3). For comparison, the AGN in Arp 299-A, as found from VLBI observations has a 5.0 GHz flux density at cm-wavelenghts of about $820\,\mu Jy\,beam^{-1}$ (Pérez-Torres *et al.*, 2010), which corresponds to a luminosity of $\nu\,L_{\nu,AGN} \sim 9 \times 10^{36}\,erg\,s^{-1}$, and accounts for no more than about 11% of the compact VLBI 5.0 GHz flux. This luminosity value is also less than 1% of the total 5.0 GHz emission, as traced by e-MERLIN within the region where all SNe/SNRs are exploding (see Fig. 4 and sect. 3.3 in Bondi *et al.*, 2012). The corresponding 5.0 GHz luminosity of a putative AGN in NGC 1614 is therefore no more than $\nu\,L_{\nu,AGN} \sim 7.1 \times 10^{37}\,erg\,s^{-1}$ and, if most of this luminosity comes in turn from a nuclear starburst, the AGN must be even fainter.

The ratio of the 8.7 μm/Paα emission also suggests that region N is powered by a burst of star formation. In fact, the ratio in the central $\sim$90 pc agrees well with the ratios obtained for nuclei of H II systems, and is significantly lower than obtained for the nuclei of Sy/Sy 2 systems (Table 3 in Díaz-Santos *et al.*, 2008), which are known to host an AGN.

Similarly, the *Chandra* X-ray emission supports a starburst driven scenario for the central regions of NGC 1614. We calculated hardness ratios, which are model-independent, for different apertures. We defined the hardness ratio as HR $= (H - S)(H + S)$, being H and S the hard [2.0–10.0] keV and soft [0.5–2.0] keV bands, respectively. For an aperture of $3''$ in radius, we get HR$= -0.40$, while for an aperture of $0.3''$ (coincident with region N) we get a significantly harder spectrum, HR$=+0.69$. The point at which HR becomes positive (i.e., the hard emission dominates) is $\lesssim 0.4''$. The weak hard X-ray emission could easily be due to the presence of X-ray binaries in a compact starburst in the central $0.3''$ (i.e., ~ 110 pc), in agreement with the sizes of the starbursts seen in, e.g., Arp 299-A (Pérez-Torres *et al.*, 2009a; Bondi *et al.*, 2012) and Arp 220 (Parra *et al.*, 2007). While we cannot rule out completely that an AGN makes also some contribution, the presence of emission lines of Mg XI, Si XIII and S XV in the spectrum (see Fig. 3.4) suggests the existence of SNe and/or SNRs. Although the temperature is somewhat higher than expected for SNRs, with typical values of kT=0.5 keV (see, e.g., Soria & Wu, 2003), they are in good agreement with values obtained for young supernovae (e.g., SN2001gd in NGC 5033 had kT=1.1 keV; Pérez-Torres *et al.*, 2005).

Additionally, using the multi-wavelength optical, radio, and soft X-rays diagnostic diagram from Perez-Olea & Colina (1996), region N would be in the starburst dominated region, as can be seen in Fig. 3.7, with $\log(L_X/L_{5\mathrm{GHz}}) < 4.77$ and $\log(L_X/L_{\mathrm{H}\alpha}) < -0.43$. (The inequality accounts for the fact that the radio and Hα luminosity are for region N, while the X-ray luminosity corresponds to a $3''$ aperture.)

We also used archival data from *Spitzer* IRS to check the high-resolution spectra for NGC 1614 looking for [Ne V] lines at 14.3 and 24.3 μm, which would be indicative of the existence of an AGN (Genzel *et al.*, 1998; Armus *et al.*, 2007), but found no evidence of their presence.

Finally, we also fitted the multi-wavelength SED with a combination of starburst models and AGN torus models (Efstathiou & Rowan-Robinson, 1995) and found that the contribution of the AGN to the total bolometric luminosity, if any, would be at most $\sim 10\%$.

In summary, all evidence shows that the bulk of the observed emission (at all wavelengths) from the circumnuclear region of NGC 1614 can be explained with the existence of a powerful starburst, without any need to advocate the existence of an AGN.

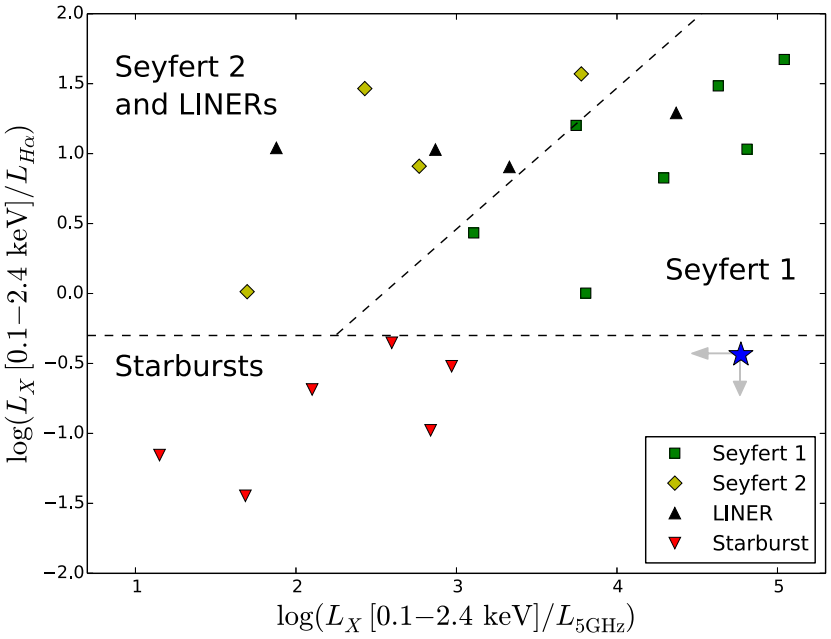

Figure 3.7: Multi-wavelength diagnostic plot discriminating starbursts from AGN - NGC 1614 is plotted as a blue star. Since the used X-ray aperture (3″) is larger than the Hα and 5 GHz ones (region N, 0.6″), NGC 1614 real position in the diagram will necessarily move down and to the left, making NGC 1614 fall clearly in the starburst dominated region. We derive an X-ray luminosity in the range [0.1–2.4] keV of $10^{40.90}$ erg/s. Adapted from Perez-Olea & Colina (1996).

3.5 Notes on the extinction dependence: a pixel-by-pixel correction

As explained above, one of the assumptions that was made to disentangle the thermal and non-thermal radio emission of the circumnuclear region of NGC 1614 at X-band, was the use of a constant extinction $A_V = 4$ within all the region. This was motivated by two main reasons: (i) the relatively constant values for the extinction reported in the literature, and (ii) the smaller importance of the extinction in the near-IR data (Paα) with respect to the optical, that should have made the constant approximation a valid assumption.

Anyhow, it is actually possible to do a simple yet powerful test to prove our previous assumptions by creating an extinction map of the circumnuclear region of NGC 1614. We generated a stellar population synthesis model using Starburst99 (v7.0.0 Leitherer *et al.*, 1999). We modeled an instantaneous burst of star formation using a Kroupa IMF and solar metallicity. We used a 0.1 Myr step for starburst ages ranging from 0.01 to 50 Myr. The model output provides the SED of the continuum at the specified ages, together with the nebular emission from hydrogen recombination lines.

We used near-IR continuum (F110M, F160W, and F222M) and emission line (F187N, F190N) bands from *HST* NICMOS data (Alonso-Herrero *et al.*, 2001). Figure 3.8 shows a schematic diagram illustrating the procedure we have followed:

1. Using the emission line bands from NICMOS, we create a Paα equivalent width (EW) image of the nuclear region of NGC 1614. We compare this image with the predicted EW obtained from the Starburst99 model to obtain a pixel-by-pixel estimate of the age of the starburst. However, the derived ages are upper limits since the presence of an older, underlying stellar population would increase the near-IR continuum.

2. We convolve the model IR SED with our three available continuum filters (F110M, F160W, and F222M) for each time step; thus, we obtain the theoretical near-IR colors, defined as the ratios between two bands (i.e., F110M/F160W, F110M/F222M, and F110M/F222M). Interpolating for each age, we obtain an intrinsic near-IR color map of our region of interest.

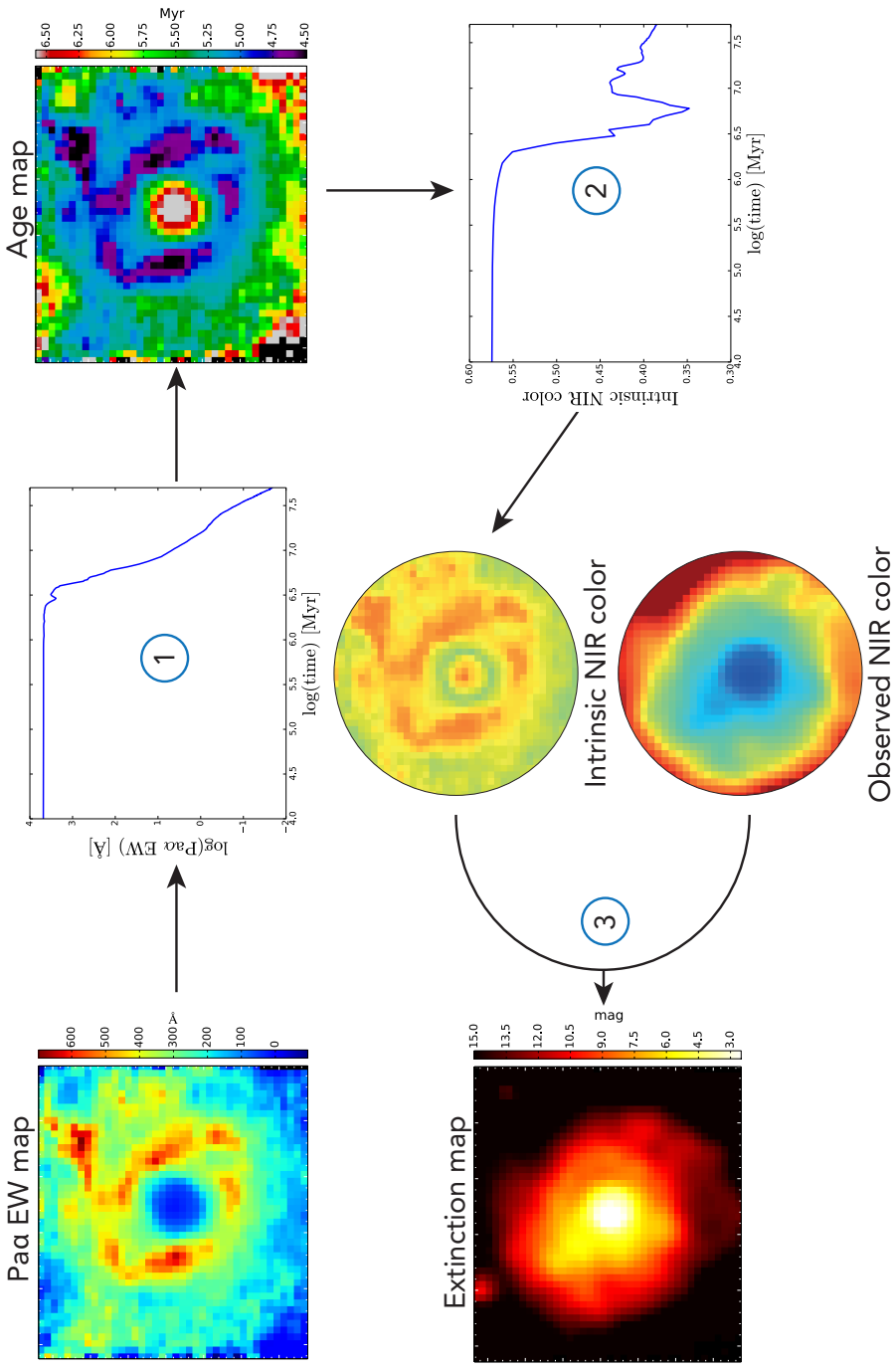

Figure 3.8: Obtention of an extinction map for NGC 1614 - Schematic diagram explaining the procedure we follow to obtain an extinction map for NGC 1614. The steps, explained in the text, are the following: (1) From Starburst99 we obtain the temporal evolution of the Paα equivalent width and created the correspondent age map; (2) We obtain the theoretical near-IR color as a function of time and create an intrinsic near-IR color map considering the age map obtained in step 1; (3) Comparing the intrinsic and observed near-IR color maps, we derive the extinction map for all the region.

3. Comparing the intrinsic and observed near-IR color maps, we can create the extinction map. To do so, we have used Calzetti *et al.* (2000) dust-attenuation law.

With the three available filters, we obtained the three possible near-IR color maps and the three corresponding obscuration maps. We averaged them to get the final A_V map. Figure 3.9 shows how the use of the extinction map affects the thermal and non-thermal decomposition with respect to the original approach of a constant A_V. The most noticeable differences appear in the innermost region, where the thermal emission was overestimated in the original approach. However, averaging over region N, the difference between both methods is $\sim 8\%$. This region is still thermal dominated following the new method, confirming our previous conclusions. The emission decomposition for the regions in the ring shows larger average variations ranging from $\sim 9\%$ (region D) to $\sim$ 35% (region B), proving that the constant A_V approximation is valid for those galaxies provided they have a small and relatively regular extinction, as NGC 1614. This way to estimate the extinction towards NGC 1614 will be publish in the frame of a comparison between 8.4 GHz radio continuum and ALMA CO (6-5) data in Xu *et al.* (2014, *submitted to ApJ*).

3.6 Summary

I have presented sub-arcsecond angular resolution radio, mid-infrared , optical, and X-ray observations of the central kiloparsec region of NGC 1614. The main results of this study are the following:

1. The continuum emission of the circumnuclear ring, as traced by 3.6 cm Very Large Array (VLA), T-ReCS 8.7 μm and *HST*/NICMOS Paα show remarkable morphological similarities, suggesting a common origin for both radio, mid-IR, and hydrogen recombination line emission in the ring, likely recent star-forming activity along the ring.

2. The analysis of multi-epoch VLA observations at 3.6 and 6.0 cm spanning almost 20 years show that the total radio luminosity of the ring is quite stable, and the possible variations are not significant. Still, if such variability was real, it could be ascribed to CCSN activity, since the luminosities involved in them ($L_\nu \sim$

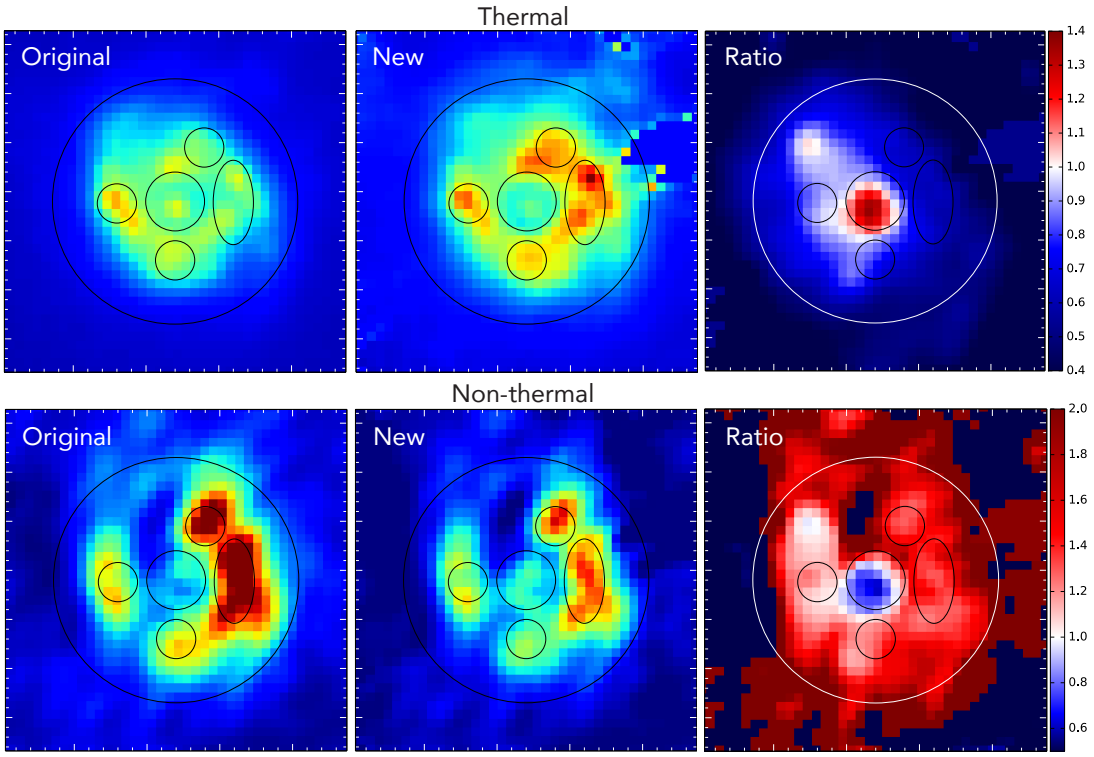

Figure 3.9: Comparison of thermal/non-thermal decomposition methods in NGC 1614 - Left panels show, the thermal and non-thermal emission maps obtained using the original method of decomposition described in section 3.3.4. Middle panels show the decomposition using the derived extinction map, as described in section 3.5. Right panels show the ratio between the original and the new method for both the thermal and non-thermal emission. Note the differences in the nucleus, and the overall agreement within a $\sim 30\%$. The color scale used for the four emission maps is the same.

$(1.0 - 1.5) \times 10^{27}$ erg s^{-1} Hz^{-1}), are typical of Type IIb/IIL supernovae. The steady radio emission of NGC 1614 is rather high in the whole circumnuclear ring, likely due to significant thermal free-free emission from massive stars and H II regions, as well as to diffusion of synchrotron emission produced in the shocks of SNe and SNRs.

3. From the Paα image of the circumnuclear ring, we measured the ionizing photon flux for the ring and the nucleus, and predicted the (thermal) free-free radio emission assuming a constant extinction. We then estimated, from our radio images, the intrinsic non-thermal synchrotron contribution to the observed radio continuum. We found that the circumnuclear (radio) ring surrounds a faint and compact ($r \lesssim 90$ pc) source at the very center of the galaxy, with a non-thermal steep spectrum ($\alpha_{\rm syn} \simeq -1.3$), suggesting that the central source is not powered by an AGN, but rather by a compact starburst. In any case, a putative AGN would contribute at most $\sim 8\%$ to the total radio luminosity.

4. We studied the validity of the constant extinction approximation by obtaining a pixel-by-pixel extinction map through the comparison of an *HST* near-IR color map with a theoretical one coming from a stellar population synthesis model. We found that the conclusions drawn from assuming a constant extinction remain valid.

5. We modeled the X-ray spectrum of the central 3-kpc region of NGC 1614, using *Chandra* X-ray data. This region is well described by a pure thermal model with $kT \sim 1.7$ keV), with the presence of lines indicative of SNe/SNR. The circumnuclear region has a hardness ratio HR $\simeq -0.40$, in good agreement with expectations for a starburst, while the inner $\sim 0.4''$ (~ 120 pc) of NGC 1614 shows HR$\simeq +0.69$, which could be explained by a population of high-mass X-ray binaries.

6. We also used several diagnostic diagrams, which suggest that region N (the nuclear region) has no AGN inside (e.g., Perez-Olea & Colina, 1996; Asmus *et al.*, 2011) and is dominated by a starburst.

7. Finally, we used publicly available infrared data to perform a model-fit to the spectral energy distribution of NGC 1614. We found that the circumnuclear star-forming region in NGC 1614 can be well described by an exponentially decaying burst that started $\lesssim 30$ Myr, and which has an average core-collapse supernova rate of ~ 0.4 SN yr^{-1} and an average SFR rate of ~ 58 M$_{\odot}$ yr^{-1}.

In summary, although a dust-enshrouded AGN cannot be completely ruled out by our observations, there is no need to advocate its existence, since the starburst completely dominates the observed properties of both the circumnuclear star-forming ring and the nuclear region.

Equipped with his five senses, man explores the Universe around him and calls the adventure Science.

Edwin Hubble

4

The study of LIRGs under a multiwavelength approach

The previous chapter has shown the potential of a multiwavelength strategy in the case study NGC 1614. It is worth extending the applied methods to other galaxies. In this chapter, we combine near-IR and radio observations at high angular resolution to characterize the central region of a sample of local LIRGs. We analyze the morphological properties and discuss the differences found at both wavelengths. We also study and compare the physical parameters such as the CCSN rate and the spectral behavior. Finally, we model the complete SED of the LIRGs in our sample to derive a reliable SFR as well as to isolate the luminosity contribution of the putative AGNs of the sample, comparing this contribution with the one obtained through mid-IR indicators.

Although our initial motivation for this work was aimed at unveiling the hidden population of SNe in LIRGs, difficulties affecting our VLA observations led us to the multiwavelength study presented here.

4.1 Background

The observed rate at which stars with masses $\gtrsim 8M_{\odot}$ explode as CCSNe can be used as a direct measure of the current star formation rate for an assumed initial mass function (IMF). In fact, CCSNe are beginning to be used as probes of the massive SFR at both low and high redshift (e.g., Li *et al.*, 2011; Dahlen *et al.*, 2004; Botticella *et al.*, 2008) with the aim of providing a new independent measurement of the star formation history of the Universe, which is free from assumptions about the contribution of old stars to the IR luminosity of galaxies (Kennicutt, 1998). A large fraction of the massive star formation at high-z took place in LIRGs and ULIRGs (Magnelli *et al.*, 2009, see Fig. 1.2), and their high SFRs are expected to result in CCSN rates a couple of orders of magnitude higher than in ordinary field galaxies.

However, most of the SNe occurring in (U)LIRGs are likely to be obscured by large amounts of dust in the nuclear starburst environment and have therefore remained undiscovered by optical SN searches. Fortunately, it is possible to discover most of these SNe through high-resolution radio observations, as the radio emission is free from extinction effects. Furthermore, CCSNe are expected, as opposed to thermonuclear SNe, to become strong radio emitters when the SN ejecta interact with the circumstellar medium (CSM) that was ejected by the progenitor star before its explosion as a supernova (Chevalier, 1982b; Weiler *et al.*, 2002). The starburst activity in the circumnuclear regions of LIRGs ensures both the presence of a high number of massive stars and a dense surrounding medium, so bright radio SNe are expected to occur. A handful of such events were discovered and studied by members of our team. This includes SN2000ft in NGC 7469 (Colina *et al.*, 2001), SN2004ip in IRAS 18293-3413 (Mattila *et al.*, 2007a; Pérez-Torres *et al.*, 2007), SN2008cs in IRAS 17138-1017 (Perez-Torres *et al.*, 2008; Kankare *et al.*, 2008), as well as the powerful SN factories in Arp 299-A (Pérez-Torres *et al.*, 2009b; Ulvestad, 2009) and in Arp 220 (e.g., Parra *et al.*, 2007).

Another, complementary tool to discover SNe in LIRGs that has recently shown success is by means of near-IR, 2.2μm observations (Mattila & Meikle, 2001; Maiolino *et al.*, 2002; Mannucci *et al.*, 2003; Mattila *et al.*, 2007a,b). Furthermore, the introduction of adaptive optics (AO) for 8-meter class telescopes now enables near-IR searches for SNe at an angular resolution of ~ 0.1 arcsec, comparable or even better than that obtained with some of the radio studies carried out with the VLA. Therefore, the radio

and near-IR searches can now effectively complement each other to obtain the most complete picture so far of the SN activity in nuclear regions of LIRGs. In particular, near-IR searches will allow us to obtain accurate extinction measurements towards the central regions of the LIRGs, and permit the classification of SNe based on deep optical or near-IR spectra.

Our initial radio strategy consisted of X-band (8.4 GHz; 3.6 cm) observations at three different epochs aimed at detecting and characterizing possible CCSNe. A first epoch was granted and observed, prior to the expected enhancement of the VLA receivers, between 9 June and 1 July 2011 (project 11A-160; PI: M. Á. Pérez-Torres). The proposal for the second epoch was also approved and was observed between 5 October and 26 December 2012, shortly after the new receivers were actually installed, increasing the sensitivity of the original epoch by a factor of eight. The third and final epoch was proposed and although approved, only two of the sources were finally observed, on 20 February 2014 (14A-270; PI: M. Á. Pérez-Torres), but no SN candidate was found on them. In summary we got a first epoch with a relatively low sensitivity, a complete second epoch with our required sensitivity, and a third epoch with only two out of the eleven proposed LIRGs.

Our original aims of searching for new CCSNe and estimate the complete CCSN rate in the sample were compromised due to the lack of at least two complete epochs with a high sensitivity, which would have allowed us to do a systematic comparison. Yet, the radio data still have a high scientific interest, especially when combined with data at other wavelengths. We complemented our radio data with near-IR observations and archival data, which allowed us to study and compare the multiwavelength properties of the sample, which is useful to investigate the physical properties of (U)LIRGs, as shown in Chapter 3.

4.2 The sample

The sample was chosen from the *IRAS* Revised Bright Galaxy Sample (Sanders *et al.*, 2003), after applying distance ($D < 110$ Mpc), luminosity ($\log(L_{\rm IR}/L_{\odot}) > 11.20$), and declination ($\delta > -35^{\circ}$) cutoffs. Furthermore, we excluded *warm* LIRGs with *IRAS* color $f_{25}/f_{60} < 0.2$ to avoid contamination from obscured AGN activity (e.g., Farrah *et al.*, 2007) and finally also excluded galaxies with no nearby reference star to guide

Table 4.1: Galaxy sample properties

Name	RA (J2000)	Dec. (J2000)	$\log(L_{\rm IR})$ ($L_\odot$)	$D_{\rm L}$ (Mpc)	Merger state[c]	q-factor
MCG+08-11-002	05 40 43.7	+49 41 41	11.41	77.2	d	2.61
NGC 3690W[a]	11 28 29.8	+58 33 43	11.88[b]	47.7	c	2.30[b]
NGC 3690E[a]	11 28 33.5	+58 33 45	11.88[b]	47.7	c	2.30[b]
ESO 440-IG058	12 06 51.9	−31 56 54	11.36	100.5	b	2.32
IC 883	13 20 35.3	+34 08 22	11.67	100.0	d	2.34
CGCG 049-057	15 13 13.1	+07 13 32	11.27	59.1	N	2.74
NGC 6240	16 52 58.9	+02 24 03	11.85	103.9	d	1.83
IRAS 16516-0948	16 54 24.0	−09 53 21	11.24	96.9	d	2.08
IRAS 17138-1017	17 16 35.8	−10 20 39	11.42	75.9	d	2.47
IRAS 17578-0400	18 00 31.9	−04 00 53	11.35	58.6	b	2.64
IRAS 18293-3413	18 32 41.1	−34 11 27	11.81	77.8	c	2.33
NGC 6926	20 33 06.1	−02 01 39	11.26	81.9	d	1.97

Note. — IR luminosities and luminosity distances were obtained from Sanders *et al.* (2003).

[a]Component of Arp 299. See Appendix B for details.

[b]The quoted IR luminosity and q-factor correspond to the whole Arp 299 system.

[c]From the visual inspection of the IRAC 3.6 μm images (Stierwalt *et al.*, 2013). The code is as follows: (N) non merger; (a) pre-merger; (b) early-stage merger; (c) mid-stage merger; (d) late stage merger.

the adaptive optics (AO) observations with the Gemini-N or the VLT. In Table 4.1 we show our final sample, which consists of 11 LIRGs, all of them included in the GOALS sample (Armus *et al.*, 2009), together with their IR luminosity and luminosity distance. We also include the merger state as derived from IRAC 3.6 μm morphology (Stierwalt *et al.*, 2013), and the q-factor values (Helou *et al.*, 1985), obtained using the *IRAS* fluxes from the *IRAS* Revised Bright Galaxy Sample and the 1.4 GHz fluxes from the NRAO VLA Sky Survey (NVSS; Condon *et al.*, 1998). An optical image of each of the sources in our sample is shown in Fig. 4.1.

A short individual description of each source, some of which has been barely studied, is shown below.

4.2.1 MCG +08-11-002

This galaxy, also named IRAS 05368+4940, lays very close to the galactic plane ($b = 9.96°$). It is a barred spiral galaxy (type SBab), in a late stage of merging. Its extended

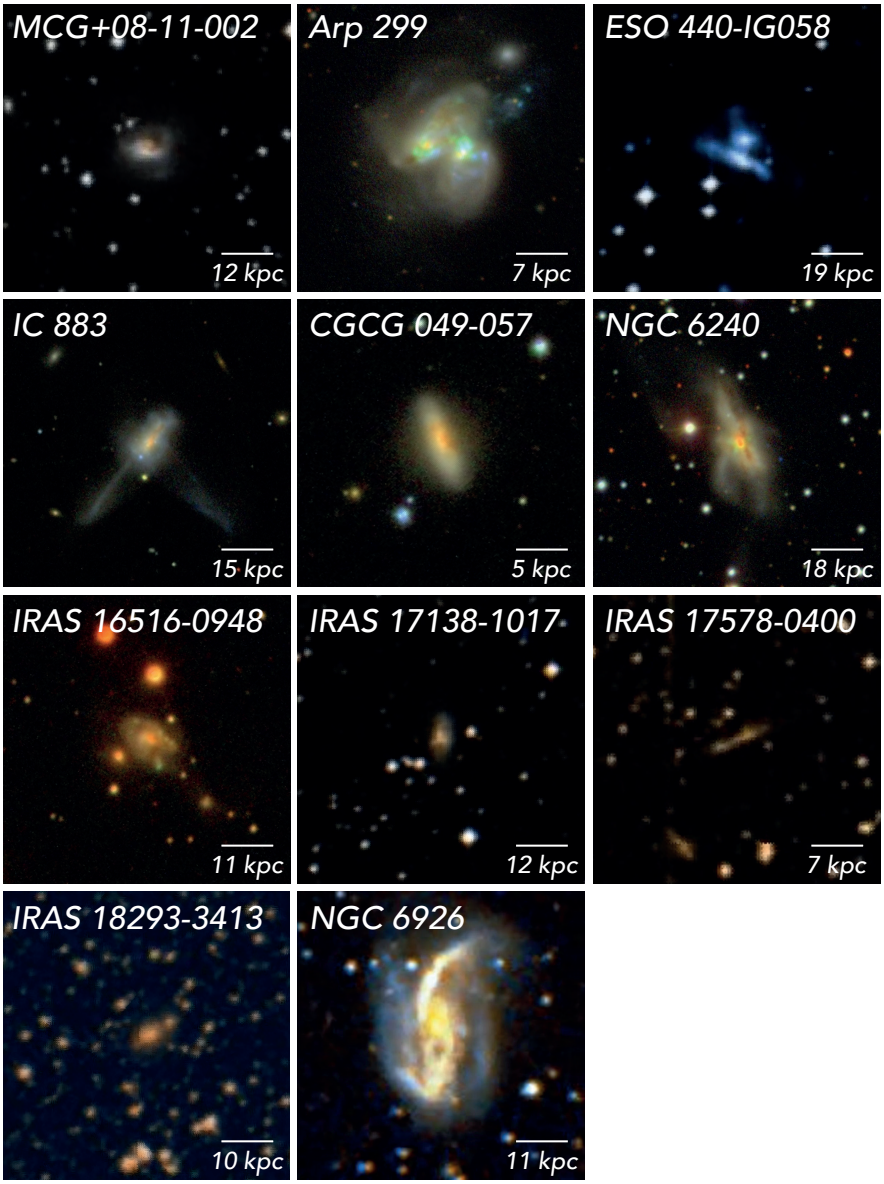

Figure 4.1: Optical color composite of the LIRGs in our sample - The images come from the Sloan Digital Sky Survey (SDSS) DR9 when available, or from the STScI Digitized Sky Survey (DSS) otherwise.

emission is clearly silicate dominated (Díaz-Santos *et al.*, 2011).

4.2.2 Arp 299

Arp 299 is one of the most luminous LIRGs in the local Universe. It is in an early state of merging according to Keel & Wu (1995) or in a mid-stage according to Stierwalt *et al.* (2013). Arp 299 (see Fig. 4.2) is formed by two galaxies and exhibits two clear radio nuclei (Gehrz *et al.*, 1983): A (which will be thoroughly described further in Chapter 5) and B, and two secondary nuclei, C and C′. The remaining compact structure, D, is believed to be a background quasar, unrelated to the system (Ulvestad, 2009). To avoid confusion, in this thesis the two galactic components of Arp 299 are named NGC 3690 East and NGC 3690 West. An explanation for this nomenclature can be found in Appendix B.

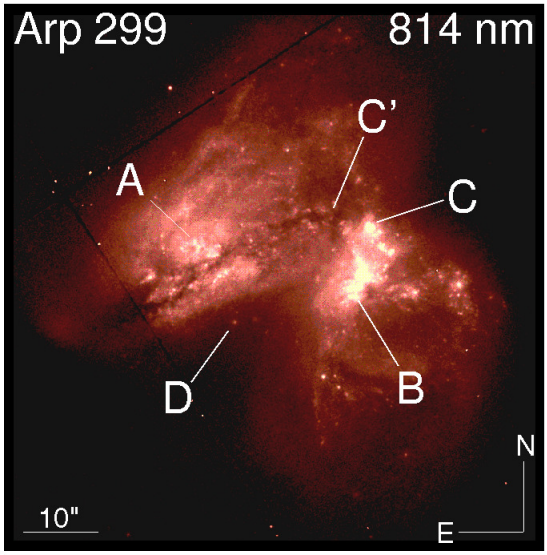

Figure 4.2: *HST* WFPC2 814 nm image of Arp 299 - The radio nuclei, as originally defined by Gehrz *et al.* (1983), are labeled. Arp 299-A is the main component of NGC 3690E, while B, C and C′ belong to NGC 3690W. The IR luminosity of nucleus A is $\sim 50\%$ of the total IR luminosity of the galaxy pair. From Neff *et al.* (2004).

4.2.3 ESO 440-IG058

This LIRG, also known as IRAS 12042-3140, consists of two merging galaxies separated $\sim$ 6 kpc one from each other. The northern component is very compact, has

been classified as a LINER (Corbett *et al.*, 2003), and is dominated by star formation (Monreal-Ibero *et al.*, 2010). The southern galaxy, on the other hand, appears to be dominated by young stars and shocks ($v = 100 - 200\,\mathrm{km\,s^{-1}}$).

ESO 440-IG058 has a star formation rate of $36.3\,M_\odot\,\mathrm{yr}^{-1}$ and an expected SN rate of $0.43\,\mathrm{SN\,yr}^{-1}$ (Miluzio *et al.*, 2013). Rodríguez-Zaurín *et al.* (2011) derived an age of the stellar population of $t \lesssim 6.5\,\mathrm{Myr}$.

4.2.4 IC 883

IC 883, also known as UGC 8387, is a late-merger LIRG ($L_{\mathrm{IR}} = 4.7 \times 10^{11} L_\odot$) at a distance of 100 Mpc, showing a peculiar morphology, with perpendicular extended tidal tails visible in the optical and near-IR (Smith *et al.*, 1995; Scoville *et al.*, 2000; Modica *et al.*, 2012). It was optically classified as a LINER (Kim *et al.*, 1995; Veilleux *et al.*, 1995), and later reclassified as an AGN/SB composite (Yuan *et al.*, 2010; Modica *et al.*, 2012). A strong indication of the presence of an active nucleus was found by Romero-Cañizales *et al.* (2012), who found a compact radio source consistent with an AGN. They also found evidences for this source to be a supernova factory. IC 883 also presents strong PAH emission, silicate absorption and a steep spectrum beyond $20\,\mu$m (Vega *et al.*, 2008).

4.2.5 CGCG 049-057

Also known as IRAS 15107+0724, this is the only isolated LIRG in our sample, showing no interaction with any nearby galaxy. It hosts an OH megamaser (Bottinelli *et al.*, 1986; Baan *et al.*, 1987). Although optically classified as a pure starburst, Baan & Klöckner (2006) suggested that an AGN may be buried in an optically dominating circumnuclear SB, based on multi-band radio observations.

4.2.6 NGC 6240

This bright LIRG ($L_{\mathrm{IR}} = 7 \times 10^{11} L_\odot$) is a late-stage merger at a distance of ~ 104 Mpc. It host one of the few binary AGN detected so far using *Chandra* hard X-ray observations (Komossa *et al.*, 2003), later supported by the detection of two compact unresolved sources at radio wavelengths with inverted spectral indices ($\alpha = +1.0$ and $\alpha = +3.6$ for the north and south component respectively; see Gallimore & Beswick, 2004). Close

to the southern nucleus, a water-vapor megamaser was found (Nakai *et al.*, 2002; Sato *et al.*, 2005).

4.2.7 IRAS 16516-0948

This unexplored LIRG was optically identified as a star forming galaxy (Mauch & Sadler, 2007), and classified as a late merger from its infrared morphology (Stierwalt *et al.*, 2013). Despite the minor concern of this galaxy, we found it to be an interesting source, as shown below.

4.2.8 IRAS 17138-1017

This LIRG is a highly obscured starburst galaxy (Depoy *et al.*, 1988) in a late stage of interaction. An extremely extinguished supernovae ($A_V = 15.7 \pm 0.8$ mag) was discovered in IRAS 17138-1017 using infrared K-band observations (Kankare *et al.*, 2008), years after the report of a previous one (SN2002bw; Li, 2002; Matheson *et al.*, 2002).

4.2.9 IRAS 17578-0400

This is an early stage merger ~ 60 Mpc away. The lack of bibliography about this source is almost complete.

4.2.10 IRAS 18293-3413

This poorly known source was classified as an H II galaxy based on its optical spectrum (Veilleux *et al.*, 1995). It was detected in hard X-rays at a 5σ level by Risaliti *et al.* (2000), finding no evidence of an AGN contribution to the X-ray spectrum. There are discrepancies on the merger stage determination of this LIRG. While Stierwalt *et al.* (2013) classified it as a mid-stage merger from the visual inspection of IRAC 3.6 μm images, Haan *et al.* (2011) classified it as a very early merger, with intact disks and no tidal tails based on its *HST* morphology. Supernovae SN2004ip was discovered in this galaxy by people from our group (Mattila *et al.*, 2007b; Pérez-Torres *et al.*, 2007).

4.2.11 NGC 6926

This relatively low luminosity LIRG is a spiral galaxy in a very early phase of interaction with the dwarf elliptical NGC 6929, located 4′ to the east. Optically identified as a Seyfert 2 (Veilleux *et al.*, 1995), NGC 6926 has a powerful water-vapor megamaser (Greenhill *et al.*, 2003; Sato *et al.*, 2005).

This is the only source for which we don't have near-IR data, but only radio observations.

4.3 Observations and data reduction

We observed our sample at both radio and IR wavelengths. Table 4.2 shows a summary of the observations.

4.3.1 Radio

The radio data used in this chapter are X-band (8.4 GHz, 3.6 cm) observations in full polarization mode and with a total bandwidth of 2048 MHz (project 12B-105; PI: M. Á. Pérez-Torres) between 5 October and 26 December 2012 taking advantage of the new VLA capabilities. We used the *Common Astronomy Software Applications (CASA)* package for the data reduction. It consisted of standard amplitude and phase calibration. We imaged the sources using a Briggs weighting (with `ROBUST = 0.5`) to obtain the best compromise between sensitivity and resolution. To correct for the spectral behavior along the wide bandwidth of the data (2048 MHz), we used a multiscale multifrequency synthesis deconvolution algorithm (Rau & Cornwell, 2011). Table 4.2 show the beam size, noise achieved and peak flux density for each image.

Although in Table 4.2 we quote the original values, to compare our radio images with the near-IR data, we had to re-calibrate the radio data from Jy beam^{-1} to Jy pix^{-1}.

4.3.2 Near-IR data

We used ALTAIR/NIRI from the Gemini-North telescope (PI: S. Ryder) and NACO from the VLT (PI: S. Mattila) to obtain near-IR K-band (2.2 μm) adaptive optics (AO) images. These instruments have a pixel scale of 0.022″ px^{-1} (ALTAIR/NIRI), and 0.027″ px^{-1} (NACO, with camera S27), except for ESO 440-IG058, where the

NACO camera S54 was used (hence the pixel scale was $0.054''\,\mathrm{px}^{-1}$). IRAS 18293-3413, ESO 440-IG058 and NGC 6240 were observed using NACO, while the remaining targets were observed with ALTAIR/NIRI. The near-IR data were reduced using *IRAF*-based tasks, including flat-fielding and sky subtraction. The final images were created by average-combining individual frames from different epochs after shifting them to a common reference. A detailed description of the reduction process is presented in Randriamanakoto *et al.* (2013). No near-IR data are available for NGC 6926.

The IR data were obtained at different epochs. Those from NACO come from a multiepoch survey intended for CCSNe detection. The NACO images used in this chapter are a combination of data from 2007 to 2010. ALTAIR/NIRI observations were performed on 13 September 2004 (IRAS 18293-3414), 22 January 2011 (ESO 440-IG058), and 31 May 2011 (NGC 6240).

4.3.3 Astrometry calibration and image convolution

Due to the small Field of View (FoV) of the near-IR images, we first calibrated archival data from NOT or *HST*/ACS using stars from Guide Star Catalogue-2 or 2MASS K_S-band catalogue. We then added the WCS information in the FITS header of our targets using these intermediate images.

Given the significantly different resolution of the radio and near-IR images (see Table 4.2), we convolved the IR images with a Gaussian with the size of the radio beam for each case, and then regridded to match the radio pixel size ($0.04''$). In the case of ESO 440-IG058, with an IR pixel size of $0.056''$, we regridded the radio image to the near-IR image pixel size.

4.4 Results and discussion

4.4.1 Radio and IR comparison

Figure 4.3 shows the correlation between L_{IR} and the radio luminosity at 1.4 GHz, spanning 5 orders of magnitude. The sources in our sample are plotted as stars while dots correspond to a crossmatch between the *IRAS* Revised Bright Galaxy Sample by Sanders *et al.* (2003) and the New VLA Sky Survey by Yun *et al.* (2001). NGC 6240, the only source from our sample known to host a dual AGN, is the source with the highest radio emission and the larger discrepancy with the correlation.

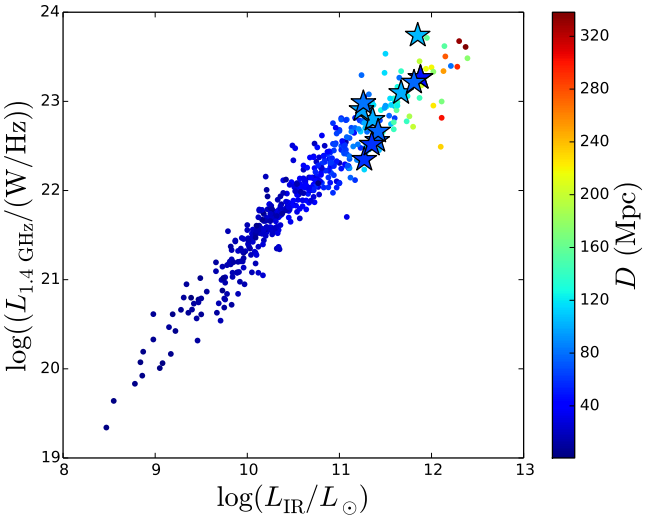

Figure 4.3: Infrared/radio correlation - Infrared ($8 - 1000\,\mu$m) vs radio (1.4 GHz) luminosity plotted for a sample of *IRAS* galaxies (dots) and our sample (stars). Colors indicate distance.

In Chapter 3, we focused in a radio and mid-IR comparison, which shows, for the nuclear region of NGC 1614, morphological similarities between both wavelengths that suggest a common origin for both emission mechanisms. However, near-IR, although presenting an overall correlation with radio emission (except for some remarkable cases shown in this section), traces different processes. Red supergiants, used as indicators of young stellar populations, radiate most of their energy in the near-IR (Oliva *et al.*, 1995). Near-IR also includes an important contribution from thermally pulsating asymptotic giant branch (TP-AGB) stars, with young to intermediate populations, up to 2 Gyr (Maraston, 1998). This range of the spectrum can be used to effectively trace star formation in galaxies where the relatively high extinction hinder their study in the optical (e.g., Dametto *et al.*, 2014). This makes near-IR a good spectral window in which to study (super) star clusters (e.g., Díaz-Santos *et al.*, 2007; Randriamanakoto *et al.*, 2013).

Figure 4.5 shows both our radio 3.6 cm and near-IR 2.2 μm images, as well as the ratio between them (reddish for radio dominated regions; blueish for IR dominated ones; white implies a ratio of 1). Any pixel that is not simultaneously above three times the correspondent rms at 3.6 cm and 2.2 μm, is masked out in the ratio maps. There is not a common trend in all the sources.

Table 4.2: Observations summary

	Radio (3.6 cm)			IR (2.2 μm)			
Name	FWHM (arcsec)	rms (μJy beam^{-1})	Peak (mJy beam^{-1})	Pixel size (arcsec)	rms (μJy)	Peak (mJy)	Shift (arcsec)
MCG+08-11-002	0.26×0.21	8.64	0.73	0.022	0.06	0.006	0.15
NGC 3690W	0.24×0.20	12.59	8.85	0.022	0.01	0.404	0.27
NGC 3690E	0.24×0.20	16.91	24.85	0.022	0.03	0.017	0.27
ESO 440-IG058	0.60×0.18	8.12	1.07	0.054	0.01	0.023	0.00
IC 883	0.27×0.21	13.52	10.51	0.022	0.02	0.006	0.15
CGCG 049-057	0.24×0.21	23.77	19.73	0.022	0.02	0.002	0.15
NGC 6240	0.27×0.20	29.26	19.70	0.027	0.20	2.327	0.18
IRAS 16516-0948	0.33×0.20	8.28	0.09	0.022	0.001	0.0002	0.16
IRAS 17138-1017	0.33×0.20	7.61	0.68	0.022	0.03	0.004	0.15
IRAS 17578-0400	0.55×0.21	9.66	17.21	0.022	0.005	0.002	0.28
IRAS 18293-3413	0.60×0.17	11.64	0.83	0.027	0.001	0.039	0.21
NGC 6926	0.25×0.19	7.26	3.99	...	...	...	...

Note. — The radio images correspond to the epoch with the highest sensitivity data (2012 epoch). The angular resolution for all IR images is $\sim 0.07''$, which corresponds to the diffraction-limited FWHM at K-band (adaptive-optics system was used).

Three LIRGs in our sample are completely radio-dominated in their common emission region: IC 883, and CGCG 049-057, and IRAS 16516-0948, although near-IR extends further than the radio emission.

On the other side, only one source is totally dominated by the near-IR emission, NGC 6240. The nature of the two main compact structures (labeled N1 and N2 in Figure 4.4) is well determined as a dual AGN (Komossa *et al.*, 2003; Gallimore & Beswick, 2004; Risaliti *et al.*, 2006). The nature of the fainter northwest radio component (N3 in Fig. 4.4), however, is not so clear. This component was first reported by Colbert *et al.* (1994) at 3.6 cm, estimating its $L_{\rm IR}$ in $\sim 0.2 \times 10^{11}$. They suggested that, considering its steep spectral index ($\alpha = -1.1$), it could be a clump of ejected electrons (a superwind; Heckman *et al.*, 1993), possibly ejected from a powerful starburst in the nearby compact bright region. Beswick *et al.* (2001) found a consistent 1.4 GHz structure using MERLIN (FWHM: $0.31'' \times 0.15''$), but did not detect the source at 5.0 GHz with the same instrument (FWHM: $0.10'' \times 0.06''$), due to the steep spectral index and the limited sensitivity at 5.0 GHz to detect the diffuse emission. They suggested a starburst origin for the region. Further deep VLBA observations at 1.7, 2.4, and 8.4 GHz by Gallimore & Beswick (2004) do not show any detection, giving support to a diffuse origin. The peak reported by Colbert *et al.* (1994) for this relatively faint peak is 1.10 mJy/beam, in agreement with our deeper VLA image (1.06 ± 0.23 mJy/beam; see Fig. 4.5). Confirming NGC 6240 composite AGN and SB nature, a supernova was discovered between N1 and N2 (Gallimore & Beswick, 2000, 2004).

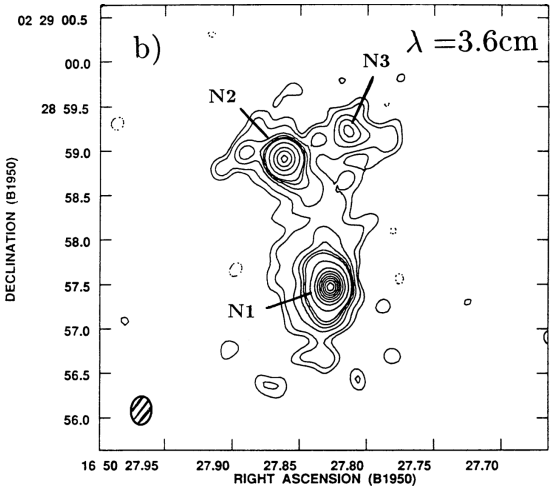

Figure 4.4: 3.6 cm VLA map of NGC 6240 from 1991 - From Colbert *et al.* (1994).

In the remaining sources, radio and near-IR emission dominate in different regions. In general, radio emission is more concentrated in compact nuclear regions dominating the emission. We remark, however, the radio silence of bright near-IR knots in three sources: ESO 440-IG058, IRAS 18293-3413, and specially IRAS 16516-0948, which will be discussed in section 4.4.2. The northern source detected in IRAS 17578-1017 is not in this list, as it is a field star, which does not look a compact Gaussian emission due to the image convolution with the radio beam. Complementarily, IRAS 18293-3413 has an important compact radio emission ~ 18 arcsec to the east of the main component that does not show a near-IR counterpart.

A particularly interesting case is NGC 3690W (the western component of Arp 299). Its different knots show completely different behaviors regarding their radio and near-IR correlation. While near-IR dominates the emission of nucleus B (see Fig. 4.2), nucleus C has a comparable emission, and nucleus C$'$ is very faint at 2.2 μm. This near-IR faintness was discussed by Alonso-Herrero *et al.* (2000), whose starburst models predict a persistence of the emission at 2 μm after their assumed Gaussian burst with a FWHM of 5 Myr. They conclude then that the star formation episode must have been shorter in C$'$. Indeed, (Leitherer & Heckman, 1995) models nicely fit an instantaneous burst, which yields a mass of the SB episode of $3 \times 10^7 M_\odot$, with an age of 4 Myr, supporting this idea.

Radio emission at 3.6 cm is dominated by two mechanisms: radio thermal emission (tracing current star formation) and non-thermal synchrotron emission (tracing emission from SN remnants, i.e., older populations). On the other hand, near-IR traces both young and intermediate stellar populations. This explains the general correlation between radio and near-IR, but at the same time, makes the interpretation of the ratio images problematic. In this sense, we find that it is not possible to use the ratios as age maps, unless we are able to, at least, decompose the thermal and non-thermal radio emission as done for NGC 1614 in Chapter 3. Furthermore, although near-IR can penetrate efficiently through dust, very dust obscured regions can hinder even near-IR emission, adding an uncertainty to an age interpretation.

4.4.2 An off-nuclear star forming region in IRAS 16516-0948

Figure 4.5 shows an enigmatic uncorrelation between the studied bands for IRAS 16516-0948. Figure 4.6 shows our near-IR and radio data contours overplotted on archival

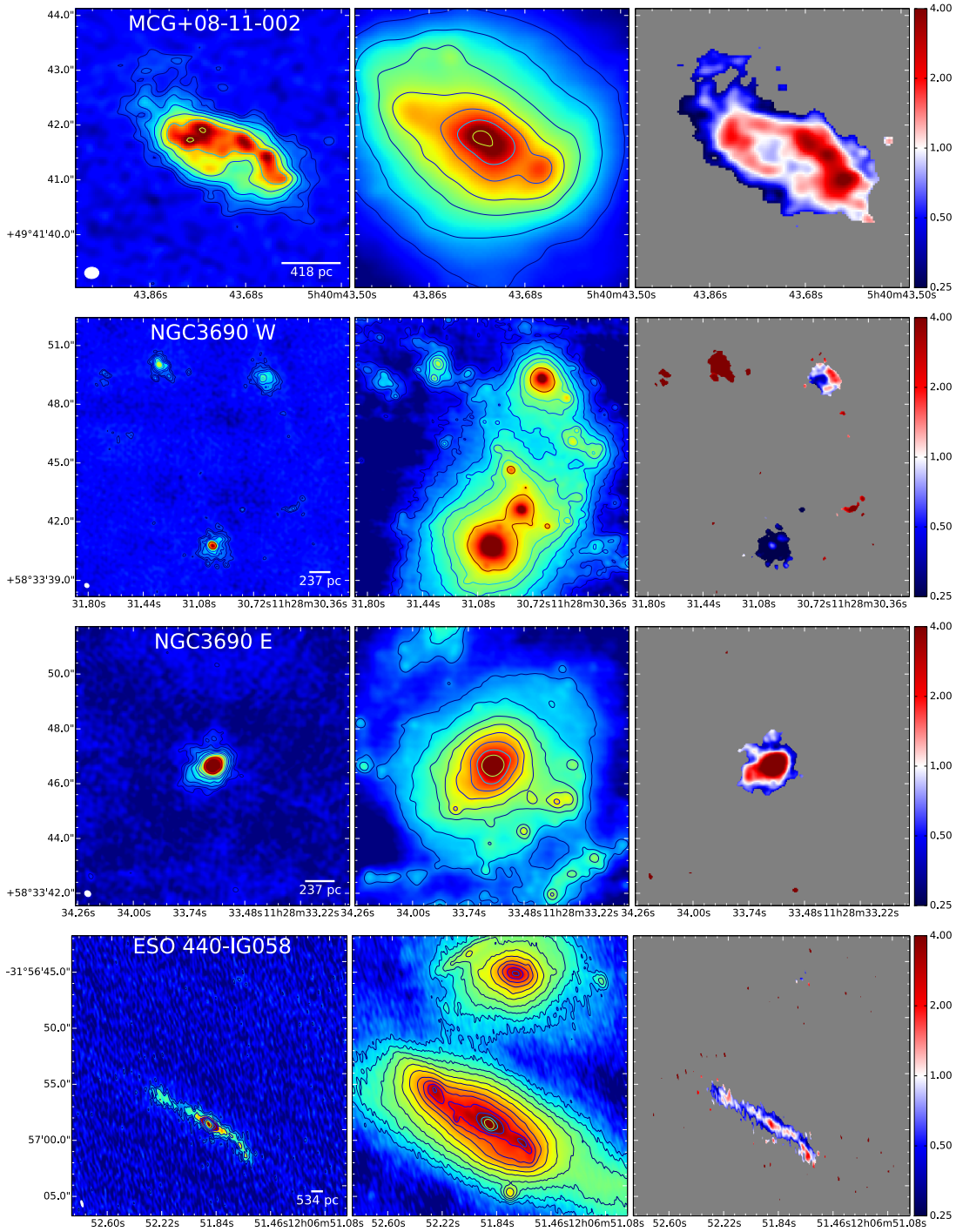

Figure 4.5: Radio and near-IR comparison of our sample - The image shows the 3.6 cm radio maps (left), the 2.2 μm IR maps (middle) and the ratio between radio and IR (right), where redder colors imply radio dominated regions in contrast with bluer colors.

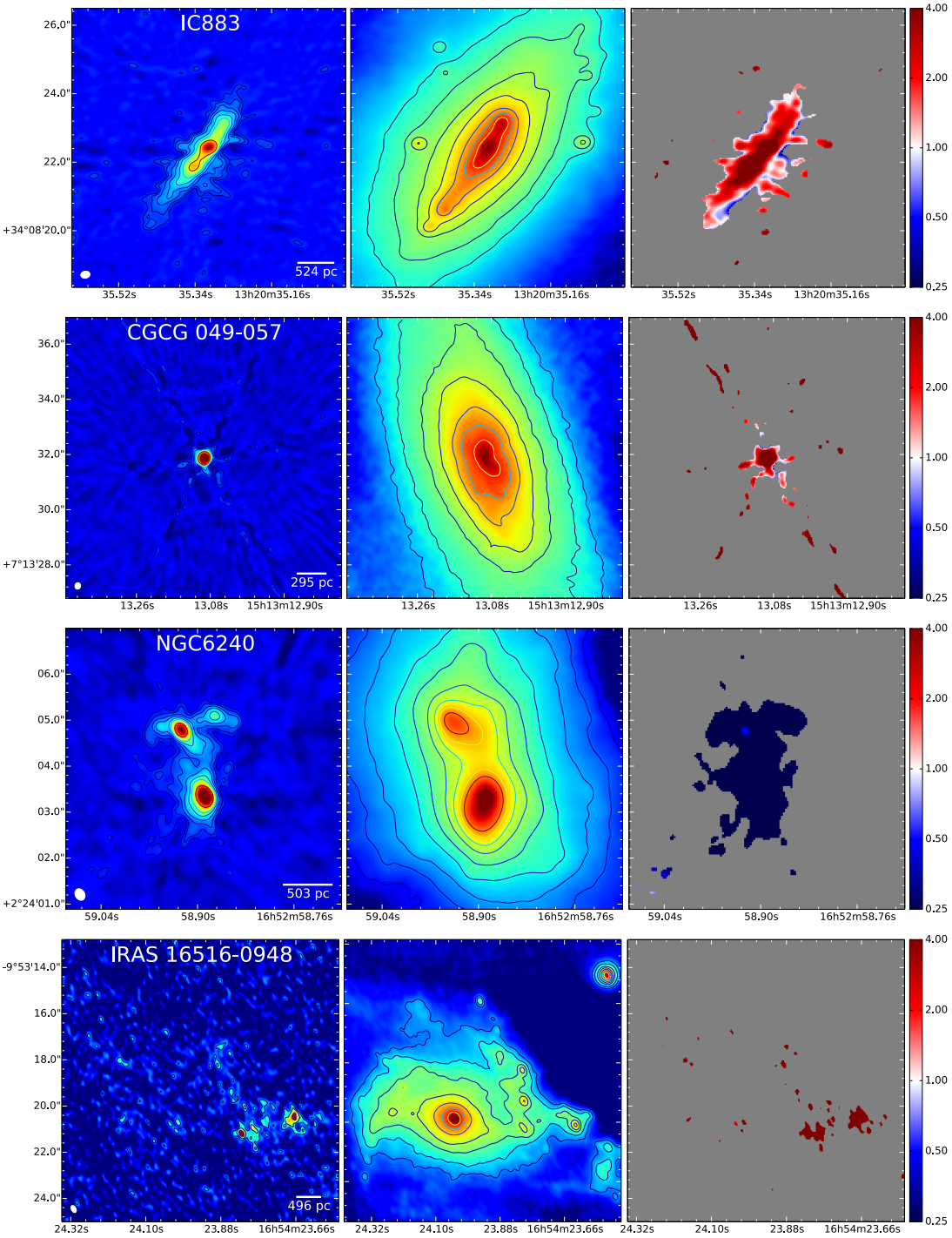

Figure 4.5: Radio and near-IR comparison of our sample - *Continued.*

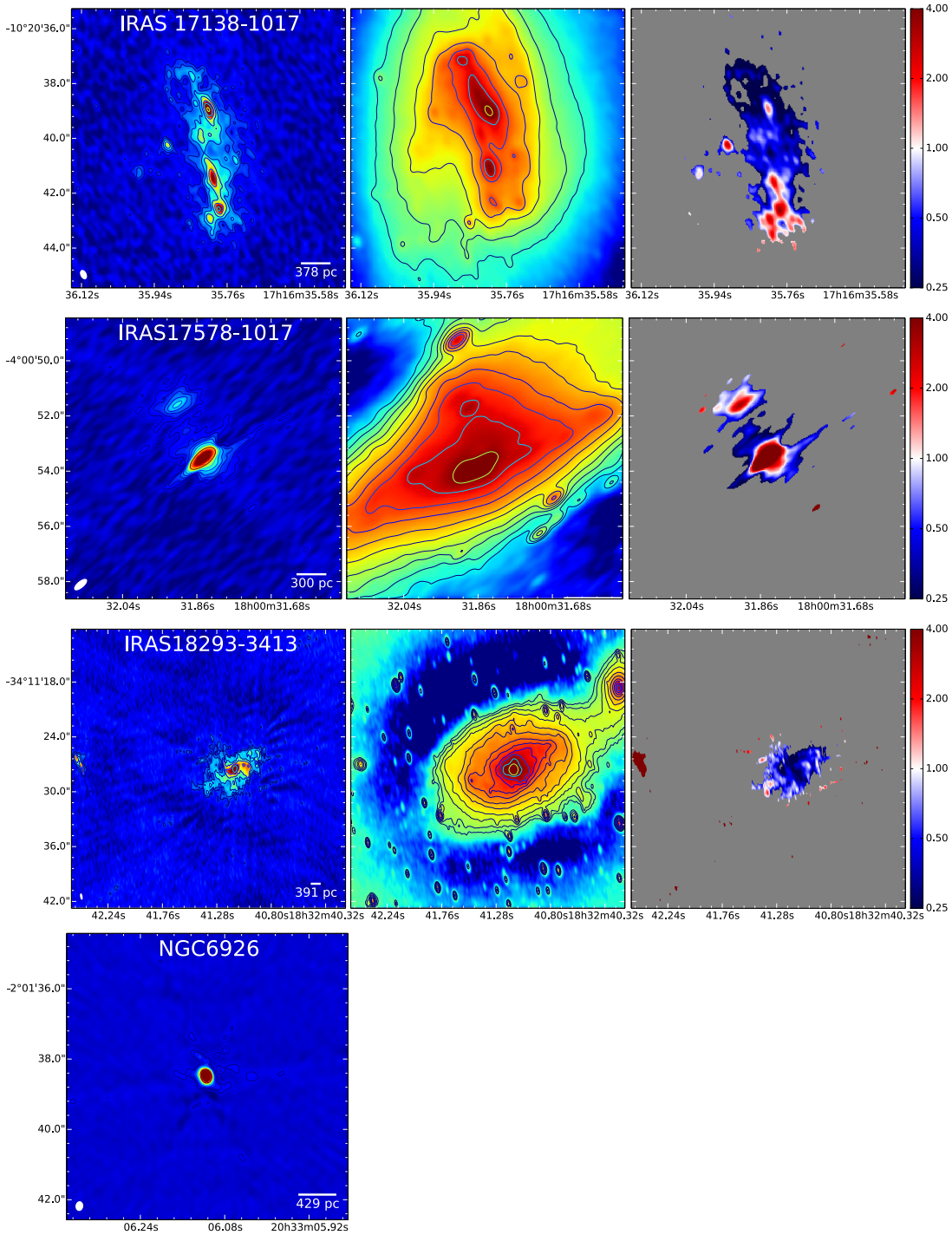

Figure 4.5: Radio and near-IR comparison of our sample - *Continued.*

Spitzer images of IRAS 16516-0948. It is clear from the figure that at increasing wavelength the infrared peak is shifting its position towards the west. The surroundings of this galaxy present enough compact sources to ensure unequivocal relative astrometry. The shift in the peak of the 8.0 μm with respect to the 3.6 μm peak is $\sim 5''$ The radio contours correlate well with the peak at 8.0 μm.

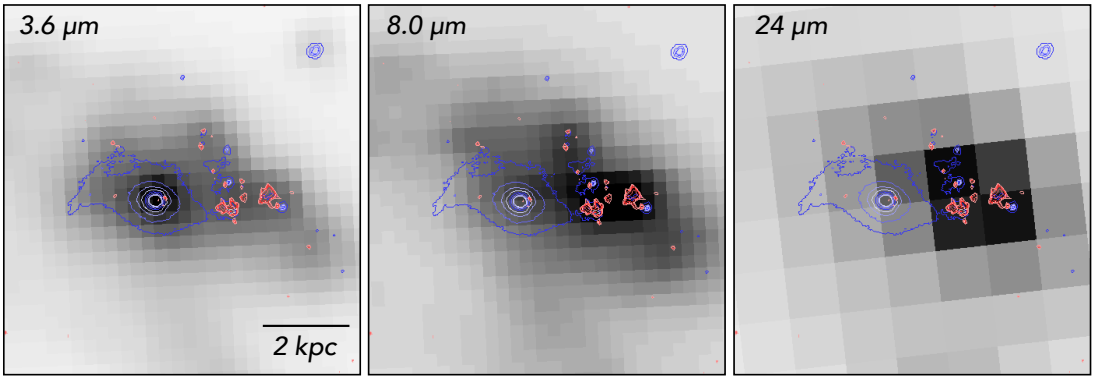

Figure 4.6: Near-IR and radio contours of IRAS 16516-0948 overplotted on Spitzer images - Left: IRAC 3.6 μm. Middle: IRAC 8.0 μm. Right: MIPS 24 μm We have overplotted our near-IR K-band (blue) and radio X-band (red) contours. North is up, east is left. Note how the peak IR emission clearly shifts to the west as wavelength increases.

The case of IRAS 16516-0948 is rare, but not unique among (U)LIRGs: a clear example is the merger II Zw 096 ($\log(L_{\rm IR}/L_{\odot}) = 11.94$), where 80% of its total IR luminosity comes from a compact optical-invisible source $\sim 5''$ away from the optical peak (see Fig. 2 in Inami *et al.*, 2010), and can have a SFR density up to $780 M_{\odot}\,{\rm yr}^{-1}\,{\rm kpc}^{-2}$. As in IRAS 16516-0948, radio observations from II Zw 096 correlates well with the MIPS peak, suggesting that in the region with the intense mid-IR and radio emission intense star formation is occurring. Further examples are IC 1623, ESO 593-IG008, IRAS 14348-1447 or the spiral galaxy NGC 5257 (see Fig. 4.7).

Haan *et al.* (2011) suggested an explanation for this phenomenon: these galaxies are possibly not yet relaxed with off-nuclear starburst and/or strong shocks, with the off-nuclear emission being associated with spiral arms, a possible secondary nucleus or the region between the merging nuclei. The sample by Haan *et al.* (2011) contains 73 LIRGs from the GOALS sample, and find off-nuclear mid-IR emission in six of them ($\sim 9.5\%$). A single case in our sample of 11 LIRGs agrees with this proportion.

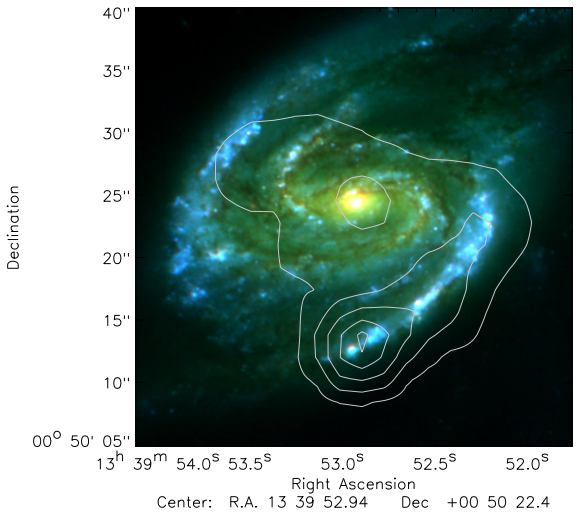

Figure 4.7: Color composite image of NGC 5257 - The color image is a composite of H-band (red), I-band (green), and B-band(blue). Contours correspond to MIPS 24 μm. From Haan *et al.* (2011).

4.4.3 Spectral behavior

Although our sample was observed in a single radio band (3.6 cm), the VLA X-band receivers have enough bandwidth to allow us to obtain an approximate spectral index, α.

Given the large bandwidth of our 3.6 cm radio data (2 GHz), we imaged our sources using multiscale multifrequency synthesis (`mode = mfs` within *CASA*; see Rau & Cornwell, 2011), which models the wide-band sky brightness as a linear combination of Gaussian-like functions whose amplitudes follow a Taylor-polynomial in frequency. The task performs a Taylor expansion to the second order (`nterms = 2`) of the function:

$$I_{\nu}^{\mathrm{sky}} = I_{\nu_0}^{\mathrm{sky}} \left(\frac{\nu}{\nu_0} \right)^{\alpha}, \tag{4.1}$$

where I^{sky} is the multiscale image, ν_0 is the reference frequency (in our case $\nu_0 = 8.459$ GHz), and α is the spectral index.

The two output images are the two first coefficients of the expansion, i.e.:

$$I_0 = I_{\nu_0} \qquad\qquad I_1 = I_{\nu_0}\alpha. \tag{4.2}$$

We then obtained the radio spectral index map of each source simply with the ratio I_1/I_0.

An alternative way to obtain a spectral index map is to image separately the external chunks of the band (e.g., one image from 8.0 to 8.5 GHz and another from 9.5 to 10.0 GHz), and then obtain α directly from equation 4.1. This method has two drawbacks:

1. *The drop in sensitivity:* in case we consider the external 512 MHz chunks of the band to create the images, their sensitivity would decrease by a factor of 4 compared to the original 2 GHz image.

2. *The short frequency separation:* even if the sensitivity in the side-band images is enough, the frequency separation in logarithmic units of both sub-bands ($\sim$ 0.07 dex) is too small to precisely determine a two-point spectral index.

Figure 4.8 shows the spectral index maps of the sources, and Table 4.3 quotes the average spectral indices above 10σ, to ensure robustness in the spectral index calculation. We note that the signal-to-noise ratio of the radio image of IRAS 16516-0948 is not enough to create a reliable spectral index map, since only a few pixels are above the quoted 10σ threshold.

Our reported values for the spectral indices are consistent with those found in the literature, e.g., the faint northwest component in NGC 6240, for which we obtain $\alpha = -1.2$ ($\alpha = -1.1$ according to Colbert *et al.*, 1994), or $\alpha = -0.68$ in IC 883 ($\alpha = -0.67$, Murphy, 2013).

We find that, with the exception of NGC 3690W and IC 883, those sources with a steeper spectral index (e.g., $\alpha < -0.8$) show extended diffuse emission. Murphy *et al.* (2013) studied a sample of 36 compact starbursts finding the same trend. This can be explained with radio emission arising from radio continuum bridges and tidal tails, result of the interactions, which does not have a direct stellar origin; instead, its emission is due to relativistic electrons cooling down in those regions and producing the steep spectrum.

We do not find a correlation between the spectral index maps and the emission ratios shown in Figure 4.5. However, the spectral index values obtained for IRAS 18293-3413 are significantly different compared to the rest of the sources, with extremely steep α values for a starburst galaxy.

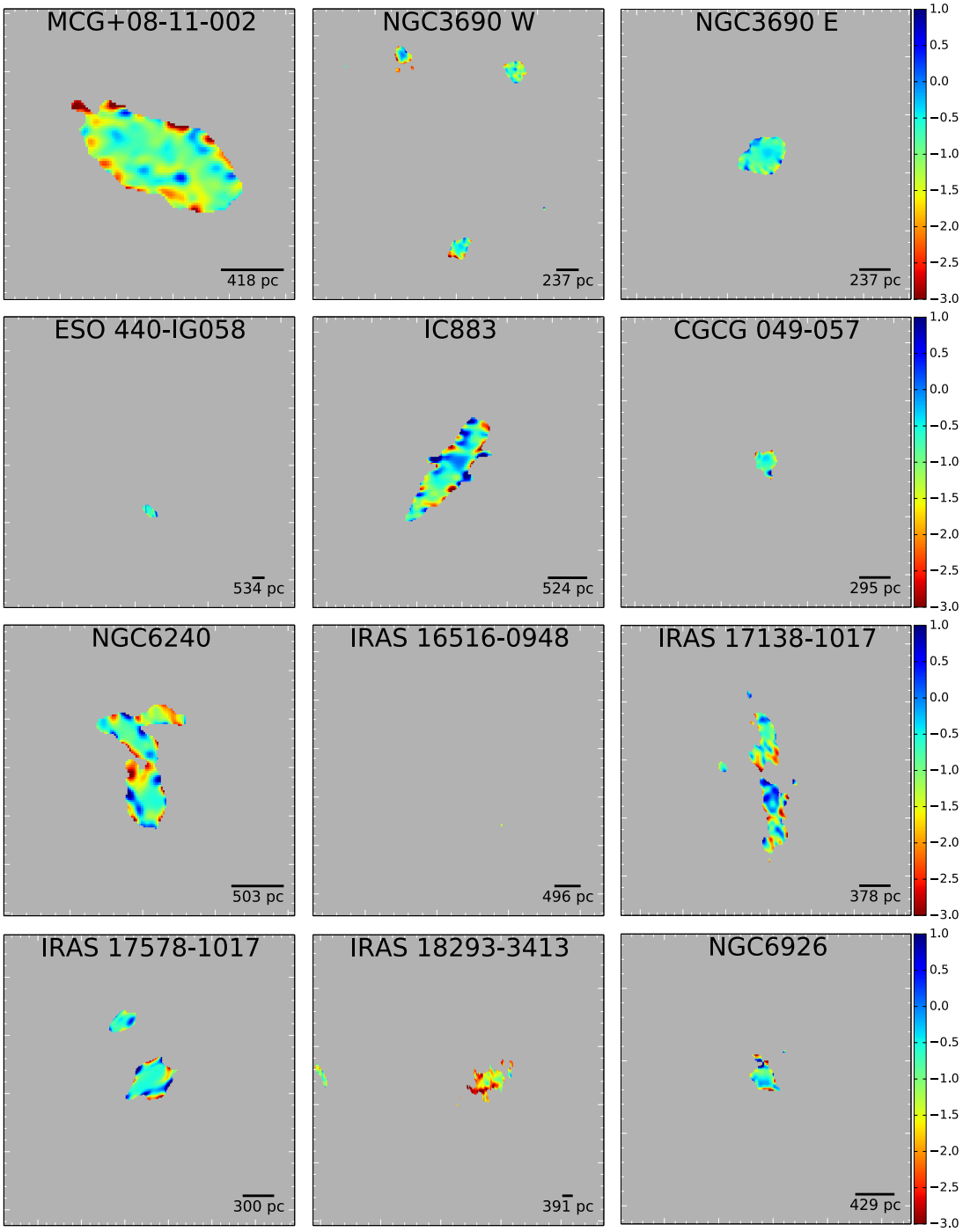

Figure 4.8: Spectral index maps of our sample - We have masked the maps in any point with a flux density below 10σ to ensure the reliability of the spectral indices. The used color scale is consistent for all the plots. See main text for details on the obtention of these maps.

Table 4.3: Average Spectral indices

Name	Average α
MCG+08-11-002	-1.09 ± 0.58
NGC 3690W	-1.01 ± 0.64
NGC 3690E	-0.65 ± 0.35
ESO 440-IG058	-0.60 ± 0.36
IC 883	-0.68 ± 0.90
CGCG 049-057	-0.78 ± 0.54
NGC 6240	-0.99 ± 0.76
IRAS 16516-0948	...
IRAS 17138-1017	-0.85 ± 0.80
IRAS 17578-0400	-0.64 ± 0.70
IRAS 18293-3413	-1.73 ± 0.70
NGC 6926	-0.76 ± 1.00

Note. — The spectral index values were obtained clipping the spectral index maps where the 3.6 cm flux is below 7 × rms, and then averaging the spectral index for every pixel. The quoted uncertainties correspond to the standard deviation of the individual (pixel) spectral indices, and are thus a measurement of the uniformity of the spectral index across the region.

4.4.4 SED modeling and AGN contribution

As we did for NGC 1614 in Chapter 3, we have modeled the near-IR to sub-millimeter SED for the sources in our sample. We combined the starburst models from Efstathiou & Siebenmorgen (2009) with the AGN models from Efstathiou *et al.* (2013), The modeling also takes into account galactic disc geometry (Efstathiou & Siebenmorgen, 2014, *in prep.*). Starlight is modeled following Bruzual & Charlot (2003) prescriptions with additional extinction, while cirrus models come from Efstathiou & Siebenmorgen (2009).

We obtained the SED points from public data through the VizieR photometry tool. Additionally we included the *Spitzer* IRS spectra. So far, have been able to obtain satisfactory models for six out of our twelve sources. The model fits are shown in Figure 4.9, and the parameters obtained from those models are quoted in Table 4.4. From the six fitted sources, we found two of them to be best modeled without any AGN contribution, i.e., pure starbursts (MCG+08-11-002 and IRAS 16516-0948). According to our models, the older starburst corresponds to MCG+08-11-002 with $\sim$ 48 Myr, while the youngest one is NGC 6926 with only $\sim$ 8 Myr. Two of the sources show a high CCSN rate: IC 883 with 0.64 SN yr^{-1}, compatible with previous studies ($\nu_{\rm CCSN} = 1.1^{+1.3}_{-0.6}$, Romero-Cañizales *et al.*, 2012), and IRAS 18293-3413 which present a rate of 0.81 SN yr^{-1}. Together with its controversy on its merger stage and its extremely steep spectrum ($\alpha = -1.73 \pm 0.70$), this makes IRAS 18293-3413 an interesting case, likely hosting a very wealthy starburst.

There are a number of AGN indicators in the mid-IR range of the spectrum. It is possible to compare the results obtained from the SED model fits with these mid-IR indicators. In particular, we focus on the 6.2 μm polycyclic aromatic hydrocarbon (PAH) equivalent width (EW), and in the 14.3 μm [Ne V] over 12.8 μm [Ne II] and 25.9 μm [O IV] over 12.8 μm [Ne II] line ratios.

Several PAH EW lines can be used to estimate the presence and contribution of AGNs. In particular, the feature at 6.2 μm has the advantage of not being blended with other PAH features and is less affected by silicate absorption (Stierwalt *et al.*, 2013). Pure SB galaxies have a 6.2 μm PAH EW with values between 0.5 and 0.7 μm (Brandl *et al.*, 2006), while smaller values are usually indicative of an excess of hot dust due to the presence of an AGN (e.g., Genzel *et al.*, 1998; Sturm *et al.*, 2000; Wu *et al.*, 2009).

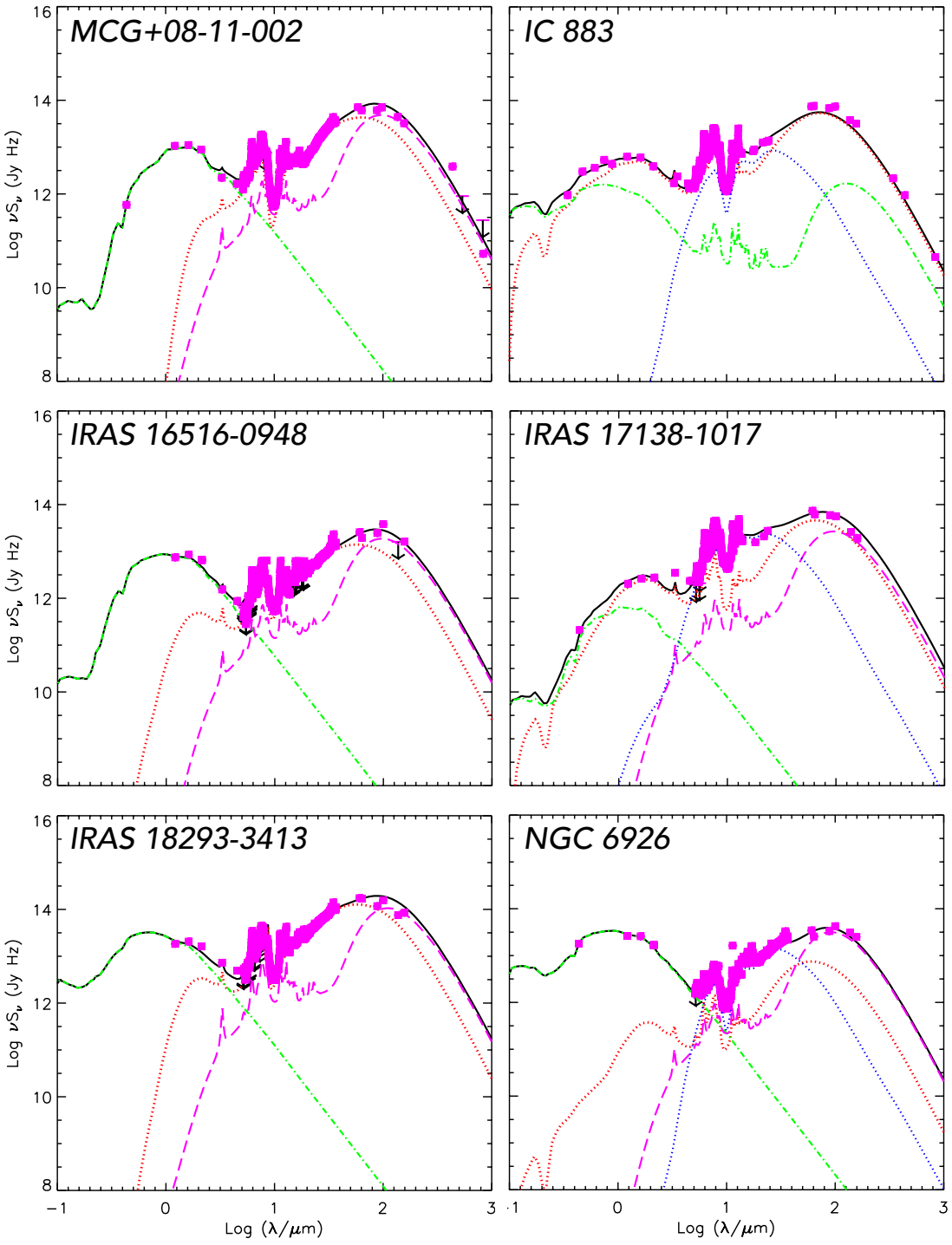

Figure 4.9: SED fitting for six sources from our sample - Pink points are the fitted points. Lines show the overall fit (solid black), the starburst contribution (dotted red), the AGN contribution (dotted blue), the host galaxy contribution (dashed-dotted green),and the cirrus spectra (dashed magenta). An SED fitting for the two components of Arp 299 can be found in Mattila *et al.* (2012). See main text for details.

Table 4.4: SED model fitting parameters

Name	$L_{\rm tot}$	$L_{\rm SB}$	$L_{\rm AGN}$	$\rm SFR_{max}$	$\rm SFR_{mean}$	$\rm t_{exp}$	$\rm Age_{SB}$	$\nu_{\rm CCSN}$
	$(10^{11}L_{\odot})$	$(10^{11}L_{\odot})$	$(10^{11}L_{\odot})$	$(M_{\odot}\,\rm yr^{-1})$	$(M_{\odot}\,\rm yr^{-1})$	(Myr)	(Myr)	$(\rm SN\,yr^{-1})$
(1)	(2)	(3)	(4)	(5)	(6)	(7)	(8)	(9)
MCG+08-11-002	2.52	1.24	0	19.1	15.2	100.0	47.9	0.14
IC 883	3.21	2.33	0.74	709.3	96.3	4.7	34.3	0.64
IRAS 16516-0948	1.52	0.61	0	350.3	27.2	2.1	27.1	0.16
IRAS 17138-1017	1.73	1.03	0.20	272.1	29.8	1.0	9.1	0.10
IRAS 18293-3413	6.33	3.44	0	1333.4	141.6	2.4	22.4	0.81
NGC 6926	3.67	0.21	1.63	43.2	5.6	1.0	7.7	0.02

Note. — (1) Source name; (2) Total bolometric luminosity; (3) Starburst luminosity; (4) AGN luminosity; (5) Maximum star formation rate; (6) Star formation rate averaged over the SB age; (7) e-folding time of the SB; (8) SB age; (9) Core-collapse supernova rate.

Table 4.5: Mid-IR AGN indicators

Name	6.2 μm PAH EW (μm)	12.8 μm [Ne II] (10^{-17} W m^{-2})	14.3 μm [Ne V] (10^{-17} W m^{-2})	25.9 μm [O IV] (10^{-17} W m^{-2})
MCG+08-11-002	0.56 ± 0.01	67.3 ± 0.6	< 0.8	1.7 ± 0.4
NGC 3690W	0.12 ± 0.02	103.8 ± 2.7	< 3.9	28.9 ± 3.8
NGC 3690E	0.38 ± 0.03	237.4 ± 2.7	< 4.7	16.1 ± 14.3
ESO 440-IG058	0.66 ± 0.01	48.9 ± 0.4	< 1.0	1.3 ± 0.5
IC 883	0.62 ± 0.01	117.6 ± 1.0	1.6 ± 0.1	6.9 ± 1.4
CGCG 049-057	0.51 ± 0.04	7.3 ± 0.2	< 0.1	< 0.2
NGC 6240	0.35 ± 0.01	177.1 ± 0.6	3.4 ± 0.2	22.1 ± 2.8
IRAS 16516-0948	0.69 ± 0.01	27.4 ± 0.3	< 0.3	1.2 ± 0.3
IRAS 17138-1017	0.68 ± 0.01	92.2 ± 1.4	< 1.0	< 7.9
IRAS 17578-0400	0.68 ± 0.01	46.1 ± 0.7	< 1.1	< 2.9
IRAS 18293-3413	0.63 ± 0.01	303.5 ± 2.3	< 2.7	7.4 ± 1.0
NGC 6926	0.37 ± 0.01	7.3 ± 0.1	1.3 ± 0.1	4.6 ± 0.2

Note. — The PAH equivalent width at 6.2 μm were obtained from Stierwalt *et al.* (2013), while the line fluxes come from Inami *et al.* (2013). We quote upper limits for non-detections.

High-ionization lines in the mid-IR (e.g., [Ne II], [Ne III], [Ne V], [O IV]) are also often used as tracers of AGN activity (e.g., Genzel *et al.*, 1998; Armus *et al.*, 2007; Pereira-Santaella *et al.*, 2010), although some of these lines can be produced, with lower luminosities, in supernova remnants (Oliva *et al.*, 1999).

We obtained the 6.2 μm EW PAH for our sample from Stierwalt *et al.* (2013), while mid-IR line fluxes were taken from Inami *et al.* (2013). Table 4.5 shows these mid-IR indicators for our sample, where upper limits are quoted for non-detections.

We have plotted these indicators together in Fig. 4.10 and Fig. 4.11, as done before by other authors (Armus *et al.*, 2007; Petric *et al.*, 2011; Vardoulaki *et al.*, 2014). In those figures we have plotted the sources from our sample, together with two comparative samples: one of AGN dominated systems (Weedman *et al.*, 2005), and other formed by SB dominated galaxies (Brandl *et al.*, 2006).

Two of the galaxies in our sample (NGC 3690W and NGC 6926) clearly diverge from the rest of the SB dominated galaxies in the [Ne V] / [Ne II] vs PAH EW diagram and two more (NGC 6240 and NGC 3690E show a slight shift (see Fig. 4.10), which is more clear in the [O IV] / [Ne II] vs PAH EW diagram shown in Fig. 4.11 The results shown by the mid-IR diagnostics are in good agreement with our model fits. In particular, NGC 6926 is clearly AGN dominated. With respect to NGC 3690W, Mattila *et al.*

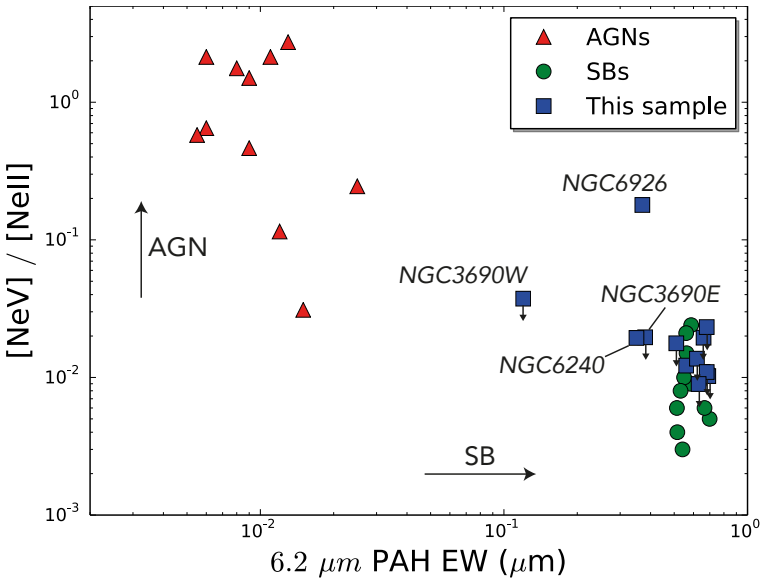

Figure 4.10: [Ne V]/[Ne II] against 6.2 μm PAH EW - Our sample is plotted with blue squares. For comparison, we have also plotted a sample of AGN dominated galaxies (red triangles; from Weedman *et al.*, 2005), and a sample of SB dominated sources (green circles; from Brandl *et al.*, 2006).

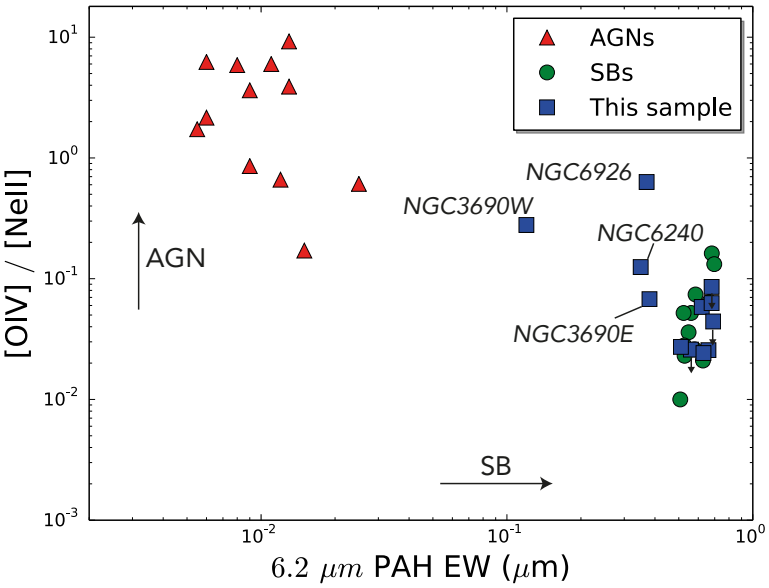

Figure 4.11: [O IV]/[Ne II] against 6.2 μm PAH EW - Color codes and samples are the same as in Fig. 4.10. Although with a lower ionization potential than [Ne V], [O IV] is detected in a larger number of sources.

(2012) modeled its SED and found an important AGN contribution, compatible with the mid-IR diagnostics and previous observations (e.g., Ballo *et al.*, 2004).

4.4.5 Summary

1. We have compared the radio (3.6 cm) and near-IR (2.2 μm) emission of the central kpc region of a sample of 11 LIRGs. Despite a general correlation, there are significant differences in the morphology and relative contributions. In general, due to the large range of ages with a significant contribution to the near-IR, it is not possible to date the regions without further spectral or photometric information. Furthermore, very high extinction values can partially hinder the near-IR emission, adding degeneracy to an age estimation based on both radio and near-IR data.

2. Based on our images, we have found an off-nuclear starburst region in IRAS 16516-0948, found in $\sim 9.5\%$ of LIRGs, and likely triggered during the merging phase.

3. Using our wide-band radio images, we have obtained spectral index maps, showing typical average values for LIRGs, with the exception of IRAS 18293-3413, which presents an anomalous spectral index ($\alpha = -1.73$). Observations at other band with similar resolution are needed to confirm such a steep spectral index and study the possible causes.

4. We have modeled the complete SED of six of the sources in our sample with a combination of starburst and AGN models to derive their ages, supernova rates, and AGN contribution. We found our results to be compatible with mid-IR AGN diagnostics. We also found a very high CCSN rate in IRAS 18293-3413. This rate and its extremely steep spectrum justifies further observations.

5. From the sources modeled, we have found three to be pure starbursts (MCG+08-11-002, IRAS 16516-0948, and IRAS 18293-3413), two have a moderate AGN contribution (IC 883 and IRAS 17138-1017), and one source (NGC 6926) exhibits a very strong AGN contribution with respect to the starburst emission.

Sailors on a becalmed sea, we sense the stirring of a breeze.

Carl Sagan

5

Massive star formation in the prolific LIRG Arp 299

Partially based on the results published in Bondi et al. *(2012), Herrero-Illana* et al. *(2012b), Romero-Cañizales, Herrero-Illana et al. (2014), and Kankare* et al. *(2014).*

In previous chapters I have discussed local LIRGs and ULIRGs considering both their overall structure (Chapter 2) and their inner-kiloparsec region (Chapters 3 and 4). It is extremely useful in terms of discriminating the nature of the compact sources at the galaxy nuclear region, though, to go one step further and investigate the properties of these objects at very high resolution, resolving their innermost regions. In this chapter, I present observations of the LIRG Arp 299 that led to the detection and classification of a new SNe in the outskirts of one of its nuclei. I introduce as well very long baseline interferometry (VLBI) radio observations aimed at resolving Arp 299 brightest nucleus (Arp 299-A), showing the power of this tool to study the

starburst/AGN connection.

5.1 Radio emission from core-collapse supernovae

The most common supernovae classification is based on their optical spectrum (Minkowski, 1941). Type I SNe show broad emission features and no signs of hydrogen in their spectra, while Type II SNe have Balmer emission lines that dominate their spectra. Further sub-classification of Type I SNe was made decades later by Harkness & Wheeler (1990) based on the presence of two spectral features: in case a Si feature is detected at 6355 Å they are designated Type Ia; otherwise we call them Type Ib SNe, if they show a He I line at 5876 Å, or Type Ic, if they don't.

There is yet another sub-classification among Type II SNe. Based on the shape of their light curve (Barbon *et al.*, 1979), they can be linear (Type IIL) or show a plateau (Type IIP). Their spectra can also show narrow emission lines (Type IIn, Schlegel, 1990). And finally, Type IIb are a transition class between Type II and Type Ib SNe.

Physically, Type Ia SNe have a thermonuclear origin, while the rest, namely Ib, Ic and II, are core-collapse supernovae (CCSNe), i.e., produced by the collapse of massive stars ($M \gtrsim 8M_{\odot}$) once they run out of nuclear fuel and their core can no longer compensate their own gravitational field. Typical kinetic energies released in these processes are of the order of $\sim 10^{51}\,\mathrm{erg\,s^{-1}}$ (e.g., Smartt, 2009). Different CCSNe subtypes are indicative of differences in their progenitors and evolution, and they have different prevalence as shown in Figure 5.1

During the precursory phase of a CCSNe, the progenitor stars ejects mass via stellar winds. If the CSM is dense enough, once the SN event has occurred, the interaction between the medium and the ejecta results in a shock where circumstellar non-thermal synchrotron radio emission is produced (Chevalier, 1982a,b), as detected for all CCSN types. On the contrary, Type Ia SNe have not been detected at radio wavelengths so far (e.g., Panagia *et al.*, 2006; Perez-Torres *et al.*, 2014). This fact has been used to distinguish the nature of SNe when spectroscopic identification was not possible (e.g., Pérez-Torres *et al.*, 2007, 2009a).

Among CCSNe, it is possible to characterize them by modeling their light curve. Assuming no internal absorption and uniformity in the external absorbers, the flux

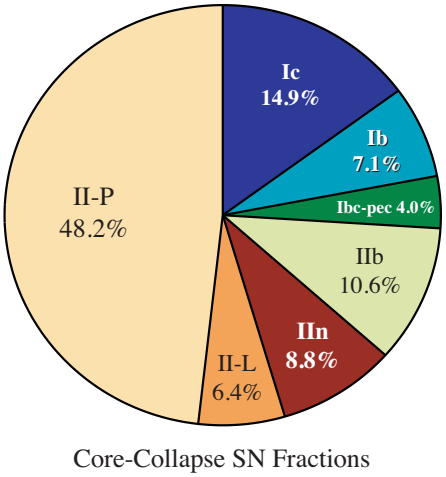

Figure 5.1: CCSN fractions - Relative fractions of CCSN types in a volume-limited sample from the Lick Observatory Supernovae Search (LOSS). From Smith *et al.* (2011).

density at a given frequency, ν, varies with time following the next relation (Weiler *et al.*, 2002):

$$S_\nu(t) = K_1 \left(\frac{\nu}{5\,\mathrm{GHz}}\right)^\alpha \left(\frac{t-t_0}{1\,\mathrm{day}}\right)^\beta e^{-\tau_\nu}, \tag{5.1}$$

where K_1 is a constant, t_0 is the SN explosion time, α is the spectral index in the optically thin phase, β is a time dependence parameter, and τ_ν is the optical depth due to the external absorption.

In the very obscured domain of (U)LIRGs, optical/IR spectroscopically classification is a challenging task, and not always possible. A radio modeling of the light curve is then a powerful tool to identify and categorize SNe. However, given their stochastic nature, any blind search will need to balance both a fine angular resolution and a reasonably large field of view. As shown below, the interferometer e-MERLIN fulfills both conditions, and is an excellent instrument for such kind of studies in the dusty environments of (U)LIRGs.

5.2 e-MERLIN & LIRGI

The electronic Multi-Element Remotely Linked Interferometry Network (e-MERLIN) is an array formed by seven dishes across England. It consists of five different 25 m antennas, one of 32 m of diameter, and one of 76 m (see Fig. 5.2), with a maximum

Table 5.1: e-MERLIN capabilities summary

Receiver	Frequency range (GHz)	Bandwidth (GHz)	Resolution (mas)	Field of View (arcmin)
L-band	1.3 — 1.7	0.4	150	30
C-band	4.0 — 8.0	2.0	40	7
K-band	22.0 — 24.0	2.0	12	2

baseline of 217 km. e-MERLIN is an upgrade of a previous array (MERLIN), which drastically improved its receivers, increasing its sensitivity by a factor of between 10 and 30, and the link between stations. Table 5.1 shows the current capabilities for the three available bands. The large baselines in the array make the angular resolution $\sim$ 9 times finer than the one achieved with the Karl G. Jansky Very Large Array (VLA) at its most extended configuration at the same observing frequency. There are tentative plans to expand e-MERLIN and eventually integrate it into the European VLBI Network (Kloeckner *et al.*, 2011).

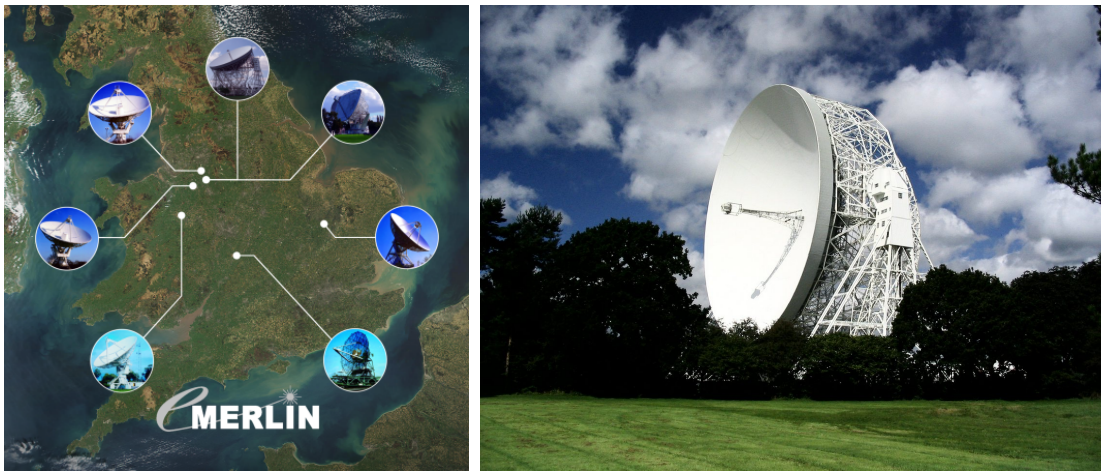

Figure 5.2: e-MERLIN interferometer - Left: The seven dishes from e-MERLIN are, clockwise from north, Jodrell Bank Lovell, Jodrell Bank Mark II, Cambridge, Defford, Knockin, Darnhall and Pickmere. Right: Lovell Telescope, with 76.2 m in diameter, is the third largest fully steerable radio telescope in the world. Credit: Jodrell Bank Centre for Astrophysics, University of Manchester (e-MERLIN image) & Anthony Holloway, Jodrell Bank Centre for Astrophysics (Lovell picture).

With the idea of addressing cutting-edge questions in Astronomy and provide a

legacy to the community, e-MERLIN approved a list of 12 large legacy projects, one of which is the *Luminous Infrared Galaxy Inventory*[1] (LIRGI; PIs: J. Conway & M.Á. Pérez-Torres). LIRGI aims at characterizing 42 of the most luminous northern (U)LIRGs selected from the IRAS Revised Bright Galaxy Sample (Sanders *et al.*, 2003). LIRGI is a declination ($\delta > 8°$), distance ($D < 260\,\mathrm{Mpc}$), and luminosity ($\log(L_{\mathrm{IR}}/L_{\odot}) > 11.4$) selected sample, and is a sub-sample of the NASA Great Observatory All-sky LIRG Survey (GOALS; Armus *et al.*, 2009), already introduced in Chapter 2).

The idea behind LIRGI, which was granted 353 hours of observation at both L- and C-band, is to establish a phenomenological sequence and timescale for the evolution of a nuclear starburst for a statistically significant sample of (U)LIRGs in the local Universe. LIRGI specific goals are: (i) to map the diffuse radio emission to provide a reliable estimation of starburst size and structure; (ii) to trace the free-free absorption with high resolution; (iii) to perform polarization and rotation measure observations to constrain 3D magnetic field strengths; (iv) to study several molecular transitions (H I, OH, and H_2CO) at high resolution to estimate dynamical masses and constrain spatial variations in chemistry and physical conditions; and (v) to produce a complete atlas of uniform quality images of legacy value for the whole astrophysical community.

5.3 A supernova detection in Arp 299 LIRGI data

Monitoring programs have proved to be an useful tool to determine the physical properties of Arp 299. Romero-Cañizales *et al.* (2011) analyzed X-band VLA observations spanning ~ 11 years and studied the variability of the compact sources, deriving a limit for the CCSN rate compatible with previous IR studies (Alonso-Herrero *et al.*, 2000; Neff *et al.*, 2004).

Due to technical issues affecting e-MERLIN performance, LIRGI observations have just recently (summer 2014) started to fulfill the sensitivity requirements of the project. Nonetheless, several commissioning observations were carried out in the last four years, in whose reduction I have been actively involved. In particular, Figure 5.3 shows an e-MERLIN LIRGI image of Arp 299, from data taken during the commissioning phase of the instrument on 4 and 5 April 2011 and reduced during my stay in the Jodrell

[1] `http://lirgi.iaa.es`

Bank Centre for Astrophysics in Manchester, in Fall 2011. Table 5.2 shows the flux densities for each component.

Arp 299 has been extensively introduced in Chapter 4. As it has been pointed out, it is formed by two main (A and B) nuclei and two secondary (C and C′) ones. The remaining compact structure, D, is believed to be a background quasar, unrelated to the system (Ulvestad, 2009). The southern emission from nucleus C′ observed in Fig. 5.3, however, is not part of the steady emission of the region, but happened to be the supernova 2010P (flux density of $585 \pm 69\,\mu$Jy), which exploded 540 days before the e-MERLIN observations, and whose discovery at near-IR wavelengths was reported in Mattila & Kankare (2010) and in Mattila *et al.* (2010). SN2010P was initially classified as a Type Ib SN (Ryder *et al.*, 2010) based on Nordic Optical Telescope (NOT) observations.

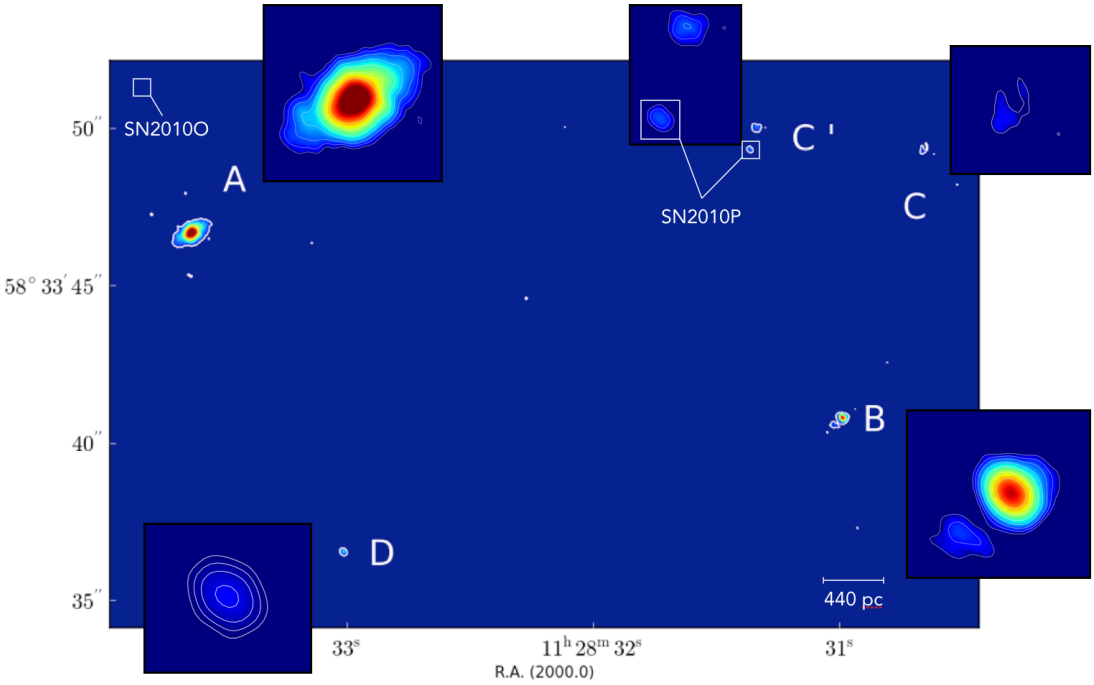

Figure 5.3: e-MERLIN commissioning data image of Arp 299 at C-band - Outer panels show a zoom to their closest region. This is one of the first images from e-MERLIN. The observations were done during the commissioning phase of LIRGI, on April $4^{\text{th}} - 5^{\text{th}}$, 2011. The total on-source time was ~ 25 hours, but intense data flagging was needed. The achieved off-source rms of the image is $39\,\mu$Jy beam^{-1} and the beam size $0.19'' \times 0.14''$.

Table 5.2: Arp 299 e-MERLIN flux densities at C-band

Source	Peak ($\mathrm{mJy\,beam^{-1}}$)	Integrated flux density (mJy)
A	14.43	61.48
B	8.52	9.33
C	0.34	0.37
C′	0.62	0.83
SN2010P	0.59	0.39
D	1.23	0.92

Note. — We measured the quoted integrated fluxes above 5 times the off-source rms of the image.

No radio counterpart was found with MERLIN observations between 29 January 2010 and 1 February 2010. However, we checked other images from our team and found a previous detection in data obtained with the VLA (program AP592; PI: M. Á. Pérez-Torres) in 15 June, 2011 at 8.459 GHz. The flux density of the VLA detected radio counterpart was $541 \pm 92\,\mu\mathrm{Jy\,beam^{-1}}$, which corresponds to an approximate luminosity of $1.3 \times 10^{27}\,\mathrm{erg\,s^{-1}\,Hz^{-1}}$ at the assumed distance to Arp 299 of 44.8 Mpc, and is located at $11^{\mathrm{h}}28^{\mathrm{m}}31^{\mathrm{s}}.362 + 58°33'49''.35$ (J2000) within one sigma of the position reported in (Mattila & Kankare, 2010). Our radio detection at 8.459 GHz, 521 days after the explosion (which happened on 10 January 2010), ruled out a Type Ib origin for SN2010P. Based on its radio luminosity and the optical classification, we initially suggested instead that the SN was a Type IIb with a slow evolution. This radio detection was reported in Herrero-Illana *et al.* (2012b).

Barely six days after the original near-IR detection of SN2010P, a new supernova was discovered at optical wavelengths (Newton *et al.*, 2010) in the outskirts of Arp 299-A. It was named SN2010O after confirmation. SN2010O exploded on 7 January 2010 (only three days before SN2010P), and was classified by Mattila *et al.* (2010) as a Type Ib based on a low-resolution optical spectrum from NOT. Despite several attempts to detect its radio emission, both early-time (18 days) and late-time (1 to 3 years after the explosion), SN2010O remains undetected at radio wavelengths. I show its location in Fig. 5.3.

We presented two studies of both SNe based on near-IR data (Kankare *et al.*, 2014), and on radio observations (Romero-Cañizales *et al.*, 2014), where we modeled the radio

light curve of SN2010P (see Figure 5.4) using data at four different radio bands and from 13 epochs, both from our team and from the archives. We found it to be consistent with a Type IIb supernova, as we had initially suggested, making SN2010P one of the only 12 Type IIb SNe detected at radio wavelengths so far. It is also the first radio SN detected in the outskirts of one of the bright radio nuclei of Arp 299, despite its intense radio monitoring. We note that while SN2010P lays close to Type IIL SNe in the luminosity vs time-to-peak diagram (see Fig. 5.5), the lack of strong hydrogen lines discards this nature. Regarding the SN2010O radio silence, we concluded that either it was an intrinsically weak SN, with a luminosity $L < 3\times^{26}\,\mathrm{erg\,s^{-1}\,Hz^{-1}}$ (see Fig. 5.5), or its radio emission was absorbed by the dense circumstellar medium (CSM) of its progenitor at early-time observations, and due to a fast-evolving nature compatible with a Type Ib, its short radio lifetime prevented its detection in our late-time radio observations.

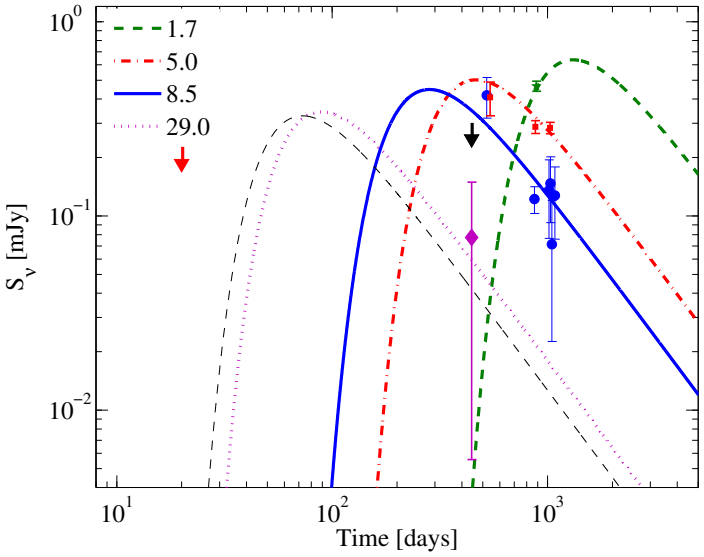

Figure 5.4: Parametrized radio light curve of SN2010P - Free-free absorption model at 1.7 GHz (green), 5.0 GHz (red), 8.5 GHz (blue) and 29.0 GHz (magenta). Downward arrows represent 3σ upper limits. The black dashed line is the predicted light curve at 36.0 GHz. From Romero-Cañizales *et al.* (2014).

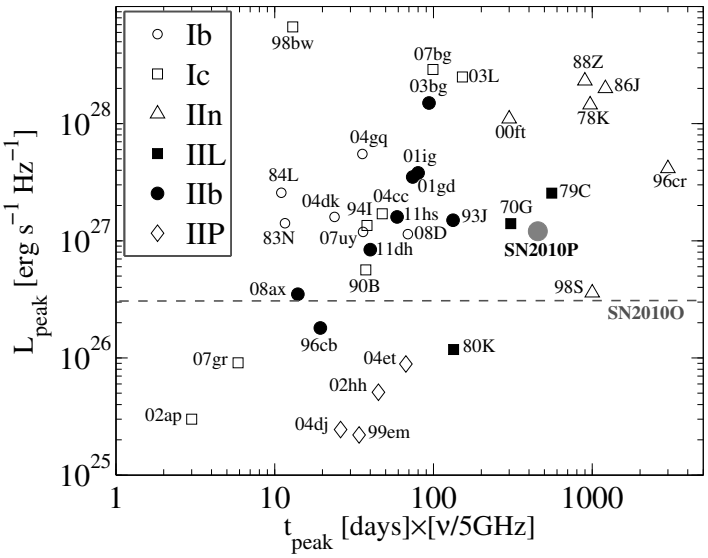

Figure 5.5: Peak monochromatic luminosity vs time to peak from explosion date - SN from different types are plotted together with SN2010P. The dashed line shows the upper luminosity limit for SN2010O. From Romero-Cañizales *et al.* (2014).

5.4 Digging deeper into Arp 299: Arp 299-A

The most prominent nucleus of Arp 299, Arp 299-A, responsible of $\sim 50\%$ of the far infrared luminosity of this LIRG (Charmandaris *et al.*, 2002), is also the most dust-enshrouded source in the system (Alonso-Herrero *et al.*, 2000), with visual extinction as high as $A_V \sim 40$ (Gallais *et al.*, 2004; Alonso-Herrero *et al.*, 2009). IR observations can solve partially the issue of obscuration, and indeed several studies have shed light on the unknowns of this galaxy (see, e.g., Alonso-Herrero *et al.*, 2009, 2013b; Anderson *et al.*, 2011). VLBI radio observations have two important characteristics: they are not affected by extinction, and allow for milliarcsecond angular resolution. Using this technique: first, a supernova factory was found buried in Arp 299-A (Neff *et al.*, 2004; Pérez-Torres *et al.*, 2009b; Ulvestad, 2009; Bondi *et al.*, 2012), and later, one of the discovered compact sources was identified as a low-luminosity AGN (Pérez-Torres *et al.*, 2010) based on its flat spectrum, variability, and radio to X-ray ratio (Terashima & Wilson, 2003).

Multi-epoch EVN monitoring observations of Arp 299-A have allowed us to study the nature and evolution of the compact sources detected in this system, and eventually constrain the CCSN rate of the system. In Bondi *et al.* (2012) we published the results

from 6 cm observations (PI: M. Á. Pérez-Torres) taken in April 2008 (experiment code RP009), December 2005 (RP014A), June 2009 (EP063B), December 2009 (RP014C), May 2010 (EP068A), and November 2010 (RP014D). We confirmed 25 compact sources above a 5σ threshold in the six-epoch average image (see Fig. 5.6), with at least two new exploding CCSNe in our 2.5 yr study, yielding a CCSN rate of $\nu_{\rm SN} \gtrsim 0.80^{+1.06}_{-0.52}\,{\rm SN\,yr^{-1}}$ and suggesting that most of the star formation in Arp 299-A is taking place in the central ~ 150 pc. Although most of our detected sources are SNe or SN remnants, we also found evidence of a microquasar.

Ulvestad (2009) reported as well SNe detections at 2.3 and 8.4 GHz using the VLBA. Although most of the sources were common to both studies, the faintness of these compact sources, together with their intrinsic variability and spectral indices, result in different number of detections for different frequencies and epochs (as shown in Fig. 5.7).

The distribution of the sources presented in Bondi *et al.* (2012), together with the additional detections by Ulvestad (2009, ; overplotted as red crosses in Fig. 5.6) are the basis of the next chapter.

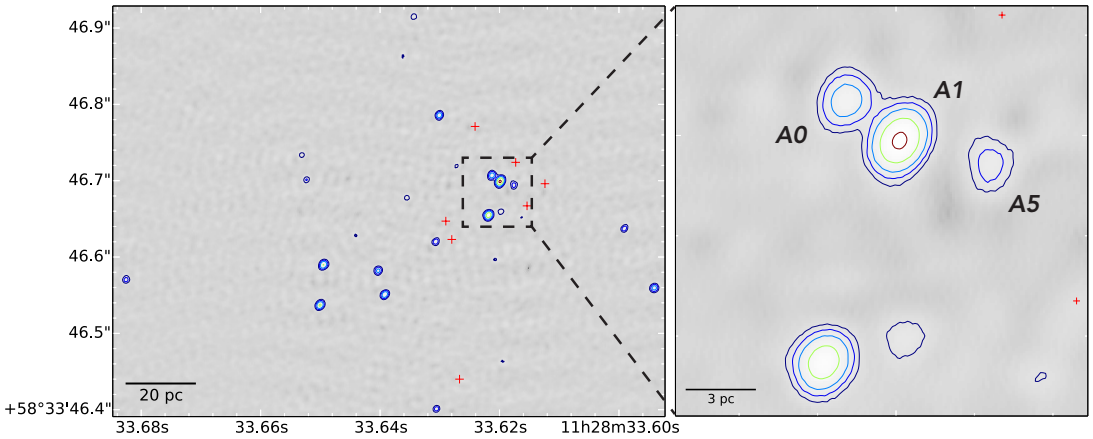

Figure 5.6: Arp 299-A EVN image stacking at 5 GHz - Beam size is 10×8 mas, PA $= -25°$. The noise of the image is $18.5\,\mu{\rm Jy\,beam^{-1}}$ and contours are plotted at $(5, 9, 15, 27, 45) \times$ rms. Red crosses indicate the position of the additional compact sources found by Ulvestad (2009) at 2.3 and 8.4 GHz. Right panel is a zoom to the image, showing the low-luminosity AGN (A1) and its jet (A5), and the closest supernova to the AGN (A0).

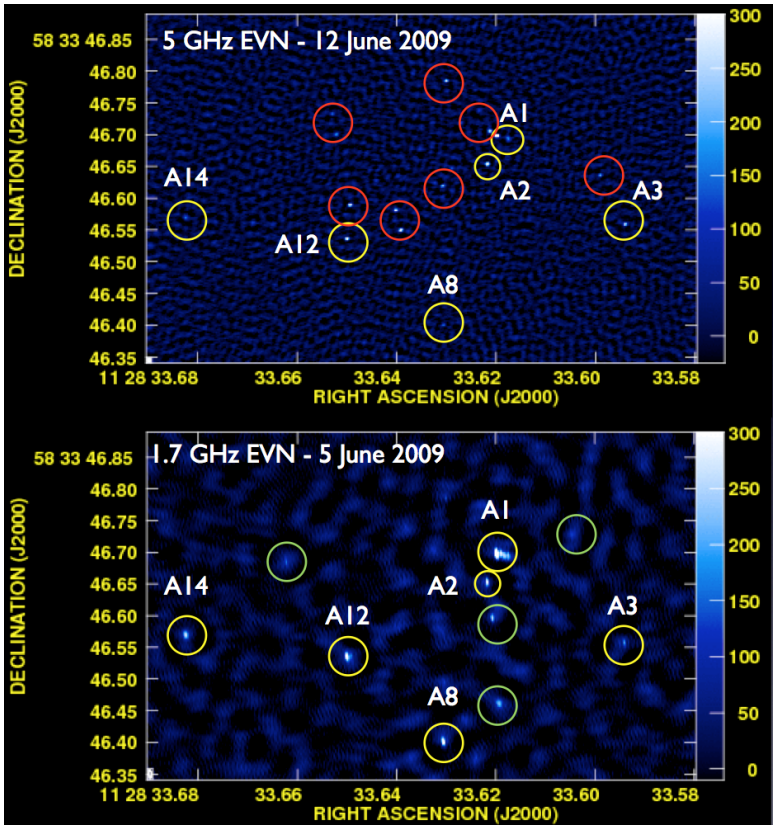

Figure 5.7: 1.7 and 5.0 GHz EVN observations of Arp 299-A - Red circles are plotted around detections only at 5.0 GHz, green circles are for 1.7 GHz detections, and yellow circles correspond to common detections at both bands.

If the Lord Almighty had consulted me before embarking upon Creation, I should have recommended something simpler.

Alfonso X of Castile
(attributed)

6

The core of LIRGs as traced by their radial distribution of supernovae

Based on the results published in Herrero-Illana et al. *(2012a).*

The study of (U)LIRGs at very high angular resolution using VLBI is a powerful tool to investigate the massive star formation processes triggered at nuclear scales (see Chapter 5 for the case of Arp 299-A). Indeed, Arp 299-A belongs to the exclusive group of galaxies where, so far, a supernova factory has been found in such scales. These supernova factories can be used to indirectly trace their nuclear physical properties. In this chapter, I present a study of the radial distribution of supernovae in the innermost regions of three of these galaxies: Arp 299-A, the ULIRG Arp 220, and the starburst galaxy M82, at slightly larger scales. As I will show, our results

vary significantly with respect to previous studies carried out at galactic scales, which we interpret as evidence for the presence of nuclear disks around the centers of these starburst-dominated galaxies.

6.1 The radial distribution of supernovae

The interaction between galaxies is assumed to provide large amounts of dense molecular gas that eventually reach the central regions of the galaxies, where they are responsible for triggering massive star formation and possibly accretion onto an SMBH (e.g., Di Matteo *et al.*, 2007). While interactions and bars seem to aid the transport of the molecular gas into the kiloparsec region of galaxies (e.g., Simkin *et al.*, 1980), it has been recognized that a major difficulty is in driving the gas from the kiloparsec region down to the central parsec, or parsecs, of (U)LIRGs, where a nuclear starburst and/or an active galactic nucleus (AGN) are expected to exist. Several mechanisms have been proposed to overcome this problem, including tidal torques driven by either stellar bars (Shlosman *et al.*, 1990) or major and minor mergers (Mihos & Hernquist, 1994, 1996), gas drag and dynamical friction in a dense nuclear star cluster (Norman & Scoville, 1988), or radiation drag (Umemura, 2001; Kawakatu & Umemura, 2002). However, not all the accumulated gas is expected to be accreted directly onto the putative SMBH, since the removal of the angular momentum of the gas is very inefficient (Umemura, 2001). The angular momentum that is not removed will then permit the accreted gas to form a reservoir, namely a nuclear disk in the central $\sim$100 pc around the AGN (e.g., Wada & Norman, 2002; Kawakatu & Wada, 2008, and references therein; see Fig. 6.1). Furthermore, if the gas in the nuclear starburst is dense enough, vigorous star formation is expected to occur, which can be detected via, e.g., high-angular resolution observations of recently exploded supernovae (e.g., in the LIRG Arp 299, as shown in Chapter 5, or in the ULIRG Arp 220 (Lonsdale *et al.*, 2006)). The nuclear starburst is also expected to affect the growth of the SMBH, since the radiation and/or supernova feedback caused by starbursts can eventually trigger the mass accretion onto a SMBH (e.g., Umemura *et al.*, 1997; Wada & Norman, 2002).

Kawakatu & Wada (2008) proposed an scenario for (U)LIRGs, where a nuclear disk is supported by the turbulent pressure of SNe. In their model, the turbulence

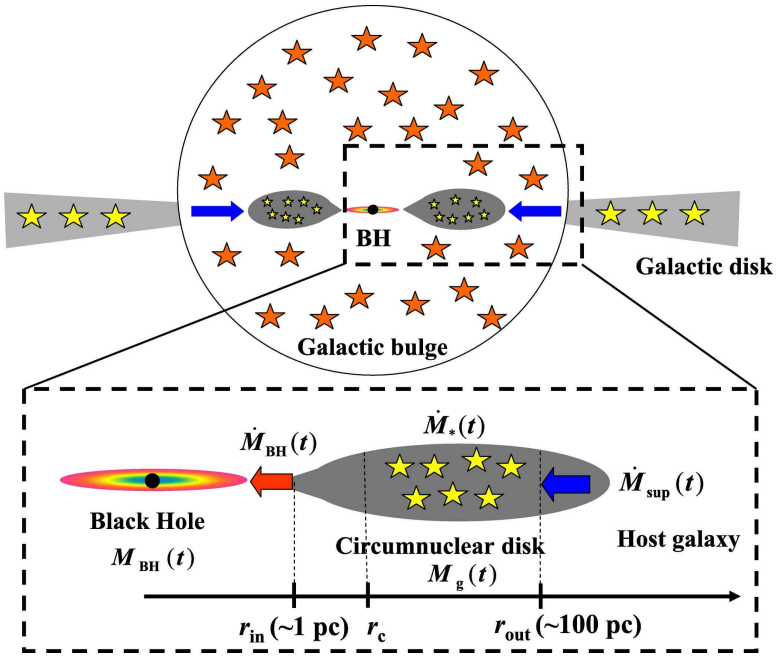

Figure 6.1: SMBH growth schematic diagram - The figure represents the model of a circumnuclear disk supported by the turbulent pressure via supernova explosions. $M_{\rm BH}$, $M_{\rm g}$, $\dot{M}_{\rm BH}$, $\dot{M}_*$ and $\dot{M}_{\rm sup}$ are the mass of the SMBH, the gas mass, the stellar mass, the BH growth rate, the star formation rate, and the mass supply rate from the host galaxy, respectively. From Kawakatu & Wada (2008).

due to supernova activity transports the angular momentum toward the central pc-scale region. One of the implications of the model developed by Kawakatu & Wada (2008) is that the BH growth rate depends on the spatial distribution of both young stars and SNe in the nuclear disk. However, the study of this spatial distribution is a challenging observational task for two main reasons. First, the huge column densities present in nuclear starbursts cause enormous extinction towards the central regions of (U)LIRGs at optical and infrared wavelengths, such that essentially no supernova would be detected at those wavelengths in the central few hundred parsecs of a (U)LIRG. Second, the enormous angular resolution needed to discern individual objects at the typical distances to (U)LIRGs ($\gtrsim 50\,\mathrm{Mpc}$) requires milliarcsecond angular resolution to resolve individual core-collapse supernovae (CCSNe) and/or supernova remnants (SNRs).

We have used high-angular radio observations from the literature, as well as data obtained by us, of three starburst galaxies in the local universe (M82, Arp 299-A, and Arp 220) to analyze the radial distribution of CCSNe/SNRs in their central few hundred parsecs, which may have strong implications for the (co)-evolution of AGN and (nuclear) starbursts in galaxies, in general, and in (U)LIRGs in particular. The complete study was published in Herrero-Illana *et al.* (2012a).

The radial distribution of SNe[1] on galactic scales has been thoroughly studied (see, e.g., Bartunov *et al.*, 1992; van den Bergh, 1997; Anderson & James, 2009; Hakobyan *et al.*, 2009). Optical observations have been very useful for this purpose, as dust extinction plays a minor role in the external regions of most galaxies. However, the dust-enshrouded environments of the nuclear regions in (U)LIRGs, as well as the need for milliarcsecond angular resolution to pinpoint individual SNe, have prevented this kind of studies in the central regions of local (U)LIRGs. Fortunately, both issues —obscuration and (angular) resolution— can be overcome by means of VLBI radio observations of the central regions of (U)LIRGs, since radio is dust-extinction free, and VLBI provides milliarcsecond angular resolution.

[1]For simplicity, I use the term SNe to denote both CCSNe and SNRs.

6.2 Methods

To derive the radial distribution of supernovae, our approach consisted in model fitting the surface density profile of CCSNe and SNR, by determining the number of sources in concentric rings around the center of the galaxy. For this purpose, we carried out a very similar data analysis to the one used by Hakobyan *et al.* (2009), hereafter H09.

The first step is to know how sources are distributed in the galactic disks. In Figure 6.2, I show a geometric scheme of a supernovae (symbolized by a star) in the disk of a galaxy, ideally an ellipse. In general, galactic disks are not facing us directly, hence, the apparent distance between two positions on the disk are projected distances. To de-project them, we need to know $\Delta\alpha$ and $\Delta\delta$, which are the angular distances we measure directly from our observations, the center of the disk to use as origin of coordinates and two parameters that define the orientation of the galactic disk: the position angle on the sky of the apparent major axis of the disk ellipse, PA, and the inclination angle between our line of sight and the polar axis, i. Both parameters have been derived from observations for hundred of thousands of objects and can be extracted from the *HyperLeda Database for physics of galaxies*[1].

To change then from our observing reference coordinate system N-E (north-east) to the U-V system, is enough to perform a rotation of the axes, i.e.,

$$U = \Delta\alpha \sin \mathrm{PA} + \Delta\delta \cos \mathrm{PA} \tag{6.1}$$

$$V = \Delta\alpha \cos \mathrm{PA} - \Delta\delta \sin \mathrm{PA}. \tag{6.2}$$

Then, the true radial distance of any point, namely a supernova, to the galactic center will be

$$R_{\mathrm{SN}} = \sqrt{U^2 + \left(\frac{V}{\cos i}\right)^2}. \tag{6.3}$$

Every source distance to the nuclei is then normalized to the host galaxy radius, considering it as the major axis at the isophotal level $25\,\mathrm{mag/arcsec}^2$ in Johnson B-band. Isophotal radii (R_{25}) were obtained also from the Hyperleda Database. Naming $\tilde{r}$ the normalized radii we have that

$$\tilde{r} = R_{\mathrm{SN}}/R_{25}. \tag{6.4}$$

[1] `http://leda.univ-lyon1.fr/`

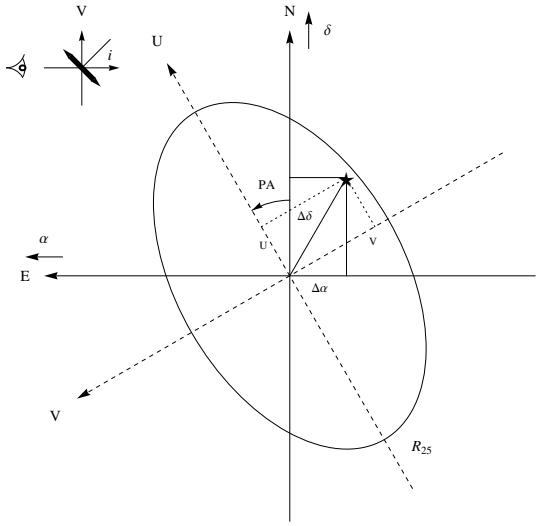

Figure 6.2: Location of a SN within its host galaxy - Both coordinate systems, our observation system N-E and the system U-V are shown. PA is the major position angle of the galaxy and i is the inclination of the galactic disk. R_{25} refers to the isophotal radius at the 25^{th} magnitude. From Hakobyan *et al.* (2009).

We then derived the surface density profile by determining the number of sources in concentric rings around the nucleus. For every ring of width $(\tilde{r}_{i+1} - \tilde{r}_i)$ we have then a surface density of

$$\frac{n_{\text{SN}}}{\pi(\tilde{r}_{i+1}^2 - \tilde{r}_i^2)}, \tag{6.5}$$

where n_{SN} is the number of supernovae in a certain ring.

We assume that the resulting distribution follows an exponential function of the form

$$\Sigma^{\text{SN}} = \Sigma_0^{\text{SN}} \exp\left(-\tilde{r}/\tilde{h}_{\text{SN}}\right), \tag{6.6}$$

where Σ_0^{SN} is the central surface density of sources, $\tilde{r}$ is the normalized radius and $\tilde{h}_{\text{SN}}$ is then the scale length of the distribution. This exponential distribution assumes that the SN distribution follows the radial surface brightness density in spiral disks as proposed by Freeman (1970). To fit the data obtained from the studied samples to the exponential function in Equation 6.6, it is necessary to perform a non-linear fit. To that end, we used the Levenberg-Marquardt algorithm, and in particular `optimize.curve_fit` from

the `scipy`[1] module in Python.

Each of the values for the surface density should be weighted by its corresponding uncertainty. Due to the small number of sources in each of the analyzed samples, the uncertainties were calculated using Poisson statistics rather than Gaussian statistics. The error bar will then be asymmetric, and considering n events detected, upper and lower limits (λ_u and λ_l respectively) are defined for a confidence level of CL in such a way that

$$\sum_{x=0}^{n} \frac{\lambda_u^x e^{-\lambda_u}}{x!} = 1 - \mathrm{CL}, \tag{6.7}$$

$$\sum_{x=0}^{n-1} \frac{\lambda_l^x e^{-\lambda_l}}{x!} = 1 - \mathrm{CL} \quad (n \neq 0). \tag{6.8}$$

The confidence level used was of CL = 0.8413, a level that would correspond to a 1σ Gaussian statistics (see, e.g., Gehrels, 1986).

The bin size used to determine the area of the concentric rings where the surface density was calculated plays a crucial role in the fitting procedure. Indeed, small bins would map the distribution in more detail, but in this case, where we are in the regime of small number statistics, a too small bin could have as few as one, or even no sources in them, thus leading to large uncertainties; on the other hand, too large bins would result in very little points to be used in our fitting procedure, which would also yield large uncertainties in our fitted estimates. After testing with different bin sizes, the best compromise was reached by using 12 bins for each of the cases.

Since the supernova sample for all galaxies are relatively small, the uncertainty in the (formal) results from our non-linear fits could be rather large. To assess the robustness of our analysis, and also to extract as much information as possible from our data, we performed a series of Monte Carlo (MC) simulations, implemented as follows. For each supernova sample, we generated 10 000 sets of random numbers, uniformly distributed along the error length of every point, and fit them using the same procedure as in the original fit. Due to the large error bars some of the combinations will not converge. If that is the case, or if the $\tilde{h}_{\mathrm{SN}}$ obtained has a standard deviation higher than five times this value, that data set is rejected and a new random one is generated. In this way, we obtained a distribution of 10 000 different fitting values for

[1] `http://www.scipy.org`

the scale length parameter, $\tilde{h}_{\rm SN}$ (see Figure 6.3). This approach allowed us to get a much more reliable value of $\tilde{h}_{\rm SN}$, as well as of its uncertainty, since no assumption about the Gaussianity of the distributions of both the scale length and its error, is made (see below). Thus, we took the median value of the distribution of our MC generated 10 000 values as the most reliable estimate for $\tilde{h}_{\rm SN}$, and took the 90% confidence level as the uncertainty in our estimate of the scale length.

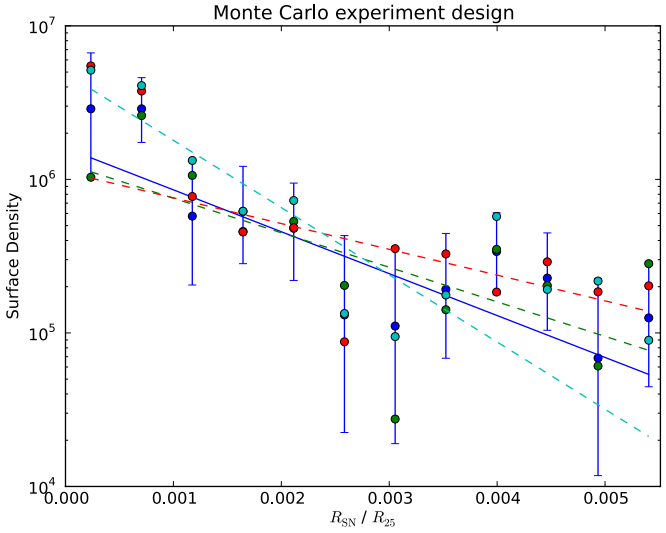

Figure 6.3: Illustration of the designed Monte Carlo experiment - Original points, error bars and fit are plotted in blue. New sets of points (in other colors) are chosen randomly within the error bar of each original point and fits are made for each data set (dashed lines). If the fitting algorithm doesn't converge or if its standard deviation is over 5 times the fitting value, the set is discarded and a new one is generated. Only three extra fits are shown here for the sake of clarity, but a total of 10 000 data sets were generated for each nuclear starburst studied.

To test our method, we re-analyzed the sample used by H09 for 239 CCSNe within 216 host galaxies. The explicit list of CCSNe used for that study is not given in their paper, and therefore we could not reproduce their sample exactly, but following their selection criteria we got 236 sources. We obtained a value of $\tilde{h}_{\rm SN} = 0.29^{+0.02}_{-0.01}$ (the error bar published in H09 is 0.29 ± 0.01). This value is in remarkably good agreement with our estimate, and confirms both the robustness of our method and the uncertainties in our estimates. Figure 6.4 shows the distribution of the values of $\tilde{h}_{\rm SN}$ from MC fits

for that sample, where we can see the necessity and the precision of the Monte Carlo experiment.

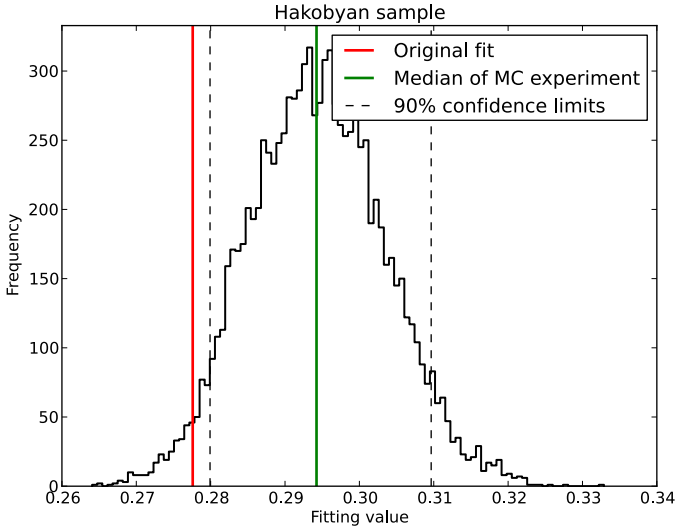

Figure 6.4: Monte Carlo results histogram for the sample from H09 - The red line is the original non-linear fit and the green line is the median of all the Monte Carlo fits. The scale length obtained by H09 is 0.29 ± 0.01. Note how the original $\tilde{h}_{\rm SN}$ obtained was even outside the confidence limits, which underscores the necessity of this procedure.

Following the same approach, we performed two additional analysis, as stated above:

- A fit to an exponential distribution without radius normalization, from which we obtain a scale length parameter $h_{\rm SN}$ (in contrast to $\tilde{h}_{\rm SN}$), measured in parsecs, which we can use to physically characterize the size of the disks.

- A fit to a power law distribution profile, namely,

$$\Sigma^{\rm SN} = \Sigma_0^{\rm SN} \left(\frac{r}{r_{\rm out}} \right)^{-\gamma}, \tag{6.9}$$

  where r is the non-normalized radii and $r_{\rm out}$ is the radius of the farthest SN analyzed, considered here to be the outer boundary of the putative nuclear disk. This was done to probe the profiles predicted by numerical simulations (Wada & Norman, 2002).

A final consideration was taken into account: for those cases in which the position of the AGN was known with little precision, we shifted its location randomly up to a

certain distance a hundred times (each case is discussed in detail in the next section) and performed the whole simulations.

In summary, the three relevant parameters we obtain are the scale length parameters of the exponential distribution for both normalized and non-normalized radii ($\tilde{h}_{\rm SN}$ and $h_{\rm SN}$ respectively) and the exponent of the power law profile (γ).

6.3 Results

6.3.1 Arp 299-A

The sample of supernovae from Arp 299-A used for this study comes both from observations from the European VLBI Network (EVN) at 5.0 GHz, presented in Pérez-Torres *et al.* (2009b) and deeply analyzed in Bondi *et al.* (2012), and data from the Very Long Baseline Array (VLBA) at 2.3 and 8.4 GHz from Ulvestad (2009). The existence and precise location of a low luminosity AGN (LLAGN) in the galaxy was reported by Pérez-Torres *et al.* (2010), hence its position was used to calculate accurate de-projected distances for all SNe in the nuclear region of Arp 299-A (see Figure 5.6 and Table 6.1). The galaxy major axis position angle is PA = 163.6° and the inclination of the galactic disk is $i = 52.4°$. The sample has a total of 31 sources. However, although the furthest source is as far as $\tilde{r} = 11.4 \times 10^{-2}$, the next one in distance is at $\tilde{r} = 6.6 \times 10^{-2}$, so the latter value of $\tilde{r}$ was used as the limiting radius for our study, giving a final number of 30 sources. The scale length obtained using the non-linear fit is $\tilde{h}_{\rm SN} = 1.6 \times 10^{-3}$ (see Figure 6.5). After performing the Monte Carlo analysis explained in the previous section we obtained a final $\tilde{h}$ of $\left(1.9^{+1.9}_{-0.8}\right) \times 10^{-3}$. The resulting histogram is shown in Figure 6.6. Power law fitting analysis is shown in Figures 6.7 and 6.8.

6.3.2 Arp 220

Arp 220 is an interacting system at a distance of 77 Mpc, and the closest and most studied ULIRG. High-angular resolution radio observations from its two nuclear regions were first obtained by Lonsdale *et al.* (2006) using global VLBI, who found a total of 49 radio supernovae in both East (20) and West (29) nuclei. We used the position of the peak flux density from a delay-rate VLBI map as the estimated position for the center of each galactic nucleus (Parra *et al.*, 2007). Figure 6.9 shows both the sources and the contours from which nuclei positions were derived. Detailed information is given

Table 6.1: Arp 299-A source list

Name	$\Delta\alpha$ (J2000.0)	$\Delta\delta$ (J2000.0)	Deprojected dist. (mas)
A3	33.5941	46.560	252.3
A15	33.5991	46.637	190.9
33.612+46.70[a]	33.6124	46.696	71.3
33.615+46.67[a]	33.6154	46.667	47.9
A26	33.6163	46.652	55.6
33.617+46.72[a]	33.6173	46.724	44.2
A18	33.6195	46.463	276.6
A19	33.6198	46.660	45.1
A6	33.6207	46.597	122.6
A0	33.6212	46.707	13.2
A2	33.6218	46.655	60.5
A27	33.6221	46.692	25.06
33.624+46.77[a]	33.6241	46.771	81.9
33.627+46.44[a]	33.6267	46.440	331.2
A28	33.6272	46.719	66.8
33.628+46.62[a]	33.6280	46.623	135.8
33.629+46.65[a]	33.6290	46.647	121.6
A7	33.6301	46.786	117.7
A8	33.6305	46.401	394.6
A9	33.6307	46.620	159.4
A29	33.6344	46.915	249.6
A22	33.6355	46.677	160.6
A30	33.6362	46.863	209.1
A10	33.6392	46.551	291.6
A11	33.6403	46.582	272.9
A31	33.6441	46.629	271.1
A12	33.6495	46.590	347.3
A4	33.6500	46.537	394.0
A25	33.6523	46.701	311.8
A13	33.6531	46.733	309.6
A14	33.6825	46.570	666.2

Note. — Coordinates are given with respect to $\alpha = 11^{\rm h}28^{\rm m}00^{\rm s}.0000$ and $\delta = +58^\circ33'00''.000$.

[a]Sources from Ulvestad (2009).

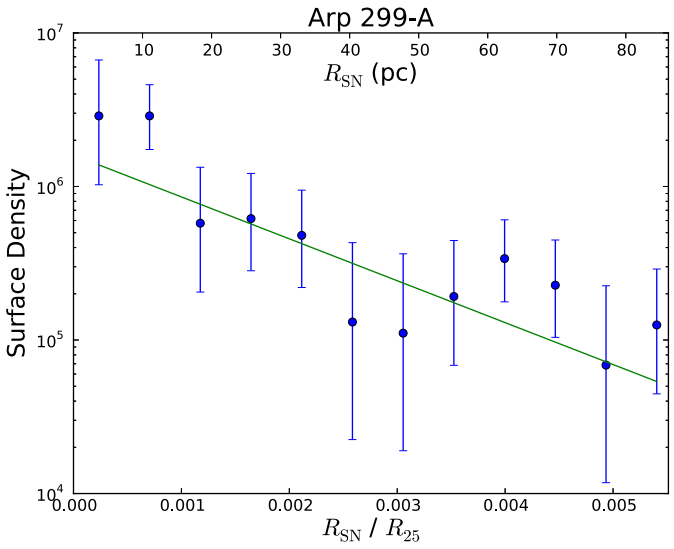

Figure 6.5: Surface density profile of Arp 299-A - Non-linear fit for the 30 inner SNe in Arp 299-A. The solid green line is a non-linear fit to an exponential function with $\tilde{h}_{SN} = 1.6 \times 10^{-3}$.

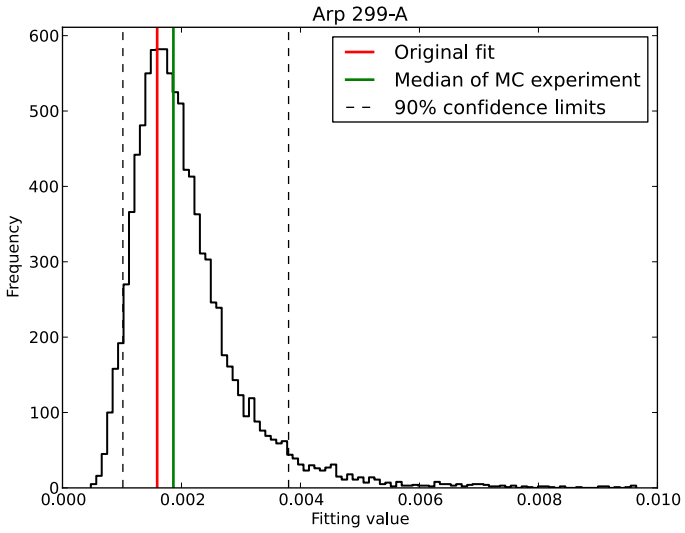

Figure 6.6: Monte Carlo results for Arp 299-A - Histogram for the fitting results for $\tilde{h}_{SN}$ in Arp 299-A. The original non-linear fit is shown in red, and the median of the distribution created with the MC experiment is shown in green. Confidence levels are shown as dashed lines and are chosen in a way that a 5% at both extremes of the distribution are left outside it. The final scale length is then 1.9×10^{-3}.

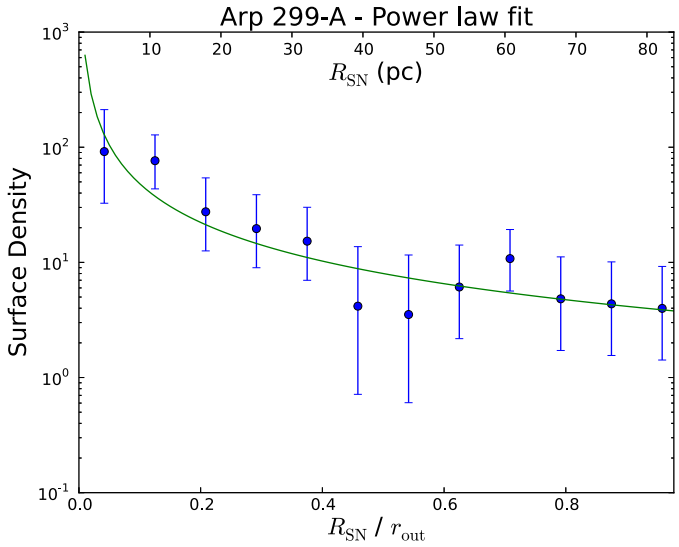

Figure 6.7: Arp 299-A power law fitting - Surface density of SNe vs radii normalized to the furthest source, $r_{\rm out}$, in Arp 299-A and non-linear fit to a power law with $\gamma = 1.1$.

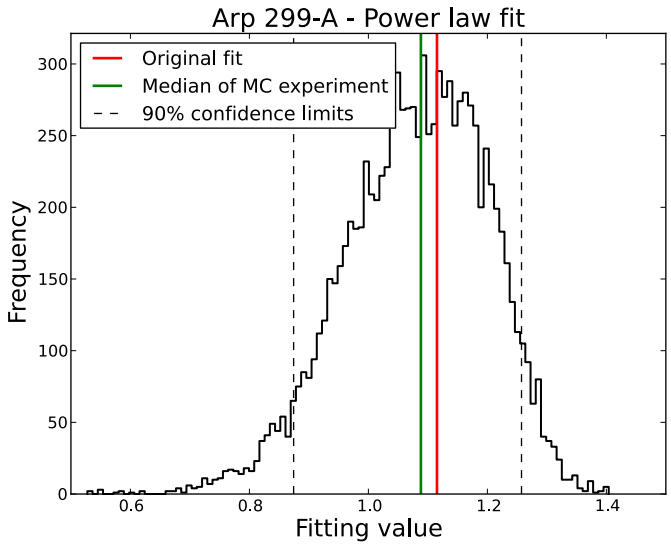

Figure 6.8: Monte Carlo power law results for Arp 299-A - MC histogram for the fitting results to a power law for Arp 299-A. The original non-linear fit is shown in red, and the median of the distribution obtained through MC simulations equals $\gamma = 1.1$, and is shown in green. The dashed lines correspond to 90% confidence limits.

in Tables 6.2 and 6.3. The inclination angle of the galaxy is 57.0°, with a major axis position angle of 96.5°. One of the compact sources in the Arp 220 East nucleus is at a much larger distance than the rest of them, which we did not use it in our fit, thus limiting the normalized radii to $\tilde{r} = 0.011$. Therefore, a total 48 SNe were considered in the fits, which we carried both separately, for each nucleus, and for the combined data set (Fig. 6.10). Similarly, we performed MC simulations for each of the two nuclei, as well as for the combined sample (see Fig. 6.11). In this way, we obtained a scale length for the East and West nuclei of $\left(3.1^{+2.0}_{-0.7}\right) \times 10^{-3}$ and $\left(3.4^{+1.5}_{-0.9}\right) \times 10^{-3}$, respectively, and a combined scale length for Arp 220 is $\left(3.3^{+0.6}_{-0.4}\right) \times 10^{-3}$. To quantify the effect due to the uncertain position of the putative AGNs, we shifted them 100 times randomly around our nominal position, given by the peak flux density, by a maximum value of

$$\sigma_{(\alpha,\delta)} = \frac{\mathrm{FWHM}}{2\,S/N}, \tag{6.10}$$

where FWHM is the full-width at half maximum, and S/N is the signal-to-noise ratio, resulting in 4.2 mas for the East nucleus and 1.4 mas for the West one, and then fitted the data. The maximum differences obtained were considered as a systematic error, which we added to our nominal values, so that the combined scale length becomes $\tilde{h}_{\mathrm{SN}} = \left(3.3^{+0.7}_{-0.9}\right) \times 10^{-3}$. Additionally, see Figures 6.12 and 6.13 for physical scale analysis, where no radii normalization was performed, and Figures 6.14 and 6.15 for power law fitting.

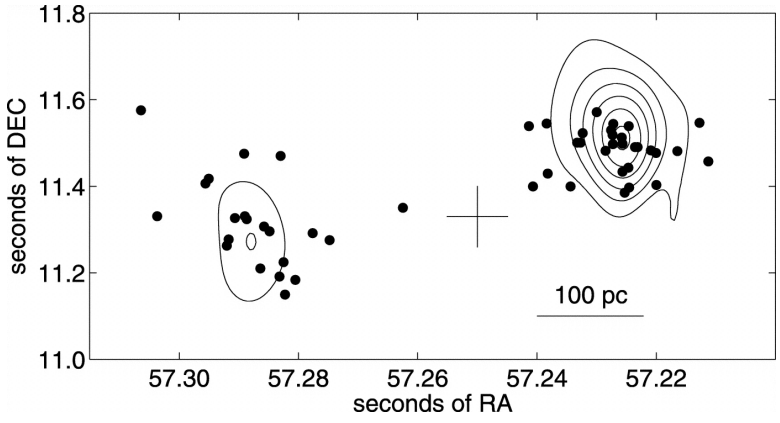

Figure 6.9: Arp 220 nuclear region - Dots represent the position of the 49 supernovae detected by Lonsdale *et al.* (2006). Contours are from 6 m observations. Coordinates are given with respect to $15^{\mathrm{h}}34^{\mathrm{m}}00^{\mathrm{s}}.00$ $+23°30'00''.00$. From Parra *et al.* (2007).

Table 6.2: Arp 220 East source list

Name	$\Delta\alpha$ (J2000.0)	$\Delta\delta$ (J2000.0)	Deprojected dist. (mas)
E22	57.2758	11.277	169.3
E21	57.2789	11.293	127.4
E20	57.2821	11.185	189.2
E19	57.2840	11.151	235.3
E18	57.2843	11.226	104.8
E17	57.2850	11.193	156.5
E16	57.2848	11.472	361.0
E14	57.2868	11.297	46.8
E13	57.2878	11.308	66.3
E12	57.2885	11.212	109.5
E11	57.2910	11.325	111.7
E10	57.2914	11.332	126.4
E09	57.2915	11.477	384.8
E08	57.2931	11.328	132.9
E07	57.2943	11.279	90.5
E06	57.2946	11.264	91.2
E05	57.2980	11.419	319.7
E04	57.2986	11.408	306.3
E03	57.3073	11.333	305.8
E01	57.3103	11.577	676.1

Note. — Coordinates are given with respect to $\alpha = 15^{\mathrm{h}}34^{\mathrm{m}}00^{\mathrm{s}}.0000$ and $\delta = +23^{\circ}30'00''.000$.

Table 6.3: Arp 220 West source list

Name	$\Delta\,\alpha$ (J2000.0)	$\Delta\,\delta$ (J2000.0)	Deprojected dist. (mas)
W46	57.2066	11.459	310.4
W44	57.2082	11.548	254.8
W42	57.2123	11.482	215.6
W41	57.2161	11.405	264.9
W40	57.2162	11.478	167.4
W39	57.2171	11.484	150.3
W34	57.2195	11.492	112.1
W33	57.2200	11.492	106.0
W30	57.2211	11.398	235.7
W29	57.2212	11.445	157.1
W28	57.2212	11.541	82.8
W27	57.2219	11.387	251.9
W26	57.2223	11.435	164.4
W25	57.2223	11.500	69.0
W24	57.2224	11.514	58.1
W19	57.2240	11.499	48.9
W18	57.2240	11.546	62.8
W17	57.2241	11.520	34.3
W16	57.2244	11.531	39.7
W15	57.2253	11.483	62.4
W14	57.2270	11.573	107.1
W12	57.2295	11.524	47.1
W11	57.2300	11.503	50.0
W10	57.2306	11.502	57.8
W09	57.2318	11.401	209.3
W08	57.2360	11.431	186.6
W07	57.2362	11.547	154.4
W03	57.2387	11.401	248.7

Note. — Coordinates are given with respect to $\alpha = 15^{\rm h}34^{\rm m}00^{\rm s}.0000$ and $\delta = +23^\circ30'00''.000$.

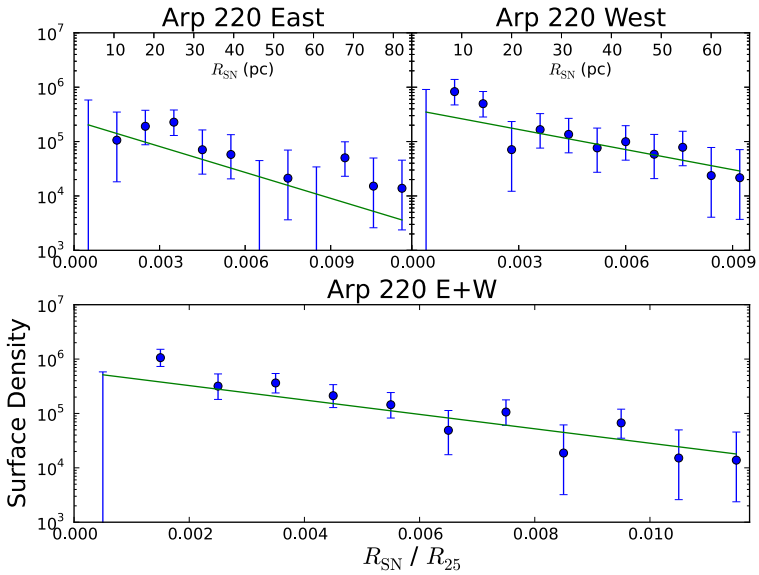

Figure 6.10: Surface density profile of Arp 220 - Non-linear fits for the inner SNe in Arp 220. Top left: Fit for the 19 inner sources in the eastern nucleus ($\tilde{h}_{SN} = 2.7 \times 10^{-3}$). Top right: Same for the 29 sources in the western nucleus ($\tilde{h}_{SN} = 3.5 \times 10^{-3}$). Bottom: Altogether analysis with the 48 combined sources ($\tilde{h}_{SN} = 3.3 \times 10^{-3}$). Note that although some of the points correspond to rings where no sources where detected and therefore the corresponding surface density is zero (not possible to plot in a logarithmic scale), the upper limits are drawn and those points are used in the fit.

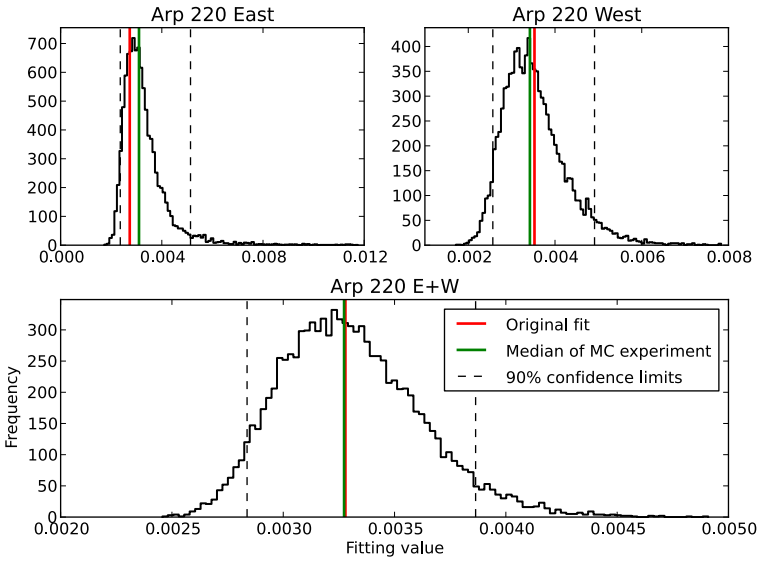

Figure 6.11: Monte Carlo results for Arp 220 - Histograms for the fitting results to $\tilde{h}_{\rm SN}$ in Arp 220 for the east nucleus (top left panel), west nucleus (top right panel), and the combination of both nuclei (bottom panel). The original non-linear fit is shown in red, and the median of the MC distribution is shown in green –note both lines almost overlap in the bottom panel. Confidence levels are shown as dashed lines and are chosen in a way that a 5% at both extremes of the distribution are left outside it. Partial scale lengths are 3.1×10^{-3} and 3.4×10^{-3} for east and west nuclei respectively. The final result for the combined data is $\tilde{h}_{\rm SN} = 3.3 \times 10^{-3}$.

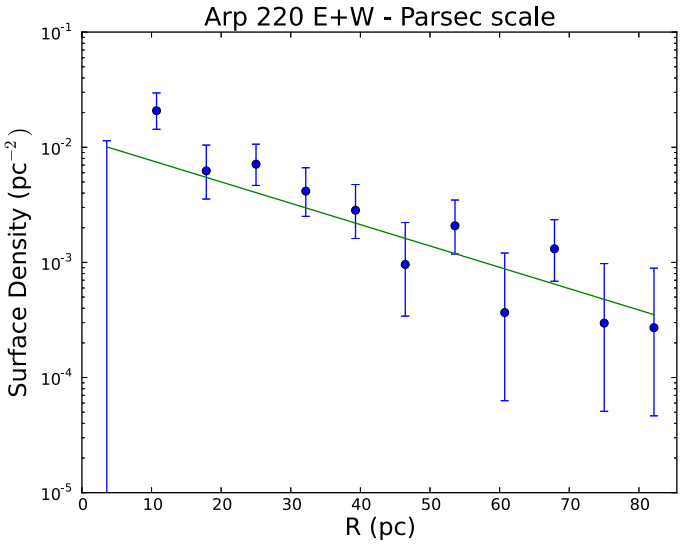

Figure 6.12: Surface density profile in parsec scale of combined nuclei in Arp 220 - Non-linear fit of the combined sources for the East and West nuclei of Arp 220, in parsecs. It yields a scale length of $h_{\rm SN} = 23.4\,{\rm pc}$.

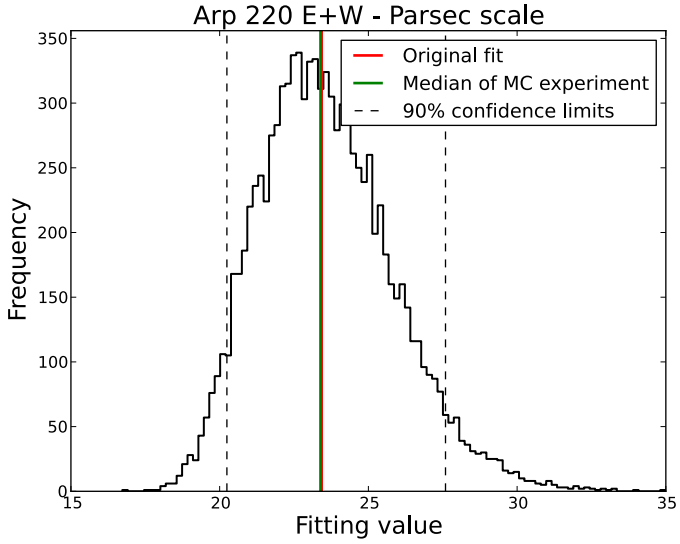

Figure 6.13: Monte Carlo results for combined nuclei in Arp 220 - MC histogram for the fitting of the combined SN sample of both East and West nuclei in Arp 220. The resulting scale length is $h_{\rm SN} = 23.4\,{\rm pc}$.

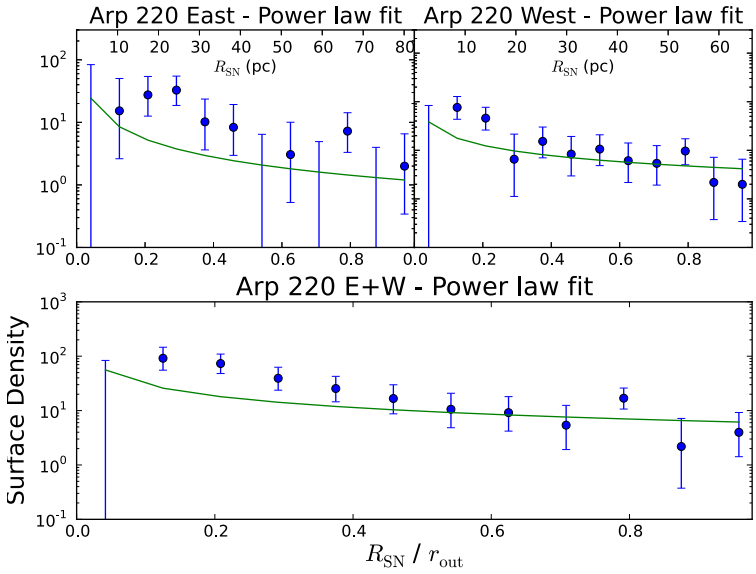

Figure 6.14: Arp 220 power law fitting - Non-linear power law fits of the surface density of SNe vs radius, normalized to the furthest source, $r_{\rm out}$, in Arp 220. *Top left*: East nucleus, with $\gamma = 1.0$. *Top right*: West nucleus, with $\gamma = 0.7$. *Bottom*: Combined analysis for the East and West nuclei (48 sources), yielding $\gamma = 0.7$. Note that some of the points are in rings where no sources were detected. While their corresponding surface density is zero, their upper limits were used in the fit.

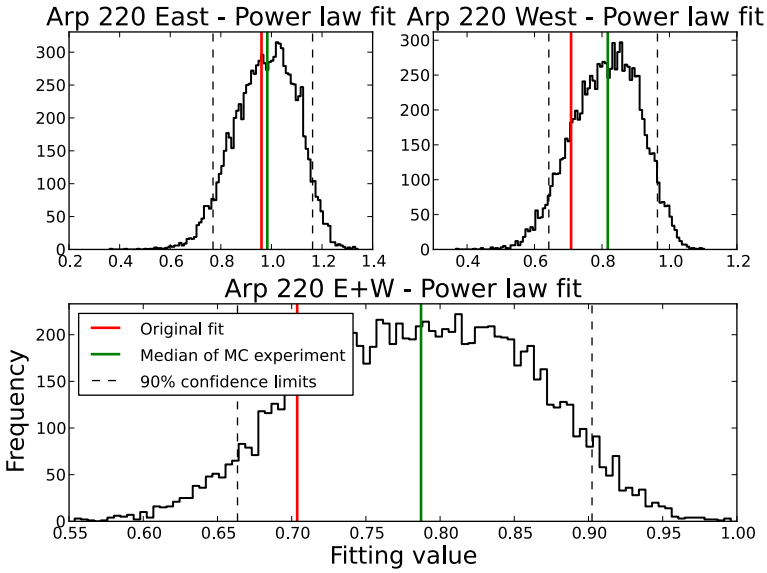

Figure 6.15: Monte Carlo power law results for Arp 220 - MC histograms for the fitting results to to a power law in Arp 220 for the East nucleus (top left panel), West nucleus (top right panel), and the combination of both nuclei (bottom panel). The original non-linear fit is shown in red, and the median of the MC distribution is shown in green. The dashed lines correspond to 90% confidence levels. The γ values are 1.1 and 0.8 for the East and West nuclei, respectively. The resulting value from combining all data is $\gamma = 0.8$.

6.3.3 Combination of Arp 299-A and Arp 220

The normalized radii of Arp 299-A and Arp 220 (both East and West nuclei) are comparable. We can thus combine every source prior to the analysis to obtain an average scale length parameter with lower errors that would characterize both nuclear starbursts. The scale length obtained for the combined samples is $\tilde{h}_{\rm SN} = \left(2.0^{+0.3}_{-0.2}\right) \times 10^{-3}$. The original non-linear fit is shown in Figure 6.16 and our MC analysis results are shown in Figure 6.17. After taking into account systematic errors due to the uncertainty in the precise location of the AGNs of the Arp 220 East and West nuclei, the final value for the scale length is $\tilde{h}_{\rm SN} = \left(2.0^{+0.3}_{-0.4}\right) \times 10^{-3}$. For parsec and power law analysis see Figures 6.18 and 6.19 and Figures 6.20 and 6.21 respectively.

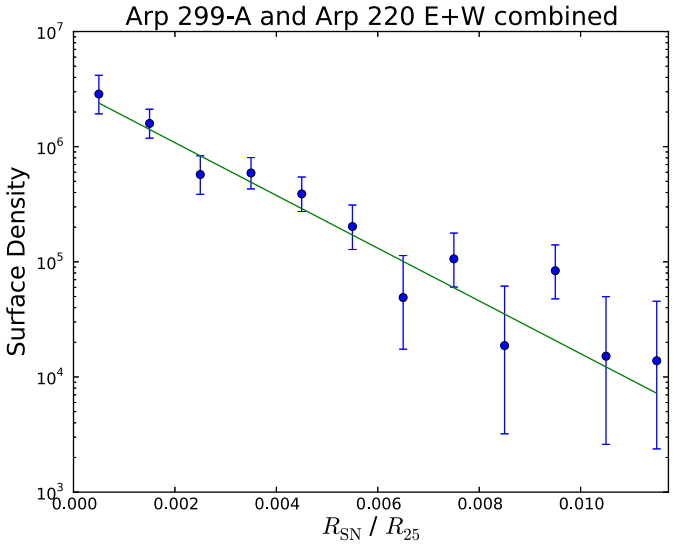

Figure 6.16: Surface density combined profile of Arp 299-A and Arp 220 - Non-linear fit for the combined sources from both Arp 299-A and Arp 220. Scale length is $\tilde{h}_{\rm SN} = 1.9 \times 10^{-3}$.

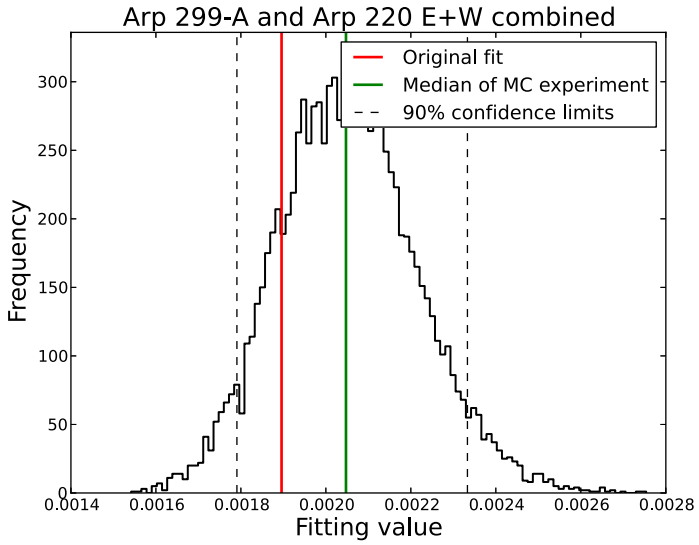

Figure 6.17: Monte Carlo combined results for Arp 299-A and Arp 220 - Histogram of $\tilde{h}_{\rm SN}$ for the combined sources from Arp 299-A and the two nuclei of Arp 220.The original non-linear fit is shown in red, and the median of the distribution created with the MC experiment is shown in green. Confidence levels are shown as dashed lines and are chosen in a way that a 5% at both extremes of the distribution are left outside it. The final scale length is then 1.9×10^{-3}.

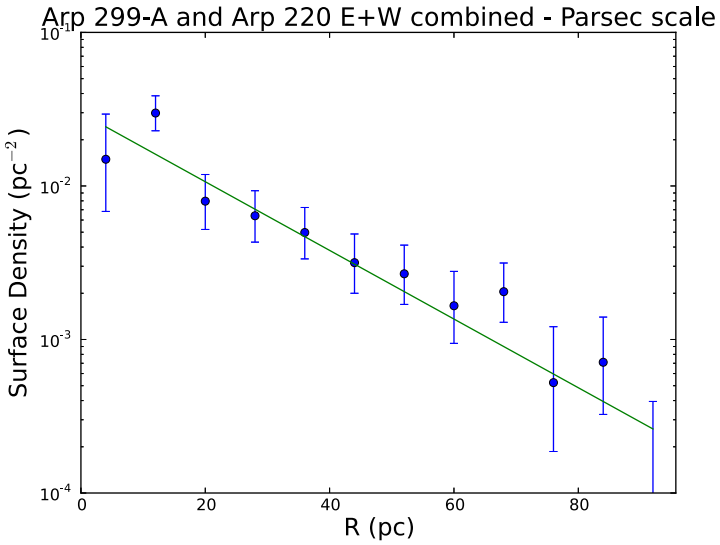

Figure 6.18: Surface density profile in parsec scale of Arp 299-A and Arp 220 - Non-linear fit for Arp 299-A and Arp 220, in parsecs. It yields a scale length of $h_{\rm SN} = 19.4\,{\rm pc}$.

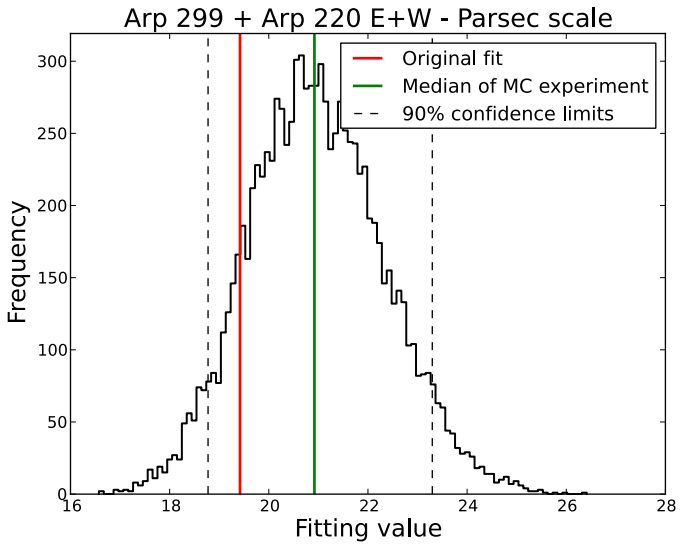

Figure 6.19: Monte Carlo combined results in parsec scale for Arp 299-A and Arp 220 - MC histogram from parsec scale fitting of combined sources from Arp 299-A and Arp 220. Resulting scale length is $h_{\rm SN} = 20.9\,{\rm pc}$.

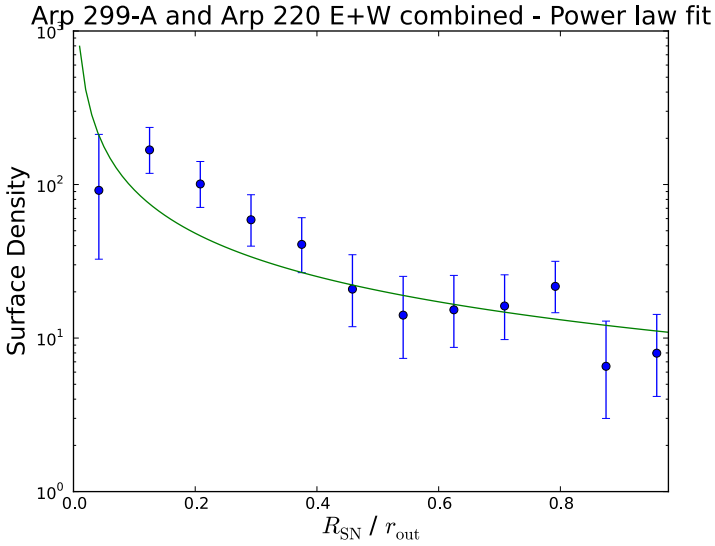

Figure 6.20: Arp 299-A and Arp 220 combination power law fitting - Surface density of SNe vs radii normalized to the furthest source, $r_{\rm out}$, for the combined sample of SNe from Arp 299-A and the two nuclei of Arp 220. A non-linear fit to a power law with radius yields $\gamma = 0.9$.

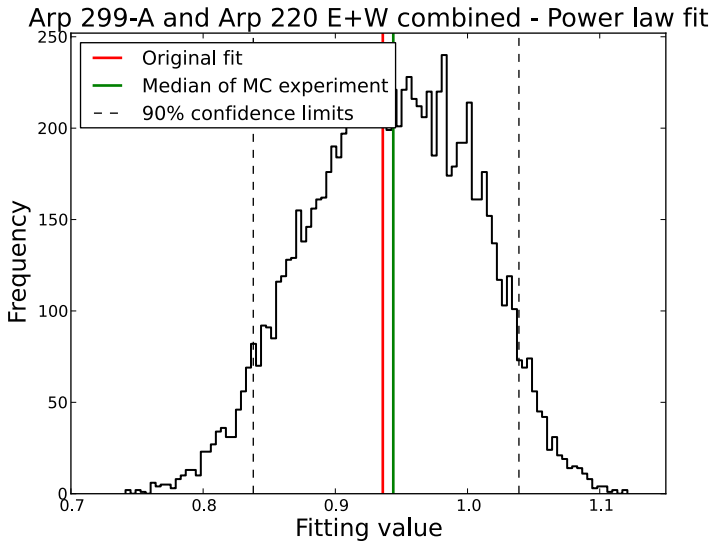

Figure 6.21: Monte Carlo power law results for Arp 299-A and Arp 220 combination - MC histogram for the fitting results to a power law for the combined sample of SNe from Arp 299-A and the two nuclei of Arp 220. The original non-linear fit is shown in red, and the median of the distribution obtained through MC simulations yields a value of $\gamma = 0.9$, and is shown in green. The dashed lines correspond to the 90% confidence limits.

6.3.4 M82

At a distance of 3.2 Mpc (Burbidge *et al.*, 1964), M82 is one of the most studied nearby galaxies, and is the prototype of starburst galaxy. Many observations at high-angular resolution have been performed in M82. For this study, we combined those sources catalogued as SNe (or SNR) detected by Wills *et al.* (1997), Allen & Kronberg (1998), McDonald *et al.* (2002), Fenech *et al.* (2008), and Brunthaler *et al.* (2009). These comprise observations at several frequencies with MERLIN, the VLA and the VLBA. A total of 39 sources are analyzed. Since no AGN has been confirmed yet in M82, we used instead the radio kinematic center of M82 (Weliachew *et al.*, 1984) as the position for its nucleus. M82 has a major position angle of 67.5° and an inclination of 79.4°. The scale length obtained with the MC simulation is $\tilde{h}_{\rm SN} = \left(3.1^{+0.5}_{-0.4}\right) \times 10^{-2}$. Although the radio kinematic center is likely to be very close, if not exactly coincident, with the putative nucleus of M82, we nevertheless quantified the effect that an error in the position chosen as the nucleus of M82 would have in the fits. In particular, we shifted our fiducial position for the nucleus up to the distance of the separation of kinematic centers measured in different wavelengths, namely 20 parsecs, in several directions, and then fitted the data. The maximum differences were considered as a systematic error which we added to our nominal value, thus yielding $\tilde{h}_{\rm SN} = \left(3.1^{+0.9}_{-0.7}\right) \times 10^{-2}$. Unlike in the previous results, the fitting of the data from M82 to a power law distribution (Figure 6.25) does not seem consistent at all with a nuclear disk that follows a power law distribution.

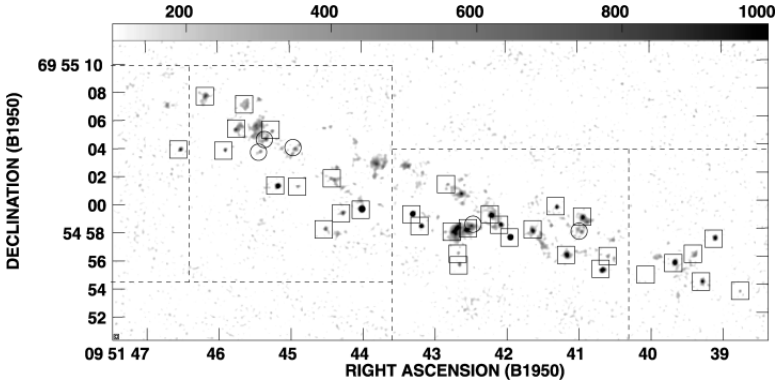

Figure 6.22: Radio image of M82 - VLA A-configuration and Pie Town image of the central regions of M82 at 15 GHz. Boxes indicate the positions of some of the sources studied. From McDonald *et al.* (2002).

Table 6.4: M82 source list

Name[a]	$\Delta\alpha$ (J2000.0)	$\Delta\delta$ (J2000.0)	Deprojected dist. (mas)
39.10+57.3	47.87	43.74	37.03
39.40+56.2	48.16	42.53	29.20
39.64+53.3	48.41	39.68	20.00
39.77+56.9	48.54	43.36	27.84
40.32+55.2	49.07	41.53	16.98
40.61+56.3	49.32	42.19	15.93
40.68+55.1	49.42	41.42	14.13
41.30+59.6	50.05	45.92	20.40
41.95+57.5	50.70	44.00	6.94
42.61+60.7	51.35	46.89	9.35
42.66+51.6	51.38	47.76	13.21
42.67+55.6	51.37	41.78	17.44
42.67+56.3	51.40	42.65	13.42
42.80+61.2	51.54	47.53	10.25
SN2008iz	51.55	45.79	2.41
43.18+58.2	51.91	44.58	8.70
43.31+59.2	52.03	45.42	5.75
43.40+62.6	52.11	48.74	10.22
43.55+60.0	52.27	46.31	4.22
43.72+62.6	52.43	48.79	7.63
43.82+62.8	52.54	48.98	7.71
44.01+59.6	52.72	45.77	12.03
44.08+63.1	52.75	49.46	8.50
44.28+59.3	52.99	45.53	16.33
44.34+57.8	53.05	43.94	24.65
44.40+61.8	53.13	47.87	8.35
44.51+58.2	53.22	44.36	24.59
44.89+61.2	53.61	47.35	15.69
45.17+61.2	53.88	47.41	18.61
45.24+65.2	53.96	51.36	12.15
45.42+67.4	54.13	53.53	18.13
45.52+64.7	54.22	50.94	12.94
45.75+65.3	54.44	51.43	14.17
45.79+64.0	54.50	50.22	16.24
45.89+63.8	54.60	49.98	17.85
46.52+63.9	55.21	50.05	24.19
46.56+73.8	55.26	59.90	38.39
46.70+67.1	55.41	53.16	19.71
47.37+68.0	56.10	54.00	24.01

Note. — Coordinates are given with respect to $\alpha = 09^{\rm h}55^{\rm m}00^{\rm s}.00$ and $\delta = +69^\circ 40' 00''.00$.

[a]Names from the literature are derived from B1950 coordinates.

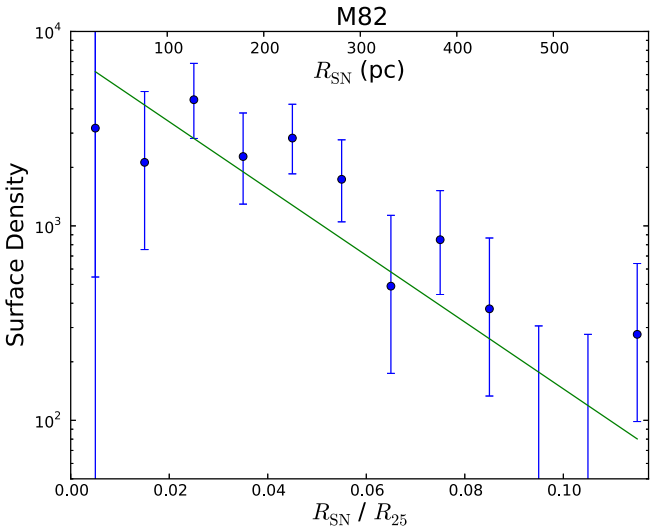

Figure 6.23: Surface density profile of M82 - Non-linear fit for the 39 inner SNe in M82. The solid green line is a non-linear fit to an exponential function with $\tilde{h}_{SN} = 2.9 \times 10^{-2}$. Note that although some of the points correspond to rings where no sources where detected and therefore the corresponding surface density is zero (not possible to plot in a logarithmic scale), the upper limits are drawn and those points are used in the fit.

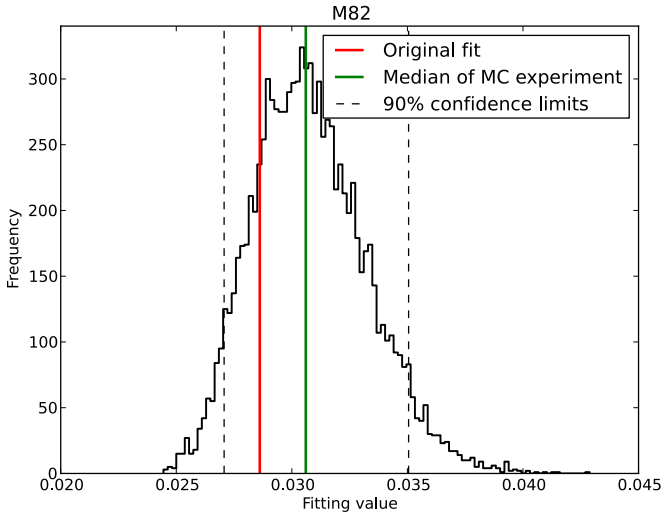

Figure 6.24: Monte Carlo combined results for M82 - Histogram for the fitting results for $\tilde{h}_{SN}$ in M82. The original non-linear fit is shown in red, and the median of the distribution created with the MC experiment is shown in green. Confidence levels are shown as dashed lines and are chosen in a way that a 5% at both extremes of the distribution are left outside it. The final scale length is then 3.1×10^{-2}.

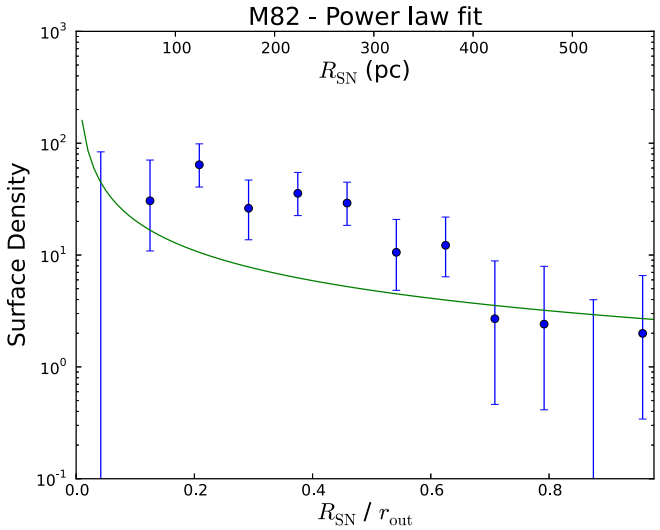

Figure 6.25: M82 power law fitting - Surface density of SNe vs radii normalized to the furthest source, $r_{\rm out}$ and non-linear fit to a power law. The poor correlation of the fit does not give support to a nuclear disk whose SN surface density follows a power law from the central few pc up to $\sim 200\,$pc.

The errors derived from the AGN shift tests for the corresponding nuclei are detailed in Table 6.5. This test was not performed for Arp 299-A, since its AGN is precisely located.

6.4 Discussion

The main goal of this work was to probe the radial distribution of supernovae in the central few hundred parsecs of three starburst-dominated galaxies. The main results are summarized in Table 6.6 and Figure 6.26, where we show the scale lengths, index of the power law supernova profile, and the radial distribution of SNe for the three galaxies, as well as for the sample of spiral galaxies from H09.

Note that the scale lengths for the exponential disk fits to the radial distribution of SNe in the (circum)nuclear regions of the starburst galaxies, are at least an order of magnitude smaller that those obtained by H09 for the whole disks of spiral galaxies. In particular, $\tilde{h}_{\rm SN}$ is two orders of magnitude smaller for the case of Arp 299-A and Arp 220. Correspondingly, the physical sizes inferred for the scale lengths of the disks (column 3 in Table 6.6) are $\sim$20 – 30 pc for the nuclear disks in Arp 299-A or Arp 220,

Table 6.5: Effects of AGN shifting

	$\tilde{h}_{\rm SN}$		$h_{\rm SN}$		γ	
Nucleus	Upper[a] (%)	Lower[b] (%)	Upper[a] (%)	Lower[b] (%)	Upper[a] (%)	Lower[b] (%)
Arp 220 East	1.4	4.4	1.1	4.4	0.3	5.6
Arp 220 West	2.3	18.5	2.2	18.6	13.4	0.6
Arp 220 E+W	1.9	14.8	2.2	14.8	4.3	5.3
Arp 299 + Arp 220	0.6	9.2	1.1	0.6	1.9	2.4
M82	13	12.1	9.4	10.2	···	···

Note. — Shift tests were made around AGN in random directions and distances up to 4.2 mas for Arp 220 East nucleus (equivalent to 1.6 parsecs), 1.4 mas for Arp 220 West nucleus (0.5 pc) and 1.27 arcsec for M82 (20 pc). These errors are considered as systematic and added to the calculated errors. See text for further details.

[a]Maximum upper difference.

[b]Maximum lower difference.

Table 6.6: Scale length parameters for the galaxies discussed in this work

Nucleus	$\tilde{h}_{\rm SN}/10^{-3}$	$h_{\rm SN}$ (pc)	γ
Arp 299-A	$1.9^{+1.9}_{-0.8}$	$29.3^{+29.6}_{-13.7}$	$1.1^{+0.2}_{-0.2}$
Arp 220 East	$3.1^{+2.0}_{-0.9}$	$22.2^{+14.4}_{-6.2}$	$1.0^{+0.2}_{-0.3}$
Arp 220 West	$3.4^{+1.6}_{-1.5}$	$24.4^{+11.2}_{-10.8}$	$0.8^{+0.3}_{-0.2}$
Arp 220 E+W	$3.3^{+0.7}_{-0.9}$	$23.4^{+4.7}_{-6.6}$	$0.8^{+0.1}_{-0.2}$
Arp 299 + Arp 220	$2.0^{+0.3}_{-0.4}$	$20.9^{+2.6}_{-2.3}$	$0.9^{+0.1}_{-0.1}$
M82	$\left(3.1^{+0.9}_{-0.7}\right) \times 10^1$	$155.8^{+38.1}_{-33.1}$	-
H09 sample[a]	$\left(2.9^{+0.2}_{-0.1}\right) \times 10^2$	-	-

[a]Scale length for non-nuclear regions of spiral galaxies, re-calculated from the sample of Hakobyan *et al.* (2009). The quoted uncertainties correspond to the 90% confidence limits.

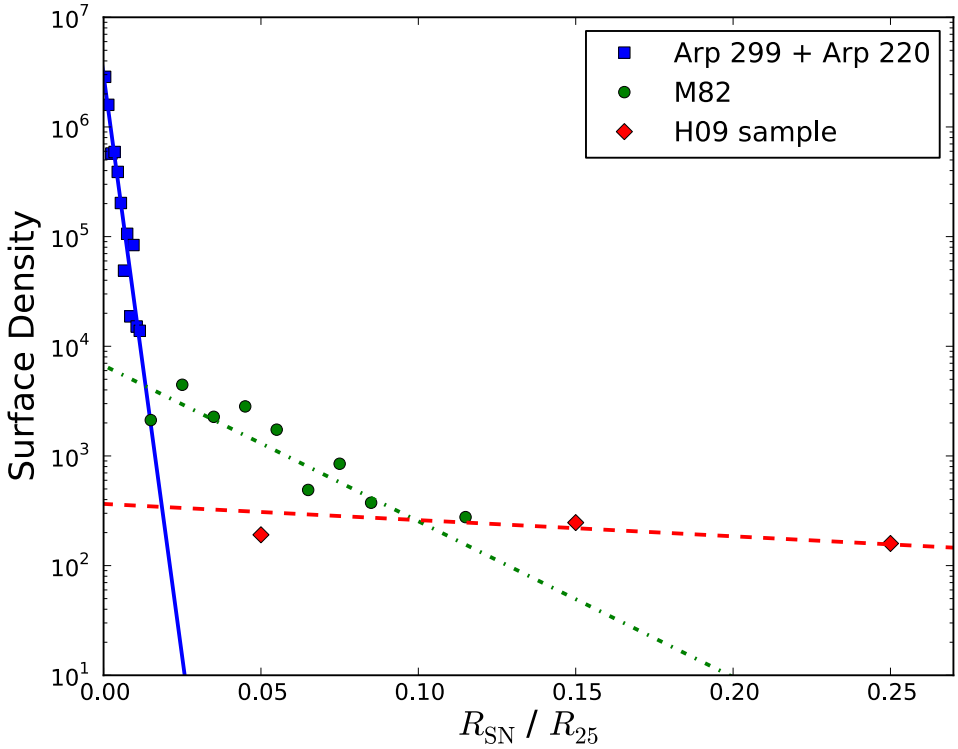

Figure 6.26: Radial distribution of supernovae for nuclear starbursts and spiral galaxies - The data correspond to the combined Arp 299-A + Arp 220 sample (blue squares), M82 (green circles), and the H09 sample of spiral galaxies (red diamonds), and the fitted lines are for Arp 299-A + Arp 220 (solid line), M82 (dotted-dashed line) and H09 (dashed line). For the sake of clarity, only the innermost part of the H09 sample is shown in the plot.

which is similar to the size derived for the nuclear starburst of the LIRG NGC 7469 (30 – 60 pc; Davies *et al.*, 2004b), using CO interferometric observations, and ∼160 pc for M82, which is also similar to the scale length of the nuclear disk in the ULIRG/QSO Mrk 231 (Davies *et al.*, 2004a).

We show in Figure 6.26 the radial distribution of SNe in our three starburst galaxies and, for comparison, also for spiral galaxies (from the H09 sample), along with the fits to these data. Note the clear existence of three different regimes: one characterized by a very steep profile of the surface number density of SNe, typical of strong, nuclear starbursts (Arp 299-A + Arp 220); a second, less steep profile, as indicated for the (circum)nuclear starburst in M82; and a third, flatter profile, typical of very large disks, as those in spiral galaxies (H09 sample). These results suggest that the surface density of SNe, and hence of available gas to be converted into stars, is maximum in the vicinities of the SMBH in LIRGs and ULIRGs. We also show in column 4 of Table 6.6 the fits to a power law disk profile, which are consistent with the fiducial value of $\gamma = 1$ used by Wada & Norman (2002) and Kawakatu & Wada (2008) for the nuclear disk, and appears to yield further support to their modeling.

Following our approach, Kangas *et al.* (2013) analyzed the radial distribution of 86 CCSNe in a sample of galaxies from the *IRAS* Revised Bright Galaxy Catalog (Sanders *et al.*, 2003), considering galactic scales, but obtaining a scale length parameter of $\tilde{h}_{\rm SN} = 0.23^{+0.03}_{-0.02}$, statistically significantly below they value by Hakobyan *et al.* (2009). They also found that Type Ibc and IIb SNe are in general more centrally located in their host galaxies than Type II, giving support to a previous study by Habergham *et al.* (2012). Furthermore, different types of SNe are correlated with the physical parameters of their host galaxy and the properties of their nuclei (e.g., Anderson & James, 2009; Wang *et al.*, 2010; Hakobyan *et al.*, 2012). Multi-frequency monitoring of nuclear SN factories will allow us to categorize them and prove if these results are also valid in the innermost regions of (U)LIRGs. The results provided by LIRGI (see Section 5.2) will be of high interest in that field.

It is worth discussing wether all detected sources used in our study are indeed SNe or our samples may be contaminated by sources with another nature, e.g., ultra compact H II regions. In the case of M82, the closest of the three galaxies discussed here, we used the source list in McDonald *et al.* (2002) and Fenech *et al.* (2008), where the authors already discriminate SNe from H II regions based on their spectral shape, brightness

temperature, and observed shell structure. In the cases of the more distant galaxies, Arp 299 and Arp 220, we used available spectral information from the literature, and especially, the brightness temperatures inferred from VLBI observations, which for all of the sources correspond to non-thermal radio emitters (e.g., Pérez-Torres *et al.* (2009b) for Arp 299A, Parra *et al.* (2007) for Arp 220).

Single or multiple ultra compact H II regions can be ruled out because their ionizing radiation is normally dominated by a single O star, whose maximum free-free thermal radio luminosity is several orders of magnitude below the radio luminosity from any of the objects detected in either Arp 299-A or Arp 220. The expected thermal radio emission from super star clusters (SSCs), which can host up to a few 10^5 stars, similarly cannot be responsible for the observed emission. At the distances of Arp 299 and Arp 220, the VLBI beam sizes correspond to $\sim 1.5\,\mathrm{pc}$, implying radial sizes of at most about 0.8 pc. Young massive stellar clusters of this size have a mass of at most $5\times10^5\,M_\odot$ (e.g. Portegies Zwart *et al.*, 2010). Assuming a Kroupa initial mass function with $\alpha = -1.0$ between 0.1 and $0.5\,M_\odot$, and $\alpha = -2.35$ between 0.5 and $100\,M_\odot$, the number of O6 and earlier type stars is 142 (out of a total of 10^5 stars), hence the maximum attainable thermal radio luminosity would be $\sim 2\times10^{25}\,\mathrm{erg\,s^{-1}\,Hz^{-1}}$, which is at least an order of magnitude lower than observed in Arp 299-A or Arp 220.

6.5 Summary

We modeled, for the first time, the radial distribution of SNe in the nuclear starbursts of M82, Arp 299-A and Arp 220. Our main conclusions are the following:

1. We have derived scale length values for exponential disks, which are in the range between ∼20 pc and ∼160 pc, two orders of magnitude lower than the scale length derived for whole galactic disks.

2. We have also modeled those SNe distributions as power law disk profiles, and found that they are in agreement with state-of-the art numerical simulations of nuclear disks around SMBHs. We interpret our results as evidence of nuclear disks around the centers, i.e., AGNs, of starburst-dominated galaxies, and they seem to yield also support to evolutionary scenarios where a nuclear disk of size $\lesssim 100\,\mathrm{pc}$ is formed in LIRGs and ULIRGs (Kawakatu & Wada, 2008).

3. In particular, the scale length obtained for the LIRG Arp 299-A and the low luminosity AGN nature of its SMBH (Pérez-Torres *et al.*, 2010), suggests that its nuclear disk is likely supported by gas pressure, so that the accretion onto the SMBH is smaller than for a turbulent-supported disk. It is very likely that this is also the case of the ULIRG Arp 220.

4. Future deep VLBI observations of a significantly large sample of (U)LIRGs, which would result in the discovery of new SN factories, will be of much use for deriving statistically meaningful results on the size of nuclear disks, and will set useful constraints among the different proposed evolutionary scenarios.

5. Additionally, multi-frequency VLBI monitoring of these SN factories will allow us to classify most of the compact non-thermal sources, specially the most recent ones, and to study how different SN types are correlated with the properties of their hosts.

Whatever else Astronomy may or may not be, who can doubt it to be the most beautiful of the sciences?

Isaac Asimov

7 Conclusions

THROUGHOUT this thesis, I have presented the results of our study of local LIRGs and ULIRGs following a multiwavelength approach. We have made use of radio, mm, mid- and near-IR, optical, and X-ray observations, taking advantage of both imaging and spectroscopy techniques. These are the main key conclusions we draw from this work:

- We have studied the molecular gas properties of a sample of 56 (U)LIRGs from the GOALS sample using the IRAM 30 m telescope. Although we observed several tracers, we focused our study on carbon monoxide (CO). We studied the relation between the ^{12}CO$(1-0)$ luminosity and the infrared luminosity. We have confirmed the known correlation and found that AGN dominated systems tend to have larger CO luminosities, likely due to the extra contribution of gas feeding into the SMBH. We have also used a complete far-IR model fitting to confirm that the use of IRAS 60 μm and 100 μm to obtain the dust temperature is an underestimation that only takes into account warm ($T_{\rm dust} \gtrsim 25$ K) dust. We have also confirmed the relation of the isotopic ratio ^{12}CO / ^{13}CO with dust tem-

perature. Finally, we have studied our observed ^{12}CO line profiles, and compared them with the available profiles of ^{13}CO , HCN, and HCO$^+$. We have found that inclination effects themselves are not enough to explain the observed profiles, with the distribution of gas playing also an important role.

- We have analyzed the circumnuclear ring in the LIRG NGC 1614, which shows remarkable morphological similarities between the radio (3.6 cm), mid-IR (8.7 μm), and Paα (1.9 μm) emission, suggesting that the underlying emission mechanisms are tightly related, likely due to recent star-forming activity along the ring. We have developed a method to disentangle the thermal free-free and non-thermal synchrotron radio emission in a pixel-by-pixel basis using the unabsorbed Paα emission, from which we obtained the intrinsic synchrotron power law for different regions within the central kpc of NGC 1614. We have found that the circumnuclear ring surrounds a low-emission and compact ($r \lesssim 90$ pc) region at the very center of the galaxy, with a non-thermal steep spectrum ($\alpha_{\rm syn} \simeq -1.3$), suggesting that the central source is not powered by an AGN, but rather by a compact starburst. Furthermore, our modelings of both the SED and the *Chandra* X-ray spectrum supports this scenario, with no need to invoke an AGN to explain the observed bolometric properties of the galaxy.

- We have also performed a multiwavelength analysis on a sample of 11 additional local LIRGs, for which NGC 1614 was a case study. We used VLA X-band radio images (3.6 cm) and near-IR K-band (2.2 μm) from both Gemini and the VLT. We have found an overall correlation, although the radio-to-near-IR ratio does not follow a common pattern. We have also found an off-nuclear starburst region in the LIRG IRAS 16516-0948, likely triggered by the interaction and merging process. We have also studied the spectral indices of the sources, which are mostly consistent with what is expected for starburst galaxies, with the exception of IRAS 18293-3413, which presents a very steep spectrum. Finally, we have modeled the complete SED with a combination of starburst and AGN models to derive the relevant physical parameters of six of the LIRGs in our sample. Our SED modeling results are compatible with those obtained from the mid-IR AGN indicators. Five out of the six LIRGs modeled are SB dominated (two are pure starbursts), while NGC 6926 is dominated by its AGN emission.

- We have monitored the main radio component of the LIRG NGC 3690E, Arp 299-A, through multi-epoch very high resolution EVN observations, and studied the nature and evolution of the compact sources detected in the system. We confirmed 25 compact sources, most of them being SNe or SN remnants, with al least two new exploding CCSNe in our 2.5 yr study. We found a CCSN rate $\gtrsim 0.80\,\mathrm{SN\,yr^{-1}}$, with most of the star formation in Arp 299-A taking place in the central ~ 150 pc.

- The analysis of preliminary e-MERLIN data of the legacy project LIRGI led us to the discovery of the radio counterpart of the supernova 2010P in the outskirts of Arp 299, and its classification as a Type IIb through the modeling of its light curve at four different radio bands in 13 epochs. SN2010P is the first radio SN detected in the outskirts of a bright component of Arp 299 so far. We have also studied the properties of another supernova, SN2010O, which exploded only three days before SN2010P. The lack of detection in both early- and late-time observations suggests a Type Ib for this SN.

- We have studied the radial distribution of supernovae in the innermost region of one ULIRG (Arp 220), one LIRG (Arp 299) and one lower luminosity starburst galaxy (M82) using radio-VLBI techniques, which provide very high angular resolution with no dust obscuration effects. Standard models of nuclear starbursts are based on the premise of streams of gas inflows driven to the galactic nuclear regions, where large reservoirs of gas, namely nuclear disks, are formed and where the conditions for massive bursts of star formation are met. We have found evidences of the existence of these nuclear disks of molecular gas through the study of the radial distribution of supernovae. We derived scale length values between ~ 20 pc and ~ 160 pc. Our results are in good agreement with numerical simulations that predict nuclear disks of sizes $\lesssim 100$ pc forming around SMBHs.

Nothing is so dangerous to the progress of the human mind than to assume that our views of Science are ultimate, that there are no mysteries in Nature, that our triumphs are complete and that there are no new worlds to conquer.

Humphry Davy

8

Future perspectives

In the short-term, our aim is to complete and publish our work on the molecular gas observations with the IRAM 30 m telescope and on the multiwavelength analysis of our sample of 11 LIRGs. Besides that, there are several medium-term projects directly linked with the study of (U)LIRGs in which I have already been working or whose outline is defined:

- **LIRGI project** - Quality LIRGI observations are now starting to be performed with e-MERLIN. I have been involved in the preparation and the strategy of the observations. I have also worked with commissioning data, as well as in the characterization of the sample, and I will also work in the reduction and analysis of the data. Moreover, polarization and rotation measure observations will allow us to constrain the magnetic field properties of these galaxies. Simultaneously, EVN observations are being carried out on the 42 LIRGI sources, complementing e-MERLIN data with the innermost compact nuclear structures of these sources.

- **The radial distribution of supernovae** - The next step in this line of research is to obtain a statistically significant number of (U)LIRGs for which their radial

distribution can be obtained, thus allowing us to generalize the results presented in this work. Due to the high resolution needed to detect individual supernovae in the inner few hundred parsecs around the nuclei of other galaxies, available data are scarce. However, the EVN LIRGI observations mentioned in the previous point is observing potential candidates to host new SN factories, which will allow to extend our study and confirm our results.

- **Core-collapse supernova detection simulations** - There is a mismatch of a factor of ~ 2 between the measured CCSN rate from optical surveys and the cosmic massive star formation rate (Horiuchi *et al.*, 2011). At least $\sim 20\%$ of the exploding CCSNe in the local Universe are hidden behind dust (Mattila *et al.*, 2012), and this fraction increases with redshift. Although radio observations are not affected by dust extinction, there are several conditions under which CCSN detections can be hindered. We are performing simulations using mock-up compact sources injected in the uv-plane under different scenarios to study this effect and estimate the real CCSN rate.

- **Multiple AGN activity** - There is a growing evidence that mergers are the way through which SMBH form and evolve. Identifying AGN systems and close AGN pairs is crucial to our understanding of the black hole assembly history. I am involved in a project[1] aimed at unveiling multiple AGN activity in galaxy mergers using a multiwavelength approach. Very recently, we submitted a VLA proposal aimed at studying the radio properties of a sample of 16 multiple AGN systems (proposal code: 15A-057; PI: R. Herrero-Illana).

Furthermore, results from both our CO sample from Chapter 2 and LIRGI will lead to select the most suitable sources for which to obtain interferometric mm-observations using ALMA and/or the Plateau de Bure Interferometer (PdBI) to spatially resolve their molecular gas and study them in detail.

Many questions remain open in the field of (U)LIRGs. With the sensitivity and resolution achieved by new and coming instrumentation (e.g., ALMA, SKA or E-ELT), our comprehension of the classical questions are beginning to be answered and new questions are arising.

[1] Our ISSI team website is located in `http://www.issibern.ch/teams/agnactivity`

The study of local LIRGs and ULIRGs, especially with the high spatial resolution provided by current and future astronomical facilities, remain an essential ingredient to understand the star-forming galaxies at high redshift, where they dominate the cosmic infrared emission and play a key role in the formation and evolution of galaxies.

References

Aalto, S., Booth, R.S., Black, J.H. & Johansson, L.E.B. (1995). Molecular gas in starburst galaxies: line intensities and physical conditions. *A&A*, **300**, 369. 20, 47, 48

Alberdi, A., Colina, L., Torrelles, J.M., Panagia, N., Wilson, A.S. & Garrington, S.T. (2006). Evolution of the Circumnuclear Radio Supernova SN 2000ft in NGC 7469. *ApJ*, **638**, 938–945. 70

Allen, M.L. & Kronberg, P.P. (1998). Radio Spectra of Selected Compact Sources in the Nucleus of M82. *ApJ*, **502**, 218. 148

Alonso-Herrero, A., Rieke, G.H., Rieke, M.J. & Scoville, N.Z. (2000). Extreme Star Formation in the Interacting Galaxy Arp 299 (IC 694+NGC 3690). *ApJ*, **532**, 845–866. 57, 96, 115, 119, 184

Alonso-Herrero, A., Engelbracht, C.W., Rieke, M.J., Rieke, G.H. & Quillen, A.C. (2001). NGC 1614: A Laboratory for Starburst Evolution. *ApJ*, **546**, 952–965. 4, 54, 57, 67, 68, 73, 77

Alonso-Herrero, A., Rieke, G.H., Rieke, M.J. & Kelly, D.M. (2003). The [Fe II] 1.644 Micron Emission in M82 and NGC 253: Is It a Measure of the Supernova Rate? *AJ*, **125**, 1210–1225. 66

Alonso-Herrero, A., Rieke, G.H., Rieke, M.J., Colina, L., Pérez-González, P.G. & Ryder, S.D. (2006). Near-Infrared and Star-forming Properties of Local Luminous Infrared Galaxies. *ApJ*, **650**, 835–849. 8

Alonso-Herrero, A., Rieke, G.H., Colina, L., Pereira-Santaella, M., García-Marín, M., Smith, J.D.T., Brandl, B., Charmandaris, V. & Armus, L. (2009). The Extreme Star Formation Activity of Arp 299 Revealed by Spitzer IRS Spectral Mapping. *ApJ*, **697**, 660–675. 119

Alonso-Herrero, A., Pereira-Santaella, M., Rieke, G.H. & Rigopoulou, D. (2012). Local Luminous Infrared Galaxies. II. Active Galactic Nucleus Activity from Spitzer/Infrared Spectrograph Spectra. *ApJ*, **744**, 2. 2, 54

Alonso-Herrero, A., Pereira-Santaella, M., Rieke, G.H., Diamond-Stanic, A.M., Wang, Y., Hernán-Caballero, A. & Rigopoulou, D. (2013a). Local Luminous Infrared Galaxies. III. Co-evolution of Black Hole Growth and Star Formation Activity? *ApJ*, **765**, 78. 10, 54

Alonso-Herrero, A., Roche, P.F., Esquej, P., González-Martín, O., Pereira-Santaella, M., Ramos Almeida, C., Levenson, N.A., Packham, C., Asensio Ramos, A., Mason, R.E., Rodríguez Espinosa, J.M., Alvarez, C., Colina, L., Aretxaga, I., Díaz-Santos, T., Perlman, E. & Telesco, C.M. (2013b). Uncovering the Deeply Embedded Active Galactic Nucleus Activity in the Nuclear Regions of the Interacting Galaxy Arp 299. *ApJ*, **779**, L14. 119

Anderson, J.P. & James, P.A. (2009). Comparisons of the radial distributions of core-collapse supernovae with those of young and old stellar populations. *MNRAS*, **399**, 559–573. 126, 154

Anderson, J.P., Habergham, S.M. & James, P.A. (2011). On the multiple supernova population of Arp 299: constraints on progenitor properties and host galaxy star formation characteristics. *MNRAS*, **416**, 567–579. 119, 184

Armus, L., Charmandaris, V., Bernard-Salas, J., Spoon, H.W.W., Marshall, J.A., Higdon, S.J.U., Desai, V., Teplitz, H.I., Hao, L., Devost, D., Brandl, B.R., Wu, Y., Sloan, G.C., Soifer, B.T., Houck, J.R. & Herter, T.L. (2007). Observations of Ultraluminous Infrared Galaxies with the Infrared Spectrograph on the Spitzer Space Telescope. II. The IRAS Bright Galaxy Sample. *ApJ*, **656**, 148–167. 75, 108

Armus, L., Mazzarella, J.M., Evans, A.S., Surace, J.A., Sanders, D.B., Iwasawa, K., Frayer, D.T., Howell, J.H., Chan, B., Petric, A., Vavilkin, T., Kim, D.C., Haan, S., Inami, H., Murphy, E.J., Appleton, P.N., Barnes, J.E., Bothun, G., Bridge, C.R., Charmandaris, V., Jensen, J.B., Kewley, L.J., Lord, S., Madore, B.F., Marshall, J.A., Melbourne, J.E., Rich, J., Satyapal, S., Schulz, B., Spoon, H.W.W.,

REFERENCES

Sturm, E., U, V., Veilleux, S. & Xu, K. (2009). GOALS: The Great Observatories All-Sky LIRG Survey. *PASP*, **121**, 559–576. 20, 86, 115

Arp, H. (1966). Atlas of Peculiar Galaxies. *ApJS*, **14**, 1. 183

Asmus, D., Gandhi, P., Smette, A., Hönig, S.F. & Duschl, W.J. (2011). Mid-infrared properties of nearby low-luminosity AGN at high angular resolution. *A&A*, **536**, A36. 81

Baan, W.A. & Klöckner, H.R. (2006). Radio properties of FIR-megamaser nuclei. *A&A*, **449**, 559–568. 89

Baan, W.A., Henkel, C. & Haschick, A.D. (1987). ZW 15107 + 0724 and the family of OH megamasers. *ApJ*, **320**, 154–158. 89

Baker, J.G. & Menzel, D.H. (1938). Physical Processes in Gaseous Nebulae. III. The Balmer Decrement. *ApJ*, **88**, 52. 68

Ballo, L., Braito, V., Della Ceca, R., Maraschi, L., Tavecchio, F. & Dadina, M. (2004). Arp 299: A Second Merging System with Two Active Nuclei? *ApJ*, **600**, 634–639. 110

Barbon, R., Ciatti, F. & Rosino, L. (1979). Photometric properties of type II supernovae. *A&A*, **72**, 287–292. 112

Barnes, J.E. & Hibbard, J.E. (2009). Identikit 1: A Modeling Tool for Interacting Disk Galaxies. *AJ*, **137**, 3071–3090. 8

Bartunov, O.S., Makarova, I.N. & Tsvetkov, D.I. (1992). The radial distribution of supernovae in galaxies. *A&A*, **264**, 428–432. 126

Batejat, F., Conway, J.E., Hurley, R., Parra, R., Diamond, P.J., Lonsdale, C.J. & Lonsdale, C.J. (2011). Resolution of the Compact Radio Continuum Sources in Arp220. *ApJ*, **740**, 95. 65

Bertram, T., Eckart, A., Fischer, S., Zuther, J., Straubmeier, C., Wisotzki, L. & Krips, M. (2007). Molecular gas in nearby low-luminosity QSO host galaxies. *A&A*, **470**, 571–583. 49

Beswick, R.J., Pedlar, A., Mundell, C.G. & Gallimore, J.F. (2001). A MERLIN neutral hydrogen absorption study of the luminous infrared merger NGC 6240. *MNRAS*, **325**, 151–158. 95

Bolatto, A.D., Wolfire, M. & Leroy, A.K. (2013). The CO-to-H_2 Conversion Factor. *ARA&A*, **51**, 207–268. 20

Bondi, M., Pérez-Torres, M.A., Herrero-Illana, R. & Alberdi, A. (2012). The nuclear starburst in Arp 299-A: from the 5.0 GHz VLBI radio light-curves to its core-collapse supernova rate. *A&A*, **539**, A134. 65, 74, 75, 111, 119, 120, 132

Botticella, M.T., Riello, M., Cappellaro, E., Benetti, S., Altavilla, G., Pastorello, A., Turatto, M., Greggio, L., Patat, F., Valenti, S., Zampieri, L., Harutyunyan, A., Pignata, G. & Taubenberger, S. (2008). Supernova rates from the Southern inTermediate Redshift ESO Supernova Search (STRESS). *A&A*, **479**, 49–66. 84

Bottinelli, L., Gouguenheim, L., Le Squeren, A.M., Martin, J.M., Dennefeld, M. & Paturel, G. (1986). New Extragalactic OH Megamasers. *IAU Circ.*, **4231**, 2. 89

Brandl, B.R., Bernard-Salas, J., Spoon, H.W.W., Devost, D., Sloan, G.C., Guilles, S., Wu, Y., Houck, J.R., Weedman, D.W., Armus, L., Appleton, P.N., Soifer, B.T., Charmandaris, V., Hao, L., Higdon, J.A., Marshall, S.J. & Herter, T.L. (2006). The Mid-Infrared Properties of Starburst Galaxies from Spitzer-IRS Spectroscopy. *ApJ*, **653**, 1129–1144. 105, 108, 109

Brunthaler, A., Menten, K.M., Reid, M.J., Henkel, C., Bower, G.C. & Falcke, H. (2009). Discovery of a bright radio transient in M 82: a new radio supernova? *A&A*, **499**, L17–L20. 148

Bruzual, G. & Charlot, S. (2003). Stellar population synthesis at the resolution of 2003. *MNRAS*, **344**, 1000–1028. 73, 105

Bryant, P.M. & Scoville, N.Z. (1999). High-Resolution CO Observations of Luminous Infrared Galaxies. *AJ*, **117**, 2632–2655. 20

Burbidge, E.M., Burbidge, G.R. & Rubin, V.C. (1964). A Study of the Velocity Field in M82 and its Bearing on Explosive Phenomena in that Galaxy. *ApJ*, **140**, 942–+. 148

Bushouse, H.A. (1986). Star-formation rates in the nuclei of violently interacting galaxies. *AJ*, **91**, 255–270. 4

REFERENCES

Calzetti, D., Armus, L., Bohlin, R.C., Kinney, A.L., Koornneef, J. & Storchi-Bergmann, T. (2000). The Dust Content and Opacity of Actively Star-forming Galaxies. *ApJ*, **533**, 682–695. 79

Calzetti, D., Kennicutt, R.C., Engelbracht, C.W., Leitherer, C., Draine, B.T., Kewley, L., Moustakas, J., Sosey, M., Dale, D.A., Gordon, K.D., Helou, G.X., Hollenbach, D.J., Armus, L., Bendo, G., Bot, C., Buckalew, B., Jarrett, T., Li, A., Meyer, M., Murphy, E.J., Prescott, M., Regan, M.W., Rieke, G.H., Roussel, H., Sheth, K., Smith, J.D.T., Thornley, M.D. & Walter, F. (2007). The Calibration of Mid-Infrared Star Formation Rate Indicators. *ApJ*, **666**, 870–895. 61

Cardelli, J.A., Clayton, G.C. & Mathis, J.S. (1989). The relationship between infrared, optical, and ultraviolet extinction. *ApJ*, **345**, 245–256. 68

Casey, C.M. (2012). Far-infrared spectral energy distribution fitting for galaxies near and far. *MNRAS*, **425**, 3094–3103. 43

Chandrasekhar, S. (1931). The Maximum Mass of Ideal White Dwarfs. *ApJ*, **74**, 81. 5

Charmandaris, V., Stacey, G.J. & Gull, G. (2002). Resolving the Buried Starburst in Arp 299. *ApJ*, **571**, 282–287. 119

Chevalier, R.A. (1982a). Are young supernova remnants interacting with circumstellar gas. *ApJ*, **259**, L85–L89. 112

Chevalier, R.A. (1982b). The radio and X-ray emission from type II supernovae. *ApJ*, **259**, 302–310. 84, 112

Colbert, E.J.M., Wilson, A.S. & Bland-Hawthorn, J. (1994). The radio emission from the ultraluminous far-infrared galaxy NGC 6240. *ApJ*, **436**, 89–101. 95, 102

Colina, L. (1993). Forbidden Fe II 1.64 micron emission in high-luminosity and ultraluminous IRAS galaxies. *ApJ*, **411**, 565–569. 66

Colina, L. & Perez-Olea, D. (1992). On the origin of the radio emission in IRAS galaxies with high and ultrahigh luminosity - The starburst-AGN controversy. *MNRAS*, **259**, 709–724. 66

Colina, L., Sparks, W.B. & Macchetto, F. (1991). IC 5063 - A merger remnant with a hidden luminous active nucleus. *ApJ*, **370**, 102–117. 68

Colina, L., Alberdi, A., Torrelles, J.M., Panagia, N. & Wilson, A.S. (2001). Discovery of a Bright Radio Supernova in the Circumnuclear Starburst of the Luminous Infrared Seyfert 1 Galaxy NGC 7469. *ApJ*, **553**, L19–L22. 84

Condon, J.J. (1992). Radio emission from normal galaxies. *ARA&A*, **30**, 575–611. 5, 11, 68

Condon, J.J. & Broderick, J.J. (1988). Radio identifications of UGC galaxies - Starbursts and monsters. *AJ*, **96**, 30–61. 6

Condon, J.J. & Broderick, J.J. (1991). Radio properties of extragalactic IRAS sources. *AJ*, **102**, 1663–1679. 6

Condon, J.J., Cotton, W.D., Greisen, E.W., Yin, Q.F., Perley, R.A., Taylor, G.B. & Broderick, J.J. (1998). The NRAO VLA Sky Survey. *AJ*, **115**, 1693–1716. 54, 86

Corbett, E.A., Kewley, L., Appleton, P.N., Charmandaris, V., Dopita, M.A., Heisler, C.A., Norris, R.P., Zezas, A. & Marston, A. (2003). COLA. II. Radio and Spectroscopic Diagnostics of Nuclear Activity in Galaxies. *ApJ*, **583**, 670–688. 89

Corwin, H.G. (2004). History and Accurate Positions for the NGC/IC Objects. *VizieR Online Data Catalog*, **7239**, 0. 184

Costagliola, F., Aalto, S., Rodriguez, M.I., Muller, S., Spoon, H.W.W., Martín, S., Peréz-Torres, M.A., Alberdi, A., Lindberg, J.E., Batejat, F., Jütte, E., van der Werf, P. & Lahuis, F. (2011). Molecules as tracers of galaxy evolution: an EMIR survey. I. Presentation of the data and first results. *A&A*, **528**, A30. 22, 44, 48

Cram, L., Hopkins, A., Mobasher, B. & Rowan-Robinson, M. (1998). Star Formation Rates in Faint Radio Galaxies. *ApJ*, **507**, 155–160. 4

Crocker, A., Krips, M., Bureau, M., Young, L.M., Davis, T.A., Bayet, E., Alatalo, K., Blitz, L., Bois, M., Bournaud, F., Cappellari, M., Davies, R.L., de Zeeuw, P.T., Duc, P.A.,

Emsellem, E., Khochfar, S., Krajnović, D., Kuntschner, H., Lablanche, P.Y., McDermid, R.M., Morganti, R., Naab, T., Oosterloo, T., Sarzi, M., Scott, N., Serra, P. & Weijmans, A.M. (2012). The ATLAS^{3D} project - XI. Dense molecular gas properties of CO-luminous early-type galaxies. *MNRAS*, **421**, 1298–1314. 48

Dahlen, T., Strolger, L.G., Riess, A.G., Mobasher, B., Chary, R.R., Conselice, C.J., Ferguson, H.C., Fruchter, A.S., Giavalisco, M., Livio, M., Madau, P., Panagia, N. & Tonry, J.L. (2004). High-Redshift Supernova Rates. *ApJ*, **613**, 189–199. 84

Dametto, N.Z., Riffel, R., Pastoriza, M.G., Rodríguez-Ardila, A., Hernandez-Jimenez, J.A. & Carvalho, E.A. (2014). Probing the circumnuclear stellar populations of starburst galaxies in the near-infrared. *MNRAS*, **443**, 1754–1778. 93

Davies, R., Mark, D. & Sternberg, A. (2012). Dense molecular gas around AGN: HCN/CO in NGC 3227. *A&A*, **537**, A133. 49

Davies, R.I., Tacconi, L.J. & Genzel, R. (2004a). The Nuclear Gas Dynamics and Star Formation of Markarian 231. *ApJ*, **613**, 781–793. 154

Davies, R.I., Tacconi, L.J. & Genzel, R. (2004b). The Nuclear Gasdynamics and Star Formation of NGC 7469. *ApJ*, **602**, 148–161. 154

de Jong, T., Klein, U., Wielebinski, R. & Wunderlich, E. (1985). Radio continuum and far-infrared emission from spiral galaxies - A close correlation. *A&A*, **147**, L6–L9. 5

de Vaucouleurs, G., de Vaucouleurs, A., Corwin, H.G., Jr., Buta, R.J., Paturel, G. & Fouqué, P. (1991). *Third Reference Catalogue of Bright Galaxies. Volume I: Explanations and references. Volume II: Data for galaxies between 0^h and 12^h. Volume III: Data for galaxies between 12^h and 24^h.*. New York: Springer. 54

Depoy, D.L., Wynn-Williams, C.G., Hill, G.J. & Becklin, E.E. (1988). IRAS 17138 - 1017 - A highly obscured luminous starburst galaxy. *AJ*, **95**, 398–407. 90

Di Matteo, P., Combes, F., Melchior, A.L. & Semelin, B. (2007). Star formation efficiency in galaxy interactions and mergers: a statistical study. *A&A*, **468**, 61–81. 124

Diamond-Stanic, A.M. & Rieke, G.H. (2012). The Relationship between Black Hole Growth and Star Formation in Seyfert Galaxies. *ApJ*, **746**, 168. 7

Díaz-Santos, T., Alonso-Herrero, A., Colina, L., Ryder, S.D. & Knapen, J.H. (2007). Resolving the Stellar Populations in the Circumnuclear Ring of NGC 7469. *ApJ*, **661**, 149–164. 93

Díaz-Santos, T., Alonso-Herrero, A., Colina, L., Packham, C., Radomski, J.T. & Telesco, C.M. (2008). Understanding the 8 μm versus Paα Relationship on Subarcsecond Scales in Luminous Infrared Galaxies. *ApJ*, **685**, 211–224. 57, 60, 61, 74

Díaz-Santos, T., Alonso-Herrero, A., Colina, L., Packham, C., Levenson, N.A., Pereira-Santaella, M., Roche, P.F. & Telesco, C.M. (2010). A High Spatial Resolution Mid-Infrared Spectroscopic Study of the Nuclei and Star-Forming Regions in Luminous Infrared Galaxies. *ApJ*, **711**, 328–349. 61

Díaz-Santos, T., Charmandaris, V., Armus, L., Stierwalt, S., Haan, S., Mazzarella, J.M., Howell, J.H., Veilleux, S., Murphy, E.J., Petric, A.O., Appleton, P., Evans, A.S., Sanders, D.B. & Surace, J.A. (2011). The Spatial Extent of (U)LIRGS in the Mid-infrared. II. Feature Emission. *ApJ*, **741**, 32. 88

Dicke, R.H., Peebles, P.J.E., Roll, P.G. & Wilkinson, D.T. (1965). Cosmic Black-Body Radiation. *ApJ*, **142**, 414–419. 10

Dickey, J.M. & Lockman, F.J. (1990). H I in the Galaxy. *ARA&A*, **28**, 215–261. 66

Diehl, R., Halloin, H., Kretschmer, K., Lichti, G.G., Schönfelder, V., Strong, A.W., von Kienlin, A., Wang, W., Jean, P., Knödlseder, J., Roques, J.P., Weidenspointner, G., Schanne, S., Hartmann, D.H., Winkler, C. & Wunderer, C. (2006). Radioactive ^{26}Al from massive stars in the Galaxy. *Nature*, **439**, 45–47. 5

Downes, D. & Solomon, P.M. (1998). Rotating Nuclear Rings and Extreme Starbursts in Ultraluminous Galaxies. *ApJ*, **507**, 615–654. 20, 43, 49

REFERENCES

Efstathiou, A. & Rowan-Robinson, M. (1995). Dusty discs in active galactic nuclei. *MNRAS*, **273**, 649–661. 75

Efstathiou, A. & Siebenmorgen, R. (2009). Starburst and cirrus models for submillimeter galaxies. *A&A*, **502**, 541–548. 73, 105

Efstathiou, A., Rowan-Robinson, M. & Siebenmorgen, R. (2000). Massive star formation in galaxies: radiative transfer models of the UV to millimetre emission of starburst galaxies. *MNRAS*, **313**, 734–744. 4, 73

Efstathiou, A., Christopher, N., Verma, A. & Siebenmorgen, R. (2013). Active galactic nucleus torus models and the puzzling infrared spectrum of IRAS F10214+4724. *MNRAS*, **436**, 1873–1882. 105

Esquej, P., Alonso-Herrero, A., González-Martín, O., Hönig, S.F., Hernán-Caballero, A., Roche, P., Ramos Almeida, C., Mason, R.E., Díaz-Santos, T., Levenson, N.A., Aretxaga, I., Rodríguez Espinosa, J.M. & Packham, C. (2014). Nuclear Star Formation Activity and Black Hole Accretion in Nearby Seyfert Galaxies. *ApJ*, **780**, 86. 7

Fabian, A.C. (1999). Active Galactic Nuclei. *Proceedings of the National Academy of Science*, **96**, 4749–4751. 6

Farrah, D., Afonso, J., Efstathiou, A., Rowan-Robinson, M., Fox, M. & Clements, D. (2003). Starburst and AGN activity in ultraluminous infrared galaxies. *MNRAS*, **343**, 585–607. 2

Farrah, D., Bernard-Salas, J., Spoon, H.W.W., Soifer, B.T., Armus, L., Brandl, B., Charmandaris, V., Desai, V., Higdon, S., Devost, D. & Houck, J. (2007). High-Resolution Mid-Infrared Spectroscopy of Ultraluminous Infrared Galaxies. *ApJ*, **667**, 149–169. 85

Farrah, D., Connolly, B., Connolly, N., Spoon, H.W.W., Oliver, S., Prosper, H.B., Armus, L., Houck, J.R., Liddle, A.R. & Desai, V. (2009). An Evolutionary Paradigm for Dusty Active Galaxies at Low Redshift. *ApJ*, **700**, 395–416. 8

Fenech, D.M., Muxlow, T.W.B., Beswick, R.J., Pedlar, A. & Argo, M.K. (2008). Deep MERLIN 5GHz radio imaging of supernova remnants in the M82 starburst. *MNRAS*, **391**, 1384–1402. 148, 154

Freeman, K.C. (1970). On the Disks of Spiral and so Galaxies. *ApJ*, **160**, 811. 128

Gallais, P., Charmandaris, V., Le Floc'h, E., Mirabel, I.F., Sauvage, M., Vigroux, L. & Laurent, O. (2004). Dust enshrouded star-forming activity in Arp 299. *A&A*, **414**, 845–855. 119

Gallimore, J.F. & Beswick, R. (2000). Possible Radio Supernova in NGC 6240. *IAU Circ.*, **7428**, 1. 95

Gallimore, J.F. & Beswick, R. (2004). Parsec-Scale Radio Structure of the Double Active Nucleus of NGC 6240. *AJ*, **127**, 239–251. 89, 95

Garrett, M.A. (2002). The FIR/Radio correlation of high redshift galaxies in the region of the HDF-N. *A&A*, **384**, L19–L22. 6

Gehrels, N. (1986). Confidence limits for small numbers of events in astrophysical data. *ApJ*, **303**, 336–346. 129

Gehrz, R.D., Sramek, R.A. & Weedman, D.W. (1983). Star bursts and the extraordinary galaxy NGC 3690. *ApJ*, **267**, 551–562. 88, 185

Genzel, R., Lutz, D., Sturm, E., Egami, E., Kunze, D., Moorwood, A.F.M., Rigopoulou, D., Spoon, H.W.W., Sternberg, A., Tacconi-Garman, L.E., Tacconi, L. & Thatte, N. (1998). What Powers Ultraluminous IRAS Galaxies? *ApJ*, **498**, 579. 12, 75, 105, 108

Graciá-Carpio, J., García-Burillo, S., Planesas, P. & Colina, L. (2006). Is HCN a True Tracer of Dense Molecular Gas in Luminous and Ultraluminous Infrared Galaxies? *ApJ*, **640**, L135–L138. 22, 44

Greenhill, L.J., Kondratko, P.T., Lovell, J.E.J., Kuiper, T.B.H., Moran, J.M., Jauncey, D.L. & Baines, G.P. (2003). The Discovery of H_2O Maser Emission in Seven Active Galactic Nuclei and at High Velocities in the Circinus Galaxy. *ApJ*, **582**, L11–L14. 91

REFERENCES

Greenhouse, M.A., Woodward, C.E., Thronson, H.A., Jr., Rudy, R.J., Rossano, G.S., Erwin, P. & Puetter, R.C. (1991). Near-infrared forbidden Fe II emission of M82 supernova remnants - Implications for tracing the supernova content of galaxies. *ApJ*, **383**, 164–173. 66

Haan, S., Surace, J.A., Armus, L., Evans, A.S., Howell, J.H., Mazzarella, J.M., Kim, D.C., Vavilkin, T., Inami, H., Sanders, D.B., Petric, A., Bridge, C.R., Melbourne, J.L., Charmandaris, V., Diaz-Santos, T., Murphy, E.J., U, V., Stierwalt, S. & Marshall, J.A. (2011). The Nuclear Structure in Nearby Luminous Infrared Galaxies: Hubble Space Telescope NICMOS Imaging of the GOALS Sample. *AJ*, **141**, 100. 90, 100, 101

Habergham, S.M., James, P.A. & Anderson, J.P. (2012). A central excess of stripped-envelope supernovae within disturbed galaxies. *MNRAS*, **424**, 2841–2853. 154

Hakobyan, A.A., Mamon, G.A., Petrosian, A.R., Kunth, D. & Turatto, M. (2009). The radial distribution of core-collapse supernovae in spiral host galaxies. *A&A*, **508**, 1259–1268. 126, 127, 128, 130, 131, 151, 152, 153, 154

Hakobyan, A.A., Adibekyan, V.Z., Aramyan, L.S., Petrosian, A.R., Gomes, J.M., Mamon, G.A., Kunth, D. & Turatto, M. (2012). Supernovae and their host galaxies. I. The SDSS DR8 database and statistics. *A&A*, **544**, A81. 154

Harkness, R.P. & Wheeler, J.C. (1990). Classification of supernovae. In A. G. Petschek, ed., *Supernovae*, 1–29. 112

Heckman, T.M., Lehnert, M.D. & Armus, L. (1993). Galactic Superwinds. In J.M. Shull & H.A. Thronson, eds., *The Environment and Evolution of Galaxies*, vol. 188 of *Astrophysics and Space Science Library*, 455. 95

Heesen, V., Beck, R., Krause, M. & Dettmar, R.J. (2011). Cosmic rays and the magnetic field in the nearby starburst galaxy NGC 253 III. Helical magnetic fields in the nuclear outflow. *A&A*, **535**, A79. 74

Helou, G., Soifer, B.T. & Rowan-Robinson, M. (1985). Thermal infrared and nonthermal radio - Remarkable correlation in disks of galaxies. *ApJ*, **298**, L7–L11. 5, 54, 86

Hernández-García, L., González-Martín, O., Márquez, I. & Masegosa, J. (2013). X-ray spectral variability of seven LINER nuclei with XMM-Newton and Chandra data. *A&A*, **556**, A47. 58

Herrero-Illana, R., Pérez-Torres, M.Á. & Alberdi, A. (2012a). Evidence of nuclear disks in starburst galaxies from their radial distribution of supernovae. *A&A*, **540**, L5. 123, 126

Herrero-Illana, R., Romero-Canizales, C., Perez-Torres, M.A., Alberdi, A., Kankare, E., Mattila, S. & Ryder, S.D. (2012b). Radio detection of the near-IR discovered supernova 2010P. *The Astronomer's Telegram*, **4432**, 1. 111, 117

Herrero-Illana, R., Pérez-Torres, M.Á., Alonso-Herrero, A., Alberdi, A., Colina, L., Efstathiou, A., Hernández-García, L., Miralles-Caballero, D., Väisänen, P., Packham, C.C., Rajpaul, V. & Zijlstra, A.A. (2014). A Multi-wavelength View of the Central Kiloparsec Region in the Luminous Infrared Galaxy NGC 1614. *ApJ*, **786**, 156. 53

Hewish, A., Bell, S.J., Pilkington, J.D.H., Scott, P.F. & Collins, R.A. (1968). Observation of a Rapidly Pulsating Radio Source. *Nature*, **217**, 709–713. 10

Hibbard, J.E. & Yun, M.S. (1999). A 180 Kiloparsec Tidal Tail in the Luminous Infrared Merger ARP 299. *AJ*, **118**, 162–185. 183

Hopkins, P.F. (2012). Dynamical delays between starburst and AGN activity in galaxy nuclei. *MNRAS*, **420**, L8–L12. 10

Hopkins, P.F., Hernquist, L., Cox, T.J. & Kereš, D. (2008). A Cosmological Framework for the Co-Evolution of Quasars, Supermassive Black Holes, and Elliptical Galaxies. I. Galaxy Mergers and Quasar Activity. *ApJS*, **175**, 356–389. 8, 9

Horiuchi, S., Beacom, J.F., Kochanek, C.S., Prieto, J.L., Stanek, K.Z. & Thompson, T.A. (2011). The Cosmic Core-collapse Supernova Rate Does Not Match the Massive-star Formation Rate. *ApJ*, **738**, 154. 162

REFERENCES

Hulse, R.A. & Taylor, H.J. (1974). Discovery of a Pulsar in a Close Binary System. In *Bulletin of the American Astronomical Society*, vol. 6 of *Bulletin of the American Astronomical Society*, 453. 10

Imanishi, M. & Nakanishi, K. (2006). Infrared 2-4 Micrometer Spectroscopy and Millimeter Interferometric HCN and HCO^+ Observations of the Individual Merging Components of Arp 299. *PASJ*, **58**, 813–828. 49

Imanishi, M. & Nakanishi, K. (2013). High-density Molecular Gas Properties of the Starburst Galaxy NGC1614 Revealed with ALMA. *AJ*, **146**, 47. 61

Inami, H., Armus, L., Surace, J.A., Mazzarella, J.M., Evans, A.S., Sanders, D.B., Howell, J.H., Petric, A., Vavilkin, T., Iwasawa, K., Haan, S., Murphy, E.J., Stierwalt, S., Appleton, P.N., Barnes, J.E., Bothun, G., Bridge, C.R., Chan, B., Charmandaris, V., Frayer, D.T., Kewley, L.J., Kim, D.C., Lord, S., Madore, B.F., Marshall, J.A., Matsuhara, H., Melbourne, J.E., Rich, J., Schulz, B., Spoon, H.W.W., Sturm, E., U, V., Veilleux, S. & Xu, K. (2010). The Buried Starburst in the Interacting Galaxy II Zw 096 as Revealed by the Spitzer Space Telescope. *AJ*, **140**, 63–74. 100

Inami, H., Armus, L., Charmandaris, V., Groves, B., Kewley, L., Petric, A., Stierwalt, S., Díaz-Santos, T., Surace, J., Rich, J., Haan, S., Howell, J., Evans, A.S., Mazzarella, J., Marshall, J., Appleton, P., Lord, S., Spoon, H., Frayer, D., Matsuhara, H. & Veilleux, S. (2013). Mid-infrared Atomic Fine-structure Emission-line Spectra of Luminous Infrared Galaxies: Spitzer/IRS Spectra of the GOALS Sample. *ApJ*, **777**, 156. 108

Ishihara, D., Onaka, T., Kataza, H., Salama, A., Alfageme, C., Cassatella, A., Cox, N., García-Lario, P., Stephenson, C., Cohen, M., Fujishiro, N., Fujiwara, H., Hasegawa, S., Ita, Y., Kim, W., Matsuhara, H., Murakami, H., Müller, T.G., Nakagawa, T., Ohyama, Y., Oyabu, S., Pyo, J., Sakon, I., Shibai, H., Takita, S., Tanabé, T., Uemizu, K., Ueno, M., Usui, F., Wada, T., Watarai, H., Yamamura, I. & Yamauchi, C. (2010). The AKARI/IRC mid-infrared all-sky survey. *A&A*, **514**, A1. 73

Israel, F. (2000). Extragalactic H_2 and its Variable Relation to CO. In F. Combes & G. Pineau Des Forets, eds., *Molecular Hydrogen in Space*, 293. 20

Iwasawa, K., Sanders, D.B., Teng, S.H., U, V., Armus, L., Evans, A.S., Howell, J.H., Komossa, S., Mazzarella, J.M., Petric, A.O., Surace, J.A., Vavilkin, T., Veilleux, S. & Trentham, N. (2011). C-GOALS: Chandra observations of a complete sample of luminous infrared galaxies from the IRAS Revised Bright Galaxy Survey. *A&A*, **529**, A106. 66

Jansky, K.G. (1933). Electrical phenomena that apparently are of interstellar origin. *Popular Astronomy*, **41**, 548–555. 10

Jha, S., Garnavich, P., Kirshner, R., Koranyi, D. & Calkins, M. (1998). Supernova 1998V in NGC 6627. *IAU Circ.*, **6844**, 1. 184

Johnson, H.L. (1966). Infrared Photometry of Galaxies. *ApJ*, **143**, 187. 2

Kalberla, P.M.W., Burton, W.B., Hartmann, D., Arnal, E.M., Bajaja, E., Morras, R. & Pöppel, W.G.L. (2005). The Leiden/Argentine/Bonn (LAB) Survey of Galactic HI. Final data release of the combined LDS and IAR surveys with improved stray-radiation corrections. *A&A*, **440**, 775–782. 66

Kangas, T., Mattila, S., Kankare, E., Kotilainen, J.K., Väisänen, P., Greimel, R. & Takalo, A. (2013). Spatial distributions of core-collapse supernovae in infrared-bright galaxies. *MNRAS*, **436**, 3464–3479. 154

Kankare, E., Mattila, S., Ryder, S., Pérez-Torres, M.A., Alberdi, A., Romero-Canizales, C., Díaz-Santos, T., Väisänen, P., Efstathiou, A., Alonso-Herrero, A., Colina, L. & Kotilainen, J. (2008). Discovery of a Very Highly Extinguished Supernova in a Luminous Infrared Galaxy. *ApJ*, **689**, L97–L100. 84, 90

Kankare, E., Mattila, S., Ryder, S., Fraser, M., Pastorello, A., Elias-Rosa, N., Romero-Cañizales, C., Alberdi, A., Hentunen, V.P., Herrero-Illana, R., Kotilainen, J., Pérez-Torres, M.A. & Väisänen, P. (2014). The nature of supernovae 2010O and 2010P in Arp 299 - I. Near-infrared and optical evolution. *MNRAS*, **440**, 1052–1066. 111, 117

REFERENCES

Kawakatu, N. & Umemura, M. (2002). Radiation drag driven mass accretion in a clumpy interstellar medium: implications for the supermassive black hole-to-bulge relation. *MNRAS*, **329**, 572–578. 124

Kawakatu, N. & Wada, K. (2008). Coevolution of Supermassive Black Holes and Circumnuclear Disks. *ApJ*, **681**, 73–83. 124, 125, 126, 154, 155

Keel, W.C. & Wu, W. (1995). The Local Merger Rate of Disk Galaxies. *AJ*, **110**, 129. 88

Kennicutt, R.C. & Evans, N.J. (2012). Star Formation in the Milky Way and Nearby Galaxies. *ARA&A*, **50**, 531–608. 19

Kennicutt, R.C., Jr. (1998). Star Formation in Galaxies Along the Hubble Sequence. *ARA&A*, **36**, 189–232. 4, 84

Kennicutt, R.C., Jr., Roettiger, K.A., Keel, W.C., van der Hulst, J.M. & Hummel, E. (1987). The effects of interactions on spiral galaxies. II - Disk star-formation rates. *AJ*, **93**, 1011–1023. 4

Kewley, L.J., Dopita, M.A., Sutherland, R.S., Heisler, C.A. & Trevena, J. (2001). Theoretical Modeling of Starburst Galaxies. *ApJ*, **556**, 121–140. 4

Kim, D.C., Sanders, D.B., Veilleux, S., Mazzarella, J.M. & Soifer, B.T. (1995). Optical Spectroscopy of Luminous Infrared Galaxies. I. Nuclear Data. *ApJS*, **98**, 129. 89

Kloeckner, H.., Rawlings, S., Heywood, I., Beswick, R., Muxlow, T.W.B., Garrington, S.T., Hatchell, J., Hoare, M.G., Jarvis, M.J., Jones, I. & van Langevelde, H.J. (2011). Goonhilly: a new site for e-MERLIN and the EVN. *ArXiv e-prints*. 114

Kohno, K., Ishizuki, S., Matsushita, S., Vila-Vilaró, B. & Kawabe, R. (2003). Enhanced HCN (1-0) Emission in the Type-1 Seyfert Galaxy NGC 1097. *PASJ*, **55**, L1–L5. 49

Komossa, S., Burwitz, V., Hasinger, G., Predehl, P., Kaastra, J.S. & Ikebe, Y. (2003). Discovery of a Binary Active Galactic Nucleus in the Ultraluminous Infrared Galaxy NGC 6240 Using Chandra. *ApJ*, **582**, L15–L19. 89, 95

König, S., Aalto, S., Muller, S., Beswick, R.J. & Gallagher, J.S. (2013). The NGC 1614 interacting galaxy. Molecular gas feeding a "ring of fire". *A&A*, **553**, A72. 54, 61, 69

Kormendy, J., Bender, R. & Cornell, M.E. (2011). Supermassive black holes do not correlate with galaxy disks or pseudobulges. *Nature*, **469**, 374–376. 8

Kotilainen, J.K., Reunanen, J., Laine, S. & Ryder, S.D. (2001). Near-infrared line imaging of the starburst galaxies NGC 520, NGC 1614 and NGC 7714. *A&A*, **366**, 439–450. 68

Kruegel, E., Chini, R. & Steppe, H. (1990). CO in Markarian galaxies. *A&A*, **229**, 17–27. 49

Lacki, B.C. & Thompson, T.A. (2010). The Physics of the Far-infrared-Radio Correlation. II. Synchrotron Emission as a Star Formation Tracer in High-redshift Galaxies. *ApJ*, **717**, 196–208. 6

Lacki, B.C., Thompson, T.A. & Quataert, E. (2010). The Physics of the Far-infrared-Radio Correlation. I. Calorimetry, Conspiracy, and Implications. *ApJ*, **717**, 1–28. 6

Lagache, G., Puget, J.L. & Dole, H. (2005). Dusty Infrared Galaxies: Sources of the Cosmic Infrared Background. *ARA&A*, **43**, 727–768. 2

Langer, W.D. & Penzias, A.A. (1990). C-12/C-13 isotope ratio across the Galaxy from observations of C-13/O-18 in molecular clouds. *ApJ*, **357**, 477–492. 21

Larson, R.B. (1981). Turbulence and star formation in molecular clouds. *MNRAS*, **194**, 809–826. 20

Leitherer, C. & Heckman, T.M. (1995). Synthetic properties of starburst galaxies. *ApJS*, **96**, 9–38. 4, 96

Leitherer, C., Schaerer, D., Goldader, J.D., González Delgado, R.M., Robert, C., Kune, D.F., de Mello, D.F., Devost, D. & Heckman, T.M. (1999). Starburst99: Synthesis Models for Galaxies with Active Star Formation. *ApJS*, **123**, 3–40. 4, 73, 77

Li, W., Chornock, R., Leaman, J., Filippenko, A.V., Poznanski, D., Wang, X., Ganeshalingam, M. & Mannucci, F. (2011). Nearby

supernova rates from the Lick Observatory Supernova Search - III. The rate-size relation, and the rates as a function of galaxy Hubble type and colour. *MNRAS*, **412**, 1473–1507. 84

Li, W.D. (2002). Supernova 2002bw in Pgc 59990. *IAU Circ.*, **7864**, 2. 90

Lisenfeld, U., Voelk, H.J. & Xu, C. (1996). The FIR/radio correlation in starburst galaxies: constraints on starburst models. *A&A*, **314**, 745–753. 6

Lonsdale, C.J., Diamond, P.J., Thrall, H., Smith, H.E. & Lonsdale, C.J. (2006). VLBI Images of 49 Radio Supernovae in Arp 220. *ApJ*, **647**, 185–193. 124, 132, 136

Low, F.J. & Aumann, H.H. (1970). Observations of Galactic and Extragalactic Sources Between 50 and 300 Mi-Crons. *ApJ*, **162**, L79. 2

Magnelli, B., Elbaz, D., Chary, R.R., Dickinson, M., Le Borgne, D., Frayer, D.T. & Willmer, C.N.A. (2009). The 0.4 < z < 1.3 star formation history of the Universe as viewed in the far-infrared. *A&A*, **496**, 57–75. 4, 84

Maiolino, R., Vanzi, L., Mannucci, F., Cresci, G., Ghinassi, F. & Della Valle, M. (2002). Discovery of two infrared supernovae: A new window on the SN search. *A&A*, **389**, 84–92. 84

Mannucci, F., Maiolino, R., Cresci, G., Della Valle, M., Vanzi, L., Ghinassi, F., Ivanov, V.D., Nagar, N.M. & Alonso-Herrero, A. (2003). The infrared supernova rate in starburst galaxies. *A&A*, **401**, 519–530. 84

Maraston, C. (1998). Evolutionary synthesis of stellar populations: a modular tool. *MNRAS*, **300**, 872–892. 93

Marconi, A. & Hunt, L.K. (2003). The Relation between Black Hole Mass, Bulge Mass, and Near-Infrared Luminosity. *ApJ*, **589**, L21–L24. 7

Matheson, T., Jha, S., Challis, P., Kirshner, R. & Calkins, M. (2002). Supernova 2002bw in Pgc 59990. *IAU Circ.*, **7872**, 2. 90

Mattila, S. & Kankare, E. (2010). Supernova 2010P in Arp 299. *Central Bureau Electronic Telegrams*, **2145**, 1. 116, 117

Mattila, S. & Meikle, W.P.S. (2001). Supernovae in the nuclear regions of starburst galaxies. *MNRAS*, **324**, 325–342. 5, 71, 84

Mattila, S., Väisänen, P., Farrah, D., Efstathiou, A., Meikle, W.P.S., Dahlen, T., Fransson, C., Lira, P., Lundqvist, P., Östlin, G., Ryder, S. & Sollerman, J. (2007a). Adaptive Optics Discovery of Supernova 2004ip in the Nuclear Regions of the Luminous Infrared Galaxy IRAS 18293-3413. *ApJ*, **659**, L9–L12. 84

Mattila, S., Vaisanen, P., Meikle, P., Dahlen, T., Efstathiou, A., Farrah, D., Fransson, C., Lira, P., Lundqvist, P., Ostlin, G., Ryder, S. & Sollerman, J. (2007b). Supernova 2004ip in IRAS 18293-3413 = Psn K0409-001. *Central Bureau Electronic Telegrams*, **858**, 1. 84, 90

Mattila, S., Kankare, E., Datson, J. & Pastorello, A. (2010). Supernovae 2010O and 2010P. *Central Bureau Electronic Telegrams*, **2149**, 1. 116, 117

Mattila, S., Dahlen, T., Efstathiou, A., Kankare, E., Melinder, J., Alonso-Herrero, A., Pérez-Torres, M.Á., Ryder, S., Väisänen, P. & Östlin, G. (2012). Core-collapse Supernovae Missed by Optical Surveys. *ApJ*, **756**, 111. 106, 110, 162

Mauch, T. & Sadler, E.M. (2007). Radio sources in the 6dFGS: local luminosity functions at 1.4GHz for star-forming galaxies and radio-loud AGN. *MNRAS*, **375**, 931–950. 90

McDonald, A.R., Muxlow, T.W.B., Wills, K.A., Pedlar, A. & Beswick, R.J. (2002). A parsec-scale study of the 5/15-GHz spectral indices of the compact radio sources in M82. *MNRAS*, **334**, 912–924. 148, 154

Mihos, J.C. & Hernquist, L. (1994). Triggering of starbursts in galaxies by minor mergers. *ApJ*, **425**, L13–L16. 124

Mihos, J.C. & Hernquist, L. (1996). Gasdynamics and Starbursts in Major Mergers. *ApJ*, **464**, 641. 124

Miluzio, M., Cappellaro, E., Botticella, M.T., Cresci, G., Greggio, L., Mannucci, F., Benetti, S., Bufano, F., Elias-Rosa, N., Pastorello, A., Turatto, M. & Zampieri, L.

(2013). HAWK-I infrared supernova search in starburst galaxies. *A&A*, **554**, A127. 89

Minkowski, R. (1941). Spectra of Supernovae. *PASP*, **53**, 224–225. 112

Miralles-Caballero, D., Colina, L., Arribas, S. & Duc, P.A. (2011). Characterization of Optically Selected Star-Forming Knots in (U)LIRGs. *AJ*, **142**, 79. 58

Modica, F., Vavilkin, T., Evans, A.S., Kim, D.C., Mazzarella, J.M., Iwasawa, K., Petric, A., Howell, J.H., Surace, J.A., Armus, L., Spoon, H.W.W., Sanders, D.B., Wong, A. & Barnes, J.E. (2012). Multi-wavelength GOALS Observations of Star Formation and Active Galactic Nucleus Activity in the Luminous Infrared Galaxy IC 883. *AJ*, **143**, 16. 89

Monreal-Ibero, A., Arribas, S., Colina, L., Rodríguez-Zaurín, J., Alonso-Herrero, A. & García-Marín, M. (2010). VLT-VIMOS integral field spectroscopy of luminous and ultraluminous infrared galaxies. II. Evidence for shock ionization caused by tidal forces in the extra-nuclear regions of interacting and merging LIRGs. *A&A*, **517**, A28. 89

Moorwood, A.F.M. & Oliva, E. (1988). Infrared spectroscopy of forbidden Fe II, H2, and H line emission in galactic nuclei. *A&A*, **203**, 278–288. 66

Murphy, E.J. (2013). The Role of Merger Stage on Galaxy Radio Spectra in Local Infrared-bright Starburst Galaxies. *ApJ*, **777**, 58. 102

Murphy, E.J., Condon, J.J., Schinnerer, E., Kennicutt, R.C., Calzetti, D., Armus, L., Helou, G., Turner, J.L., Aniano, G., Beirão, P., Bolatto, A.D., Brandl, B.R., Croxall, K.V., Dale, D.A., Donovan Meyer, J.L., Draine, B.T., Engelbracht, C., Hunt, L.K., Hao, C.N., Koda, J., Roussel, H., Skibba, R. & Smith, J.D.T. (2011). Calibrating Extinction-free Star Formation Rate Diagnostics with 33 GHz Free-free Emission in NGC 6946. *ApJ*, **737**, 67. 6

Murphy, E.J., Stierwalt, S., Armus, L., Condon, J.J. & Evans, A.S. (2013). Radio and Mid-infrared Properties of Compact Starbursts: Distancing Themselves from the Main Sequence. *ApJ*, **768**, 2. 102

Nakai, N., Sato, N. & Yamauchi, A. (2002). Detection of Water Maser Flare in the Seyfert/LINER, NGC 6240. *PASJ*, **54**, L27–L30. 90

Narayanan, D., Groppi, C.E., Kulesa, C.A. & Walker, C.K. (2005). Warm, Dense Molecular Gas in the ISM of Starbursts, LIRGs, and ULIRGs. *ApJ*, **630**, 269–279. 20, 49

Neff, S.G., Hutchings, J.B., Standord, S.A. & Unger, S.W. (1990). NGC 1614 - an IR-luminous merger but not (yet?) an active galaxy. *AJ*, **99**, 1088–1099. 54, 68

Neff, S.G., Ulvestad, J.S. & Teng, S.H. (2004). A Supernova Factory in the Merger System Arp 299. *ApJ*, **611**, 186–199. 5, 88, 115, 119

Newton, J., Puckett, T. & Orff, T. (2010). Supernova 2010O in NGC 3690. *Central Bureau Electronic Telegrams*, **2144**, 2. 117

Norman, C. & Scoville, N. (1988). The evolution of starburst galaxies to active galactic nuclei. *ApJ*, **332**, 124–134. 124

Oliva, E., Origlia, L., Kotilainen, J.K. & Moorwood, A.F.M. (1995). Red supergiants as starburst tracers in galactic nuclei. *A&A*, **301**, 55. 93

Oliva, E., Moorwood, A.F.M., Drapatz, S., Lutz, D. & Sturm, E. (1999). Infrared spectroscopy of young supernova remnants heavily interacting with the interstellar medium. I. Ionized species in RCW 103. *A&A*, **343**, 943–952. 108

Olsson, E., Aalto, S., Thomasson, M. & Beswick, R. (2010). Star-formation in the central kpc of the starburst/LINER galaxy NGC 1614. *A&A*, **513**, A11. 54, 55, 61, 70

Osterbrock, D.E. (1989). *Astrophysics of gaseous nebulae and active galactic nuclei*. Mill Valley, CA: University Science Books. 68

Padovani, P. (1999). High energy emission from AGN and unified schemes. In F. Giovannelli & G. Mannocchi, ed., *Vulcano Workshop 1998: Frontier Objects in Astrophysics and Particle Physics*, 159. 6

Panagia, N., Van Dyk, S.D., Weiler, K.W., Sramek, R.A., Stockdale, C.J. & Murata, K.P. (2006). A Search for Radio Emission from Type Ia Supernovae. *ApJ*, **646**, 369–377. 112

REFERENCES

Papadopoulos, P.P., van der Werf, P., Xilouris, E., Isaak, K.G. & Gao, Y. (2012a). The Molecular Gas in Luminous Infrared Galaxies. II. Extreme Physical Conditions and Their Effects on the X $_{co}$ Factor. *ApJ*, **751**, 10. 43

Papadopoulos, P.P., van der Werf, P.P., Xilouris, E.M., Isaak, K.G., Gao, Y. & Mühle, S. (2012b). The molecular gas in luminous infrared galaxies - I. CO lines, extreme physical conditions and their drivers. *MNRAS*, **426**, 2601–2629. 20

Parra, R., Conway, J.E., Diamond, P.J., Thrall, H., Lonsdale, C.J., Lonsdale, C.J. & Smith, H.E. (2007). The Radio Spectra of the Compact Sources in Arp 220: A Mixed Population of Supernovae and Supernova Remnants. *ApJ*, **659**, 314–330. 65, 75, 84, 132, 136, 155

Penzias, A.A. & Wilson, R.W. (1965). A Measurement of Excess Antenna Temperature at 4080 Mc/s. *ApJ*, **142**, 419–421. 10

Pereira-Santaella, M., Diamond-Stanic, A.M., Alonso-Herrero, A. & Rieke, G.H. (2010). The Mid-infrared High-ionization Lines from Active Galactic Nuclei and Star-forming Galaxies. *ApJ*, **725**, 2270–2280. 108

Pereira-Santaella, M., Alonso-Herrero, A., Santos-Lleo, M., Colina, L., Jiménez-Bailón, E., Longinotti, A.L., Rieke, G.H., Ward, M. & Esquej, P. (2011). The X-ray emission of local luminous infrared galaxies. *A&A*, **535**, A93. 66

Perez-Olea, D.E. & Colina, L. (1995). Evolutionary models of the radio emission in compact starbursts. *MNRAS*, **277**, 857–895. 69

Perez-Olea, D.E. & Colina, L. (1996). X-Ray Emission of Active Galactic Nuclei with Circumnuclear Star-forming Rings: NGC 1097 and NGC 7469. *ApJ*, **468**, 191. 75, 76, 81

Pérez-Torres, M.A., Alberdi, A., Marcaide, J.M., Guirado, J.C., Lara, L., Mantovani, F., Ros, E. & Weiler, K.W. (2002). A distorted radio shell in the young supernova SN 1986J. *MNRAS*, **335**, L23–L28. 65

Pérez-Torres, M.A., Alberdi, A., Marcaide, J.M., Guerrero, M.A., Lundqvist, P., Shapiro, I.I., Ros, E., Lara, L., Guirado, J.C., Weiler, K.W. & Stockdale, C.J. (2005). High-resolution observations of SN 2001gd in NGC 5033. *MNRAS*, **360**, 1055–1062. 75

Pérez-Torres, M.A., Mattila, S., Alberdi, A., Colina, L., Torrelles, J.M., Väisänen, P., Ryder, S., Panagia, N. & Wilson, A. (2007). Radio Detection of Supernova 2004ip in the Circumnuclear Region of the Luminous Infrared Galaxy IRAS 18293-3413. *ApJ*, **671**, L21–L24. 84, 90, 112

Perez-Torres, M.A., Romero, C., Alberdi, A., Colina, L., Alonso-Herrero, A., Diaz Santos, T., Mattila, S., Kankare, E. & Ryder, S. (2008). Supernova 2008cs in IRAS 17138-1017. *Central Bureau Electronic Telegrams*, **1390**, 2. 84

Pérez-Torres, M.A., Alberdi, A., Colina, L., Torrelles, J.M., Panagia, N., Wilson, A., Kankare, E. & Mattila, S. (2009a). Radio monitoring of NGC 7469: late-time radio evolution of SN 2000ft and the circumnuclear starburst in NGC 7469. *MNRAS*, **399**, 1641–1649. 70, 71, 75, 112

Pérez-Torres, M.A., Romero-Cañizales, C., Alberdi, A. & Polatidis, A. (2009b). An extremely prolific supernova factory in the buried nucleus of the starburst galaxy IC 694. *A&A*, **507**, L17–L20. 5, 65, 70, 84, 119, 132, 155, 184

Pérez-Torres, M.A., Alberdi, A., Romero-Cañizales, C. & Bondi, M. (2010). Serendipitous discovery of the long-sought active galactic nucleus in Arp 299-A. *A&A*, **519**, L5+. 74, 119, 132, 156

Perez-Torres, M.A., Lundqvist, P., Beswick, R., Bjornsson, C.I., Muxlow, T.W.M., Paragi, Z., Ryder, S., Alberdi, A., Fransson, C., Marcaide, J.M., Marti-Vidal, I., Ros, E., Argo, M. & Guirado, J.C. (2014). Constraints on the progenitor system and the environs of SN 2014J from deep radio observations. *ArXiv e-prints*. 112

Petric, A.O., Armus, L., Howell, J., Chan, B., Mazzarella, J.M., Evans, A.S., Surace, J.A., Sanders, D., Appleton, P., Charmandaris, V., Díaz-Santos, T., Frayer, D., Haan, S., Inami, H., Iwasawa, K., Kim, D., Madore, B., Marshall, J., Spoon, H., Stierwalt, S., Sturm, E., U, V., Vavilkin, T. & Veilleux, S. (2011). Mid-Infrared Spectral Diagnostics of Luminous Infrared Galaxies. *ApJ*, **730**, 28. 6, 7, 108

Portegies Zwart, S.F., McMillan, S.L.W. & Gieles, M. (2010). Young Massive Star Clusters. *ARA&A*, **48**, 431–493. 155

REFERENCES

Privon, G.C., Barnes, J.E., Evans, A.S., Hibbard, J.E., Yun, M.S., Mazzarella, J.M., Armus, L. & Surace, J. (2013). Dynamical Modeling of Galaxy Mergers Using Identikit. *ApJ*, **771**, 120. 8

Puxley, P.J. & Brand, P.W.J.L. (1994). Dust Extinction in Starburst Galaxies - NGC1614 and NGC7714. *MNRAS*, **266**, 431. 68

Randriamanakoto, Z., Väisänen, P., Ryder, S., Kankare, E., Kotilainen, J. & Mattila, S. (2013). The K-band luminosity functions of super star clusters in luminous infrared galaxies, their slopes and the effects of blending. *MNRAS*, **431**, 554–569. 92, 93

Rau, U. & Cornwell, T.J. (2011). A multi-scale multi-frequency deconvolution algorithm for synthesis imaging in radio interferometry. *A&A*, **532**, A71. 91, 101

Risaliti, G., Gilli, R., Maiolino, R. & Salvati, M. (2000). The hard X-ray emission of luminous infrared galaxies. *A&A*, **357**, 13–23. 55, 90

Risaliti, G., Sani, E., Maiolino, R., Marconi, A., Berta, S., Braito, V., Della Ceca, R., Franceschini, A. & Salvati, M. (2006). The Double Active Galactic Nucleus in NGC 6240 Revealed through 3-5 μm Spectroscopy. *ApJ*, **637**, L17–L20. 95

Robitaille, T.P. & Whitney, B.A. (2010). The Present-Day Star Formation Rate of the Milky Way Determined from Spitzer-Detected Young Stellar Objects. *ApJ*, **710**, L11–L15. 4

Rodríguez-Zaurín, J., Arribas, S., Monreal-Ibero, A., Colina, L., Alonso-Herrero, A. & Alfonso-Garzón, J. (2011). VLT-VIMOS integral field spectroscopy of luminous and ultraluminous infrared galaxies. III. The atlas of the stellar and ionized gas distribution. *A&A*, **527**, A60. 89

Romero-Cañizales, C., Mattila, S., Alberdi, A., Pérez-Torres, M.A., Kankare, E. & Ryder, S.D. (2011). The core-collapse supernova rate in Arp 299 revisited. *MNRAS*, **415**, 2688–2698. 115

Romero-Cañizales, C., Pérez-Torres, M.A., Alberdi, A., Argo, M.K., Beswick, R.J., Kankare, E., Batejat, F., Efstathiou, A., Mattila, S., Conway, J.E., Garrington, S.T., Muxlow, T.W.B., Ryder, S.D. & Väisänen, P. (2012). e-MERLIN and VLBI observations of the luminous infrared galaxy IC 883: a nuclear starburst and an AGN candidate revealed. *A&A*, **543**, A72. 89, 105

Romero-Cañizales, C., Herrero-Illana, R., Pérez-Torres, M.A., Alberdi, A., Kankare, E., Bauer, F.E., Ryder, S.D., Mattila, S., Conway, J.E., Beswick, R.J. & Muxlow, T.W.B. (2014). The nature of supernovae 2010O and 2010P in Arp 299 - II. Radio emission. *MNRAS*, **440**, 1067–1079. 111, 117, 118, 119

Rosenberg, M.J.F., van der Werf, P.P. & Israel, F.P. (2012). [FeII] as a tracer of supernova rate in nearby starburst galaxies. *A&A*, **540**, A116. 66, 68, 73

Rothberg, B., Fischer, J., Rodrigues, M. & Sanders, D.B. (2013). Unveiling the σ-discrepancy. II. Revisiting the Evolution of ULIRGs and the Origin of Quasars. *ApJ*, **767**, 72. 8

Ryder, S., Mattila, S., Kankare, E. & Perez-Torres, M. (2010). Supernova 2010P. *Central Bureau Electronic Telegrams*, **2189**, 1. 116

Ryle, M. (1952). A New Radio Interferometer and Its Application to the Observation of Weak Radio Stars. *Royal Society of London Proceedings Series A*, **211**, 351–375. 10

Sanders, D. & Ishida, C. (2004). Luminous Infrared Galaxies: Optical Morphology and Photometry, Molecular Gas Masses, and Starburst/AGN Activity versus Infrared Luminosity. In S. Aalto, S. Huttemeister & A. Pedlar, eds., *The Neutral ISM in Starburst Galaxies*, vol. 320 of *Astronomical Society of the Pacific Conference Series*, 230. 8

Sanders, D.B. & Mirabel, I.F. (1996). Luminous Infrared Galaxies. *ARA&A*, **34**, 749. 2, 8, 184

Sanders, D.B., Soifer, B.T., Elias, J.H., Madore, B.F., Matthews, K., Neugebauer, G. & Scoville, N.Z. (1988). Ultraluminous infrared galaxies and the origin of quasars. *ApJ*, **325**, 74–91. 8

Sanders, D.B., Scoville, N.Z. & Soifer, B.T. (1991). Molecular gas in luminous infrared galaxies. *ApJ*, **370**, 158–171. 20, 45, 46, 47

REFERENCES

Sanders, D.B., Mazzarella, J.M., Kim, D.C., Surace, J.A. & Soifer, B.T. (2003). The IRAS Revised Bright Galaxy Sample. *AJ*, **126**, 1607–1664. 21, 24, 44, 54, 85, 86, 92, 115, 154

Sato, N., Yamauchi, A., Ishihara, Y., Sorai, K., Kuno, N., Nakai, N., Balasubramanyam, R. & Hall, P. (2005). Water-Vapor Maser Survey for Active Galactic Nuclei: A Megamaser in NGC 6926. *PASJ*, **57**, 587–594. 90, 91

Schlegel, E.M. (1990). A new subclass of Type II supernovae? *MNRAS*, **244**, 269–271. 112

Scoville, N., Aussel, H., Sheth, K., Scott, K.S., Sanders, D., Ivison, R., Pope, A., Capak, P., Vanden Bout, P., Manohar, S., Kartaltepe, J., Robertson, B. & Lilly, S. (2014). The Evolution of Interstellar Medium Mass Probed by Dust Emission: ALMA Observations at z = 0.3-2. *ApJ*, **783**, 84. 45

Scoville, N.Z., Evans, A.S., Thompson, R., Rieke, M., Hines, D.C., Low, F.J., Dinshaw, N., Surace, J.A. & Armus, L. (2000). NICMOS Imaging of Infrared-Luminous Galaxies. *AJ*, **119**, 991–1061. 89

Shao, L., Lutz, D., Nordon, R., Maiolino, R., Alexander, D.M., Altieri, B., Andreani, P., Aussel, H., Bauer, F.E., Berta, S., Bongiovanni, A., Brandt, W.N., Brusa, M., Cava, A., Cepa, J., Cimatti, A., Daddi, E., Dominguez-Sanchez, H., Elbaz, D., Förster Schreiber, N.M., Geis, N., Genzel, R., Grazian, A., Gruppioni, C., Magdis, G., Magnelli, B., Mainieri, V., Pérez García, A.M., Poglitsch, A., Popesso, P., Pozzi, F., Riguccini, L., Rodighiero, G., Rovilos, E., Saintonge, A., Salvato, M., Sanchez Portal, M., Santini, P., Sturm, E., Tacconi, L.J., Valtchanov, I., Wetzstein, M. & Wieprecht, E. (2010). Star formation in AGN hosts in GOODS-N. *A&A*, **518**, L26. 8

Shields, J.C. (1992). Normal O stars in dense media generate LINERs. *ApJ*, **399**, L27–L30. 7

Shlosman, I., Begelman, M.C. & Frank, J. (1990). The fuelling of active galactic nuclei. *Nature*, **345**, 679–686. 124

Simkin, S.M., Su, H.J. & Schwarz, M.P. (1980). Nearby Seyfert galaxies. *ApJ*, **237**, 404–413. 124

Skrutskie, M.F., Cutri, R.M., Stiening, R., Weinberg, M.D., Schneider, S., Carpenter, J.M., Beichman, C., Capps, R., Chester, T., Elias, J., Huchra, J., Liebert, J., Lonsdale, C., Monet, D.G., Price, S., Seitzer, P., Jarrett, T., Kirkpatrick, J.D., Gizis, J.E., Howard, E., Evans, T., Fowler, J., Fullmer, L., Hurt, R., Light, R., Kopan, E.L., Marsh, K.A., McCallon, H.L., Tam, R., Van Dyk, S. & Wheelock, S. (2006). The Two Micron All Sky Survey (2MASS). *AJ*, **131**, 1163–1183. 73

Smartt, S.J. (2009). Progenitors of Core-Collapse Supernovae. *ARA&A*, **47**, 63–106. 71, 112

Smith, D.A., Herter, T., Haynes, M.P., Beichman, C.A. & Gautier, T.N., III (1995). The luminous starburst galaxy UGC 8387. *ApJ*, **439**, 623–636. 89

Smith, N., Li, W., Filippenko, A.V. & Chornock, R. (2011). Observed fractions of core-collapse supernova types and initial masses of their single and binary progenitor stars. *MNRAS*, **412**, 1522–1538. 113

Soifer, B.T. & Neugebauer, G. (1991). The properties of infrared galaxies in the local universe. *AJ*, **101**, 354–361. 2

Soifer, B.T., Boehmer, L., Neugebauer, G. & Sanders, D.B. (1989). The IRAS Bright Galaxy Sample. IV - Complete IRAS observations. *AJ*, **98**, 766–797. 2

Soifer, B.T., Neugebauer, G., Matthews, K., Egami, E., Weinberger, A.J., Ressler, M., Scoville, N.Z., Stolovy, S.R., Condon, J.J. & Becklin, E.E. (2001). High-Resolution Mid-Infrared Imaging of Infrared-Luminous Starburst Galaxies. *AJ*, **122**, 1213–1237. 73

Solomon, P.M., Downes, D. & Radford, S.J.E. (1992). Warm molecular gas in the primeval galaxy IRAS 10214 + 4724. *ApJ*, **398**, L29–L32. 26

Solomon, P.M., Downes, D., Radford, S.J.E. & Barrett, J.W. (1997). The Molecular Interstellar Medium in Ultraluminous Infrared Galaxies. *ApJ*, **478**, 144–161. 20, 43

Soria, R. & Wu, K. (2003). Properties of discrete X-ray sources in the starburst spiral galaxy M 83. *A&A*, **410**, 53–74. 75

REFERENCES

Stierwalt, S., Armus, L., Surace, J.A., Inami, H., Petric, A.O., Diaz-Santos, T., Haan, S., Charmandaris, V., Howell, J., Kim, D.C., Marshall, J., Mazzarella, J.M., Spoon, H.W.W., Veilleux, S., Evans, A., Sanders, D.B., Appleton, P., Bothun, G., Bridge, C.R., Chan, B., Frayer, D., Iwasawa, K., Kewley, L.J., Lord, S., Madore, B.F., Melbourne, J.E., Murphy, E.J., Rich, J.A., Schulz, B., Sturm, E., Vavilkin, T. & Xu, K. (2013). Mid-infrared Properties of Nearby Luminous Infrared Galaxies. I. Spitzer Infrared Spectrograph Spectra for the GOALS Sample. *ApJS*, **206**, 1. 7, 44, 45, 86, 88, 90, 105, 108

Sturm, E., Lutz, D., Tran, D., Feuchtgruber, H., Genzel, R., Kunze, D., Moorwood, A.F.M. & Thornley, M.D. (2000). ISO-SWS spectra of galaxies: Continuum and features. *A&A*, **358**, 481–493. 105

Swift, L. (1893). New Nebulæ, discovered by Lewis Swift at Warner Observatory Rochester, New York . *MNRAS*, **53**, 273. 183

Taylor, G.B., Carilli, C.L. & Perley, R.A., eds. (1999). *Synthesis Imaging in Radio Astronomy II*, vol. 180 of *Astronomical Society of the Pacific Conference Series*. 14

Terashima, Y. & Wilson, A.S. (2003). Chandra Snapshot Observations of Low-Luminosity Active Galactic Nuclei with a Compact Radio Source. *ApJ*, **583**, 145–158. 119

Tinney, C.G., Scoville, N.Z., Sanders, D.B. & Soifer, B.T. (1990). Molecular gas in intermediate luminosity IRAS galaxies. *ApJ*, **362**, 473–479. 20

Toomre, A. & Toomre, J. (1972). Galactic Bridges and Tails. *ApJ*, **178**, 623–666. 8

U, V., Sanders, D.B., Mazzarella, J.M., Evans, A.S., Howell, J.H., Surace, J.A., Armus, L., Iwasawa, K., Kim, D.C., Casey, C.M., Vavilkin, T., Dufault, M., Larson, K.L., Barnes, J.E., Chan, B.H.P., Frayer, D.T., Haan, S., Inami, H., Ishida, C.M., Kartaltepe, J.S., Melbourne, J.L. & Petric, A.O. (2012). Spectral Energy Distributions of Local Luminous and Ultraluminous Infrared Galaxies. *ApJS*, **203**, 9. 43, 46, 73

Ulvestad, J.S. (2009). Radio Emission from Young Supernovae and Supernova Remnants in Arp 299. *AJ*, **138**, 1529–1538. 84, 88, 116, 119, 120, 132, 133, 184

Umemura, M. (2001). A Radiation-Hydrodynamical Model for Supermassive Black Hole-to-Bulge Mass Relation and Quasar Formation. *ApJ*, **560**, L29–L32. 124

Umemura, M., Fukue, J. & Mineshige, S. (1997). Radiative Avalanche: Starburst-induced Fueling to Active Galactic Nuclei. *ApJ*, **479**, L97. 124

Väisänen, P., Rajpaul, V., Zijlstra, A.A., Reunanen, J. & Kotilainen, J. (2012). The nuclear polycyclic aromatic hydrocarbon emission of merger system NGC 1614: rings within rings. *MNRAS*, **420**, 2209–2220. 54, 55, 57

van den Bergh, S. (1997). Distribution of Supernovae in Spiral Galaxies. *AJ*, **113**, 197. 126

van der Kruit, P.C. (1973). High-resolution Radio Continuum Observations of Bright Spiral Galaxies at 1415 MHz: A General Discussion. *A&A*, **29**, 263. 5

Vanzi, L. & Rieke, G.H. (1997). Infrared Spectroscopy of Blue Dwarf Galaxies. *ApJ*, **479**, 694. 66

Vardoulaki, E., Charmandaris, V., Murphy, E.J., Diaz-Santos, T., Armus, L., Evans, A., Mazzarella, J.M., Privon, G.C., Stierwalt, S. & Barcos-Munoz, L. (2014). Radio continuum properties of luminous infrared galaxies. Identifying the presence of an AGN in the radio. *ArXiv e-prints*. 108

Vega, O., Clemens, M.S., Bressan, A., Granato, G.L., Silva, L. & Panuzzo, P. (2008). Modelling the spectral energy distribution of ULIRGs. II. The energetic environment and the dense interstellar medium. *A&A*, **484**, 631–653. 89

Veilleux, S., Kim, D.C., Sanders, D.B., Mazzarella, J.M. & Soifer, B.T. (1995). Optical Spectroscopy of Luminous Infrared Galaxies. II. Analysis of the Nuclear and Long-Slit Data. *ApJS*, **98**, 171. 2, 89, 90, 91

REFERENCES

Veilleux, S., Kim, D.C., Rupke, D.S.N., Peng, C.Y., Tacconi, L.J., Genzel, R., Lutz, D., Sturm, E., Contursi, A., Schweitzer, M., Dasyra, K.M., Ho, L.C., Sanders, D.B. & Burkert, A. (2009). A Deep Hubble Space Telescope H-Band Imaging Survey of Massive Gas-Rich Mergers. II. The QUEST QSOs. *ApJ*, **701**, 587–606. 8

Voelk, H.J. (1989). The correlation between radio and far-infrared emission for disk galaxies - A calorimeter theory. *A&A*, **218**, 67–70. 6

Vorontsov-Velyaminov, B.A. (1959). Atlas and catalog of interacting galaxies. 1959, Sternberg Institute, Moscow State University. In *Atlas and catalog of interacting galaxies (1959)*, 0. 184

Wada, K. & Norman, C.A. (2002). Obscuring Material around Seyfert Nuclei with Starbursts. *ApJ*, **566**, L21–L24. 124, 131, 154

Wang, J., Deng, J.S. & Wei, J.Y. (2010). Ongoing star formation in AGN host galaxy discs: a view from core-collapse supernovae. *MNRAS*, **405**, 2529–2533. 154

Webb, D. (1996). Arp's Peculiar Galaxies (Webb 1996). *VizieR Online Data Catalog*, **7192**, 0. 183

Weedman, D.W., Feldman, F.R., Balzano, V.A., Ramsey, L.W., Sramek, R.A. & Wuu, C.C. (1981). NGC 7714 - The prototype star-burst galactic nucleus. *ApJ*, **248**, 105–112. 4

Weedman, D.W., Hao, L., Higdon, S.J.U., Devost, D., Wu, Y., Charmandaris, V., Brandl, B., Bass, E. & Houck, J.R. (2005). Mid-Infrared Spectra of Classical AGNs Observed with the Spitzer Space Telescope. *ApJ*, **633**, 706–716. 108, 109

Weiler, K.W., Panagia, N., Montes, M.J. & Sramek, R.A. (2002). Radio Emission from Supernovae and Gamma-Ray Bursters. *ARA&A*, **40**, 387–438. 84, 113

Weliachew, L., Fomalont, E.B. & Greisen, E.W. (1984). Radio observations of H I and OH in the center of the galaxy M 82. *A&A*, **137**, 335–342. 148

Wills, K.A., Pedlar, A., Muxlow, T.W.B. & Wilkinson, P.N. (1997). Low-frequency observations of supernova remnants in M82. *MNRAS*, **291**, 517. 148

Wilson, C.D., Petitpas, G.R., Iono, D., Baker, A.J., Peck, A.B., Krips, M., Warren, B., Golding, J., Atkinson, A., Armus, L., Cox, T.J., Ho, P., Juvela, M., Matsushita, S., Mihos, J.C., Pihlstrom, Y. & Yun, M.S. (2008). Luminous Infrared Galaxies with the Submillimeter Array. I. Survey Overview and the Central Gas to Dust Ratio. *ApJS*, **178**, 189–224. 55

Woo, J.H. & Urry, C.M. (2002). Active Galactic Nucleus Black Hole Masses and Bolometric Luminosities. *ApJ*, **579**, 530–544. 6

Wu, Y., Charmandaris, V., Huang, J., Spinoglio, L. & Tommasin, S. (2009). Spitzer/IRS 5-35 μm Low-resolution Spectroscopy of the 12 μm Seyfert Sample. *ApJ*, **701**, 658–676. 105

Xu, C.K., Cao, C., Gao, Y., Díaz-Santos, T., Herrero-Illana, R., Meijerink, R., Privon, G., Zhao, Y.H., S., E.A., König, S., Mazzarella, J.M., Aalto, S., Appleton, P., Armus, L., Charmandaris, V., Chu, J., Haan, S., Inami, H., Murphy, E.J., Sanders, D.B., Schultz, B. & van der Werf, P. (2014). ALMA observations of CO (6-5) and 435 μm continuum in NGC 1614. *Submitted to ApJ*. 79

Yamaoka, H., Kato, T., Filippenko, A.V., van Dyk, S.D., Yamamoto, M., Balam, D., Hornoch, K. & Plsek, M. (1998). Supernova 1998T in NGC 3690. *IAU Circ.*, **6859**, 1. 184

Yao, L., Seaquist, E.R., Kuno, N. & Dunne, L. (2003). CO Molecular Gas in Infrared-luminous Galaxies. *ApJ*, **588**, 771–791. 20, 43

Young, J.S. & Sanders, D.B. (1986). Distributions of (C-13)O emission in the disks of late-type spiral galaxies. *ApJ*, **302**, 680–692. 47

Young, J.S. & Scoville, N.Z. (1991). Molecular gas in galaxies. *ARA&A*, **29**, 581–625. 43

Young, J.S., Schloerb, F.P., Kenney, J.D. & Lord, S.D. (1986). CO observations of infrared bright galaxies - The efficiency of star formation. *ApJ*, **304**, 443–458. 43

REFERENCES

Young, J.S., Xie, S., Kenney, J.D.P. & Rice, W.L. (1989). Global properties of infrared bright galaxies. *ApJS*, **70**, 699–722. 43

Yuan, T.T., Kewley, L.J. & Sanders, D.B. (2010). The Role of Starburst-Active Galactic Nucleus Composites in Luminous Infrared Galaxy Mergers: Insights from the New Optical Classification Scheme. *ApJ*, **709**, 884–911. 2, 55, 89

Yun, M.S., Reddy, N.A. & Condon, J.J. (2001). Radio Properties of Infrared-selected Galaxies in the IRAS 2 Jy Sample. *ApJ*, **554**, 803–822. 6, 92

Zaragoza-Cardiel, J., Font-Serra, J., Beckman, J.E., Blasco-Herrera, J., García-Lorenzo, B., Camps, A., Gonzalez-Martin, O., Ramos Almeida, C., Loiseau, N. & Gutiérrez, L. (2013). Kinematics of Arp 270: gas flows, nuclear activity and two regimes of star formation. *MNRAS*, **432**, 998–1009. 66

A

List of publications related to this Thesis

1. Bondi, M., Pérez-Torres, M.Á., **Herrero-Illana**, **R.** & Alberdi, A. (2012). The nuclear starburst in Arp 299-A: from the 5.0 GHz VLBI radio light-curves to its core-collapse supernova rate. *A&A*, **539**, A134.

2. **Herrero-Illana**, **R.**, Pérez-Torres, M.Á. & Alberdi, A. (2012a). Evidence of nuclear disks in starburst galaxies from their radial distribution of supernovae. *A&A*, **540**, L5.

3. **Herrero-Illana**, **R.**, Romero-Cañizales, C., Pérez-Torres, M.Á, Alberdi, A., Kankare, E., Mattila, S. & Ryder, S.D. (2012b). Radio detection of the near-IR discovered supernova 2010P. *The Astronomer's Telegram*, **4432**, 1.

4. Kankare, E., Mattila, S., Ryder, S., Fraser, M., Pastorello, A., Elias-Rosa, N., Romero-Cañizales, C., Alberdi, A., Hentunen, V.P.,

A. LIST OF PUBLICATIONS RELATED TO THIS THESIS

Herrero-Illana, **R.**, Kotilainen, J., Pérez-Torres, M.Á. & Väisänen, P. (2014). The nature of supernovae 2010O and 2010P in Arp 299 - I. Near-infrared and optical evolution. *MNRAS*, **440**, 1052–1066.

5. Romero-Cañizales, C., **Herrero-Illana**, **R.**, Pérez-Torres, M.Á., Alberdi, A., Kankare, E., Bauer, F.E., Ryder, S.D., Mattila, S., Conway, J.E., Beswick, R.J. & Muxlow, T.W.B. (2014). The nature of supernovae 2010O and 2010P in Arp 299 - II. Radio emission. *MNRAS*, **440**, 1067–1079.

6. **Herrero-Illana**, **R.**, Pérez-Torres, M.Á., Alonso-Herrero, A., Alberdi, A., Colina, L., Efstathiou, A., Hernández-García, L., Miralles-Caballero, D., Väisänen, P., Packham, C.C., Rajpaul, V. & Zijlstra, A.A. (2014). A Multi-wavelength View of the Central Kiloparsec Region in the Luminous Infrared Galaxy NGC 1614. *ApJ*, **786**, 156.

7. Xu, C.K., Cao, C., Gao, Y., Díaz-Santos, T., **Herrero-Illana**, **R.**, Meijerink, R., Privon, G., Zhao, Y.H., S., E.A., König, S., Mazzarella, J.M., Aalto, S., Appleton, P., Armus, L., Charmandaris, V., Chu, J., Haan, S., Inami, H., Murphy, E.J., Sanders, D.B., Schultz, B. & van der Werf, P. (2014). ALMA observations of CO (6-5) and 435 μm continuum in NGC 1614. *Submitted to ApJ*.

In preparation:

8. **Herrero-Illana**, **R.**, Randriamanakoto, Z., et al. (2014). A near-IR and radio comparative study of a sample of LIRGs. *In preparation.*

9. **Herrero-Illana**, **R.**, Privon, G.C., et al. (2014). The kinematics and compactness of molecular gas in LIRGs from the GOALS sample. *In preparation.*

10. Privon, G.C., **Herrero-Illana**, **R.**, et al. (2014). What do HCN $(1-0)$ and HCO^+ $(1-0)$ tell us about the dense gas in local Luminous Infrared Galaxies? *In preparation.*

B

IC 694 & NGC 3690: a tale of confusion

There is a known problem in the designation of the components of Arp 299 (see Fig. B.1, where I have labeled the sources in the system). A nicely written historical review of this confusion can be found in Hibbard & Yun (1999). In short, the problem came with the ambiguous description of IC 694 as a *"close double with NGC 3690"* by Swift (1893). The solution to the problem lays in wether believing that Swift, using a 40 cm refractor at the Rochester Observatory, was able to detect the faint galaxy to the northwest of the system (③ in Fig. B.1), or on the contrary, he was just referring to ① and ②.

To make this story more bizarre, due to a typographical error, the original *Atlas of Peculiar Galaxies* identified the interacting galaxies NGC 3690 and IC 694 (whatever that meant) with Arp 296 (*sic*, see Table 1 in Arp, 1966). The revised catalogue by Webb (1996) changed this designation to Arp 299, while Arp 296 appears since then to be accepted as a small background spiral galaxy $2.5'$ to the northeast of the controversial system (④ in Fig. B.1).

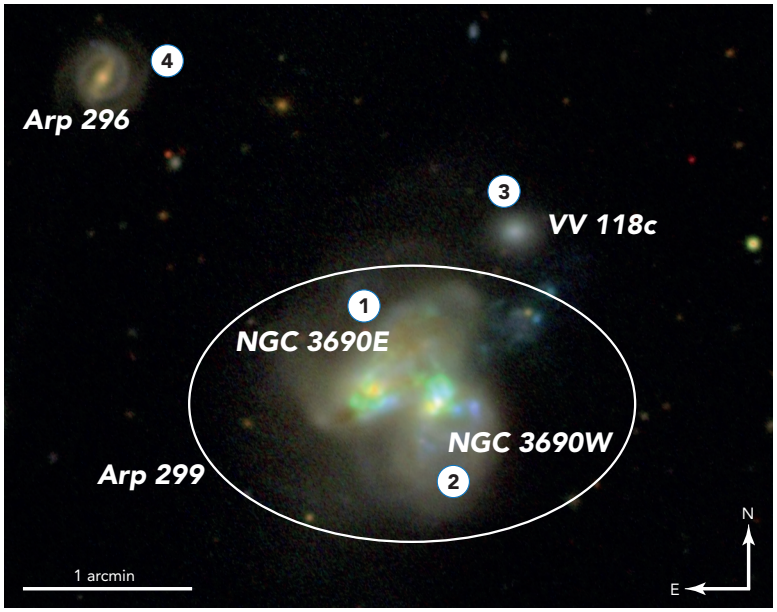

Figure B.1: SDSS DR9 color composite of the region around Arp 299 - The figure illustrates the naming convention followed in this thesis. Numbers besides each galaxy are drawn for clarity in the discussion of the historical confusion in the designation of each galaxy (see main text).

In the practice, the designation in recent works does not show consensus: while many groups consider Arp 299 to be formed by IC 694 ① and NGC 3690 ② (e.g., Sanders & Mirabel, 1996; Alonso-Herrero *et al.*, 2000; Ulvestad, 2009; Pérez-Torres *et al.*, 2009b; Anderson *et al.*, 2011), others identify IC 694 with ③, a small lenticular galaxy to the northwest of the main system (e.g., Yamaoka *et al.*, 1998; Corwin, 2004).

Beyond the curious story, it is important to proceed with caution, since it can yield to important errors (e.g., the misidentification of SN1998T in Jha *et al.*, 1998). Despite the more general use of ① being identified with IC 694, we note that Simbad (Sesame) and NED name resolvers follow the notes by Corwin (2004), who claims IC 694 to be the northwest galaxy ③, leading to often mistakes.

In this thesis, we have avoided the use of the polemic designation IC 694. Instead, we use the convention shown in Fig. B.1, with NGC 3690E and NGC 3690W being the east and west components of Arp 299, respectively, and denote ③ with the alternative designation VV 118c (from the catalogue by Vorontsov-Velyaminov, 1959). When referring to the radio structures in the system, we use the designation by Gehrz *et al.*

(1983, see Fig. 4.2), where Arp 299-A is the brightest radio structure in NGC 3690E, and Arp 299-B is the main radio knot in NGC 3690W.